

Production, Deceleration, and Detection of OH Radicals

by

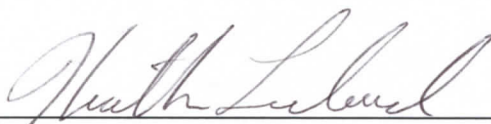
Travis C. Briles

B.S., University of Texas-Austin, 2008

A thesis submitted to the
Faculty of the Graduate School of the
University of Colorado in partial fulfillment
of the requirements for the degree of
Doctor of Philosophy
Department of Physics

2015

This thesis entitled:
Production, Deceleration, and Detection of OH Radicals
written by Travis C. Briles
has been approved for the Department of Physics



Heather J. Lewandowski



Eric Cornell

Date 25 June 15

The final copy of this thesis has been examined by the signatories, and we find that both the content and the form meet acceptable presentation standards of scholarly work in the above mentioned discipline.

, Travis C. Briles (Ph.D., Physics)

Production, Deceleration, and Detection of OH Radicals

Thesis directed by Prof. Heather J. Lewandowski

Samples of cold and ultracold polar molecules have the potential to revolutionize physical chemistry, precision measurement, and few-body quantum physics. This thesis describes experimental results for the production of cold samples of OH radicals by Stark deceleration of a supersonic beam. Since Stark deceleration cannot increase the phase space density of the sample, the initial production stage of the OH molecule is critical. The first set of experiments describes a general methodology for the production of OH beams with maximal phase space density, as well as the subsequent coupling to a Stark decelerator. Additionally, we describe the redesign of our electrostatic trap, optimized for future collision experiments of OH with co-trapped ultracold Rb atoms. The new design resulted in a 15-fold increase in total number of trapped molecules over the previous design when tested with ND₃ molecules. The second set of experiments focuses on laser-based detection of OH molecules at the exit of the decelerator based on laser induced fluorescence (LIF) and resonance enhanced multiphoton ionization (REMPI). The latter method uses vacuum-ultraviolet light at 118nm produced by third-harmonic generation in Xe/Ar gas mixtures as the ionizing step. The sensitivity of this latter technique is limited by the attainable photon flux of the ionizing radiation at 118nm. We present detailed measurements of the conversion efficiencies as well as absolute photon fluxes. Strategies to overcome these limitations as well as prospects for detection of OH molecules in a trap are discussed.

Dedication

To my father, David Briles, my first and most important scientific mentor, who taught me at a young age the importance of having a good bullshit detector.

Acknowledgements

This thesis would not have been possible without the help of many people. First, I would like to thank Heather Lewandowski for being my advisor and the other members of the Lewandowski lab that have helped with “nitty gritty” experimental details throughout the years. To this day, I am in awe of Noah Fitch’s deep understanding of electronics as well as how insightful he was even about topics that were completely new to him. I have found Yomay Shyur to be one of the most helpful and diligent people I’ve ever worked with. The time spent working with her on molecule trapping experiments is surely among my most productive and most enjoyable grad school experiences. I also wish to thank Maya Fabrikant, whose creativity always prompted me to think about things in a slightly different way. More recent additions to the lab who also deserve thanks include John Gray (who is taking over my experiments), Philip Schmid, James Greenberg, Ian Collet, and Kevin Loeffler.

I have also greatly valued input from those in the cold molecule meetings between our lab members of the EDM experiment (Cornell/Ye) and the YO (Ye) and OH (Ye) experiments. I have found the discussions at those meetings to be thought provoking and very insightful. Ultimately they have been one of the highlights of my graduate school experience. Outside of our formal meetings, I should acknowledge the frequent “hallway conversations” with Hao Wu and Dave Reens over the years that have greatly contributed to my understanding of cold OH molecules.

If any of the experiments at JILA are worthwhile, it is only possible because of the help from JILA’s world-famous technical support staff. Those who helped me the most during my time at JILA were in the instrument and electronics shop. In the instrument shop I would like to thank Hans Greene, Blaine Horner, Tracy Keep, Dave Alchenberger, Kim Hagen, Todd Asnicar, Ariel Paul, and Kels Detra. On the

electronics shop side, I have been helped immensely by Terry Brown, Carl Sauer, Mike Whitmore, and James Fung-a-Fat.

Though it didn't always seem like it, an important part of my grad school experience was found outside the lab. I have been very fortunate to have a very supportive group of friends in Boulder. These include the group I met during my first year of grad school including Kevin Mistry, Yancey Sechrest, Eric Blanshan, Tory Carr, Stephen Parham, and Carrie Delyser. I must also thank Holly Leopardi, whose support over the last year was absolutely invaluable.

My family deserves a very special "thank you". Here in Boulder, I have been treated to monthly visits to Aunt Susan and Uncle Duane Kniebes's house for dinner with their son Van. Susan deserves special recognition for doing the world's best job of editing this thesis. My nuclear family is unfortunately somewhat farther away. The support I've gotten from my parents, David and Marilyn, (literally from day one), and my appreciation for it, cannot be described in words. I can only hope that people see the qualities in me that I admire most about them: hard work, honesty, and concern for others. Though my sister, Rachel, and I have always gotten along, we have only become closer over the last several years. The care package (complete with drawings!) she sent me some years ago ranks as one of my all-time favorite gifts. Though they don't know it yet, her amazing children, Khôi and Shiloh, have brought me a great deal of joy and have played a very important role in buoying me up. I can't wait until they are old enough for long conversations and science projects.

Contents

Chapter	
1	INTRODUCTION: Why Cold Molecules? 1
1.0.1	General Features of Cold Gases 1
1.1	Routes to Cold Molecules: “Real cooling” vs. “slowing/filtering” 2
1.2	This Thesis 5
2	The OH Molecule 7
2.1	Introduction 7
2.2	Molecular Energy Level Structure 7
2.3	Classification of Electronic States 9
2.4	Hund’s Coupling Cases and “Good” Quantum Numbers 10
2.4.1	Hund’s Cases and Spatial Inversion Symmetry 13
2.5	OH Electronic Structure 14
2.6	$^2\Pi$ Rotational and Spin-Orbit Energy Level Structure 16
2.6.1	Λ -Doubling and Parity 19
2.7	$A^2\Sigma^+$ Excited State 20
2.8	OH in External Fields 22
2.8.1	OH Stark Effect: Strong Fields 23
2.8.2	OH Zeeman Shift 33

3	Molecular Beams	37
3.1	Introduction	37
3.2	Molecular Flow Regimes	39
3.3	Basic Thermodynamics of Supersonic Beams	40
3.4	Pulsed Supersonic Beams	44
3.4.1	Pulsed Valve “Shutter Function” and Effective Valve Diameter	45
3.4.2	Distribution of Molecular Velocities in a Supersonic Beam	54
3.4.3	Skimmers	56
3.5	Radical Sources: Beyond the Gas Bottle	61
3.6	Radical Beams via UV Photolysis	61
3.6.1	Photolysis of HNCO	61
3.6.2	Estimated Radical Yields	63
3.7	Basic Physics of Gas Discharges	67
3.7.1	Radical Beams by Discharge	69
3.8	Cold OH Beams Generated in Glow Discharge of Kr/H_2O	70
3.8.1	Experimental Setup	72
3.8.2	Glow Discharge Stability: Discharge Current and “Ballast” Resistor	78
3.9	Production of Cold OH Beams Optimized for Loading Stark Decelerator	79
3.9.1	Effect of Stagnation Pressure, P_0	80
3.9.2	Skimmer Interference	82
3.9.3	Dependence on Ignition Time	84
3.9.4	Total OH Yield?	84
4	Stark Deceleration and Trapping	88
4.1	Introduction	88
4.2	Liouville’s Theorem and Phase-Space	89
4.3	Determining Longitudinal Motion in a Stark Decelerator	94

4.3.1	First Order Approximations	94
4.3.2	Time Averaged Effective Potential	100
4.3.3	Calculating the Timing Sequence	103
4.4	Experimental Setup	104
4.5	Coupling a Supersonic Beam to a Stark Decelerator	105
4.6	Deceleration	109
4.6.1	Experimental Results of ND ₃ and OH Deceleration	109
4.7	Electrostatic Trapping	113
4.7.1	Model Fields for Quadrupole Trap	114
4.7.2	Trap Design and Loading Strategies	115
4.7.3	Experimental Results of Trap Optimzation	122
5	118nm Generation	129
5.1	Introduction	129
5.2	Experimental Setup for Third-Harmonic Generation	130
5.2.1	355 nm Laser	130
5.2.2	Xe/Ar Cell	132
5.2.3	MgF2 Lens Holder	133
5.2.4	Vacuum Level and Gas Purity	134
5.2.5	VUV Detection	135
5.3	Theory of Non-Resonant Third-Harmonic Generation	135
5.3.1	Phase Matching Techniques	138
5.3.2	Conversion Efficiency	142
5.4	Limitations to Conversion Efficiency	145
5.4.1	Kerr Nonlinearity	145
5.4.2	Bandwidth Considerations	146
5.4.3	Linear Absorption at Third Harmonic	149

5.4.4	Optical Breakdown	152
5.5	Conclusions	156
6	Molecular Detection	159
6.1	Monitoring Molecular Absorption	159
6.2	A Simple, Compact VUV Vacuum Photodiode	161
6.2.1	Metal Photocathodes for Detection of VUV Light	161
6.2.2	Basic Operating Principles of Vacuum Photodiodes	162
6.2.3	Design and Performance of Homebuilt Vacuum Photodiode	165
6.3	Introduction to Ionization Spectroscopy:Application to ND ₃	171
6.4	The Micro Channel Plate	173
6.4.1	RM Jordan Dual Chevron Detectors	174
6.4.2	Time of Flight Mass Spectrometers (TOFMS)	176
6.4.3	2+1 REMPI of ND ₃ near 317nm	182
6.5	Detection of OH	186
6.5.1	The AX Band	186
6.5.2	LIF Detection on the AX(1,0) band	191
6.5.3	OH Ionization Schemes	199
	Bibliography	205
	Appendix	
A	OH Cheat Sheets	221
B	Analytic Results for Modeling Supersonic Beam Properties	224
B.1	Centerline Flow Properties	224
B.1.1	The Method of Characteristics-Spatial Dependence of the Mach Number	226
B.2	Departures from the Idealized Continuum Model/Transition to Nonequilibrium conditions . .	229

B.2.1 2–body collision Rates in the Expansion 230

Tables

Table

2.1	Diatomic molecular term symbols. Possible values of the projection of \mathbf{L} on the internuclear axis (Λ) are listed on the lefthand column and the corresponding molecular term symbol is shown on the right (capital Greek letter). The analogous atomic term symbol for the total orbital angular momentum, L , is shown in parentheses.	10
3.1	NH $a^1\Delta(\nu = 0)$ radical photolysis yields from various precursors. Values of γ_{pd} for HNCO at $193nm$ are based on measurements of the H/NCO channel which imply a range of values from 0.95-0.64. A value of 0.7 is given in the table as a reasonable lower bound, which is in reasonable agreement with absolute measurements at $221.9nm$. Dissociation probabilities in the next to last column are calculated assuming a laser fluence at $193nm$ of $\frac{\Phi_p}{A} \approx 1 \times 10^{17} [\#/cm^2]$	66
3.2	OH $X^2\Pi$ radical photolysis yields from various precursors.	66
4.1	Relative Fourier coefficients (See Eq. 4.13) of the electric field magnitude $ \mathbf{E} (\theta)$ and the potential energy $W(\theta)$ for OH and ND ₃ molecules.	98

4.2	Calculated parameters for a hypothetical perfect quadrupole trap charged to $\Delta V = 2 \times 11kV$, with a single ring electrode of inner radius $R = 5.0mm$ and end cap electrodes at axial positions $z' = R/\sqrt{2}$. Note that the depth is the same in the transverse and longitudinal directions. To facilitate comparison with other types of traps (for instance magnetostatic traps from permanent magnets or optical dipole traps), the depths and associated potential gradients ($\frac{\partial}{\partial z}$ or $\frac{\partial}{\partial \rho}$) are expressed in units of temperature.	115
4.3	435 Trap Parameters for Nominal Voltage of 11kV	126
4.4	Summary of decelerator parameters for coupling to 435 Trap at 11kV. The calculation for the required phase angle assumes an ND ₃ with an initial velocity of 415m/s and an OH beam with $v_i = 436m/s$. The first phase angle is for $n = 149$ stages and the second number in parentheses is for $n = 148$ stages. The choice between these is determined by whether or not the first deceleration stage with only <i>two</i> pairs of electrodes is used. (See discussion in Sec. 4.4.)	126
5.1	Collisional broadening parameters for Xe lines near 118 nm. The last three columns give the expected width in units of $[cm^{-1}/Torr]$. Quenching rate constants of the Xe ($^2P_{3/2})5d[\frac{3}{2}]$ state for Xe and Ar buffer gas taken from [1]. Values of κ are given in $\times 10^{-10} [cm^3 s^{-1}]$, and values of a_i are given in $\times 10^6 [Torr^{-1} s^{-1}]$. The inferred contribution to the line width due to this collisional quenching $\Delta\nu_c$ is given in $[MHz/Torr]$. The natural lifetime given for Xe ($^2P_{3/2})5d[\frac{3}{2}]$ is based on the natural lifetime measurement $\tau = 1.4ns$ given in Ref [2]. It has value $115MHz = 0.00379cm^{-1}$	151
6.1	Spectroscopic constants for the OH AX band in units of $[cm^{-1}]$. A more comprehensive list can be found in Ref [3].	188
6.2	Selected vibrational spontaneous emission coefficients, $A_{\nu',\nu''}$ and oscillator strengths, $f_{\nu',\nu''}$ of the OH AX(ν',ν'') band taken from [3].	188

6.3 Summary of measured filter fractional transmissions of various filters at different wavelengths (T_λ) for OH LIF detection. Columns 6 and 7 gives the ratio of transmission at the fluorescence wavelength of 313 nm to the excitation light at 282 nm and the red-shifted light. (The exact wavelength of 420 nm is not important.) A plot of the transmission of these filters is shown in Fig. 6.23a. The abbreviations for the filter type are: CG= colored glass (absorptive), DC = dielectric coating (interference). The filter from Laser Optik is designed to be a high reflectivity mirror at 282 nm, having high transmission at 313 nm. The filter from Omega is a narrow bandpass filter. 196

Figures

Figure

- | | | |
|-----|---|---|
| 1.1 | Overview of production methods (left) and possible applications (right) as a function of the temperature and phase space density (as of 2009). Figure from [4] | 2 |
| 1.2 | “Real cooling” techniques for the direct production of cold molecules. In the top two examples, buffer gas cooling and evaporation, entropy is carried away by a material particle. In the lower two examples, laser doppler cooling and sisyphus/1-photon cooling, entropy is carried away by a spontaneously emitted photon. For details and references, see text. | 3 |
| 1.3 | Slowing and filtering cold molecule techniques. In contrast the cooling methods depicted in Fig. 1.2, these methods do not result in an increase in phase space density. These include mechanical beam deceleration (left) such as the centrifuge decelerator and the rotating nozzle technique, velocity filtering of slow cryogenic beams (top right) and electromagnetic beam deceleration (bottom) with either pulsed electric (Stark) or magnetic (Zeeman) fields. For details and references, see text. | 5 |
| 1.4 | Three basic steps for the production of cold molecules with a Stark decelerator. Step 1 (a) is the formation of a fast, but cold, supersonic beam of polar molecules. In step 2 (b) some fraction of the beam is moved to rest in the lab frame where they can be trapped in step 3 (c). For details, see text. | 6 |

2.1	Energy level structure in the ground electronic state (X) described by the term symbol $^{2S+1}\Lambda$ [Hund's case (a) or (b)]. The dependence of the electronic energy on the internuclear distance, r , is described by the potential energy curve shown by a heavy black line. The minimum of the potential is located at $r = r_e$. The vibrational sublevels are indicated by solid, red horizontal lines and the vibrational quantum number, v , is indicated on the left. The rotational sublevels within a vibrational level are indicated by horizontal, dashed blue lines and the rotational quantum number, J , is indicated on the right. The total energy stored in the bond is given by D_0 , and the energy required to dissociate the molecule from the $\nu = 0$ ground state is D_e .	8
2.2	Vector coupling diagram for Hund's case (a) and (b). For details, see text. Both (a) and (b) are taken from Ref [5].	13
2.3	OH Electronic States. From [6].	15
2.4	Dependence of the coefficients for the spin-orbit states of $^2\Pi$ molecules (Eq. 2.26) on the value of $Y = A/B$. The corresponding values for OH ($Y = A/B \approx 7.5$) are indicated by solid circles.	19
2.5	Spin-orbit/rotational energy level structure of electronic ground state $^2\Pi$ OH. The left vertical axis is the energy in wavenumbers [cm^{-1}] and the right vertical axis is in terms of the equivalent temperature in [K]. The F_1 manifold (predominantly $\Omega = 3/2$ is shown on the left in red, and the and F_2 manifold (predominantly $\Omega = 1/2$ character) is shown on the right in blue. The Λ -doublet splittings are greatly exaggerated for clarity.	21
2.6	The classical dipole moment of OH points towards the hydrogen atom. By convention, positive values of Ω point towards H also.	23
2.7	Stark shift for $^2\Pi_{3/2}$ OH radicals at relatively low electric fields (a) and high electric fields (b)	31
2.8	Parity composition of upper Λ -doublet state as a function of electric field. Here the electric field mixes parity. Plotted are the squares of the coefficients of the wavefunction when expressed in terms of the unperturbed parity levels. The vertical grid lines at $ E \approx 2.95kV/cm$ and $ E \approx 8.33kV/cm$ correspond to 25 : 75 and 40 : 60 parity state superpositions, respectively. .	33

- 2.9 Zeeman shift for the $X^2\Pi_{3/2}$ ro-vibrational ground state of OH radicals in the $|J\Omega M_J \epsilon\rangle$ basis. Since the Zeeman Hamiltonian couples only states of like parity, the two Λ -doublet levels of OH shows exactly the same field dependence. Also, the lack of coupling between e and f states causes only diabatic level crossings. Panel (a) shows the behavior from $0 - 0.175T$ and (b) shows the behavior at fields from $0 - 1T$. (a) also indicates the locations of the crossings by vertical grid lines at $1488G$, $744G$ and $496G$. Styled after Fig. 2.10 from BC Sawyer Thesis. 36
- 3.1 Generalized supersonic beam source. For an ideal isentropic expansion, flow conditions are completely determined by the stagnation parameters in the reservoir, P_0 , T_0 and the nozzle diameter, d 38
- 3.2 Comparison of effusive and supersonic beams: (a) cartoon illustrating the fundamentally different collisional properties of effusive (left) and supersonic beams (right). Figure from [7]. (b) Normalized distribution of parallel velocity for a Kr beam from a reservoir at $T_0 = 300K$ for an effusive beam (red) and a supersonic beam (blue) with an assumed final temperature of $T = 1K$ 41
- 3.3 Terminal velocities (Eq. 3.8) of supersonic expansions of rare gas atoms with reservoir temperatures of $T_0 = 300K$ 43
- 3.4 Simple model of the motion of the valve piston as a function of bias. In the first half of the oscillation cycle, the piston moves in the negative direction. When it crosses the sealing threshold (horizontal axis), the valve opens. For cases where gas flow is not limited by a downstream aperture, application of a bias to reduce the pulse duration always comes at the cost of reduced effective valve diameter, d_{eff} . Figure styled after [8], [9]. 47
- 3.5 Schematic of the PZT valve (a) closed and (b) open. The poppet (central piece, grey) is threaded into the vespel poppet holder (brown) which is tightened to the PZT disk with a PEEK lock nut. The end of the poppet is fitted with an O-ring (Shore Durometer rating A-90, size 003) which seals against the valve face plate (red). The poppet is firmly held within the poppet holder with a 0-80 set screw (not shown-see Fig. 3.6b). 50

3.6	(a) Photograph of PZT actuator broken by over tightening poppet. Cracking was extensive enough that it broke through the plastic insulation and showed significant arcing about $\sim 500V$. Note the alignment of the burn marks at the location of the cracks on both the actuator and the teflon insulator. (b) 0-80 set screw to ensure a tight fit of the poppet in the vespel poppet holder. For details see text.	51
3.7	(a) PZT valve Bistability or Hysteresis. For details, see text. (b) Effective nozzle diameter as a function of above threshold valve voltage for 4 different poppet tensions and nominal pulse durations of $100\mu s$. Measured data (colored circles) are derived from measurements of the gas load in the source chamber. The dashed curve is the expected value, calculated using Eqs. 3.12 and 3.13	54
3.8	(a) Photograph of a molecular beam skimmer, (b) shock fronts formed due to compression of background gas in a supersonic expansion. For the most part, the various shock fronts described in this figure and thousands like it are actually irrelevant for pulsed supersonic beams operated with low background pressure. Figure taken from [10] (where these parameters were relevant).	57
3.9	Mean free path of at the skimmer entrance for the rare gases at nominally equal beam intensities ($p_0d = 80[Torr \cdot cm]$).	59
3.10	Kr mean free path at skimmer entrance for varying stagnation pressures (a) and nozzle diameters (b). Panel (a) is for $d_{eff} = 400\mu m$ and krypton stagnation pressures of 1000, 2000, and 3000 Torr and (b) is for a fixed stagnation pressure of $P_0 = 2200 Torr$ and nozzle diameters of $d_{eff} = 300\mu m$, $d_{eff} = 400\mu m$, and $d_{eff} = 500\mu m$	60
3.11	Figure from [11]	62
3.12	Energy level diagram of the photolysis products of HNCO at 193 nm. (a) from [12] and (b) from [13].	63
3.13	Experimental measurements of unskimmed NH $a^1\Delta$ beams generated by photolysis of HNCO and NH ₃ under similar conditions in a test chamber.	67

3.14	A schematic IV curve of a gas discharge showing different regimes of operation. Adapted from [14] [15].	68
3.15	$e^-/\text{H}_2\text{O}$ water collisions. (a) Potential energy curves of H_2O relevant for electron impact dissociation. Figure from [16]. (b) Absolute cross-sections for the electron-water collision processes given by Eq. 3.29-3.31 based on data given in [17] and [16].	71
3.16	Simplified schematic of the gas system used to generated OH beams in a glow discharge of a Kr/ H_2O mixture. For details, see text.	72
3.17	Detailed scale drawing of the discharge plate assembly. In the cross-sectional view on the left, lengths are given in [mm] and the full opening angle in degrees.	73
3.18	Electric field properties of the discharge plates used to generate OH in Kr/ H_2O mixture for -900V applied to downstream electrode.	73
3.19	Schematic of the asymmetric flow conditions of the electrons and cations in a flowing discharge medium. It is critical that the downstream electrode be biased negatively and the upstream electron be grounded. Figure from [18].	74
3.20	(a) shows a simplified electrical circuit diagram for the pulsed glow discharge. (b) and (c) depict two different ways to measure the discharge current based on directly measuring the voltage on discharge electrodes (b) and monitoring the voltage slew rate off the storage capacitor (c). For details, see text.	76
3.21	Comparison of the two different methods used to measure the discharge current for three different valve durations (a) $50\mu\text{s}$, (b) $100\mu\text{s}$, and (c) $150\mu\text{s}$. For all three, the capacitor slew rate data (blue squares) has been shifted forward by $10\mu\text{s}$ to be in the center of the $20\mu\text{s}$ discharge pulse. For the measurements of the electrode voltage (red line) the bias is applied continuously, so that the measured current would map out the gas pulse as it exits the valve.	77
3.22	(a) Schematic of a discharge IV curve including the details of the electronic circuit showing two different ballast resistors R_A and R_B and two different power supply voltages \mathcal{E}_1 and \mathcal{E}_2 . (b) Measured IV curve indicating operation in the abnormal glow regime. The vertical dashed line in (b) indicates the normal operating value of the discharge current of $\approx 50\text{mA}$	77

- 3.23 Relation between voltage applied to PZT valve and resulting gas pulse measured by monitoring the discharge current. (a) shows the general dependence for nominal valve durations of $50\mu s$ (red), $100\mu s$ (blue) and $150\mu s$ (green). In each case, the delay between the end of the PZT valve pulse and the time of maximum discharge current (maximum Kr density between the discharge plates) is approximately $125m\mu s$. This dependence is highlighted for the case of $100\mu s$ nominal valve duration (which is used for all OH deceleration data presented in this thesis) in panel (b). 78
- 3.24 OH beams as a function of stagnation pressure, p_0 , for fixed valve parameters ($20\mu s$ discharge pulse fired $200\mu s$ after valve trigger, $900V$ nominal voltage). (a) Raw TOF data (b) Beam properties extracted from TOF fits. Vertical axis labels are suppressed to minimize cluttering of figures (see legend). From left, axes are peak OH density (red squares), beam velocity (blue circles), velocity width (FWHM) (green triangles), and discharge current (black hollow triangles). For details, see text. 81
- 3.25 Typical gas pulse from the PZT valve (nominal duration = $100\mu s$) mapped out using discharge current. The blue-shaded band indicates the $\sim 15\%$ fraction of the total gas pulse which the $20\mu s$ discharge pulse actually interacts with. 82
- 3.26 Representative behavior of OH beams for varying valve-to-skimmer distances (VSD) and fixed valve ($100\mu s$, $p_0 = 2200Torr$) and discharge parameters ($20\mu s$, $900V$). (a) shows raw TOF data and (b) shows summarized beam properties extracted from TOF fits. (Vertical axes are as in Fig. 3.24b.) The data displayed here show pronounced skimmer interference where the beam central velocity is unaffected (blue circles), but the beam intensity (red squares) and velocity width (green triangles) show increasing degradation as the valve-skimmer distance is decreased. For details, see text. 85

- 3.27 Properties of an OH beam created from a $20\mu s$ discharge pulse for varying discharge ignition times. The central velocity u and width Δv_{FWHM} are obtained by fitting TOF data to the functional form given in Eq. 3.20. Colored dashed vertical lines indicate the approximate time of the peak valve diameter and consequently largest gas density. In the bottom panel the horizontal dashed line corresponds to the expected terminal velocity for a Krypton beam at a reservoir temperature of $300K$ of $u = 385m/s$ (Eq. 3.8). 86
- 4.1 Panel (A) shows a schematic of the configuration of the potentials $W(z)$ formed. A stick and ball model of a polar diatomic molecule (such as OH) is shown in black. (b) A photograph of our pulsed decelerator (from the trap end). The four larger rods form a skeleton that holds the smaller rod electrodes [solid circles in (a)], which create the potential used to decelerate molecules. 90
- 4.2 Idealized motion in a 1-dimensional potential well. The potential, $U(q)$, is shown in the upper panel, and the phase-space trajectories for three different energies, E_B , E_C , and E_U , are shown in the lower panel. The trajectory at the critical energy, E_C , separates bound and unbound trajectories is indicated by a heavy line. For details, see text. 92
- 4.3 Time evolution of the phase space density ρ_Ω for an N -particle system. Panel (a) shows generalized contours $C_1(t = t_1)$ and $C_2(t = t_2)$ illustrating that although the shape of the contours may change, Liouville's theorem requires the enclosed area to stay constant (for $N =$ fixed). A concrete example of this behavior is shown in panel (b) for the special case of vanishing external potential which is analogous to the evolution of a gas pulse from the pulsed valve to the decelerator. For details, see text. 93
- 4.4 Diagram of potentials formed within a Stark decelerator for both electrode configurations. The reduced longitudinal position is shown on the lower horizontal axis, and the phase angle is shown on the upper horizontal axis. 95

4.5	Final velocity of OH molecules as function of phase angle, ϕ , for various initial velocities (Eq. 4.11). $\Delta K(\phi)$ was evaluated using a numerical fit to $W(\theta)$. The potential corresponds to the geometry of the decelerator in the Lewandowski lab and assumes $n = 149$ deceleration stages.	96
4.6	Longitudinal separatrices for $^2\Pi$ OH molecules at various phase angles calculated by numerically integrating Eq. 4.20.	101
4.7	Effective potentials for OH at $\phi = 0^\circ$ and $\phi = 28^\circ$. As a result of nonzero phase angles as in (b), the potential well is tilted, which reduces the overall depth causing molecules spill out the front.	102
4.8	Stark deceleration timing sequence for $^2\Pi_{3/2}$ molecules in the stretched ($M = 3/2$) state and with an initial velocity of $v_i = 436\text{m/s}$. Sequence was calculated using Eq. 4.33 and the Fourier coefficients in Table 4.1. In the early stages, the velocity is not significantly changed and the stage durations are nearly same, equal to $L/v_i = 12.52\mu\text{s}$ (for this particular example).	104
4.9	CAD drawing showing the dimensions of our decelerator as well as the labeling scheme used in the lab. On the right, only four rod pairs are shown.	105
4.10	Simplified diagram of electrical connections for the Behlke switches for (a) rods #1 and #4, (b) rods #2 and #3. The resistors shown are recommended by the manufacture for impedance matching and to minimize EMF noise.	106
4.11	Relevant distances (in $[mm]$) regarding flight of the molecules to the decelerator. These distances correspond to the valve translation stage being located at a nominal position of $z = 0$. When the decelerator is installed, the four larger rods are kept 3.0mm from the interior surface of the skimmer mounting “can” to prevent discharges.	107
4.12	Loading the Stark decelerator. The full width half max of the OH distribution is shown by a heavy black curve, and the separatrices at $\phi = 0^\circ$, $\phi = 20^\circ$, and $\phi = 40^\circ$ are shown in red, blue, and green, respectively.	108

4.13	3D numerical simulation of the deceleration of OH radicals for a phase angle of $\phi = 0$ and $\phi = 28^\circ$. In the upper panels, the intended final velocity is shown by a thick, dashed horizontal line and the bounds of the separatrix are shown as thinner horizontal lines. The vertical lines correspond to the arrival time of the central packet.	110
4.14	Deceleration of $ 1, 1, 1\rangle$ ND ₃ molecules. (a) shows the full data set and (b) shows an enlargement of the low velocity data. In both panels, the experimental data are shown in the upper portion and the results of 3D simulations are shown in the lower portion (plotted negative). .	111
4.15	Deceleration of $X^2\Pi_{3/2}, M_J = 3/2$ OH molecules. Initial velocity $u = 436\text{m/s}$ and $T_{\parallel} = 0.95\text{K}$.	112
4.16	Shrinking phase space acceptance vs. phase angle, ϕ . (a) Absolute phase space acceptance for OH and ND ₃ . The larger phase space acceptance for OH relative to ND ₃ molecules is due to the larger stark shift to mass ratio of OH. (b) Relative phase space acceptance normalized to that at $\phi = 0$. Note the logarithmic vertical scale. The relative phase space acceptance is identical for both molecules (separately normalized). See also, Eq. 4.28	113
4.17	Cartoon depicting the sequence for co-trapping cold ND ₃ molecules with ultracold Rb atoms. To facilitate loading Rb into the central trapping region, the ring electrode was split into two distinct electrodes separated by 5.0mm. Figure from [19].	116
4.18	Definition of distances relevant to trap loading.	116
4.19	Simulated phase-space distributions of an ND ₃ beam decelerated from 415m/s to 27.6m/s ($\phi = 55.1783^\circ$) at the moment the decelerator turns off. Panel (a) shows the distribution for the longitudinal coordinate, z . Locations of the rod pairs are indicated by dashed vertical lines. (b) and (c) show the distributions in the transverse directions (y and x). In each panel, the probability density for the spatial coordinate and conjugate velocity are overlaid in gray on the respective axis.	118
4.20	(a) Voltages applied to trap electrodes in different configurations and (b) general form of the potentials formed in the trapping and loading configurations.	120

- 4.21 Position spreads of slow ND_3 packets if they were allowed to free flight to trap center. Note that the widths given here are the full widths at half max (FWHM) and not the half-width (1-sided). The horizontal axis has zero corresponding to the center of the last rod pair in the decelerator. 121
- 4.22 Simulations of different trap configurations and loading strategies used in the trap optimization process. The two panels plot the survival fraction as a function of the position (a) and velocity (b) of the synchronous molecule for which the sequence was designed. The longitudinal oscillations seen in the red trace (425, 3 Hill) were caused by a slight error in the timing sequence that caused the synchronous molecule to be trapped with a nonzero average velocity. 123
- 4.23 (a) Comparison of generated electric fields at 8kV and 11kV of original (250) and modified (435) trap. (b) Electric fields in our electrostatic trap. The calculation for the analagous analytic quadrupole trap assumes $R = 0.005$ and that the endcaps are separated by $2R/\sqrt{2} \approx 7.07\text{mm}$. In the actual configuration, the separation is $\approx 7.8\text{mm}$ 124
- 4.24 (a) CAD drawing of the final design of our 435 electrostatic quadrupole-like trap. (b) Electric fields in our electrostatic trap. The calculation for the analagous analytic quadrupole trap assumes $R = 0.005$ and that the endcaps are separated by $2R/\sqrt{2} \approx 7.07\text{mm}$. In the actual configuration, the separation is $\approx 7.8\text{mm}$. (b) Simplified electrical circuit diagram used to hook up the electrostatic trap. The setup is slightly more complicated than that used for the pulsed decelerator due to the requirement of have two distinct HV configurations for trap loading (“Trapping” and “Loading”) as well as a configuration required for extracting ions from the trap. Under typical operating conditions, the $|HV| = 11\text{kV}$ and $LV = 1\text{kV}$ 125
- 4.25 Longitudinal and transverse potentials and separatrices for our 435 trap charged to $\pm 11\text{kV}$. The smaller hump in the longitudinal dimension occurs at 3.225mm. The max in the transverse direction occurs at 3.528mm. 126

4.26	Comparison of “two hill” and and “three hill” trap loading schemes for the 435 Trap charged to $\pm 8kV$. The top panel is three different scenarios to for sequence progressions to point “a”. The “peaked” red curve in the top panel, has the same is faster than the other two packets and has correspondingly had less time to spread out.	127
4.27	ND3 2Hill 11kV Trap Loading Data	128
4.28	ND ₃ Trapping.	128
5.1	Measurements of the 355 nm Laser. (a) Knife edge measurements of the spatial profile of the 355 nm beam when focused by a $f = 48.3$ cm lens (focal length measured at 355 nm). The divergence angle of $\theta \approx 6.6$ mRad indicates an underlying Gaussian beam with a confocal parameter of $b \approx 1.08$ cm. (b) Measurements of the temporal pulse shape with a $\tau_{rise} = 30$ ps photodetector (Newport, Model D-30) and a 1GHz oscilloscope.	131
5.2	MgF ₂ lens used as output window of Xe/Ar cell. (a) Spatial separation of beams due to very different focal lengths for red (f_R) and blue (f_B) light. (b) A 0-020 O-ring is used in the V-shaped groove. Lens tube threads not shown.	133
5.3	Definition of coordinates for THG in a semi-infinite nonlinear media (gray box). Traditional longitudinal coordinates (z) are defined at the bottom of the figure and the reduced longitudinal coordinate, $\xi = \frac{2(z-f)}{b}$, is defined in the upper part of the figure.	136
5.4	Phase matching function, $ F_1(b\Delta k) ^2$, (Eq. 5.10) in the tight-focusing limit, $b \ll L$. The tolerable mismatch in Δk is inversely proportional to confocal parameter, b , with the full width half maximum given approximately by $(\Delta k)_{FWHM} \approx 3.4/b$	138
5.5	Outside of the FWHM of a resonance the index of refraction increases with increasing frequency (see extreme left and right portions of above). Within a resonance width, the index of refraction decreases with increasing frequency.	139
5.6	Xenon-only phase matching for two different lenses. The effective confocal parameters obtained from fitting the normalized data to $G_1(b\Delta k)/G_1(-4)$ are also indicated.	141

- 5.7 Phase matching with xenon and argon. (a) Sample measurement obtained by adding a fixed amount of xenon (6.22 Torr in this case) and then adding argon. (b) Measured optimum pressure ratios P_{Ar}/P_{Xe} for several different xenon pressures (blue circles) with a $f = 48.3$ cm lens (at 355 nm). The four colored curves are Eq. 5.16 for $b = 3$ cm (green), $b = 1.58$ cm (blue,dotted), $b = 1.08$ cm (blue, solid) and $b = 0.5$ cm (red). The error bars in this plot are a reflection of the small number of points used to infer the peak pressure ratio. The dotted, blue curve, corresponding to $b = 1.58$ cm is the effective value obtained from a fit to xenon only data (see Fig. 5.6). The dashed blue curve, corresponding to $b = 1.08$ cm, is based on the knife-edge measurements presented in Fig. 5.1a. For details, see text. 142
- 5.8 Conversion efficiency of xenon only phase matching vs incident pump power. The Kung data, shown by red circles, are taken from [20]. Solid lines are theoretical conversion efficiencies predicted by Eq. 5.17 for different focusing conditions. 143
- 5.9 Limitation to the total conversion efficiency for phase matched (R=11.11) Xe/Ar mixtures at high powers and high total pressures. The total yield is plotted in (a) as a function of the pump power for total pressures of 16 Torr (squares), 122 Torr (circles), and 242 Torr (triangles). In (b), the 118nm flux is plotted as a function of the total pressure for a fixed pump power of $P_\omega \approx 2.6$ MW ($I_\omega \approx 6.6 \times 10^{10}$ W/cm²). 144
- 5.10 Spectral filtering of the generated third-harmonic at 118.2 nm in Xe/Ar mixtures for various xenon pressures. For each xenon pressure the ratio is assumed to be that which perfectly phase matches in the tight focusing limit. The argon wave vector mismatch is assumed to be constant in this region with value $C_{Ar} = +5.33 \times 10^{-18}$ cm². For xenon, a 2nd order interpolation to the three explicitly quoted values in Ref [21] are used. Range of interpolation is 118.295 nm (84534.4 cm⁻¹) \rightarrow 118.195 nm (84605.9 cm⁻¹). This plot was made absolute by taking Kung's value for the nonlinear coefficient in xenon of $\chi_a^{(3)} = 5.6 \times 10^{-35}$ esu. Scaled, Lorentzian laser lineshapes ($\Delta\bar{\nu} = 3$ cm⁻¹) are shown for each xenon pressure. Though the bandwidth of the generated radiation is expected to undergo some "narrowing" it does not become significant until xenon pressures in excess of 50-70 Torr. 148

- 5.11 Lorentzian (natural, collisional) and Gaussian (doppler) lineshapes with the same FWHM, $\Delta\nu$. As a result of the much slower decay of the Lorentzian lineshape, the wings ($\frac{(\nu-\nu_{ij})}{\Delta} \gg 1$) of the absorption line will be completely dominated by the Lorentzian component of the lineshape. 150
- 5.12 Pressure-broadened absorption parameters for the two Xe lines nearest to 118.2 nm. Panel (a) shows the spectral dependence of the absorption cross-section due to both the $5d$ and $7s$ lines as a function of total pressure in phase-matched mixtures. Panel (b) shows the calculated linewidth of the $5d$ and $7s$ Xe lines as a function of xenon pressure. In (c), (d) and (e), parameters are plotted as a function of xenon pressure, but argon is assumed to be present at a $R = 11.11\times$ higher density. 153
- 5.13 Inclusion of absorption into the basic theory given in Sec. 5.3. Even with the inclusion of self-broadening of Xe, for which the fractional transmission can be as small as $\approx 1.4 \times 10^{-3}$ for total pressures of 600 Torr ($P_{Xe} = 50$ Torr), absorption alone is not sufficient to explain the discrepancy between measured flux and that predicted by theory. 154
- 5.14 (a) Measurements of the intensity of the optical breakdown fluorescence. Data taken at 17mJ/6.5ns pulse, focused to $35\mu m$ beam waist. This corresponds to a peak intensity of $6.8 \times 10^{10} W/cm^2$. (b) Photograph of optical breakdown in phase matched mixture (green circles in (a)) at total pressure of $\approx 120 Torr \approx 25 mJ$. For the purposes of a photo this was taken at a higher pulse energy than normal. 155
- 5.15 Simultaneous measurements of 118nm yield and intensity of optical breakdown fluorescence as a function of a total pressure and pulse energy. 157
- 5.16 Simultaneous monitoring of 118.2 nm flux and optical breakdown fluorescence of phase matched mixtures of the “streak” with a PMT. Vertical dashed lines are located at 100 Torr (the first “knee”) and at 242 Torr, the pressure of maximum yield. 158

- 6.1 Photoelectric Yield, or Quantum efficiency of bulk copper. Blue data is digitized from [22]. The discrete data (red circles) is taken from [23]. From this data we have $\eta_{118} = 0.032$ and $\eta_{193} = 2 \times 10^{-4}$ and $\eta_{355} = 8 \times 10^{-9}$. The vertical dashed line is the work function of copper at $\phi_{Cu} = 4.65$ eV ($\lambda = 266.63$ nm) [24]. 163
- 6.2 (a) Basic setup of a vacuum photodiode and (b) Equivalent circuit used during operation. The components enclosed by the red dashed rectangle, are equivalent elements within the physical detector itself. These include the parasitic capacitance, C_p , the shunt resistance, R_{sh} due to the finite electrical insulation, and the series resistance, R_s . The other elements, including R_b and C_b , for the bias voltage, as well as C_c , R_L and C_L , are discussed in Sec. 6.2.3.2. Thanks to Kevin Loeffler for his help with this figure. 163
- 6.3 VUV vacuum photodiode base on BNC clamp plug. Panel (a) shows a cross-sectional view of the final design and panel (b) shows an annotated assembly of the first-generation detector. For the final design the kapton film insulator ($50 \mu m$ thick) of the first-generation detector was replaced with a $600 \mu m$ thick PEEK insulator (shown in (a)) and the end cap/screw was drilled out to a 6.35 mm clear aperture and shorted to a final length of 5.3 mm. The order in which the parts are installed is the same as indicated here. Note that the ID of the PEEK spacer is smaller than the OD of the copper photocathode. This is important to keep the photocathode from shifting. Detailed descriptions of the individual parts is given in Fig. 6.4 . 166
- 6.4 Construction details for the Cu photocathode and conducting center pin. (a) Detail of the copper photocathode and the modified 2-56 brass screw which becomes the center pin of the BNC connector. (b) Detailed description of the manufacturing process for the photocathode. 167
- 6.5 Detailed description of plastic (PEEK) insulators for the copper VPD. (a) shows the cup that securely holds the photocathode, insulating it from the body of the BNC connector, and (b) is the insulating “donut” that sets the anode-cathode spacing at $600 \mu m$. Thanks to Ian Collet for excellent and expedient craftsmanship on these parts for the second generation detector. 168

6.6	Irreversible damage to photocathode (a) and copper mesh (b) due to a short caused by intense 355nm when operated at high voltages. The dark squares on the photocathode (a), corresponds to the open squares in the mesh (b) After this incident, the anode-cathode spacing was increased from $50\mu m \rightarrow 600\mu m$. Since then, the detector has been operated without problems.	169
6.7	Bias voltage saturation behavior at an anode-cathode spacing of $\approx 600 \mu m$ measured with an ArF excimer at 193 nm. For details, see text.	171
6.8	Cu VPD linearity measured at 193 nm. These measurements were made with a anode-cathode spacing of $50 \mu m$. Measured signal sizes were within $\sim 50\%$ of the predicted values. Theory calculation assumes $\eta_{193} = 2 \times 10^{-4}$, $\tau_{193} = 7.5ns$. The horizontal axis corresponds to the pulse energy incident on photocathode. This is based on pulse energy measurements directly outside vacuum with a calibrated Si power meter (optimized for deep UV) and accounts for 80% and 35% transmission of vacuum window and anode mesh, respectively.	172
6.9	Microchannel plate (MCP) electron multipliers. (a) Schematic diagrams of a microchannel plate. (b) Electron multiplication within a single straight channel electron multiplier. (c) Cartoon/schematic of a chevron configuration dual MCP detector. (b) and (c) from Ref [25] .	173
6.10	Depiction of the standard voltage divider in our Jordan MCP. With this voltage divider in place, nominal voltages up to $-HV = 5kV$ ($\Delta V = 0.2 \times HV = 1 kV$ max per plate). The solid black circles on the diagram of the MCP plates indicate the alignment marks on the plates themselves.	175
6.11	Integrated signal from MCP detector (700V/ plate) with preamp ($Tz = 5.1k\Omega$, $f_{3dB} \approx 5 MHz$) vs. time for low count rates. Data were taken by attenuating 118 nm flux (by lowering flux at 355 nm) until it looked “by eye” to be in the single ion/shot limit. The resulting “blinking” seen in the left panel is indicative quantized ions being detected. The panel on the right shows a histogram of the data shown on the left, returning a value of $0.92 nVs/ion$	176

- 6.12 Schematic of different regions and voltages used to describe a generic two-electrode TOFMS, the free flight region for mass separation, and a MCP ion detector with a repeller grid. 176
- 6.13 Mass spectrum obtained by focusing 355nm light in the center of the extraction plates filled with a residual background gas of ND₃ molecules ($T \approx 295K$). This measurement was made several minutes after switching off ND₃ gas flow admitted directly into the vacuum chamber. With the gas flow on, the ND₃ peak ($m/z = 20$) is larger by a factor of 20-50). The presence of other mass peaks is attributed to the other isotopomers of ammonia, which presumably originate from a $D \rightarrow H$ substitution upon collisions with the vacuum chamber walls (or the gas supply lines). Possible molecular species assignments are indicated in both (a) and (b) with black arrows. The focused beam waist is estimated at $\approx w_f \approx 30\mu m$ 178
- 6.14 Damaged MCP plates. Panel (a) shows a photograph of an MCP taken with a standard camera. The “leopard spots” seen here fill the larger hexagonal subunits of the honeycomb structure. These features seem to be unique to this particular pair of damaged MCP plates, but at present, the origin of the discoloration is not understood. Panels (b) and (c) show images taken in the Keck lab at JILA with an optical microscope at magnifications of 5× and 10× respectively. Channel diameter is $d \approx 25 \mu m$. The honeycomb structure seen in (a) can also be seen in (b). The “holes” shown in (b) marked by yellow arrows could be the result of manufacturing defects or surface ablation from high-energy ions. The damage seen in (c), however, is almost certainly the result of high energy bombardment for intense ion bunches. (Note: This figure does not print well and is best viewed on a high resolution monitor.) . . . 179
- 6.15 Comparison of 118nm flux measurements. (a) Experimental setup for comparison of 118nm flux measurements made with Cu VPD and ND₃ backfill ionization method. Note “spotted” surface damage on the interior of the vacuum chamber walls surrounding the VPD. (b) direct comparison of two completely independent calibration methods to detect 118nm light. The discrepancy between the two methods is approximately a factor of ~ 3 182

- 6.16 Estimated focal volume for a dye laser beam focused with 50cm and 75cm lens. The effective interaction length for detection of a decelerated beam of $L_{int} = 2.0mm$ is indicated with vertical dashed lines. 183
- 6.17 Measured power laws for multiphoton ionization of ND₃. Panel (a) shows measurements for the standard 2+1 scheme at $\approx 317nm$ using the \tilde{B}^1E'' state as a 2-photon resonant intermediate. Panel (b) shows measurements made at 355nm. In both panels the relative ion yield is plotted on the vertical axis as a function of the incident pulse energy (horizontal axis). For details on the multiphoton ionization of ND₃ at 355nm shown in (b), see text. 184
- 6.18 Sensitivity of ND₃ ionization schemes. Direct photoionization at 118nm (circles) is compared to 2+1 multiphoton ionization at 317nm (squares) and 355nm (triangles). The photon fluxes used for these measurements were $\approx 10^{11}$ #/pulse at 118nm, 7mJ/pulse or 10^{16} #/pulse at 317nm, and 17mJ/pulse, 3×10^{16} #/pulse at 355nm. Panel (a) shows the raw data, with the horizontal axis corresponding to the total ND₃ density (ignoring the distribution of quantum states). The horizontal axis in panel (b) has been scaled to correspond to the density *per quantum state* and is thus a direct measure of the sensitivity of the given detection method. The inverse slopes indicated in (b) are approximately, the minimum detectable density to generate 1 ion/shot over an interaction length of $L = 0.5$ cm. 185
- 6.19 Vibrational structure of the OH $AX(\nu', \nu'')$ electronic transition. (a) Morse potentials for the $A^2\Sigma^+$ and $X^2\Pi$ electronic states, calculated using spectroscopic constants given in Ref [3]. The first three vibrational levels for both potentials are shown as horizontal dashed lines. (b) Simulated absorption spectrum [26] of a $T_{rot} = 5$ K sample of OH at an instrumental resolution of $\Delta\bar{\nu} = 1$ cm⁻¹. An expanded view of the rotational structure of the AX (1,0) band [center of panel (b)] is shown in Fig. 6.21. 187

6.20 OH AX($\nu' = 1, \nu'' = 0$) band electronic transitions observed for cold samples of OH ($T_{rot} \approx 1$ - 5 K). Spectroscopic labels are given on the right for both Hund's case (a) (blue) and case (b) (red). The splitting between the parity doublet in the $X^2\Pi(\nu'' = 0)$ state is exaggerated by a factor of $100\times$. Similarly, the ρ - doublets in the $A^2\Sigma^+$ state are exaggerated by a factor of $40\times$. In reality, the splitting ($\gamma_{NR} \approx 0.22\text{cm}^{-1}$) is comparable to the linewidth of our pulsed dye laser ($\Delta\bar{\nu}_L \approx 0.15\text{cm}^{-1}$) so that transitions to states of the same final N are only partially resolved. Transitions are grouped by the parity of the initial state due to the parity selecting properties of the Stark decelerator. The spectroscopic notation for labeling the transitions in case (a) and case (b) coupling schemes is $OPQRS \rightarrow -2, -1, 0, 1, 2$ for ΔN and ΔJ , respectively. The subscript labels the initial and final spin-orbit manifolds (either F_1 or F_2). The complete notation is $\Delta J_{F'F''}(J'')$ and $\Delta N_{F'F''}(N'')$ for case (a) and case (b), respectively. 189

6.21 Rotational structure of the OH AX($\nu' = 1, \nu'' = 0$) electronic transition band. Panel (a) shows a simulated absorption spectrum [26] for the 6 transitions indicated in Fig. 6.20 ($T_{rot} = 5$ K, instrumental resolution of $\Delta\bar{\nu} = 0.15\text{cm}^{-1}$). The initial state parities (either $|e\rangle$ or $|f\rangle$) as well as the abbreviated spectroscopic labels in Hund's case (a) (blue, upper) and (b) (red, lower) are also indicated. Enlarged views near 282nm, 281.48nm and 280.7nm are shown in panels (b), (c), and (d) respectively. Experimental data for LIF is shown in the top of each panel by blue symbols and when available, MPI data is shown in the lower portion of each panel in red. The simulated spectra shown in (a) are shown as black solid lines. For the $|f\rangle$ transitions shown in panels (b) and (d), LIF spectra taken in the source chamber (before skimmer) and trap chamber (after exit of decelerator) are shown. In the source chamber, the spectral widths are likely determined by the linewidth of our pulsed dye laser. The broader trap chamber spectra ($\sim 1\text{cm}^{-1}$) is reasonably consistent with Stark broadening from residual electric fields of magnitude $\approx 60\text{kV/cm}$ 190

- 6.22 (a) Typical spectrum of the output (after final amplifier) of our SIRAH precision scan dye laser with R6G dye dissolved in 100% ethanol. The pulse energy for a fixed crystal position at the doubled wavelength ($\approx 280.7nm$) is plotted on the right axis. The spectral width of the doubled light indicates a phase matching bandwidth of $\approx 10.5 cm^{-1}$. Panel (b) shows the SHG spectrum plotted in (a) (still on the right axis) alongside a measured LIF wavelength scan, plotted on the left axis. The linewidth observed for the LIF transition is $\approx 2-3\times$ the estimated value predicted by calculations in Sec. 6.5.2.1. 192
- 6.23 Optical filters used for LIF detection of OH in the AX (1,0) band. (a) shows an overview of the various filters tested. (b) and (c) show a selection of the two filters found to be most useful for LIF detection as well as the calculated transmission of the filter stack/cascade (2x CGA and 1x UG11) used for all OH LIF detection described in this thesis. 197
- 6.24 Sketch of the fluorescence detection assembly used for LIF detection at the end of the decelerator. The light is collimated before passing through the dielectric coating filter (10CGA-305-see Table 6.3) to prevent an angle dependent shift of the pass band. 198
- 6.25 First ten electronic states of the OH radical (of which, only four are bound). With the exception of the AX band, all transition from the ground state lie in the VUV. Figure from [6] 200
- 6.26 Energy level diagrams relevant to 1+1' REMPI of OH. (a) shows a simplified level scheme and (b) shows more detailed description of the proposed ionization mechanism [27]. The dark intermolecular potentials are the neutral OH levels, and the gray lines correspond to the OH. This figure is an annotated version of Fig. 2 of Ref. [28]. 202
- 6.27 (a) Ionization rates as a function of 118nm for various beam waists (radii). Ionization rates are calculated as $k_{2i} = \sigma_{2i} \frac{\Phi}{A}$, with $\sigma_{2i} = 1.0 \times 10^{-17}$ and assuming Gaussian pulses with FWHM of $\Delta t_{FWHM} = 6.5ns$ energies. 202
- 6.28 Initial Measurements of OH MPI at the end of a decelerator. (a) shows the ion TOF of OH⁺ detected simultaneously with ND⁺ and (b) shows the time dependence of the OH⁺ ion signal as a function of the delay between the excitation and ionization lasers. The signal to noise ratio has been improved since these measurements were taken. For details, see text. 203

6.29	Comparison of the OH deceleration time of flight for LIF and 1+1' MPI. MPI data are plotted as negative counts. Note that the vertical scale for each is $0 \rightarrow 50$ "counts." For details, including discussion of the different OH beam velocities, see text.	204
A.1	OHcheatSHEETpage1	222
A.2	OHcheatSHEETpage2	223
B.1	Plot of centerline beam flow velocity vs. Mach number (Eq. B.3) for $\gamma = 5/3$. Note that the flow velocity has been normalized to the speed of sound in the <i>reservoir</i> . The dashed line indicates the asymptotic value of $u_\infty/a_s(T_0) = \sqrt{3}$ where a_s is the speed of sound in the reservoir. An important result of this plot is very early on in the expansion, the flow velocity has already reached 98% of the terminal velocity at a Mach number of ~ 8.5	226
B.2	Plot of centerline beam temperature vs. Mach number (Eq. ??). Note that at the sonic surface (M=1) the beam temperature has already cooled to $T = 0.75 * T_0$	227
B.3	Analytic dependence of the centerline density of a supersonic beam density (normalized against the value in the reservoir, n_0) a function of Mach number, M (Eq. ??) for $\gamma = 5/3$. The dashed lines indicate particular points of interest. At the <i>sonic surface</i> where M=1 the density has already fallen to $\sim 0.65 * n_0$. At, $M \sim 3.3$ and $M \sim 7.85$ the density has fallen by a factor of 10 and 100 respectively.	227
B.4	Method of characteristics (MOC) fits for supersonic expansions. Panel (a) shows the results for the results of Ashkenas and Sherman (Eq. B.7) and panel (b) shows two the parameters for the other two expressions (Eqs B.12 and B.13). Both (a) and (b) are taken from [29]. . .	228
B.5	Number of 2-body collisions remaining in an axisymmetric expansion. The distance where the curves crosses unity, serves to identify the location of the quitting surface.	232
B.6	Calculation for the location of the quitting surface for a pure krypton beam at various effective nozzle diameters, d . For $d = 300\mu m$, we have $x_q = 300\mu m * 85.9 \approx 2.6[cm]$. For $d = 400\mu m$, we have $x_q = 400\mu m * 102 \approx 4.1[cm]$. For $d = 500\mu m$, we have $x_q = 500\mu m * 116.7 \approx 5.8[cm]$	233
B.7	Terminal Speed Ratio as a function of stagnation pressure, P_0	235

INTRODUCTION: Why Cold Molecules?

1.0.1 General Features of Cold Gases

The achievement of Bose-Einstein condensation (BEC) in dilute alkali vapors [30] [31] resulted in an explosion of interest in a wide variety of cold and ultra-cold phenomena. From a fundamental physics perspective, much of the interest can be traced to the emergence of macroscopic quantum phenomena near absolute zero. In the atomic physics community, a BEC [32] is surely the best known example, but similar phenomena occur in other cryogenic systems such as superconductors and liquid helium [33].

In general, one expects quantum effects, such as tunneling through a classically disallowed region, to become significant when the DeBroglie wavelength, $\lambda_{dB} = \frac{h}{p}$, becomes comparable to the characteristic length scale over which the potential varies. If the average momentum of a thermal gas is expressed in terms of the temperature, T , the average DeBroglie wavelength can be estimated as [34]

$$\lambda_{dB} = \left(\frac{2\pi\hbar^2}{mk_B T} \right)^{1/2} = \frac{h}{\sqrt{2\pi mk_B T}} \quad (1.1)$$

The fact that λ_{dB} increases with as the temperature is decreased provides a simple explanation for why these quantum effects only become appreciable at low temperatures. A key feature in all experiments with cold atomic and molecular gases is *phase space density*, $\rho_\Omega = n\lambda_{dB}^3$, where n is the number density of the gas. Clearly, the phase space density increases as the temperature is lowered (thus reducing the number of populated energy states) or if the number density is increased. Though not all experiments on cold gases have the maximum possible phase space density (quantum degeneracy) as the ultimate goal, they generally

benefit from a narrow distribution in the possible states.

Compared to cold atomic gases, cold molecular gases offer a number of promising possibilities. Most of these can be traced, in one way or another, to the richer (more complicated) energy level structure. Perhaps the most important of these, is the possession of a permanent dipole moment, which allows experiments such as tests of fundamental symmetries [35] [36] [37] and cold chemistry in the quantum regime [38] [39]. An overview of production methods and possible applications of cold molecules is given in Fig. 1.1.

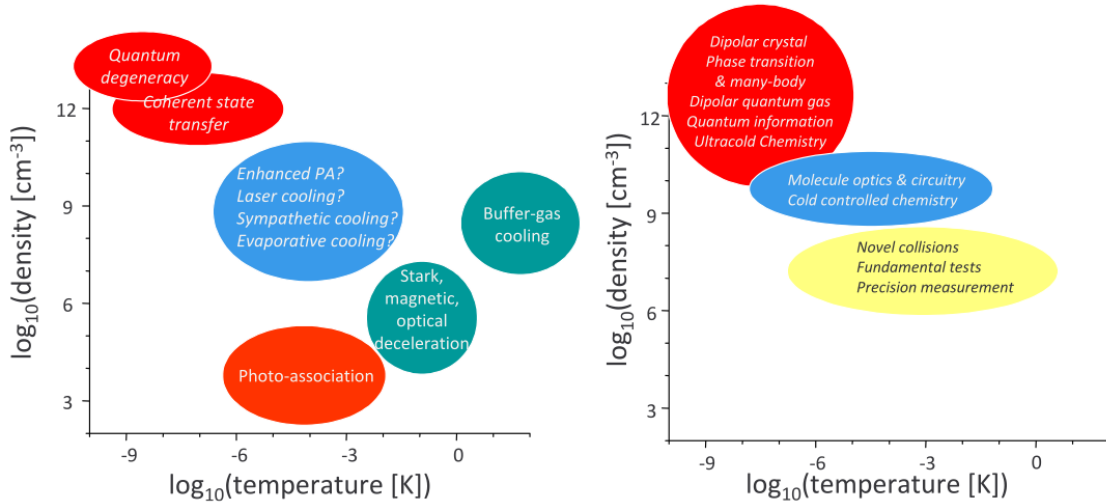


Figure 1.1: Overview of production methods (left) and possible applications (right) as a function of the temperature and phase space density (as of 2009). Figure from [4]

1.1 Routes to Cold Molecules: “Real cooling” vs. “slowing/filtering”

The promise of a richer energy level structure does not come without consequences. The work-horse of cold atomic gases is the magneto-optical trap which combines laser doppler cooling with magnetic trapping. The efficiency of this technique is due in large part to cycling transitions which allow an atom to scatter laser light many times. Due to the complications from rovibrational structure molecules do not general have cycling transitions. This presents a significant challenge for direct laser cooling of molecules, since after a few photon scatters, the molecules wind up in a dark state and no longer contribute to cooling. Though laser cooling of diatomic molecules has been demonstrated [40] [41] and recent exciting results show potential for the technique [42] [43] [44], it is not clear (at least as of yet) whether this technique will be a generally

applicable method to produce samples of cold molecules.

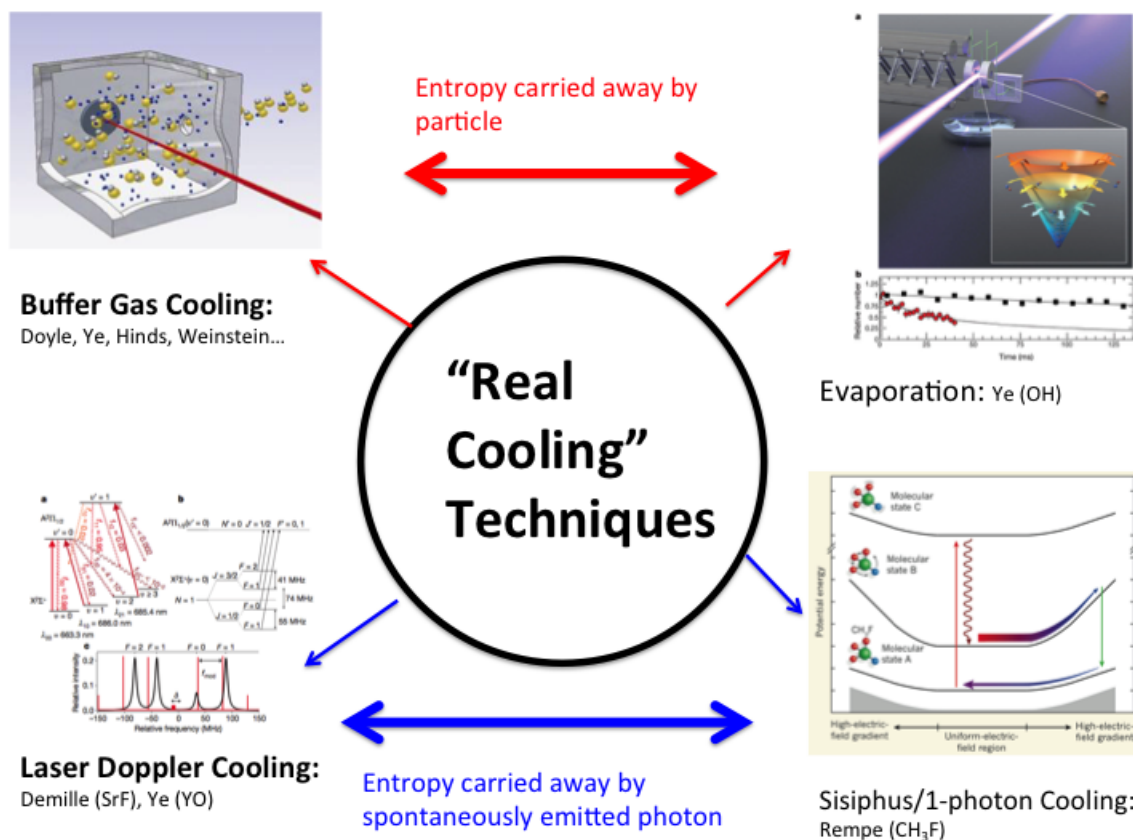


Figure 1.2: “Real cooling” techniques for the direct production of cold molecules. In the top two examples, buffer gas cooling and evaporation, entropy is carried away by a material particle. In the lower two examples, laser doppler cooling and sisyphus/1-photon cooling, entropy is carried away by a spontaneously emitted photon. For details and references, see text.

Production of cold molecules must then resort to other techniques, which can generally be classified being either “indirect” or “direct” techniques [4]. The indirect methods start with ultracold atoms which are then assembled into molecules. These methods are capable of incredible phase-space densities [45] [46] allowing for investigations of many-body quantum interactions [47]. These methods are, however, limited to species whose constituent atoms can be laser cooled. The direct methods on the other hand, start with preassembled molecules followed by one of many cooling techniques. It is this second method, which will be of interest in this thesis.

The direct methods, can be further distinguished in terms of whether or not they increase the space-

density of the molecular sample or not. A “real cooling” (see Fig. 1.2) method requires an irreversible step, where entropy is removed from the system. The four molecular premier cooling methods that result in an increase in phase space density are buffer gas cooling [48] [49] [50] [51], RF induced evaporation [52], “sisyphus” cooling [53], [54] (or single photon cooling) and the laser doppler cooling technique [40] [41] [42] [43] [44] mentioned earlier. In buffer gas cooling and evaporative cooling, collisions play the crucial role, and the entropy is taken away from the system by a material particle. Sisyphus cooling and laser doppler cooling do not require collisions, and in both of these the entropy is carried away by a spontaneously emitted photon. The sisiphus cooling technique is especially exciting, because in contrast to laser cooling, which requires scattering of $\sim 10^4$ photons (which is problematic for molecules), essentially all of the energy ($\approx 1K$ for the traps used in Ref. [53] and [54]) can be removed in a single photon scatter.

Many of the real cooling methods mentioned above are actually the second stage of a complete cooling technique. The prior stage is generally a technique that do not remove entropy, and as such are best classified as “slowing” or “filtering”, as opposed to genuine cooling. Because the phase space density of these techniques is at best constant (see Ch. 4), any decrease in the temperature of the sample of cold molecules must be accompanied by a corresponding decrease in density. Examples of these slowing and filtering techniques are given in Fig. 1.3. These include mechanical approaches to beam deceleration, such as the centrifuge decelerator [55] and the rotating nozzle, [56] [57]. Direct velocity filtering of a cold effusive beam has also been used quite effectively [58] [59]. The final technique considered is electromagnetic based deceleration of supersonic beams with inhomogeneous electric [60] [61] [62] and magnetic fields [63] [64] [65] [66]. The first of these, deceleration with electric fields, called Stark deceleration, is the technique used in for experiments described in this thesis.

Production of cold molecules by Stark deceleration is illustrated as a simplified three step process in Fig. 1.4. Step 1 consists of making a supersonic beam of polar molecules that is cold in the moving frame but moving fast in the laboratory frame (Fig. 1.4a). In step 2, the decelerator moves the fraction of the beam within the phase space acceptance to rest in the lab frame, $v_z = 0$ (Fig. 1.4b). Finally in step 3, the molecules that have been slowed to rest are coupled to a electromagnetic trap (Fig. 1.4c). In steps 2 and 3, the phase space density is conserved, so that this cold molecule technique is best referred to as “slowing” as

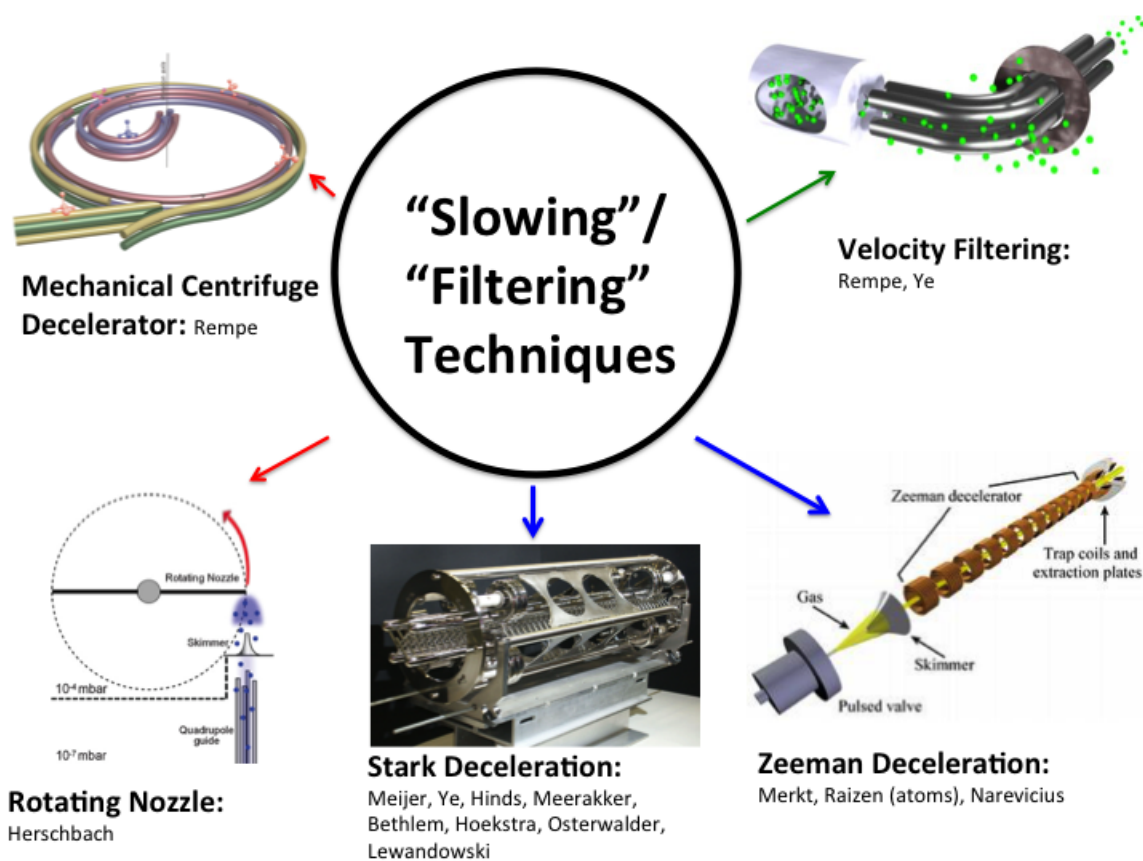


Figure 1.3: Slowing and filtering cold molecule techniques. In contrast the cooling methods depicted in Fig. 1.2, these methods do not result in an increase in phase space density. These include mechanical beam deceleration (left) such as the centrifuge decelerator and the rotating nozzle technique, velocity filtering of slow cryogenic beams (top right) and electromagnetic beam deceleration (bottom) with either pulsed electric (Stark) or magnetic (Zeeman) fields. For details and references, see text.

opposed to “real cooling.”

1.2 This Thesis

More generally, the experiments presented in this thesis are aimed at the production, deceleration and detection of cold OH samples. A major theme of these chapters can be summarized by the basic questions “how many do you have?” and “how well can you detect them?”. An overview of the OH molecule is presented in Ch. 2. The “how many” question is addressed in the next two chapters: Ch. 3 presents a detailed investigation of the production of cold molecular beams of OH and the coupling of this OH beam to the Stark Decelerator is presented in Ch. 4. Ch. 4 also presents results on the trap the optimization and

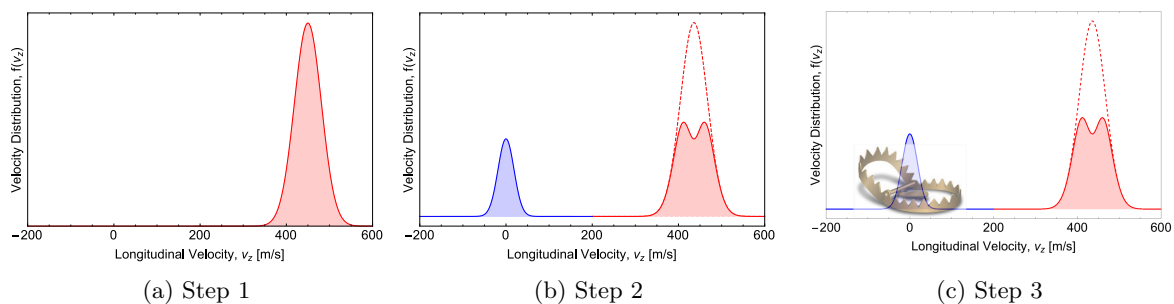


Figure 1.4: Three basic steps for the production of cold molecules with a Stark decelerator. Step 1 (a) is the formation of a fast, but cold, supersonic beam of polar molecules. In step 2 (b) some fraction of the beam is moved to rest in the lab frame where they can be trapped in step 3 (c). For details, see text.

loading of our electrostatic trap which was tested with ND_3 molecules. The “how well” question forms the final two chapters. A rather complete description of the performance and fundamental limitations of a VUV light source at 118nm is presented in Ch. 5. This light source is used a general photoionization source the ionizing step in a $1+1'$ multiphoton ionization detection scheme of OH at the end of the decelerator as described in Ch. 6.

The OH Molecule

2.1 Introduction

The energy level structure of molecules is significantly more complicated than that of atoms due to the additional degrees of freedom describing the internal motion of the nuclei. The much richer energy level structure of molecules is in fact one of the factors driving the interest in cold molecular gases following atomic gases [4]. Before delving into the details of the OH molecule, we review some general features of the energy level structure of diatomic molecules.

2.2 Molecular Energy Level Structure

The description of molecular energy levels is greatly simplified by the Born-Oppenheimer approximation [67], which exploits the fact that while the forces on electrons and nuclei are of comparable magnitude, their masses are vastly different. From a classical perspective, the heavy, sluggish nuclei (mass, M) hardly move during a characteristic orbit of the much lighter, faster electrons (mass, m_e). This means that the total molecular wave function can be factored into electronic and nuclear degrees of freedom,

$$\Psi_{tot} = \psi_{el}\psi_n. \tag{2.1}$$

where ψ_{el} and ψ_n are the wave functions for the electrons and nuclei, respectively. The total energy is then a simple sum of the independent electronic and nuclear energies, $E_{tot} = E_{el} + E_n$. The energy levels of the electrons can then be determined for a particular fixed position of the nuclei. Repeating the procedure for

different configurations of the nuclei yields an effective potential energy landscape on which the nuclei move. For a polyatomic molecule this is a multidimensional surface, but for a diatomic molecule the potential is a 1-dimensional function of the internuclear distance, called a *potential energy curve*. A schematic potential energy curve for a diatomic molecule is presented in Fig. 2.1. To make a stable molecule, the potential energy curve must support a bound state. Within a particular potential energy curve, the nuclear motion is divided further into vibration of the nuclei about the equilibrium positions within the well, r_e , and end-over-end rotations of the nuclei about the center of mass. The total energy is then partitioned as,

$$E_{tot} = E_{el} + E_{vib} + E_{rot}. \quad (2.2)$$

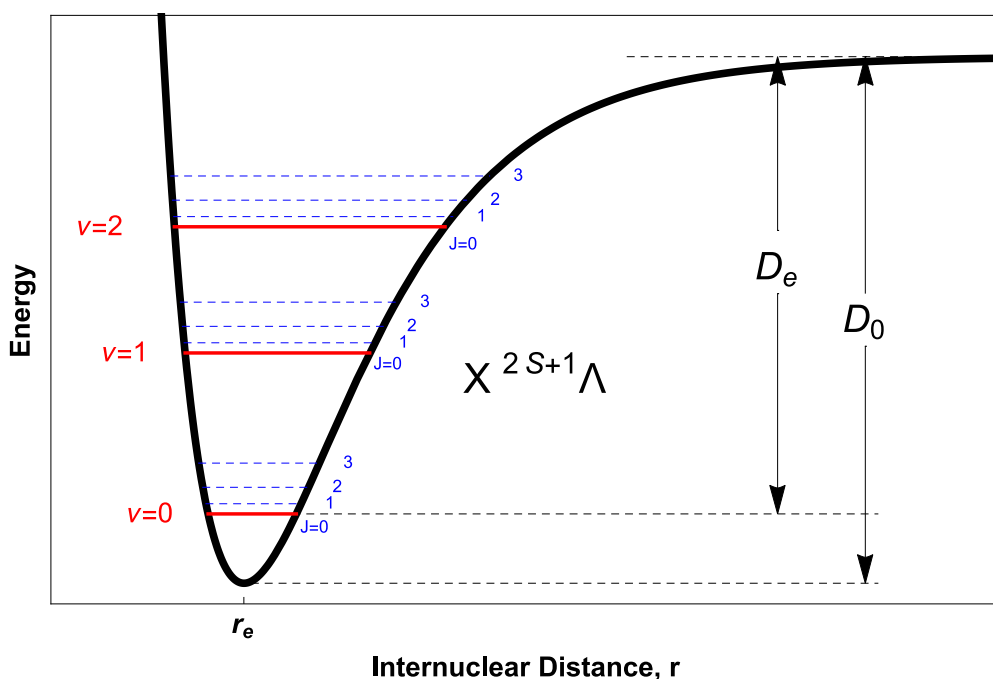


Figure 2.1: Energy level structure in the ground electronic state (X) described by the term symbol $^{2S+1}\Lambda$ [Hund's case (a) or (b)]. The dependence of the electronic energy on the internuclear distance, r , is described by the potential energy curve shown by a heavy black line. The minimum of the potential is located at $r = r_e$. The vibrational sublevels are indicated by solid, red horizontal lines and the vibrational quantum number, v , is indicated on the left. The rotational sublevels within a vibrational level are indicated by horizontal, dashed blue lines and the rotational quantum number, J , is indicated on the right. The total energy stored in the bond is given by D_0 , and the energy required to dissociate the molecule from the $\nu = 0$ ground state is D_e .

The largest energy scale in a molecule is the electronic energy levels which, as for atoms, is $\sim 1 - 10eV$

so that electronic transitions are typically in the UV-visible region of the spectrum. The energy scale of molecular vibration is smaller than the electronic energies by a factor roughly equal to $E_{vib} \sim \sqrt{\frac{m_e}{M}} E_{el}$. For a typical ratio of $(\frac{m_e}{M}) \sim 10^{-4}$, the vibrational energies will be in the mid-infrared. The rotational energies are smaller still by a factor of $E_{rot} \sim (\frac{m_e}{M}) E_{el}$, placing the rotational energies in the microwave region of the spectrum.

2.3 Classification of Electronic States

Here we briefly review the standard classification of electronic potential energy curves of diatomic molecules. Even if the exact shape of a particular potential energy curve is only poorly known (due theoretical and/or experimental difficulties), it can still be described in terms of its general properties. It is customary in spectroscopy of diatomic radicals to label the lowest potential energy curve by the capital letter X. The higher energy states are labeled by capital letters A, B, and so on. States with a spin multiplicity that differs from the ground state are labeled with lower case letters (starting with “a”) to emphasize that these states are not accessible from the ground state by electric dipole transitions [68].

Like in atomic spectroscopy, molecular electronic states are classified by their spin and orbital angular momentum, which is summarized by the spectroscopic *term symbol*. The spherical symmetry of atoms leads to the term symbol being specified by the *total* orbital angular momentum \mathbf{L} [69]. Diatomic molecules of course lack spherical symmetry, so that the total magnitude of \mathbf{L} is not conserved. However, they retain axial symmetry, which leads to the conservation of the projection of \mathbf{L} on the internuclear axis.¹ Analogous to the notation used for atomic term symbols, the value of this projection (L_z) is denoted by capital Greek Λ (lambda), which takes the values 0, 1, 2, ..., as summarized in Table 2.1. Different values of Λ are described by a capital Greek letter starting with $\Lambda = 0 \rightarrow \Sigma$, $\Lambda = 1 \rightarrow \Pi$, $\Lambda = 2 \rightarrow \Delta$. As for atoms, the spin *multiplicity* (# magnetic sub levels) is given by $2S + 1$, and is written as a superscript before the letter for the term; thus a $^3\Pi$ term denotes a molecular state with $\Lambda = 1$, $S = 1$.

In addition to axial symmetry about the internuclear axis, diatomic molecules also possess general reflection symmetry [69]. Due to the isotropy of space, the molecular Hamiltonian is invariant under a space-

¹ This is true for the majority of molecules, which can be classified as either Hund’s case (a) or (b), but is violated for more exotic, molecules, which are classified as Hund’s cases (c), (d), and (e).

Table 2.1: Diatomic molecular term symbols. Possible values of the projection of \mathbf{L} on the internuclear axis (Λ) are listed on the lefthand column and the corresponding molecular term symbol is shown on the right (capital Greek letter). The analogous atomic term symbol for the total orbital angular momentum, L , is shown in parentheses.

Λ	Molecular Term
0	Σ (S)
1	Π (P)
2	Δ (D)
...	...

fixed inversion of spatial coordinates, $\mathbf{r} \rightarrow -\mathbf{r}$. The operator affecting this transformation is termed the parity operator and is denoted here by $\hat{\mathbf{i}}_{sp}$. Because the parity operator commutes with the molecular Hamiltonian, parity becomes an additional “good” quantum number. This means that all physically realizable states must be unchanged by two applications of this operation, which gives possible eigenvalues ± 1 . Those states with eigenvalues of $+1$ are *even* under spatial inversion (positive parity), and those with eigenvalues of -1 are *odd* (negative parity).

2.4 Hund’s Coupling Cases and “Good” Quantum Numbers

In the previous section, we considered only the magnitude of the spin \mathbf{S} and the projection of \mathbf{L} on the internuclear axis. As with atoms, the spin-orbit interaction between \mathbf{L} and \mathbf{S} can result in large energy splittings in molecules. In addition, electronic degrees of freedom can couple to the rotational degrees of freedom (partial breakdown of the Born-Oppenheimer approximation). These different couplings virtually always involve an interaction that can be represented as a vector product between two or more angular momentum vectors. From a semiclassical perspective, the result of the coupling of two angular momenta (say, A and B) of the form $\mathbf{A} \cdot \mathbf{B}$, is to tie them together to make the resultant, $\mathbf{C} = \mathbf{A} + \mathbf{B}$, conserved. In a quantum picture, the coupling leads to the identification of an appropriate basis set, and to good quantum numbers such that the Hamiltonian is diagonal.

The presence of many such competing couplings destroys the idea of rigorously good quantum numbers. However, in certain idealized situations, where one interaction dominates another, the quantum numbers are “pretty good” (to borrow a phrase from John Bohn).² For a diatomic molecule, this leads to the idea of

² Experimentalists in need of a good belly laugh should see the full molecular Hamiltonian on page 118 of Ref [67].

Hund's cases [70] [71], based on the relative magnitude of the three principle "little Hamiltonians": H_{el} , H_{rot} , and H_{SO} . Before discussing the specific Hund's cases, we review the relevant angular momenta of a diatomic molecule [70] [67]. They are:

- \mathbf{L} - the electronic orbital angular momentum
- \mathbf{S} - the electronic spin angular momentum
- \mathbf{J} - the total angular momentum
- \mathbf{N} - the total angular momentum excluding electron spin, so that $\mathbf{N} = \mathbf{J} - \mathbf{S} = \mathbf{L} + \mathbf{R}$
- \mathbf{R} - the rotational angular momentum of the nuclei, so that $\mathbf{R} = \mathbf{N} - \mathbf{L}$

Nuclear spin angular momentum, I , is also usually present, but its interaction strength is usually small in comparison with the interactions of the angular momenta listed above.

2.4.0.1 Hund's Case (a)

In Hund's case (a), the orbital angular momentum \mathbf{L} is coupled to the internuclear axis by electrostatic forces. The electronic spin angular momentum \mathbf{S} is strongly coupled to \mathbf{L} , which effectively couples it to the internuclear axis. The projection of \mathbf{S} on the molecular axis is denoted by Σ (which should not be confused with term symbol for $\Lambda = 0$ states). It takes the possible values $S, S - 1, \dots, -S$. The conservation of both Λ and Σ means that the projection of the total electronic angular momentum, $\Omega = \Lambda + \Sigma$, on the internuclear axis is also conserved (see Fig. 2.2a). Ω takes the possible values $\Lambda + \Sigma, \Lambda + \Sigma - 1, \dots, \Lambda - \Sigma$ and is usually included as a subscript in the term symbol, e.g., $^{2S+1}\Lambda_{|\Omega|}$. For example, for $\Lambda = 1$ and $S = 1/2$, the two possible term symbols for $\Omega = 1/2, 3/2$ are $^2\Pi_{1/2}$ and $^2\Pi_{3/2}$, respectively.

The operator for the rotational Hamiltonian in Hund's case (a) is given by

$$H_{rot} = B(r)\mathbf{R}^2 = B(r)(\mathbf{J} - \mathbf{L} - \mathbf{S})^2 \quad \text{case (a)} \quad (2.3)$$

The end-over-end rotational angular momentum, \mathbf{R} , then couples with Ω to form the total angular momentum, $J = \Omega + R$, about which the molecule precesses. In the Born-Oppenheimer approximation, the Hund's

case (a) basis functions can be partitioned into separate electronic orbital, electronic spin, rotational, and vibrational components as [5] [67]

$$|\psi(n^{2S+1}\Lambda_{|\Omega}; \nu JM)\rangle = |n\Lambda\rangle|S\Sigma\rangle|\nu\rangle|J\Omega M\rangle \quad \text{case (a)} \quad (2.4)$$

Often, the spectator kets $|n\Lambda\rangle|S\Sigma\rangle$ are dropped in this notation since the relevant information regarding these quantum numbers is contained in the sign of Ω . The ket describing the vibrational wavefunction, $|\nu\rangle$ is also usually dropped since we are generally interested in the energy levels within a given vibrational level. The rotational wave functions $|J\Omega M\rangle$ are given by the corresponding symmetric top wave functions:

$$|J\Omega M\rangle \equiv \sqrt{\frac{2J+1}{8\pi^2}} \mathcal{D}_{M\Omega}^{J*}(\phi, \theta, \chi) \quad (2.5)$$

where (ϕ, θ, χ) are the Euler angles defining the molecular axis and $\mathcal{D}_{M\Omega}^{J*}$ is a Wigner \mathcal{D} - function.

2.4.0.2 Hund's Case (b)

In the limit of small spin-orbit coupling, \mathbf{S} is no longer tied to the internuclear axis and Ω ceases to be a good quantum number. \mathbf{L} still precesses about the internuclear axis so that Λ remains a good quantum number. Λ couples to \mathbf{R} to give \mathbf{N} , which is the total angular momentum excluding electron spin. \mathbf{N} and \mathbf{S} then couple together to form \mathbf{J} , about which the molecule precesses.

The rotational Hamiltonian in the case-b representation is

$$H_{rot} = B(r)\mathbf{R}^2 = B(r)(\mathbf{N} - \mathbf{L})^2 \quad \text{case (b)} \quad (2.6)$$

The basis functions for Hund's case-b are represented by

$$|nJSN\Lambda\rangle \quad \text{case (b)} \quad (2.7)$$

Clearly, Σ states with $\Lambda = 0$ will be case (b). Very light molecules with large rotational constants such as OH and CH are mostly case (a), but show some degree of Hund's case (b) character. Cases (a) and (b) are by far the most common cases with most molecules falling somewhere in between. Expressions for

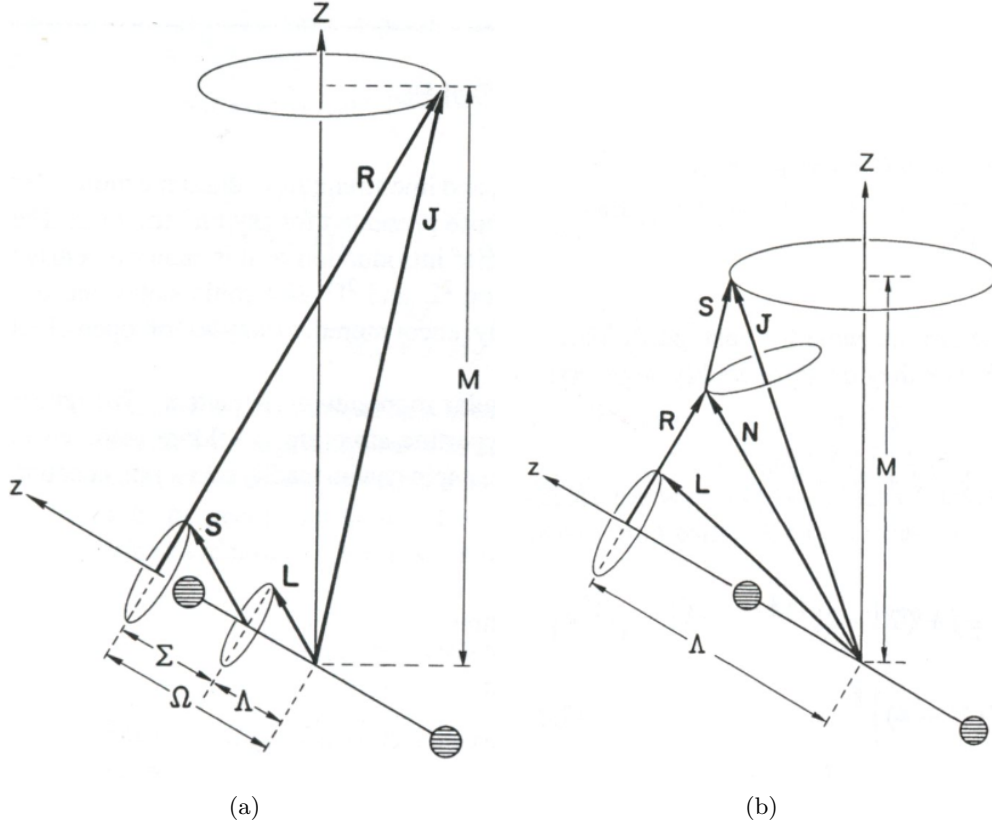


Figure 2.2: Vector coupling diagram for Hund's case (a) and (b). For details, see text. Both (a) and (b) are taken from Ref [5].

transformation between the two basis sets can be found in Refs [67] and [70]. Discussions of the less common Hund's cases, [(c), (d), and (e)] are given Refs [67] and [70].

2.4.1 Hund's Cases and Spatial Inversion Symmetry

As discussed previously, the field-free molecular eigenstates must have well-defined parities. This presents a problem, since the primitive Hund's case basis functions are specified in terms of explicitly signed quantities in the *molecular* frame and, consequently, do not have well-defined parities in the *space-fixed* frame. The effect of the parity operator on the case (a) basis states (Eq. 2.4) is given by [5] [67]

$$\hat{i}_{sp}|n\Lambda\rangle|S\Sigma\rangle|J\Omega M\rangle|\nu\rangle = (-1)^{J-S+s}|n, -\Lambda\rangle|S, -\Sigma\rangle|J, -\Omega M\rangle|\nu\rangle. \quad (2.8)$$

The parameter, s , is equal to 1 for a Σ^- state and is zero for all other states (including Σ^+) [5]. The

effect of the parity operator on the case (b) basis states (Eq. 2.7) is given by

$$\hat{i}_{sp}|n\Lambda\rangle|JNSM\rangle|\nu\rangle = (-1)^{N+s}|n, -\Lambda\rangle|S, -\Sigma\rangle|J, -\Omega M\rangle|\nu\rangle \quad (2.9)$$

As can be seen in Eq. 2.8 and Eq. 2.9, parity has no effect on the vibrational wave function, $|\nu\rangle$, and is consequently dropped in further expressions. Using Eqs. 2.8 and 2.9, it can be seen that well-defined parity states can be formed by taking linear combinations of the primitive basis states with positive and negative signed values of molecular frame quantities. For case (a) we have

$$|\psi(n^{2S+1}\Lambda_{|\Omega|}; \nu JM) \epsilon\rangle = \frac{|n, \Lambda\rangle|S, \Sigma\rangle|J, \Omega M\rangle + \epsilon(-1)^{J-S-s}|n, -\Lambda\rangle|S, -\Sigma\rangle|J, -\Omega M\rangle}{\sqrt{2}} \quad (2.10)$$

and for case (b)

$$|\psi(n^{2S+1}\Lambda; \nu; JNSM) \epsilon\rangle = \frac{|n\Lambda\rangle|JNSM\rangle + \epsilon(-1)^{N+s}|n, -\Lambda\rangle|JNSM\rangle}{\sqrt{2}} \quad (2.11)$$

The overall total parity³ for case (a) and case (b) is then

$$\wp = \epsilon(-1)^{J-S+s} \quad \text{case (a)} \quad (2.12)$$

$$\wp = \epsilon(-1)^{N+s} \quad \text{case (b)} \quad (2.13)$$

where $\epsilon = \pm 1$ is the symmetry of the formed combination. Clearly, the total parity alternates for different rotational level [J for case (a) or N for case (b)] (see for instance Fig. 6.20). For integer values of J , states with a parity of $(-1)^J$ are denoted e and states with parities of $(-1)^{J+1}$ are denoted f . For half-integer values of J , states with a parity of $(-1)^{J-1/2}$ are denoted e and those with $(-1)^{J+1/2}$ are denoted f .

2.5 OH Electronic Structure

Here we discuss general features of the electronic states of OH. The term symbols for the low-lying electronic states of OH can be predicted from the united-atom picture [68]. The ground states of the bare

³ This convention of denoting parity by \wp is not universal. Brown and Carrington, for example, use “p” to abbreviate the exponents in Eq. 2.10 and 2.11. In this thesis, the “Weierstrass p”, \wp , is used exclusively for parity.

oxygen and hydrogen atoms making up OH are given by [72]

$$(1) \text{ H: } (1s) \ ^2S$$

$$(2) \text{ O: } (1s)^2 (2s)^2 (2p)^4 \ ^3P,$$

which suggests that the united atoms will have the possible values $\Lambda = 0$ or 1 and $S = \frac{1}{2}$ or $\frac{3}{2}$. The possible term symbols for these states are $^2\Sigma^-$, $^4\Sigma^-$, $^4\Pi$, and $^2\Pi$ [72]. As can be seen in the potential energy curves shown in Fig. 2.3, the first three of these do not lead to stable molecules, but the last term correctly identifies the term symbol of the ground state as $X^2\Pi$.

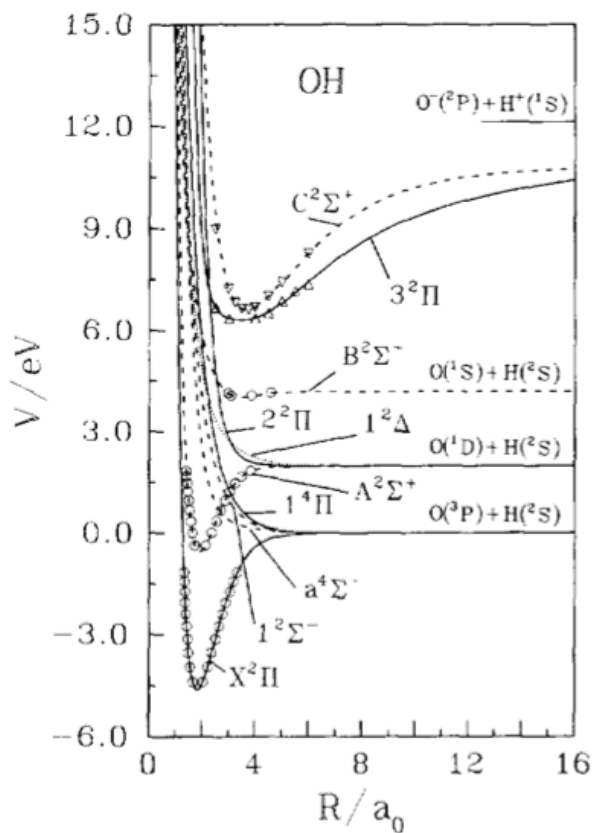


Figure 2.3: OH Electronic States. From [6].

The orbitals of the stable molecules are typically described using the method of linear combinations of atomic orbitals (LCAO) [73] [74]. The configuration of molecular orbitals for ground state OH is

$$X^2\Pi : (1s)^2(2s\sigma)^2(2p\sigma)^2(2p\pi)^3 \quad (2.14)$$

The partial filling of the $(2p\pi)$ orbital is responsible for OH being an open shell radical. This single electron, which has both spin (**S**) and orbital (**L**) angular momentum, will determine many of the properties of the electronic ground state. Because the valence electron occupies a π molecular orbital, possible values of molecular axis projections are $\Lambda = \pm 1$ and $\Sigma = \pm 1/2$. This leads to the assignment of a molecular term symbol of $X^2\Pi$ for the electronic ground state, in agreement with the united atom picture.

The next bound electronic state is formed by uniting $O(^1D) + H(^2S)$ atoms. In terms of the molecular orbital, the excited state results from the promotion of a $(2p\sigma)$ electron to fill the vacancy in the $(2p\pi)$ orbital, giving a total electron configuration of

$$A^2\Sigma^+ : (1s)^2(2s\sigma)^2(2p\sigma)^1(2p\pi)^4. \quad (2.15)$$

This results in a vanishing projection of L on the internuclear axis of $\Lambda = 0$ (due to lone σ electron). Since $\Lambda = 0$, the A-state is best described by Hund's case (b). The possible values of Ω are $\pm 1/2$.

Details on the $X^2\Pi$ and $A^2\Sigma^+$ states will be given later in the context of the $A \leftarrow X$ electronic transition used for OH detection. More information on the other OH electronic states shown in Fig. 2.3 can be found in [6].

2.6 $^2\Pi$ Rotational and Spin-Orbit Energy Level Structure

Here we describe the fine-structure of the $X^2\Pi$ electronic ground state of OH. The vibrational level spacing is approximately 3700 cm^{-1} , which is much too large to be significantly populated at the cold temperatures ($T \sim 1K$) of interest here. The dominant features of the remaining structure are due to end-over-end rotation and, spin-orbit coupling. For reasons that will soon become clear, we choose to work in the Hund's case (a) basis. Both interactions are described by an effective Hamiltonian, which acts only within a given vibrational level [67], $\mathcal{H}^{(\nu)}$,

$$\begin{aligned}
\mathcal{H}^{(\nu)} &= \mathcal{H}_{rot}^{(\nu)} + \mathcal{H}_{SO}^{(\nu)} \\
&= B_\nu (\mathbf{J} - \mathbf{L} - \mathbf{S})^2 + A_\nu \mathbf{L} \cdot \mathbf{S}
\end{aligned} \tag{2.16}$$

where B_ν and A_ν are the rotational and spin-orbit constants of the ν^{th} vibrational level, respectively, and Eq. 2.3 has been used to express $H_{rot}^{(\nu)}$ in the case (a) basis.

For ${}^2\Pi$ states, where $\Lambda = \pm 1$ and $S = \frac{1}{2}$, the possible values of the internuclear projections are $\Sigma = \pm \frac{1}{2}$ and $\Omega = \pm 3/2, \pm 1/2$. The relevant definite parity eigenstates of the primitive basis functions (Eq. 2.4) can be formed according to the recipe of Eq. 2.10 to give

$$|({}^2\Pi_{|\Omega|}; JM), \pm\rangle = \frac{|\Lambda\Sigma\rangle|J\Omega M\rangle \pm (-1)^{J-1/2} |-\Lambda, -\Sigma\rangle|J\Omega M\rangle}{\sqrt{2}} \tag{2.17}$$

The parity of the ${}^2\Pi_{|\Omega|}$ states are given by (see Eq. 2.10)

$$\varphi = \epsilon (-1)^{J-\frac{1}{2}} \quad (\text{parity, } {}^2\Pi \text{ molecules}) \tag{2.18}$$

Thus, for the rovibrational ground state of OH where $J = 3/2$, the parity is equal to $-\epsilon$. Typically, the linear combination in Eq. 2.17 is written in the following abbreviated notation,

$$|J\bar{\Omega}M_J\epsilon\rangle = \frac{|J\bar{\Omega}M_J\rangle + \epsilon|J, -\bar{\Omega}M_J\rangle}{\sqrt{2}} \tag{2.19}$$

where $\epsilon = \pm 1$ is the symmetry of each state (not the parity!) and $\bar{\Omega} = |\Omega|$, which is always a positive quantity. Based on the discussion of Sec 2.4.1, ${}^2\Pi$ stats with $\epsilon = +1$ are denoted e and those with $\epsilon = -1$ are denoted f .

The Hamiltonian matrix can be set up in terms of the parity basis functions $|{}^2\Pi_{3/2}^{(\pm)}\rangle$ and $|{}^2\Pi_{1/2}^{(\pm)}\rangle$. Because the Hamiltonian given by Eq. 2.16 does not couple states of opposite parity, the matrix will be identical for both (+/-) parity states. The matrix is given by

$$\mathcal{H} = \begin{pmatrix} A_\nu/2 + B_\nu [J(J+1) - 7/4] & -B_\nu [(J+3/2)(J-1/2)]^{1/2} \\ -B_\nu [(J+3/2)(J-1/2)]^{1/2} & -A_\nu/2 + B_\nu [J(J+1) + 1/4] \end{pmatrix} \tag{2.20}$$

Diagonalization of Eq. 2.20 yields two sets of eigenvalues, which are labeled F_1 and F_2 and are given by:

$$F_1 : \quad E(|n^2\Pi_{3/2}\nu JM\rangle) = B_\nu \left[\left(J - \frac{1}{2} \right) \left(J + \frac{3}{2} \right) - \frac{1}{2} X \right] \quad (2.21)$$

and

$$F_2 : \quad E(|n^2\Pi_{1/2}\nu JM\rangle) = B_\nu \left[\left(J - \frac{1}{2} \right) \left(J + \frac{3}{2} \right) + \frac{1}{2} X \right] \quad (2.22)$$

The X and Y parameters in Eqs. 2.21 and 2.22 are defined by,

$$X = \left[4 \left(J + \frac{1}{2} \right)^2 + Y(Y - 4) \right]^{1/2} ; \quad Y = \frac{A_\nu}{B_\nu} \quad (2.23)$$

The corresponding eigenvectors are given by

$$|\Psi(F_2)\rangle = a_J |^2\Pi_{3/2}JM\rangle - b_J |^2\Pi_{1/2}JM\rangle \quad (2.24)$$

$$|\Psi(F_1)\rangle = b_J |^2\Pi_{3/2}JM\rangle + a_J |^2\Pi_{1/2}JM\rangle \quad (2.25)$$

where a_J and b_J are given by

$$a_J = \left[\frac{X + (Y - 2)}{2X} \right]^{1/2} ; \quad b_J = \left[\frac{X - (Y - 2)}{2X} \right]^{1/2} \quad (2.26)$$

From the normalization condition, $a_J^2 + b_J^2 = 1$, the squares of the coefficients have the interpretation as the relative $\Omega = 3/2$ or $1/2$ character for the F_1 and F_2 eigenstates. Note that the assignment of $\Omega = 1/2, 3/2$ switches for the F_1 and F_2 manifolds. Molecules with positive spin-orbit constants, $A_\nu > 0$ are termed *regular*, and those with $A_\nu < 0$ are termed *inverted* (such as is the case for OH). This behavior is illustrated in Fig. 2.4

Since the spin-orbit term tends to make Ω a good quantum number (in the absence of any other interactions), the presence of two spin-orbit basis states ($\Omega = |1/2|, |3/2|$) in the F_1 and F_2 eigenfunctions can be interpreted as a departure of a pure case (a) scheme.

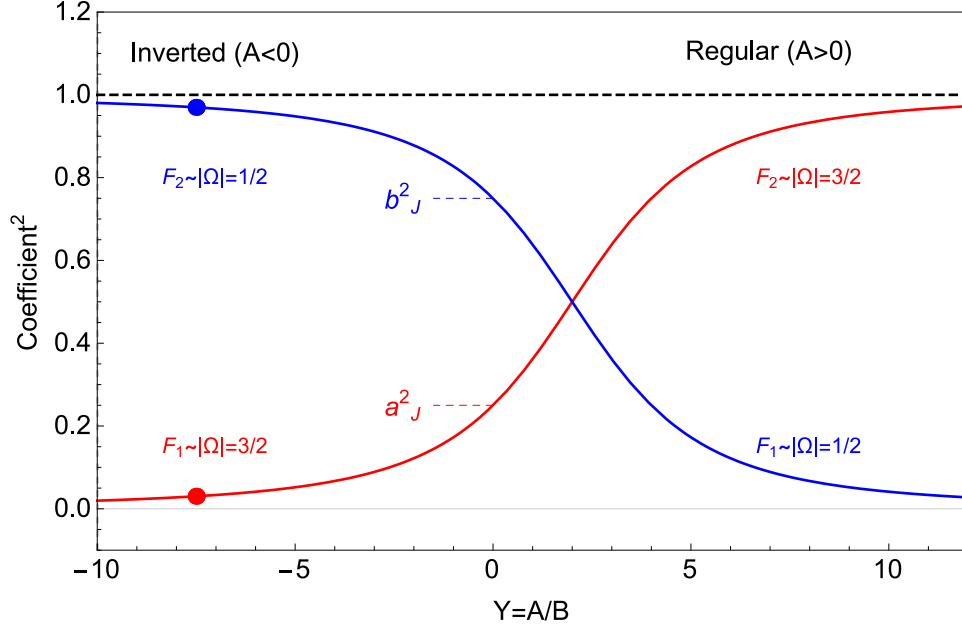


Figure 2.4: Dependence of the coefficients for the spin-orbit states of ${}^2\Pi$ molecules (Eq. 2.26) on the value of $Y = A/B$. The corresponding values for OH ($Y = A/B \approx 7.5$) are indicated by solid circles.

From the off-diagonal elements in Eq. 2.20, clearly the coupling between different values of $|\Omega = 1/2|$ and $|\Omega = 3/2|$ states increases with the rotational level, J . This uncoupling effect is due to competition between the $B_\nu \mathbf{J} \cdot \mathbf{S}$ term in the rotational Hamiltonian (obtained after expanding the first term in Eq. 2.16) and the $A_\nu \mathbf{L} \cdot \mathbf{S}$ term. As the rotational state increases, the case (b) character increases. For notational simplicity, the Hund's case (a) labels are often retained, despite the mixed character of the wave functions.

Using OH's ground state rotational and spin orbit constants $B_0 \approx 18.53 \text{ cm}^{-1}$ and $A_0 \approx -138.9 \text{ cm}^{-1}$ gives $a_J \approx 0.174$ and $b_J \approx 0.985$. The squares of the coefficients are $a_J^2 \approx 0.03$ and $b_J^2 \approx 0.970$. Thus the rovibrational ground state of OH is $\approx 97\%$ Hund's case (a) with $\Omega = 3/2$ character.

2.6.1 Λ -Doubling and Parity

The energy levels of the previous section depend only on the value of $|\Omega| = 1/2, 3/2$ but not on the *sign*. Classically, this can be interpreted as an equivalence between both senses of rotation about the internuclear axis. The degeneracy is broken by a higher order interaction, called Λ -*doubling*, that couples the orbital motion of the electrons to the rotation of the nuclei. This is described by adding a small term,

\mathcal{H}_Λ , to Eq. 2.16 to give the effective Hamiltonian that acts only in the ${}^2\Pi$ state

$$\mathcal{H}^{(\nu)} = \mathcal{H}_{rot}^{(\nu)} + \mathcal{H}_{SO}^{(\nu)} + \mathcal{H}_\Lambda. \quad (2.27)$$

A complete description of the form of \mathcal{H}_Λ for ${}^2\Pi$ molecules is given in Ref [67]. (See their Sec. 8.5.4, page 538.) For our purposes it suffices to describe the splitting by

$$F_1 : \quad E(|n^2\Pi_{3/2\nu}JM(f/e)\rangle) = B_\nu \left[\left(J - \frac{1}{2} \right) \left(J + \frac{3}{2} \right) - \frac{1}{2}X \right] \pm \frac{\Delta}{2} \quad (2.28)$$

where the upper sign corresponds to f and the lower sign corresponds to e parity states. For the F_2 manifold, the situation is reversed:

$$F_2 : \quad E(|n^2\Pi_{3/2\nu}JM(e/f)\rangle) = B_\nu \left[\left(J - \frac{1}{2} \right) \left(J + \frac{3}{2} \right) + \frac{1}{2}X \right] \pm \frac{\Delta}{2} \quad (2.29)$$

Here, Δ represents the Λ -doublet splitting, which depends on J and Ω . (A table of the Λ -doublet splitting is given in [67], page 542.) In the ${}^2\Pi_{3/2}$ rovibrational ground state, the Λ -doublet splitting is $\Delta \approx 1.667GHz \approx 0.0556cm^{-1}$. The energy level structure (including parity) of the F_1 and F_2 manifolds is shown in Fig. 2.5

2.7 $A^2\Sigma^+$ Excited State

In the $A^2\Sigma^+$ electronic state where $\mathbf{L} = 0$, $\mathbf{N} = \mathbf{R} = \mathbf{J} - \mathbf{S}$. Since there is no spin-orbit coupling in this state, case (b) is most appropriate. The effective Hamiltonian, which includes rotational and spin-rotational structure, is given by [5]:

$$\begin{aligned} \mathcal{H}^{(\nu)} &= \mathcal{H}_{rot}^{(\nu)} + \mathcal{H}_{SR}^{(\nu)} \\ &= B_\nu \mathbf{N}^2 + \gamma_\nu \mathbf{N} \cdot \mathbf{S} \\ &= B_\nu \mathbf{N}^2 + \frac{\gamma_\nu}{2} [\mathbf{J}^2 - \mathbf{N}^2 - \mathbf{S}^2] \end{aligned} \quad (2.30)$$

which has the diagonal eigenvalues:

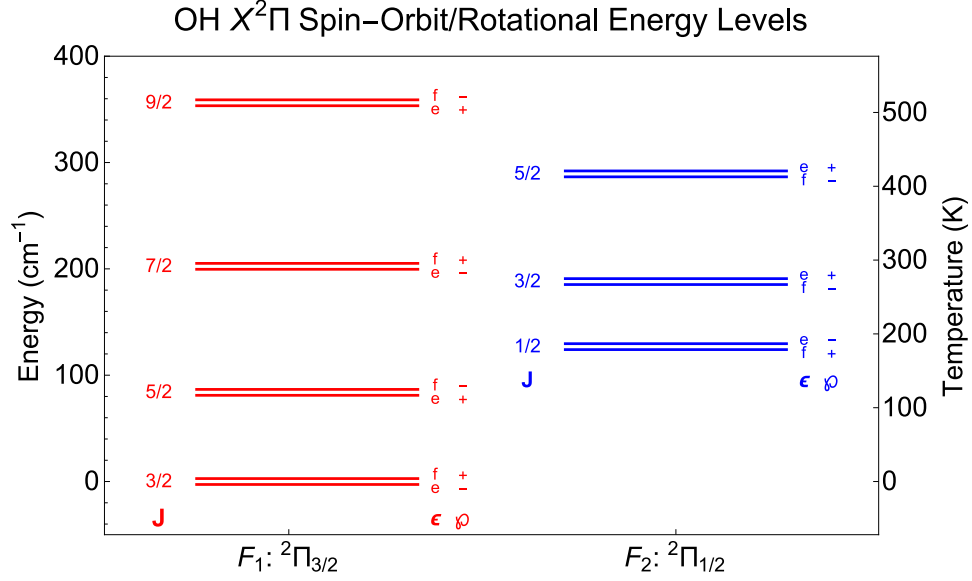


Figure 2.5: Spin-orbit/rotational energy level structure of electronic ground state ${}^2\Pi$ OH. The left vertical axis is the energy in wavenumbers [cm^{-1}] and the right vertical axis is in terms of the equivalent temperature in [K]. The F_1 manifold (predominantly $\Omega = 3/2$ is shown on the left in red, and the and F_2 manifold (predominantly $\Omega = 1/2$ character) is shown on the right in blue. The Λ -doublet splittings are greatly exaggerated for clarity.

$$E = B_\nu N(N+1) + \frac{\gamma_\nu}{2} [J(J+1) - N(N+1) - S(S+1)] \quad (2.31)$$

Eq. 2.31 simplifies considerably because $S = 1/2$ and $J = N \pm 1/2$. Levels with $J = N + 1/2$ and $J = N - 1/2$ are denoted F_1 and F_2 , respectively. In the case (b) representation, the eigenvalues are given by

$$E(F_1) = B_\nu N(N+1) + \frac{\gamma_\nu}{2} N \quad \text{case (b)} \quad (2.32)$$

$$E(F_2) = B_\nu N(N+1) - \frac{\gamma_\nu}{2} (N+1) \quad \text{case (b)} \quad (2.33)$$

In the $A^2\Sigma^+$ state, $\gamma \approx 0.226 cm^{-1}$ and $B \approx 16.96 cm^{-1}$. The splitting between the F_1 and F_2 levels for a given N is

$$\Delta E(N) = E(F_1) - E(F_2) = \gamma(N + 1/2) \quad (2.34)$$

See Sec. 6.5.1 for more information in the context of the AX band electronic transition.

2.8 OH in External Fields

One of the most important features of the OH radical is that it has both an electric and a magnetic dipole moment. The resulting Stark and Zeeman shifts are sufficiently large that a cold sample of molecules can be easily manipulated with modest laboratory fields.

In both the Stark and Zeeman effects⁴, the interaction with the externally applied field is described by adding an additional Hamiltonian, \mathcal{H}_{field} , to the molecular Hamiltonian. On the surface, both the Stark and Zeeman appear quite similar since the classical Hamiltonian for both interactions takes the form of a scalar product of a dipole moment with a vector field:

$$\mathcal{H}_{field} = -\boldsymbol{\mu}_i \cdot \mathcal{F} \quad (2.35)$$

where $\boldsymbol{\mu}_i$ is either the magnetic or electric dipole moment and \mathcal{F} represents either \mathbf{E} or \mathbf{B} . Classically, both interactions exert a torque, $\boldsymbol{\tau} = \boldsymbol{\mu}_i \times \mathcal{F}$, which tends to align the dipole in the direction of the field (where $-\boldsymbol{\mu}_i \cdot \mathcal{F}$ is a minimum). Because both dipole moments are associated with an angular momentum, they do not lie perfectly along the field but instead precess about the local field at an angular frequency of $\omega = \frac{\mu_i \mathcal{F} \sin \theta}{\hbar}$. In a semiclassical vector model, the degree of alignment between the dipole and the applied field is quantized and given by the direction cosine $\cos \theta = \hat{z} \cdot \hat{Z} = \frac{M_J}{\sqrt{J(J+1)}}$ [75], where \hat{z} is the unit vector for the internuclear axis (molecule frame) and \hat{Z} is the unit vector defining the direction of the applied field, $\mathcal{F} = \mathcal{F} \hat{Z}$.

Despite these similarities in mathematical form (for the classical expression), a key fundamental difference is the fact that the electric field is a true vector (odd under the parity operation), whereas the magnetic field is a pseudovector (even under parity). Because the field-free molecular Hamiltonian commutes with the parity operator, the molecule has a definite parity. This means that in the absence of an electric

⁴ This section benefitted greatly from enlightening discussions with Prof. John Bohn.

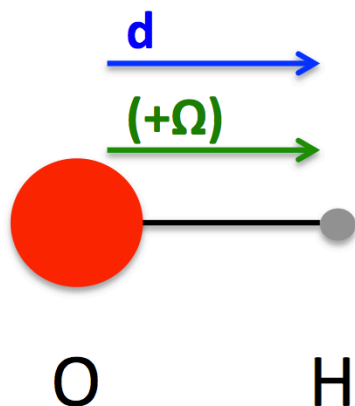


Figure 2.6: The classical dipole moment of OH points towards the hydrogen atom. By convention, positive values of Ω point towards H also.

field, the molecule is in an equal superposition of “up” and “down” electric dipole moments. The presence of the applied electric field destroys the parity quantum number resulting in a mixing of opposite parity states to *induce* a dipole moment in the molecular frame. The field-dependent eigenstates are then composed of an unequal mixture of “up” or “down” to make a nonzero expectation value of the dipole moment.

The situation is fundamentally different for the Zeeman effect since paramagnetic atoms and molecules possess a genuinely *permanent* dipole moments due to electron spin and orbital angular momentum that exist even in the absence of any applied magnetic field.

2.8.1 OH Stark Effect: Strong Fields

In this section we analyze the Stark shift of the rovibrational ground state of $^2\Pi$ OH. As a first approximation, we assume that OH is a pure Hund’s case (a) molecule with $\Omega = 3/2$ and ignore any hyperfine effects (nuclear spin, quadrupole moments, etc.). As the Stark shift tends to orient OH in the direction of the applied field, we use the *polarized* basis where the basis states are, $|J, \bar{\Omega}, M\rangle$, $|J, -\bar{\Omega}, M\rangle$. These basis functions are designed to have of explicitly signed values of Ω . The sign of Ω is chosen to be positive when the projection of J on the internuclear axis is in the same direction as the dipole moment (point from the O-end to the H-end), and negative for the reverse case (see Fig. 2.6). More complicated calculations of the Stark effect involving higher order correction terms in the Hamiltonian can still be calculated using the basic matrix elements.

2.8.1.1 Stark Matrix Elements in Polarized Basis

The classical Stark Hamiltonian is given by

$$\mathcal{H}_S = -\mathbf{d} \cdot \mathbf{E} \quad (2.36)$$

where \mathbf{d} is the electric dipole moment of the molecule and \mathbf{E} is the electric field. Applying Eq. 2.36 to molecules presents an immediate complication. The applied fields are naturally expressed in terms of the lab coordinates, while dipole moment (both electric and magnetic) are naturally expressed in the molecular frame. The transformation between the two reference frames is elegantly accomplished with standard spherical tensor algebra. Since the calculation can be somewhat confusing, we present a detailed calculation below. The basic result can then be applied to matrix elements for a Zeeman shift.

We follow the standard convention of representing the molecule coordinates by lowercase letters, $(\hat{x}, \hat{y}, \hat{z})$ and the space-fixed coordinates by uppercase letters, $(\hat{X}, \hat{Y}, \hat{Z})$. The molecular symmetry axis (\hat{n}) is taken to be the z -axis, and the applied field direction is taken to be \hat{Z} . For symmetric top molecules (of which diatomics are a special case), the electric dipole moment \mathbf{d} can lie only along the the symmetry axis of the molecule (the internal bond axis for a diatomic).

The dipole moment and the electric field vectors can be represented as irreducible spherical tensor operators of rank $k = 1$. The components of general spherical tensor operator A of rank k are represented as $T_A(k, p)$. Then Eq. 2.36 can be written in terms of spherical tensors (see Ref [67] page 161, Eq. 5.112, or [5] page 188, Eq.5.47) in the space-fixed frame as

$$\mathcal{H}_S = -\mathbf{d} \cdot \mathbf{E} = - \sum_{p=-1}^1 (-1)^p T_d(1, p) T_E(1, -p) \quad (2.37)$$

Here, T_d and T_E are defined in the space-fixed frame . We use the standard convention where p is taken to represent the spherical components in the space-fixed frame and q is taken to represent spherical components in the molecular frame.⁵

Explicitly, the space-fixed spherical components $p \in (+1, 0, -1)$, of T_d can be written in terms of the

⁵ I remember this convention with the mnemonic “p” for *sP*ace fixed.

cartesian space-fixed components (X, Y, Z) as

$$T_d(1, -1) = d_{-1} = \frac{1}{\sqrt{2}} (d_X - id_Y) \quad (2.38)$$

$$T_d(1, 0) = d_0 = d_Z \quad (2.39)$$

$$T_d(1, +1) = d_{+1} = -\frac{1}{\sqrt{2}} (d_X + id_Y) \quad (2.40)$$

Similarly, the spherical components of T_E in the space-fixed frame are given by

$$T_E(1, -1) = E_{-1} = \frac{1}{\sqrt{2}} (E_X - iE_Y) \quad (2.41)$$

$$T_E(1, 0) = E_0 = E_Z \quad (2.42)$$

$$T_E(1, +1) = E_{+1} = -\frac{1}{\sqrt{2}} (E_X + iE_Y) \quad (2.43)$$

If the space-fixed coordinate system is chosen such that electric field is parallel to the \hat{Z} -axis, $E_X = E_Y = 0$. Consequently, from Eqs. 2.41 and 2.43, $E_{-1} = E_{+1} = 0$ and the only remaining term in the sum over p (Eq. 2.37) is the $p = 0$ term. \mathcal{H}_S then reduces to

$$\mathcal{H}_S = -T_d(1, p=0) \cdot E. \quad (2.44)$$

where $T_d(1, 0)$ is the projection of the dipole moment on the space-fixed \hat{Z} -axis.

The next step is where the trickiest and, conceptually, the most important part comes in. How does one express the dipole moment \mathbf{d} , which is most naturally defined in the (rotating) molecular frame, in the space-fixed (lab) frame? Generally, the spherical components of a tensor operator in the lab frame, $T_{\mathbf{A}}(k, p)$, can be expressed in terms of the spherical components in the molecular frame, $T_{\mathbf{A}}(k, q)$ by the transformation using Wigner rotation matrices, $\mathcal{D}_{pq}^{(k)}(\phi, \theta, \chi)$ (see Ref [67] page 167, Eq. 5.143, or [5], page 179, Eq. 5.9):

$$T_{\mathbf{A}}(k, p) = \sum_q \mathcal{D}_{pq}^{k*}(\phi, \theta, \chi) T_{\mathbf{A}}(k, q) \quad (2.45)$$

Here, the Euler angles (ϕ, θ, χ) define the orientation of $(\hat{X}, \hat{Y}, \hat{Z})$ axes with respect to $(\hat{x}, \hat{y}, \hat{z})$. The choice of Euler angles is the convention used in the books by Zare [5] and Brown and Carrington [67]. For our case where $p = 0$, we can express $T_d(1, 0)$ as

$$T_d(1, 0) = \sum_q \mathcal{D}_{0q}^{(1)*}(\phi, \theta, \chi) T_d(1, q). \quad (2.46)$$

To proceed with the calculation of the matrix elements of the form $\langle J\Omega M | \mathcal{H}_S | J'\Omega' M' \rangle$, we recall that the symmetric-top wave functions $|J\Omega M\rangle$ themselves are expressed in terms of Wigner-rotation matrices (see Eq. 2.5). To tidy up notation in what follows, the three Euler angles (ϕ, θ, χ) will be represented by the single character ω . Then, for calculating matrix elements, we have explicitly for the bra and ket,

$$|J'\Omega' M'\rangle = \sqrt{\frac{2J'+1}{8\pi^2}} \mathcal{D}_{M'\Omega'}^{(J')*}(\omega) \quad (2.47)$$

$$\langle J\Omega M | = \sqrt{\frac{2J+1}{8\pi^2}} \mathcal{D}_{M\Omega}^{(J)}(\omega) \quad (2.48)$$

Then, for the matrix elements we have,

$$\begin{aligned} \langle J\Omega M | \mathcal{H}_S | J'\Omega' M' \rangle &= \langle J\Omega M | -T_d(1, 0) \cdot E | J'\Omega' M' \rangle \\ &= -E \frac{\sqrt{(2J+1)(2J'+1)}}{8\pi^2} \sum_q T_d(1, q) \langle J\Omega M | \mathcal{D}_{0q}^{(1)*} | J'\Omega' M' \rangle \\ &= -E \frac{\sqrt{(2J+1)(2J'+1)}}{8\pi^2} \sum_q T_d(1, q) \int \mathcal{D}_{M\Omega}^{(J)} \mathcal{D}_{0q}^{(1)*} \mathcal{D}_{M'\Omega'}^{(J')*} d\omega \\ &= -E (-1)^{M'-\Omega'} \frac{\sqrt{(2J+1)(2J'+1)}}{8\pi^2} \\ &\quad \times \sum_q (-1)^{-q} T_d(1, q) \int \mathcal{D}_{M\Omega}^{(J)} \mathcal{D}_{0,-q}^{(1)} \mathcal{D}_{-M',-\Omega'}^{(J')} d\omega \end{aligned} \quad (2.49)$$

where in the last step the following relation has been used to eliminate the complex conjugate (Eq. 5.147 in Ref [67])

$$\mathcal{D}_{pq}^{(k)*}(\omega) = (-1)^{p-q} \mathcal{D}_{-p, -q}^{(k)}(\omega). \quad (2.50)$$

At this point, we use the following general result for integrals over Wigner matrices⁶ (Ref [67], Eq. 5.100),

$$\int \mathcal{D}_{m'_1 m_1}^{(j_1)} \mathcal{D}_{m'_2 m_2}^{(j_2)} \mathcal{D}_{m'_3 m_3}^{(j_3)} d\omega = 8\pi^2 \begin{pmatrix} j_1 & j_2 & j_3 \\ m'_1 & m'_2 & m'_3 \end{pmatrix} \begin{pmatrix} j_1 & j_2 & j_3 \\ m_1 & m_2 & m_3 \end{pmatrix} \quad (2.52)$$

Then the integral in Eq. 2.49 reduces to

$$\int \mathcal{D}_{M\Omega}^{(J)} \mathcal{D}_{0, -q}^{(1)*} \mathcal{D}_{-M', -\Omega'}^{(J')} d\omega = 8\pi^2 \begin{pmatrix} J & 1 & J' \\ M & 0 & -M' \end{pmatrix} \begin{pmatrix} J & 1 & J' \\ \Omega & -q & -\Omega' \end{pmatrix}, \quad (2.53)$$

so that Eq. 2.49 becomes

$$\begin{aligned} \langle J\Omega M | \mathcal{H}_S | J'\Omega' M' \rangle &= -E(-1)^{M'-\Omega'} \sqrt{(2J+1)(2J'+1)} \begin{pmatrix} J & 1 & J' \\ M & 0 & -M' \end{pmatrix} \delta_{M'M} \\ &\times \sum_q (-1)^{-q} T_d(1, q) \begin{pmatrix} J & 1 & J' \\ \Omega & -q & -\Omega' \end{pmatrix} \end{aligned} \quad (2.54)$$

Because we are dealing with a symmetric-top molecule where the dipole moment is always directed along the symmetry axis of the molecule, the only non vanishing molecule frame component of the dipole moment $T_d(1, q)$ is $q = 0$. Then we have $T_d(1, 0) = d$ and Eq. 2.54 reduces to

⁶

The Wigner 3j symbols are basically equivalent to the Clebsch-Gordon coefficients, but they are written in such a way as to make the triangularity selection rules visually obvious. A result that comes in handy is the fact they are invariant under even or cyclic permutations in the order of the columns. Odd permutations and changing the sign of all magnetic quantum numbers have the effect of introducing an additional phase factor,

$$\begin{aligned} \begin{pmatrix} j_1 & j_2 & j_3 \\ m_1 & m_2 & m_3 \end{pmatrix} &= (-1)^{j_1+j_2+j_3} \begin{pmatrix} j_2 & j_1 & j_3 \\ m_2 & m_1 & m_3 \end{pmatrix} \\ &= (-1)^{j_1+j_2+j_3} \begin{pmatrix} j_2 & j_1 & j_3 \\ -m_1 & -m_2 & -m_3 \end{pmatrix} \end{aligned} \quad (2.51)$$

(see [67], Eq. 5.85)

$$\begin{aligned}
\langle J\Omega M | \mathcal{H}_S | J'\Omega' M' \rangle &= -dE \sqrt{(2J+1)(2J'+1)} (-1)^{M'-\Omega'} \\
&\times \begin{pmatrix} J & 1 & J' \\ M & 0 & -M' \end{pmatrix} \begin{pmatrix} J & 1 & J' \\ \Omega & 0 & -\Omega' \end{pmatrix} \delta_{\Omega'\Omega} \delta_{M'M} \quad (2.55)
\end{aligned}$$

The two 3j-symbols in Eq. 2.55 give the “selection rule” that $\Delta M = 0$ and $\Delta\Omega = 0$, which is another way of saying that the matrix elements are diagonal in M and Ω . We can use Eq. 2.51 to write

$$\begin{aligned}
\langle J\Omega M | \mathcal{H}_S | J'\Omega' M' \rangle &= -dE \sqrt{(2J+1)(2J'+1)} (-1)^{M'-\Omega'} (-1)^{J'+J} (-1)^{J'+J} \\
&\times \begin{pmatrix} J & 1 & J' \\ -M & 0 & M' \end{pmatrix} \begin{pmatrix} J & 1 & J' \\ -\Omega & 0 & \Omega' \end{pmatrix} \delta_{\Omega'\Omega} \delta_{M'M} \quad (2.56)
\end{aligned}$$

The large energy splitting between different J states for the ${}^2\Pi_{3/2}$ state of $\approx 80\text{cm}^{-1}$ means that we can neglect any coupling between them due to the electric field. This means that the phase factor in Eq. 2.57 for different J levels reduces to 1 in all cases. The final result is then

$$\begin{aligned}
\langle J\Omega M | \mathcal{H}_S | J\Omega' M' \rangle &= -dE (2J+1) (-1)^{M'-\Omega'} \\
&\times \begin{pmatrix} J & 1 & J' \\ -M & 0 & M' \end{pmatrix} \begin{pmatrix} J & 1 & J' \\ -\Omega & 0 & \Omega' \end{pmatrix} \delta_{\Omega'\Omega} \delta_{M'M} \quad (2.57)
\end{aligned}$$

Using the Wigner-Eckart theorem⁷ to evaluate the matrix elements between states of the same total angular momentum $J' = J$ we have,

$$\langle J\Omega' M' | n_q | J\Omega M \rangle = \delta_{\Omega'\Omega} (-1)^{J-M'} \sqrt{2J+1} \begin{pmatrix} J' & 1 & J \\ -m' & q & m \end{pmatrix} \langle J || n_q || J \rangle \quad (2.59)$$

evaluating the reduced matrix element to be

⁷ For a general spherical tensor operator $T_{\mathbf{A}}(k, q)$ of rank k , the WE theorem can be stated as

$$\boxed{\langle \eta, j, m | T_{\mathbf{A}}(k, q) | \eta', j', m' \rangle = (-1)^{j-m} \begin{pmatrix} j & k & j' \\ -m & q & m' \end{pmatrix} \langle \eta, j || T_{\mathbf{A}}(k) || \eta', j' \rangle} \quad (2.58)$$

$$\langle J||n_q||J\rangle = \frac{\Omega}{\sqrt{J(J+1)}} \quad (2.60)$$

so in all we have

$$\langle J\Omega'M'|n_q|J\Omega M\rangle = \delta_{\Omega'\Omega}(-1)^{J-M'}\sqrt{2J+1} \begin{pmatrix} J' & 1 & J \\ -m' & q & m \end{pmatrix} \frac{\Omega}{\sqrt{J(J+1)}} \quad (2.61)$$

2.8.1.2 Stark Shift with Λ -doubling

Taking into account Λ -doubling, the full Hamiltonian for OH in an electric field is

$$\mathcal{H} = \mathcal{H}_0 + \mathcal{H}_\Lambda + \mathcal{H}_S \quad (2.62)$$

Then we have for the matrix elements for the field interaction,

$$\langle J\Omega'M'|\mathcal{H}_S|J\Omega M\rangle = -Q_M \times \delta_{\Omega'\Omega}\delta_{M'M} \quad (2.63)$$

where

$$Q_M = dE \frac{M\Omega}{\sqrt{J(J+1)}} \quad (2.64)$$

and is designed to explicitly have the same sign as M . The Dirac-delta functions in the Stark interaction matrix elements indicate that only states of the same Ω and M are connected. For the Λ -doubling the matrix elements are given by

$$\langle J'\Omega'M'|H_\Lambda|J\Omega M\rangle = \frac{\Delta}{2} \times \delta_{-\Omega'\Omega}\delta_{M'M} \quad (2.65)$$

where Δ is the zero-field Λ -doublet splitting. Since we have chosen to work in the $|J\Omega M\rangle$ basis, there are two states for each M . Then for each M we have the Hamiltonian matrix:

$$H_M = \begin{pmatrix} -Q_M & \Delta/2 \\ \Delta/2 & Q_M \end{pmatrix} \quad (\text{Polarized Basis}) \quad (2.66)$$

where the rows correspond to states $|J\bar{\Omega}M\rangle$ and $|J, -\bar{\Omega}M\rangle$. The fact that the Λ -doubling interaction couples states of the opposite sign (but equal magnitude) of Ω is reflected in the matrix elements appearing off-diagonal in Eq. 2.66.

The Hamiltonian (Eq. 2.66) can be diagonalized via rotation angle η_M , where the rotation operator is described by the unitary matrix U_M :

$$U_M = \begin{pmatrix} \cos \eta_M & -\sin \eta_M \\ \sin \eta_M & \cos \eta_M \end{pmatrix} \quad (2.67)$$

$$U_M H_M U_M^{-1} = \begin{pmatrix} -Q_M \cos 2\eta_M - \frac{\Delta}{2} \sin 2\eta_M & -Q_M \sin 2\eta_M + \frac{\Delta}{2} \cos 2\eta_M \\ -Q_M \sin 2\eta_M + \frac{\Delta}{2} \cos 2\eta_M & Q_M \cos 2\eta_M + \frac{\Delta}{2} \sin 2\eta_M \end{pmatrix} \quad (2.68)$$

For this transformation to diagonalize the matrix $U_M H_M U_M^{-1}$, the off-diagonal elements must vanish,

$$Q_M \sin \eta_M = \frac{\Delta}{2} \cos \eta_M \rightarrow \frac{\Delta/2}{Q_M} = \tan \eta_M \quad (2.69)$$

Thus, for very large electric fields, $Q_M \gg \Delta/2$, we have $\eta_M = 0$. The eigenvalues of Eq. 2.66 are

$$E_S = -\epsilon \sqrt{\left(\frac{\Delta}{2}\right)^2 + Q^2} \quad (2.70)$$

where again, $\epsilon = \mp 1$ corresponds to the upper (f) and lower (e) Λ -doublet states, respectively. Eq. 2.70 is plotted in Fig. 2.7. The Stark shifts are the same for $\pm M$ so that every Λ -doublet state is split into two doubly degenerate levels.

The eigenfunctions in the polarized basis are given by

$$\Psi_f(\bar{\Omega}, M_J, |\mathbf{E}|) = \cos \eta_M |J\bar{\Omega}, M_J\rangle - \sin \eta_M |J, -\bar{\Omega}, M_J\rangle \quad (\text{Polarized Basis}) \quad (2.71)$$

$$\Psi_e(\bar{\Omega}, M_J, |\mathbf{E}|) = \sin \eta_M |J\bar{\Omega}, M_J\rangle + \cos \eta_M |J, -\bar{\Omega}, M_J\rangle \quad (\text{Polarized Basis}) \quad (2.72)$$

where the field-dependent coefficients are given by

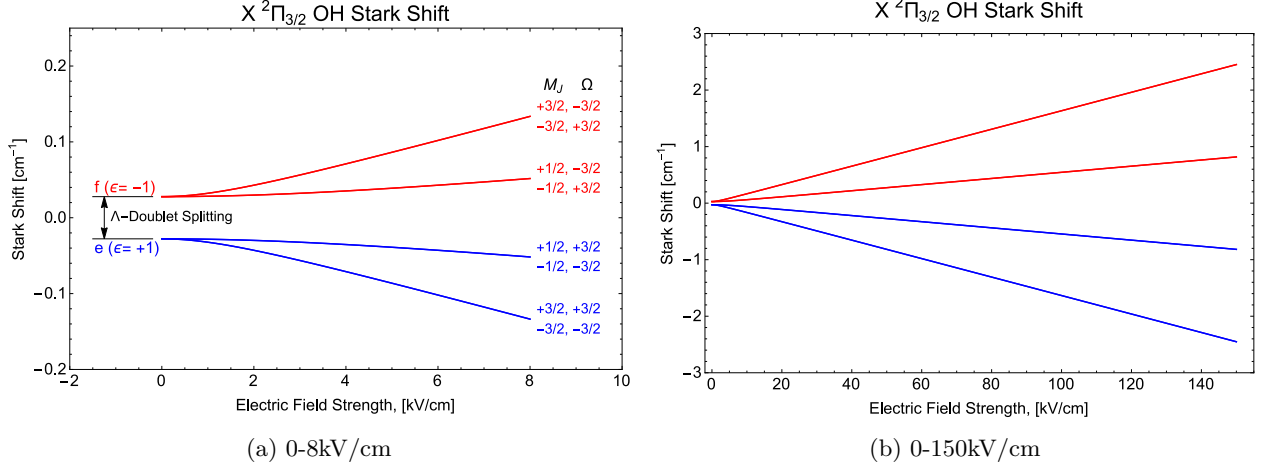


Figure 2.7: Stark shift for $^2\Pi_{3/2}$ OH radicals at relatively low electric fields (a) and high electric fields (b)

$$\cos \eta_M = \frac{Q_M}{\sqrt{Q_M^2 + (\Delta/2)^2}}; \quad \sin \eta_M = \frac{\Delta/2}{\sqrt{Q_M^2 + (\Delta/2)^2}} \quad (2.73)$$

Note that in the limit $Q_M \ll \Delta/2$, $\cos \eta_M \rightarrow 0$ and $\sin \eta_M \rightarrow 1$, and the primitive field free basis functions e/f are retained. Even though, strictly speaking, the zero-field parity states (f/e) are no longer well-defined once an electric field is applied, the labels (f/e) are retained in Eqs 2.75 and 2.76 because the states that have either an f or an e parity at zero field correlate adiabatically with those states in an applied field that are either low-field seeking ($|f\rangle$) or high-field seeking ($|e\rangle$). Conversely, when $Q_M \gg \Delta/2$, $\cos \eta_m \rightarrow 1$, and $\sin \eta_M \rightarrow 0$ and we can identify the f state as corresponding to $+\bar{\Omega}$ and the e state as that which corresponds to $-\bar{\Omega}$.

We could instead express the eigenfunctions using the $|e/f\rangle$ basis, where the states are expressed in terms of the components of the unperturbed (zero field) wave functions of the two parity levels. Of course, the parity basis is simply composed of symmetric and antisymmetric linear combinations of the polarized $|J, \pm\Omega M\rangle$ basis states. The Hamiltonian matrix would now no longer be given by Eq. 2.66 but instead by

$$H_M = \begin{pmatrix} -\Delta/2 & -Q_M \\ -Q_M & \Delta/2 \end{pmatrix} \quad (\text{Parity Basis}) \quad (2.74)$$

where the first column/row corresponds to $|e\rangle$ and the second to $|f\rangle$. Clearly Eq. 2.74 and Eq. 2.66 have the same eigenvalues, as they must. The eigenvectors could be found by diagonalizing the Hamiltonian given by Eq. 2.74 but instead we will perform a change of basis where the eigenvectors given by Eqs 2.71 2.72 are projected onto the parity basis functions. The wave functions are given by (Ref [71], page 253)

$$\Psi_f = a(E)|f\rangle + b(E)|e\rangle \quad (2.75)$$

$$\Psi_e = -b(E)|f\rangle + a(E)|e\rangle \quad (2.76)$$

where the mixing coefficients depend on the magnitude of the electric field

$$a(E) = \left[\frac{\sqrt{\Delta^2 + 4Q^2} + \Delta}{2\sqrt{\Delta^2 + 4Q^2}} \right]^{1/2} \quad (2.77)$$

$$b(E) = \left[\frac{\sqrt{\Delta^2 + 4Q^2} - \Delta}{2\sqrt{\Delta^2 + 4Q^2}} \right]^{1/2} \quad (2.78)$$

The parity composition of the upper Λ -doublet state as a function of increasing electric field is plotted in Fig. 2.8

The effects of OH being an intermediate Hund's case (a/b) makes a small correction to the form of Q_M for a pure $|J, \Omega, M\rangle$ state. Q_M then becomes

$$Q \rightarrow -dE \frac{M_J \Omega_{eff}}{J(J+1)} \quad (2.79)$$

where

$$\Omega_{eff} = \left(\frac{1}{2}a_J^2 + \frac{3}{2}b_J^2 \right) \quad (2.80)$$

Ω_{eff} represents the effective value of Ω quantum number, whose magnitude is slightly different from $\pm 3/2$ because of the mixing/coupling of the $X^2\Pi_{1/2}$ and $X^2\Pi_{3/2}$ manifolds due to the spin-orbit Hamiltonian. The parameters $a_J \approx 0.173997$ and $b_J \approx 0.984746$ are the mixing coefficients described at the end of Sec. 2.6. With these values, $\Omega_{eff} \approx 1.47048$.

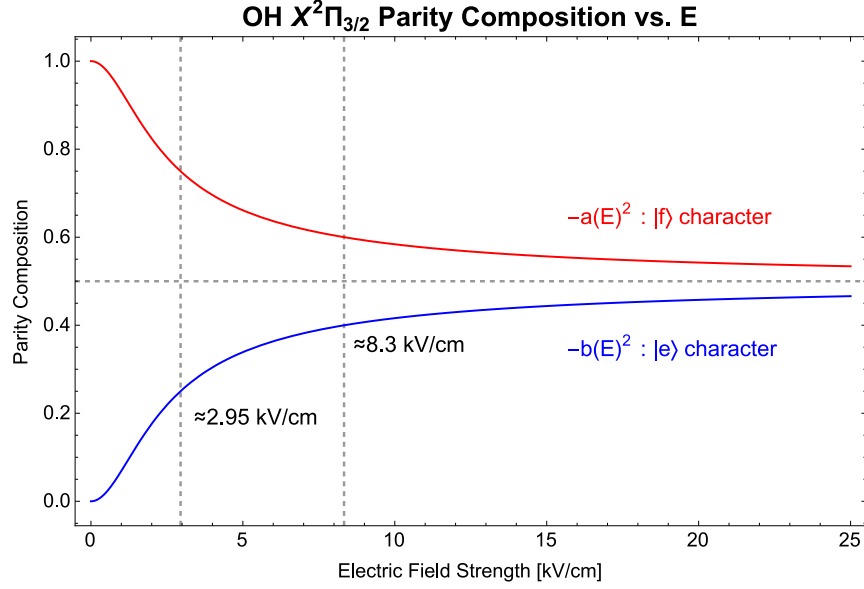


Figure 2.8: Parity composition of upper Λ -doublet state as a function of electric field. Here the electric field mixes parity. Plotted are the squares of the coefficients of the wavefunction when expressed in terms of the unperturbed parity levels. The vertical grid lines at $|E| \approx 2.95 \text{ kV/cm}$ and $|E| \approx 8.33 \text{ kV/cm}$ correspond to 25 : 75 and 40 : 60 parity state superpositions, respectively.

It is sometimes useful to express the Stark shift relative to the energy at zero field ($|\mathbf{E}| = 0$) such that the potential energy (spatially varying) can be set to zero, which can be useful in energy-based kinematics/dynamics, i.e.:

$$\Delta E_S = \sqrt{\left(\frac{\Delta}{2}\right)^2 + \left(d|\mathbf{E}|\frac{M\Omega_{eff}}{J(J+1)}\right)^2} \mp \frac{\Delta}{2} \quad (2.81)$$

2.8.2 OH Zeeman Shift

In this section we consider the strong-field Zeeman shift of OH. The classical Hamiltonian for the Zeeman effect is given by

$$\mathcal{H}_Z = -\boldsymbol{\mu}_m \cdot \mathbf{B} \quad (2.82)$$

The magnetic moment of OH has contributions from both the spin and the orbital angular momentum of the valence electron, so that Eq. 2.82 becomes,

$$\mathcal{H}_Z = -\boldsymbol{\mu}_m \cdot \mathbf{B} = \mu_B (\mathbf{L} + g_e \mathbf{S}) \cdot \mathbf{B} \quad (2.83)$$

where we identify the magnetic moment in the frame of the molecule to be

$$\boldsymbol{\mu}_m = -\mu_B (\mathbf{L} + g_e \mathbf{S}). \quad (2.84)$$

Taking \mathbf{B} to lie along \hat{Z} yields

$$\mathcal{H}_Z = \mu_B B (\hat{L}_z + g_e \hat{S}_z) \quad (2.85)$$

In the J (and parity ϵ) basis, the Zeeman Hamiltonian for $\Omega = |\Lambda| + |\Sigma|$ takes the form:

$$\langle JM_J \bar{\Omega} \epsilon | H_Z | JM_J \bar{\Omega} \epsilon' \rangle = \mu_B B (\bar{\Lambda} + g_e \bar{\Sigma}) \frac{\bar{\Omega} M_J}{J(J+1)} \delta_{\epsilon \epsilon'} \quad (2.86)$$

and for $\Omega = |\Lambda| - |\Sigma|$, we get

$$\langle JM_J \bar{\Omega} \epsilon | H_Z | JM_J \bar{\Omega} \epsilon' \rangle = \mu_B B (\bar{\Lambda} - g_e \bar{\Sigma}) \frac{\bar{\Omega} M_J}{J(J+1)} \delta_{\epsilon \epsilon'} \quad (2.87)$$

The significance of the Kronecker deltas in Eqs. 2.86 and 2.87 is that the Zeeman shift only connects states of same (well-defined) parity. Excluding excited rotational levels, H_Z is clearly diagonal in the $|JM_J \bar{\Omega} \epsilon\rangle$ basis. The strong-field Zeeman shift for the $X^2\Pi_{3/2}$ ro-vibrational ground state of OH is shown in Fig. 2.9.

For $X^2\Pi$ OH, $L = 1$ and $S=1/2$ so that $|\boldsymbol{\mu}_m| = 2\mu_B$. Here μ_B is the Bohr magneton and g_e is the electron's g factor, $g_e \approx 2.002$. The magnetic interaction term becomes comparable to the Λ -doublet splitting for magnetic fields of magnitude $\mu_m B \approx \Delta$ or $B \approx 600G$. Rotational averaging reduces the effective dipole moment to

$$\mu_m^{(eff)} = \mu_m \frac{M\Omega}{J(J+1)} \quad (2.88)$$

Taking Eq. 2.88 into account, and considering the stretched state only, $|M| = |\Omega| = J = 3/2$, the space-fixed magnetic dipole moment is reduced to $\mu_m = \frac{3}{5}2 * \mu_B$. Then the field required to get a Zeeman interaction comparable to the Λ -doublet splitting is $B \approx 1000G$.

The Zeeman shift for either parity state can be written as

$$\begin{aligned} E_Z(|\epsilon, M_J\rangle) &= \mu_B B (\bar{\Lambda} + g_e \bar{\Sigma}) \frac{\bar{\Omega} M_J}{J(J+1)} - \frac{\epsilon}{2} \Delta \\ &= \alpha M_J B - \frac{\epsilon}{2} \Delta \end{aligned} \quad (2.89)$$

The $|e, M_J = +3/2\rangle$ states cross the $|f, M_J = \pm\frac{1}{2}, -\frac{3}{2}\rangle$ states at magnetic fields given by

$$B_X(M') = \frac{\Delta}{\alpha \left(\frac{3}{2} - M'\right)} \quad (2.90)$$

where here M' refers to the $|f\rangle$ state and $\alpha = \mu_B (\bar{\Lambda} + g_e \bar{\Sigma}) \frac{\bar{\Omega}}{J(J+1)}$. The crossings are then at $B_X(+1/2) = 1488G$, $B_X(-1/2) = 744G$ and $B_X(-3/2) = 496G$. Thus, we see that the two parity manifolds first begin to cross at around $B \sim 500G$ and are completely "entangled" by $B \sim 1500G$.

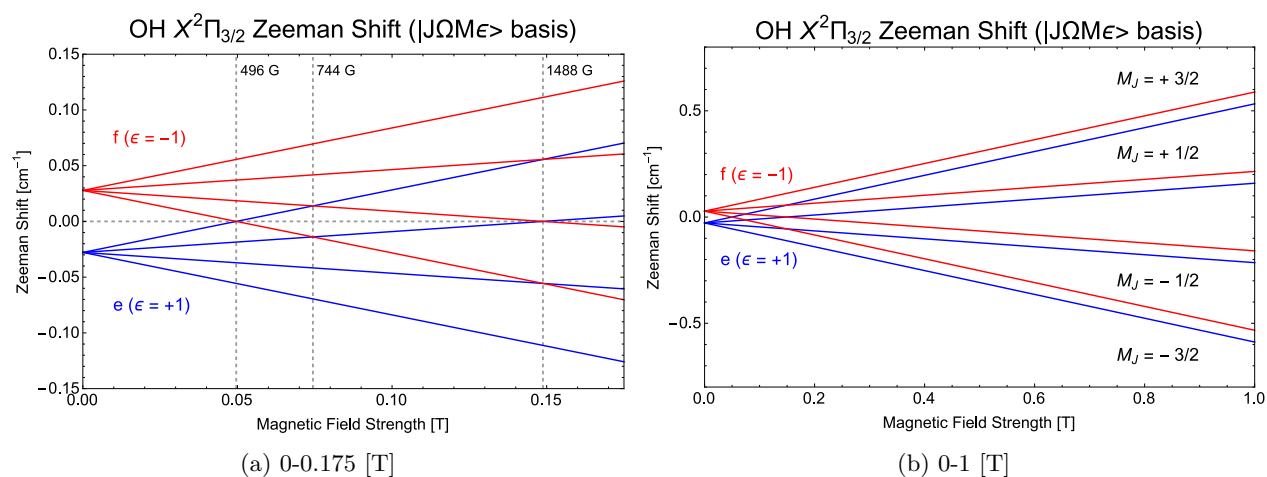


Figure 2.9: Zeeman shift for the $X^2\Pi_{3/2}$ ro-vibrational ground state of OH radicals in the $|J\Omega M_J \epsilon\rangle$ basis. Since the Zeeman Hamiltonian couples only states of like parity, the two Λ -doublet levels of OH shows exactly the same field dependence. Also, the lack of coupling between e and f states causes only diabatic level crossings. Panel (a) shows the behavior from 0 – 0.175T and (b) shows the behavior at fields from 0 – 1T . (a) also indicates the locations of the crossings by vertical grid lines at 1488G, 744G and 496G. Styled after Fig. 2.10 from BC Sawyer Thesis.

Molecular Beams

“Genius is 1% inspiration and 99% perspiration”

– Thomas A. Edison

“Edison said that because he was doing it wrong.”

– Philip C. D. Hobbs, [76] (1ed page 363)

3.1 Introduction

It is hard to overstate the profound importance that atomic and molecular beams have had in modern chemistry and physics. Their ability to produce samples of gas-phase atoms and molecules in a collisionless environment has proved invaluable for investigations into the microscopic properties of matter. The demonstration of space quantization of the magnetic moment (and thus also of angular momentum) in an atomic beam of silver atoms by Stern and Gerlach in 1922 [77] remains one of the most celebrated experiments in modern physics. The basic idea of their experiment, namely the deflection of a dipole moment in an inhomogeneous electromagnetic field to achieve spatial selection of internal quantum states is no less relevant today than it was in 1922 [78]. The inclusion of oscillating fields by Rabi led to the development of molecular beam resonance method to detect the transitions between quantum states and can be considered the first NMR spectrometer. Other landmark achievements in physics include the development of the hydrogen maser developed by Gordon, Zeiger and Townes [79], and the creation of the first atomic clock based on a Cesium

fountain by Norman Ramsey. For the chemistry community, supersonic molecular beams have revolutionized the study of molecular spectra due to the vastly simpler spectra from the cold temperatures.

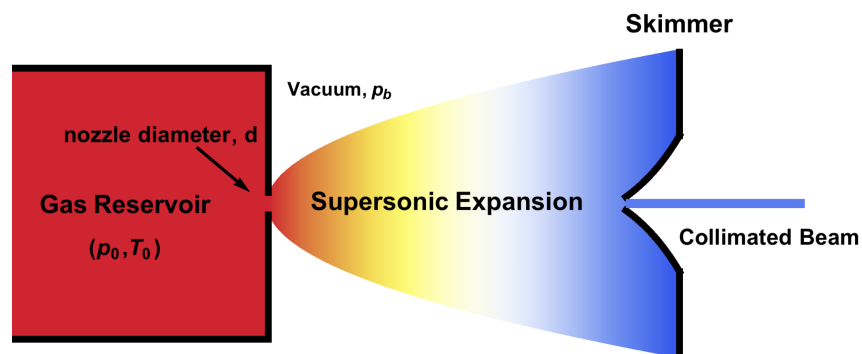


Figure 3.1: Generalized supersonic beam source. For an ideal isentropic expansion, flow conditions are completely determined by the stagnation parameters in the reservoir, P_0 , T_0 and the nozzle diameter, d .

Fig. 3.1 shows a generalized molecular beam source, which consists of three major components. The first major component is a high-pressure reservoir of gas at temperature T_0 and density n_0 (or pressure p_0) with a hole to allow gas molecules to escape into a vacuum. Throughout this chapter a subscript “zero” will be used to indicate parameters inside the reservoir (the stagnation parameters); T_0 , P_0 and n_0 , etc. The aperture is usually followed by various collimating slits/apertures (second major component) to shape the downstream flow pattern in some desired manner. The third major component of a molecular beam apparatus is a pumping system to evacuate the chamber.

The atomic, molecular, and optical (AMO) physics community in general, and those working on gases of cold atoms and molecules in particular, pride themselves on the exquisite degree of control they have over their experimental system. This is one of the reasons that AMO physics is so appealing. Compared with more typical electro-optic measurements in modern AMO labs, such as frequency locking a diode laser for laser cooling experiments, atomic beam methods can seem “dirty.” In some respects, this is unavoidable due to 1) to the statistical nature of describing thermal samples of molecules and 2) the relative scarcity of “detectors” giving useful information about molecules in the beam ¹. Nevertheless, hopefully this chapter will demonstrate the remarkable degree to which supersonic beam sources can be known in quantitative

¹ I’m still waiting for the “fiber atom laser” that can be directly coupled to a semiconductor based detector...

terms.

3.2 Molecular Flow Regimes

Gas flows of any kind are distinguished by their *molecular flow regime* [80]. These regimes are described by a single parameter known as the Knudsen number, Kn , defined as the ratio of the mean free path to a characteristic linear dimension (say the side length of the container), $Kn = \frac{\lambda}{d}$ [81]. Simple arguments [82] show that the Knudsen number can be interpreted as the ratio of the frequency of collisions with the container walls and the frequency of collisions with other molecules. At low densities, such as the densities of the background gas in a vacuum chamber, collisions with other gas molecules are exceedingly rare, with the molecules being more likely to bounce from one side of the container to the other without colliding with another gas molecule ($Kn \gg 1$). In contrast, at high densities, molecule-molecule (binary) collisions become very frequent and it makes more sense to think of the congested gas as a continuous fluid ($Kn \ll 1$). These two extremes are termed the *free molecular* (or simply effusive) and the *continuum* (or hydrodynamic) regimes, respectively.

The impact that these two regimes of gas dynamics have on a molecular beam sources is quite profound. For a beam, the relevant linear dimension for determining Kn is the aperture diameter since that is the point where beam formation begins. The relevant mean free path is the one just inside the reservoir and is denoted λ_0 . In the limit that the mean free path in the reservoir is much greater than the diameter of the aperture, molecules escape without colliding with other gas molecules. These beams with $\lambda_0 \gg d$ are typically referred to as *effusive* since the molecules effectively wander out of the aperture (see Fig. 3.2a, left). The characteristic temperature of effusive beams is a direct reflection of the temperature inside the reservoir, T_0 . (Sometimes effusive beams are called *thermal beams* for this reason). The velocity distribution outside the reservoir is somewhat skewed to higher velocities due to the fact that faster molecules are more likely to escape, but has a width comparable to that inside the reservoir,

$$f(v)dv \propto v^3 e^{-\frac{mv^2}{2k_B T_0}} \quad (3.1)$$

where v is the molecular velocity, m is the molecular mass, and k_B is Boltzmann's constant.

At the other extreme, where $\lambda_0 \ll d$ (continuum regime) the escaping gas molecules undergo many collisions during their passage through the aperture and in the downstream region (see Fig. 3.2a, right). Collisions that impart a velocity component along the beam axis (i.e., normal to hole) are most successful at getting molecules out of the reservoir. The result of the exiting molecules always being hit from behind is that there is a nearly complete conversion of thermal energy into directed bulk flow along the beam axis at velocity u . The decrease of the total internal energy of the gas from two-body collisions results in a decrease of the relative velocities between individual molecules, or equivalently a *cold* temperature associated with the moving frame. These basic ideas are depicted in Fig.3.2a.

3.3 Basic Thermodynamics of Supersonic Beams

In the continuum limit, the properties of the expanding gas are described in terms of thermodynamics. For rapid expansion in which there is negligible heat exchange between the walls of the reservoir, the expansion is adiabatic/isentropic. These expansions are termed *supersonic* because the flow velocity out of the nozzle can be faster than the local speed of sound. The flow from an ideal continuous supersonic expansion is well described by the basic results from adiabatic compressible flow theory used in the design of aircraft [83]. This theory allows the flow properties relevant to the molecular beam, such as flow velocity, temperature, and density, to be described as a function of the distance from the nozzle. The key results are used throughout this chapter to describe molecular beams, but a detailed discussion of the origin of these results is relegated to Appendix B.

The most important equation for describing supersonic beams is the first law of thermodynamics (the conservation of energy). The total energy of a gas can be partitioned into three parts: (1) the internal energy of the gas, U_{int} ; (2) the potential energy, pV , associated with the pressure (compression, etc), and (3) the kinetic-flow energy $\frac{1}{2}Wu^2$ associated with bulk flow of the gas of molar mass W (the moving frame). The total internal energy, U_{int} , includes energy stored in rotational and vibrational degrees of freedom as well as thermal translational motion associated with the center of mass of the gas. Conservation of energy, $E = U + pV + \frac{1}{2}Wu^2$, before and after the expansion demands:

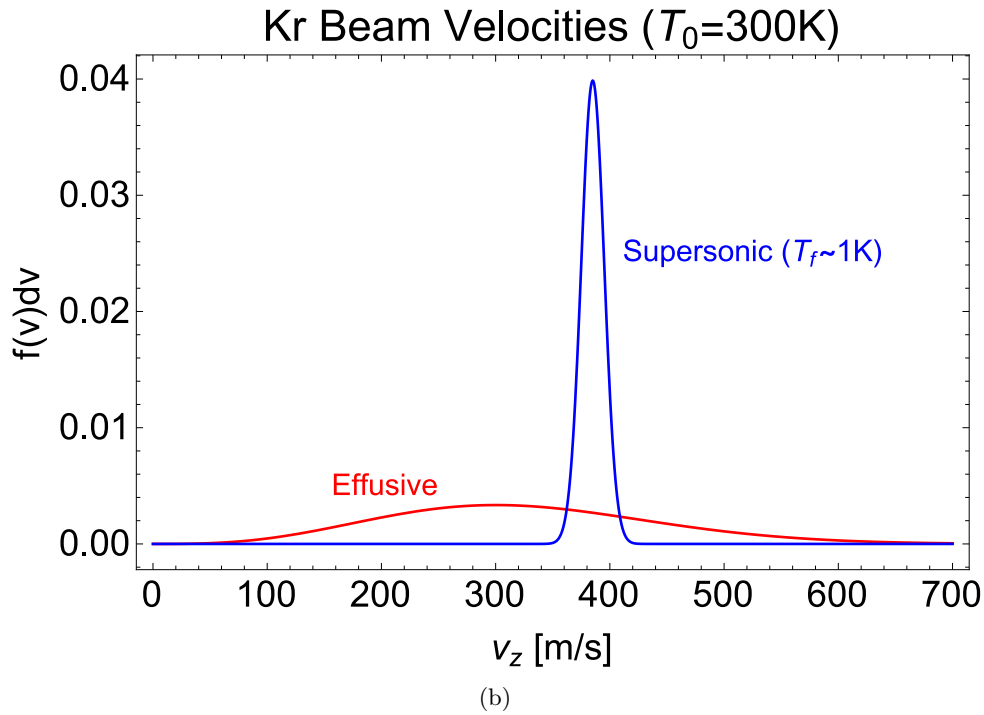
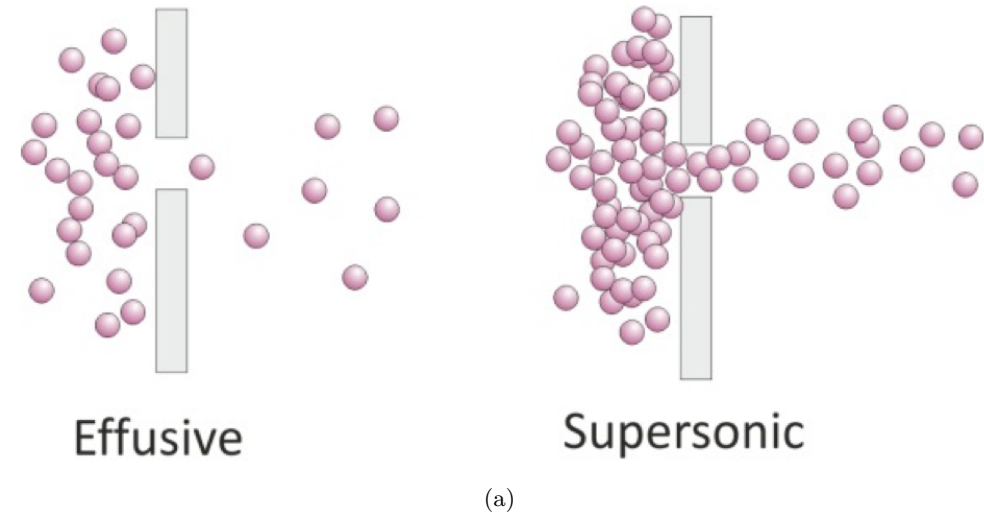


Figure 3.2: Comparison of effusive and supersonic beams: (a) cartoon illustrating the fundamentally different collisional properties of effusive (left) and supersonic beams (right). Figure from [7]. (b) Normalized distribution of parallel velocity for a Kr beam from a reservoir at $T_0 = 300K$ for an effusive beam (red) and a supersonic beam (blue) with an assumed final temperature of $T = 1K$.

$$U_0 + p_0V_0 + \frac{1}{2}Wu_0^2 = U + pV + \frac{1}{2}Wu^2. \quad (3.2)$$

For a low flow rate through the nozzle, the thermal equilibrium inside the reservoir is unperturbed, which implies $u_0 = 0$ (no temperature gradients driving pressure waves etc). Assuming the gas expands into a perfect vacuum, the pressure after the expansion can be taken to be very small ($p \ll p_0$). Setting $p = 0$ and $u_0 = 0$ in Eq. 3.2 yields:

$$U_0 + p_0 V_0 = \cancel{U} + \frac{1}{2} W u^2. \quad (3.3)$$

Eq. 3.3 is a mathematical statement of the previously qualitative statement that the supersonic expansion converts the energy inside the reservoir associated with random atomic motion ($U_0 + p_0 V_0$) into bulk flow at velocity, u . In the limit that most of the reservoir energy is converted to bulk flow energy, the internal energy of the expanding gas must drop, $U_{int} \approx 0$.

We have treated the individual energy terms separately for the purposes of developing an intuitive understanding of the final state of supersonic beam. However, when dealing with the flow of compressible gases driven by pressure gradients, it is more customary to use *enthalpy*, $H = U + pV$, instead of dealing directly with the internal energy, U_{int} . Then, setting $u_0 = 0$ in Eq.3.2 yields:

$$H_0 = H + \frac{1}{2} W u^2 \quad (3.4)$$

The enthalpy of an ideal gas is related to its temperature by $H = C_p T$ where C_p is the heat capacity at constant pressure. For an ideal gas with n_f internal degrees of freedom, C_p is given by $C_p = \frac{n_f + 2}{2} R$ where R is the gas constant. C_p is often expressed in terms of the ratio of the specific heat at constant pressure to the heat capacity at constant volume, $\gamma = \frac{C_p}{C_v}$ [83],

$$C_p = \frac{n_f + 2}{2} R = \frac{\gamma}{\gamma - 1} R \quad (3.5)$$

For a molecular gas the amount of energy stored in rotational and vibrational degrees of freedom is temperature dependent because modes get frozen out at low temperatures. For a monatomic gas, however, C_p is temperature independent. In this case Eq. 3.4 becomes

$$C_p T_0 = C_p T + \frac{1}{2} W u^2. \quad (3.6)$$

The flow velocity is expressed in terms of the beam temperature by

$$u(T) = \sqrt{\frac{2C_p}{W} (T_0 - T)} = \sqrt{\frac{2R}{W} \frac{\gamma}{\gamma - 1} (T_0 - T)} \quad (3.7)$$

Then the maximum flow velocity, commonly termed the *terminal velocity*, occurs when $T = 0$:

$$u_\infty = \sqrt{\frac{2R}{W} \frac{\gamma}{\gamma - 1} T_0} \quad (3.8)$$

Using the molar mass W in $[kg/mol]$ gives a resulting velocity in $[m/s]$. Eq. 3.8 is plotted for the rare gases (with $\gamma = 5/3$) in Fig. 3.3 for a room temperature of $T_0 = 300K$ (for details see Appendix B). It is interesting to note that the flow velocities shown in Fig. 3.3 are of the order of the average thermal velocity in the reservoir, a result that almost could have been “guessed” from energy conservation alone.

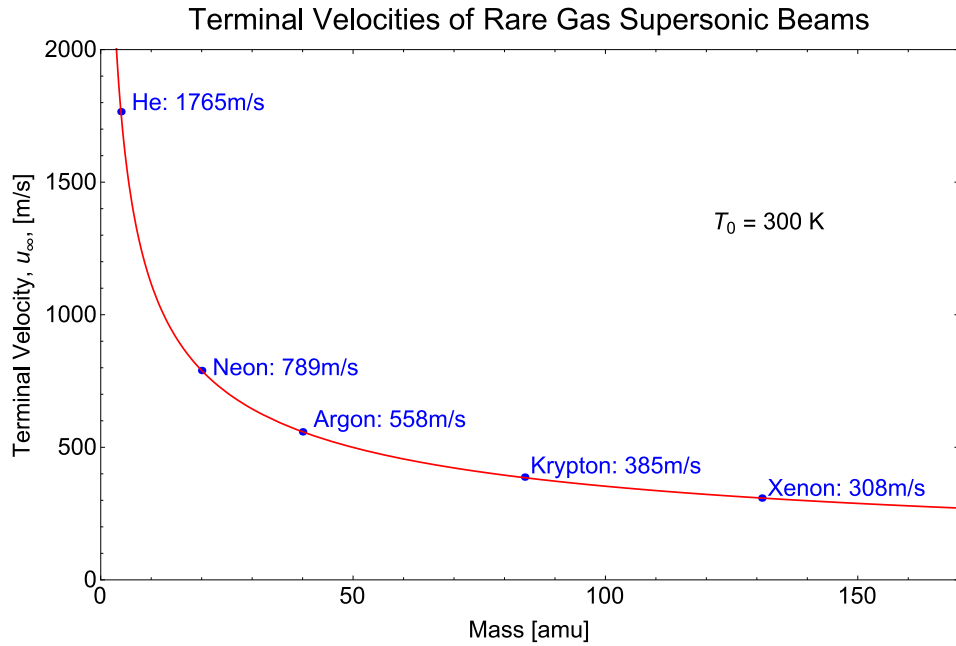


Figure 3.3: Terminal velocities (Eq. 3.8) of supersonic expansions of rare gas atoms with reservoir temperatures of $T_0 = 300K$.

Even though all gases plotted in Fig. 3.3 have the same average thermal energy in the reservoir ($\sim RT_0$), the resulting flow velocities will decrease with increasing mass as $\propto \sqrt{\frac{T_0}{W}}$. Thus, changing the

expanding gas species or the reservoir temperature is a convenient way to tune the flow velocity of the beam. This feature will prove crucial for deceleration of supersonic beams.

3.4 Pulsed Supersonic Beams

In modern molecular beam experiments, including those in the cold molecule field, continuous beams have been nearly completely replaced by *pulsed* supersonic beams. This section gives a brief discussion of the basic features of pulsed beams that explains their popularity and how to use them most efficiently in a cold molecule experiment.

In the previous section, a final beam final temperature of $T = 0$ was assumed for simplicity. In practice, temperatures around $T \approx 1K$ are more typical. The continuum model has neglected the microscopic nature of the cooling process, which is ultimately due to two-body collisions within the expanding gas. The number of these collisions a given gas molecule experiences during the expansion is finite, due to the $\sim 1/r^2$ density dependence of the expansion. Calculations using the results of compressible flow theory (Sec. B.2.1) indicate that the number of these collisions scales linearly with the parameter $p_0 * d$,

$$\text{\#2-body collisions (Cooling)} \propto p_0 d \tag{3.9}$$

where p_0 is the reservoir pressure and d is the nozzle diameter. By convention, this parameter is typically given in units of $[Torr \cdot cm]$. This result suggests that the coldest beams are those with very high stagnation pressures [84], [85]. The maximum practical value of $p_0 * d$ is largely limited by the pumping capacity used to evacuate the vacuum system. The total gas flux through the nozzle (gas load) will scale as

$$\text{Gas Load} \propto p_0 d^2 \tag{3.10}$$

which is clearly at odds with maximizing $p_0 * d$ for cold beams. In the late 70's Gentry and Giese pointed out that introducing a time-dependent gate at the nozzle [8] is a very effective way to minimize the overall gas load while simultaneously operating the source at high values of $p_0 * d$ [9]. Perhaps the best demonstration of this basic feature of pulsed supersonic beams is the ultralow temperatures ($T \approx 10mK$) reached in high

pressure ($p_0 \sim 100\text{atm}$) helium expansions with ultrafast valves [86], [87], [88].

The impressive results with helium should not be taken to mean that all supersonic beams should be operated with such high pressures. At these high pressures, condensation of monomers into Van der Waals clusters becomes important. These dimers are typically weakly bound but can exist in large numbers at the low temperatures reached in supersonic beams. The study of these Van der Waals molecules is an interesting study in its own right, with many experiments aim to maximize cluster formation. Here at JILA, the Nesbitt group has developed pulsed slit jets to enhance the clustering rate [89],[90]. For production of samples of cold molecules, cluster formation is mostly a nuisance. Cluster formation requires a 3-body collision where the third particle carries off the energy difference. This extra energy is added to the beam as heat which sets a lower limit on the minimum achievable beam temperature. Helium atoms are about as “billiard ball” of an object as nature provides (inelastic cross sections are very low). The helium dimer is so weakly bound [91] that cluster formation is greatly suppressed, thus allowing helium beams to be operated at very high pressures at virtually no cost [92]. All other gases will begin to condense at the low temperatures reached in supersonic beams. Calculations similar to those laid out in Sec. B.2.1 give an analagous scaling law for the number of 3-body collisions, i.e.:

$$\text{3-body collisions(Clustering)} \propto p_0^2 d \tag{3.11}$$

Since the ratio of 3-body to 2-body collisions scales linearly with p_0 , then for a fixed value of $p_0^2 \cdot d$, clustering formation will be minimized for larger nozzle diameters, d , and lower pressures, p_0 [93].

3.4.1 Pulsed Valve “Shutter Function” and Effective Valve Diameter

This section presents a brief discussion of the basic principles of all pulsed valves independent of their actuation mechanism. If the pulsed valve is operated such that the gas flow is limited only by the geometric nozzle diameter, and not by the opening mechanism itself, the flow is said to be *choked* [9]. In this case, the pulsed beam will have flow properties identical to those of a continuous supersonic expansion having the same source pressure, nozzle geometry, and background pressure. The validity of this notion of pulsed beams as gated or modulated continuous beams (“beamlets”) usually requires relatively long opening times

such that the flow out of the nozzle has reached a steady state. The two basic signatures of choked flow are 1) a plateauing of the chamber pressure (gas load) as a function of valve opening (e.g., applied voltage) and 2) a flat top time of flight (TOF) profile [94], [95].

As the valve pulse duration decreases, the approximation of the idealized square pulse behavior becomes questionable since real valves don't open and close instantaneously. The time dependence of the valve opening mechanism is termed the *shutter function* [9]. It can be characterized by a time-dependent nozzle conductance, $C_{pv}(t)$, or equivalently, a time-dependent effective nozzle diameter, $d_{eff}(t)$. The majority of pulsed valves operate by linearly retracting a piston, which makes a seal against a circular orifice. The linear excursion required to open the valve to choked flow will depend on how the seal is made but is generally of the order of the nozzle diameter. Given the finite response time of a massive mechanical system, the fastest acting valves are typically those based on miniaturized actuators coupled to small nozzle diameters. It is important to point out that it is possible reach a steady state, but at an effective diameter less than the geometrical nozzle diameter. In this case, the valve motion has stabilized and the gas flow is limited by failure of the valve mechanism to retract completely and not by the downstream aperture. Often the situation is further complicated by the desire for low gas loads. If operators apply pulses that are comparable to the intrinsic time response of the valve, a steady state may never be reached. Under these conditions the pulsed beam will clearly not be the "modulated" version of the equivalent continuous beam.

The motion of the valve piston can be approximated as a simple harmonic oscillator driven by an impulsive force [9]. The intrinsic time scale of the valve mechanism is then determined by the natural resonant frequency of the oscillator, f_{res} . Typically a bias tension is applied to the poppet to make a leak-tight seal and to shorten the closing time. The effect of the bias force to the poppet can be understood by the simple model presented in Fig. 3.4. Here the valve oscillator retracts in the negative direction and a bias tension against the valve face is applied to the piston in the positive direction, which reduces the effective displacement from the sealing surface located at a vertical position of zero. If the poppet were adjusted with no bias, the excited valve "oscillator" would undergo a half cycle with an open time of $\Delta t_{free} = 2/f_{res}$ before colliding with the valve face. As indicated by the red shading in Fig. 3.4, the bias effectively shortens the "open time" of the valve. If the valve is operated in choked flow, this would be the only effect. If not, the

applied bias force which limits the piston's linear travel and reduces the effective opening time, also reduces the effective valve diameter, d_{eff} (see Fig. 3.4).

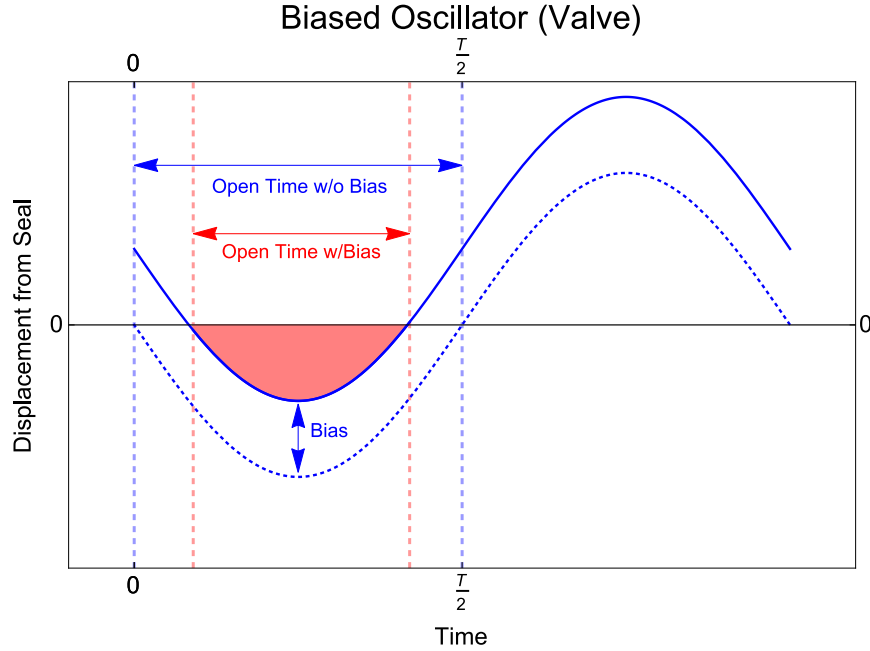


Figure 3.4: Simple model of the motion of the valve piston as a function of bias. In the first half of the oscillation cycle, the piston moves in the negative direction. When it crosses the sealing threshold (horizontal axis), the valve opens. For cases where gas flow is not limited by a downstream aperture, application of a bias to reduce the pulse duration always comes at the cost of reduced effective valve diameter, d_{eff} . Figure styled after [8], [9].

An additional limitation to the pulse durations is set by the nature of the fluid dynamics of the gas itself. Early experiments with ultrashort pulsed valves noted that the temporal profile of the escaping gas pulse was dependent on the type of gas even if the valve was operated under identical conditions [8]. This was attributed to a difference in the time required for different gases to reach supersonic flow velocity; the heavier gases simply did not respond as fast as lighter gases. A “shoot from the hip” approach to estimating the response time of a gas to a change can be found by taking the ratio of a characteristic length describing the flow (the nozzle diameter d) to a characteristic velocity, (the speed of sound in the reservoir, $a_s(T_0)$) [96]. A more complete calculation [97], [96] gives a more conservative value for the minimum time required for supersonic flow to develop: $\tau_{min} = \frac{4d}{a_s(T_0)}$. For a $d = 0.5mm$ nozzle, this time is $2\mu s$, $6.2\mu s$, and $9\mu s$ for helium, argon, and krypton, respectively. [97]. This result suggests that this minimum opening time

is not expected to play a large role for all but the fastest acting valves with pulse durations approaching $10\mu s$. Interestingly, more recent results with an ultrafast valve operated with helium [98] suggest that the simple estimate in [97], [96] may be too low, but at present this seems to be the only experimental work documenting this behavior.

3.4.1.1 The “Proch and Trickl” PZT Valve

The number and variety of pulsed valves available today is truly remarkable [9]. One of the first types of valve was based on the magnetic repulsion of two metal strips carrying large opposing currents [8],[95] and has been shown to have pulse durations as short as $10\mu s$ [8]. These *current loop* valves are now commercially available as the “Jordan valve” [99], but the pulse durations for these valves are not nearly as short as the original device reported in [8]. Recently, an ultrafast valve ($\approx 20\mu s$) similar to the current loop valve but with permanent magnets to reduce the overall heat load has been introduced [100]. Magnetically actuated solenoid valves adapted from the automotive fuel injectors [101], [102], [103] are very robust but have relatively long pulse durations (several hundred μs) [103]. The commercially available solenoid valve from the General Corp [104] is one of the most common pulsed valves currently in use (Series 9 or 99). An optimized solenoid valve capable of $10\mu s$ pulses was developed in 2000 as the “Even-Lavie” valve (or, more colloquially, the “Uzi” valve) [105]. This valve is widely considered to be the state of the art but is fairly expensive ($\approx \$10k$) and has very long lead times (in excess of 1 year) due to small scale production capabilities.

The third and final class of valves are those based on piezoelectric actuators. The primary benefit of these valves is low power consumption, which leads to very reproducible performance and minimal heating of the expanding gas even when operated at high repetition rates [106], [107], [108]. The first piezo valves suffered from low linear excursions, which limited the effective nozzle diameter, $d_{eff} < 100\mu m$, [106], [109]. In 1989 Proch and Trickl, introduced an improved valve design [107] that used a much stronger disk translator allowing more robust operation and choked flow of a $d = 1.0mm$ nozzle for $150\mu s$ pulse durations at $1kV$. Recently, a number of piezo valve designs based on based on *stack* actuators have emerged [108], [110]. These valves achieve large excursions at low voltages, and, significantly, those with the cantilever design reported

in [108] (which is based on an earlier design from D. Gerlich [111]) produces pulses as short as $7\mu s$ and allow operation at repetition rates as high as $5kHz$. At JILA, Ben Stuhl from the Ye group worked with Hans Green in the instrument shop to develop a homemade version of this valve, though currently it is not in use.

The valve used for all experiments in this thesis is similar to Proch and Trickl’s basic design but with a number of JILA-developed special features. This valve operates by the flexing motion of a piezoelectric bimorph actuator² (Physik Instrumente, P/N: 286.23) that translates a piston fitted with an O-ring. The actuator consists of a lead zirconate titanate (PZT) disk bonded to a stainless steel plate (0.5mm thick) that forms a rigid surface on which to attach the piston.

The unloaded actuator has a DC linear translation in the center of $100\mu m/1kV$ and a resonant frequency of $\approx 2.5kHz \pm 20\%$.³ The PZT valve is driven by a homemade HV switch in a MOSFET push-pull configuration. To protect the PZT from damage under excessive impulse forces, the manufacturer specifies a minimum rise/fall time of $50\mu s$, which is set by putting a resistor **R=xxxxx** in series in series with the PZT disc capacitance ($C = 65nF$). The coloring of the lead insulation for this actuator is somewhat confusing. As a rule only positive voltages should be applied to PZT’s. The side of the PZT not directly bonded to the SS plate is coated with a transparent *red* plastic insulator and is connected to the *black* wire. This side of the piezo must be kept at a lower electrical potential than the other side, which is achieved by applying *negative* voltages to the *black* wire and *grounding* the *red* wire.

The valve piston, or “poppet,” consists of a finely threaded adjustment screw (Thorlabs, 100 TPI) with a notch cut at the tip to fit a small O-ring (size 003). Empirical data suggest that slightly stiffer O-rings (Shore-A90) perform better than typical Viton O-rings (Shore-A75) [113]. The tension of the poppet O-ring seal against the valve face is controlled by manually threading the poppet into the vespel poppet holder, which can be accomplished in situ via a long hex wrench. The poppet tension must be carefully adjusted for a number of reasons. If the tension is too tight, the the front surface of the adjustment metal screw will slam into the front of the valve plate upon closing. This makes a rather loud “clanging” sound and rapidly destroys the PZT (see Fig. 3.6a). Evidence of this “cause of death” is seen in the wear on the inside surface

² For a tutorial on the various displacement modes of piezoelectric actuators, see [112].

³ The “blocking force” or max static load that the PZT can lift is $\approx 20N = 4.5lbs$. Taking the nominal piston diameter as ~ 0.19 ”, suggests that the valve may be operated up to pressures of $\sim 160psi \approx 8200Torr$ before the force from the stagnation pressure becomes problematic.

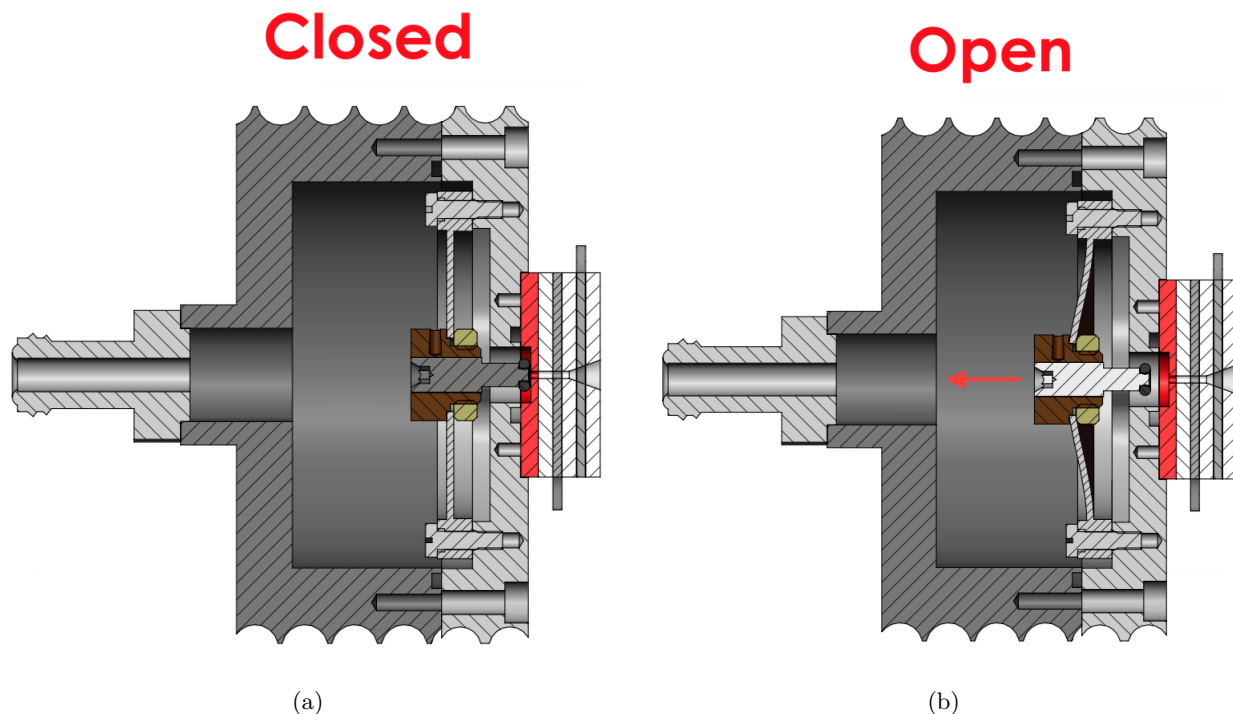


Figure 3.5: Schematic of the PZT valve (a) closed and (b) open. The poppet (central piece, grey) is threaded into the vespel poppet holder (brown) which is tightened to the PZT disk with a PEEK lock nut. The end of the poppet is fitted with an O-ring (Shore Durometer rating A-90, size 003) which seals against the valve face plate (red). The poppet is firmly held within the poppet holder with a 0-80 set screw (not shown-see Fig. 3.6b).

of the pulverized valve plate. If the tension is too loose, the valve will not make a good seal and give long, “floppy” pulses. A successful procedure for adjusting the tension of a freshly installed PZT is as follows: The valve body is assembled completely and then mounted to the vacuum chamber via the 8-in. conflat flange. At this stage the poppet O-ring is close to, but not sealing against, the front valve face. As the chamber is roughed out the poppet is slowly tightened just until the poppet seals. Ideally this is confirmed by monitoring the chamber pressure, but, in practice, simply holding a finger over a gas inlet port on the valve body to feel when the suction stops has given good results. Typically the poppet is tightened another 1/8-1/4 turn past the sealing threshold to ensure a good seal and apply a bias tension to the poppet. After any adjustments to the poppet, the wrench must be retracted before operation as this will also break the PZT for the same reasons it should not be overtightened against the valve face. During pumpout of the

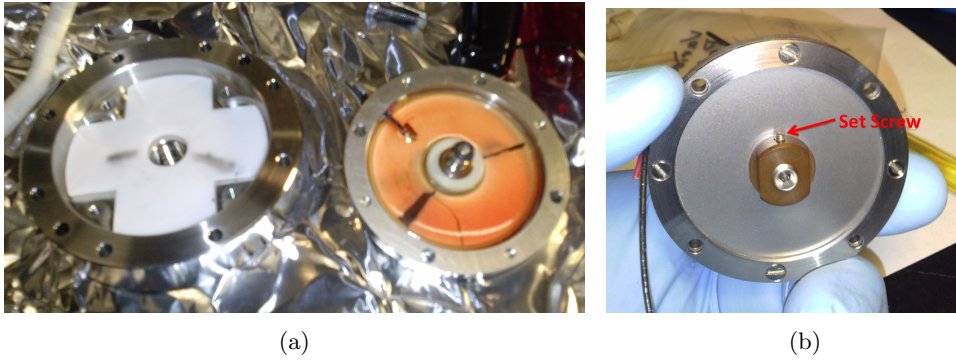


Figure 3.6: (a) Photograph of PZT actuator broken by over tightening poppet. Cracking was extensive enough that it broke through the plastic insulation and showed significant arcing about $\sim 500V$. Note the alignment of the burn marks at the location of the cracks on both the actuator and the teflon insulator. (b) 0-80 set screw to ensure a tight fit of the poppet in the vespel poppet holder. For details see text.

valve body, the HV should be switched off to prevent arcing of the PZT. At low pressures $\approx 1 - 10 Torr$ the mean free path of electrons becomes comparable to the dimension of the PZT, making discharges far more likely⁴.

A valve freshly installed following this procedure will typically begin to “open” around 100-200V (typically on the low end). This “threshold voltage” is a measure of poppet tension. Given the PZT linear excursion of $100\mu m/kV$ (at DC), a sealing threshold of say 150V, indicates that the O-ring is compressed by only $\approx 15\mu m$. This is much smaller than the linear excursion of the 100 TPI poppet *per turn* of $254\mu m$, which suggests that any adjustments made to poppet for an installed valve assembly should be very small, $\approx \frac{1}{16} - \frac{1}{8}$ of a full turn. Measurements of the sealing threshold and the chamber pressure rise as a function of applied voltage are a good first diagnostic of valve performance. Reductions in the PZT travel *per volt* over the course of an experiment (\sim several months) inferred in this way is a good indicator of the health of the PZT and overall valve performance.

A close fit of the poppet in the finely threaded poppet holder is absolutely critical for good valve performance. This is achieved by inserting an 0-80 set screw in the poppet holder whose role is rather subtle (see Fig. 3.6b). Rather than firmly “clamping” against the surface of the poppet, the set screw serves to deform the poppet holder around the poppet, making it difficult to turn the poppet. (Tap hole for set screw

⁴ Interestingly, this is exactly the same behavior that is exploited in the glow discharge of Kr/H₂O mixtures to generate OH radicals just downstream of the valve.

is under drilled). The set screw is tightened after the poppet is installed to a desired position (relative to valve face). In practice this set screw should be very tight to prevent the poppet from “wiggling free” during operation. The material of the poppet holder is also important. Poppet holders made from Vespel (which is a fairly rigid but very expensive vacuum-compatible plastic) seem to retain the fine 100 TPI threads much better than those made out of PEEK.

Interestingly, the valve also shows signs of “hysteresis” or “bistability,” as shown in Fig. 3.7a. As the applied voltage is increased from zero the blue curve is traced out. At a fairly large applied voltage whose value depends on the poppet bias, the valve will make a sudden transition to the red curve. Once in this second path, the valve will tend to stay there. For example, if initially on the red curve in the region where the two curves are separated, and the voltage is dropped to the point where the two two curves overlap, increasing the voltage to the initial voltage will retrace the red curve. This seems to suggest that something is stuck but once a threshold is reached the motion is more free. The valve can be operated along the blue curve at the normal operating point for long periods (years) provided that the threshold voltage is not exceeded.

Despite the claim in Proch and Trickl’s original paper of choked flow at $1kV$, we have found that operating the PZT valve at voltages above $\sim 500V$ can lead to unstable performance and possibly even cause the PZT to crack, which reduce the overall sensitivity of the piezo. Limited evidence suggests that a cracked PZT shows increased arcing (at least for cases where the the ceramic breaks through the insulation) which can be detected by monitoring the applied PZT voltage with a high-voltage probe (in this case arcing corresponds to a drop to zero/short in PZT voltage).

As a consequence of this practical upper limit to the applied PZT voltage ($\leq 500V$), we find that the flow out of our valve never reaches choked flow for a geometric nozzle diameter of $d_{geo} = 1.0mm$. The effective area that sets the flow rate is then due to the failure of the valve poppet to completely retract. This can then be correlated to the effective diameter by $d_{eff} = \frac{4A_{eff}}{\pi}$. The limiting area can be estimated as the surface area of cylinder (sans ends) formed by the O-ring with average radius r_0 ($r_0 = 1.5mm$ for size 003 O-ring), and the above threshold excursion of the PZT/poppet. The time-dependent, effective nozzle area can be approximated by

$$A(t) = L_{exc}(t) * 2\pi r_0 \quad (3.12)$$

where L_{exc} is the linear excursion of the PZT beyond the "sealing threshold" (see above discussion). $L_{exc}(t)$ can be approximated by

$$L_{exc}(t) = d_{13} * (V_{PZT} - V_{th}) \quad (3.13)$$

where $d_{13} = 100\mu m/1kV$ is the sensitivity of the PZT, V_{PZT} is the applied voltage and V_{th} is the threshold voltage.

Fig. 3.7b plots the effective diameter of a given valve installation, measured by recording the gas load as a function of valve voltage. This allows a calculation of the effective nozzle conductance which can then be related to the effective diameter by

$$C_p(t) = \xi d^2(t) = \xi \frac{4}{\pi} A(t) \quad [L/s] \quad (3.14)$$

where $A(t) = \pi \frac{d^2}{4}$ is the nozzle area given in $[cm^2]$ and ξ is a gas specific constant with units of $[\frac{L}{cm^2 * s}]$.

For Kr, $\xi = 9.8$.

For short pulses, $L_{exc}(t)$ will have a "shark fin" or "triangle shaped" temporal profile whose rise and fall times are given by the RC time constant of the driving electronics. For longer HV driving pulses (significantly longer than $1/RC$), $L_{exc}(t)$ will become more square shaped. The intrinsic time response of the valve is estimated by assuming that we predominantly excite the resonance of the unloaded actuator $\approx 2.5kHz$, which implies a half-cycle time of $\approx 200\mu s$. The actual opening time will be reduced somewhat due to the effect of biasing the poppet (see Fig. 3.4).

As discussed in Sec. 3.4 the practical values of $p_0 \cdot d_{eff}$ are set by the gas load ($\propto p_0 d_{eff}^2 \Delta t$) and the finite pumping capacity of the vacuum system. For low duty-cycle, pulsed beams pumped by turbo pumps, attenuation of the beam due to scattering off of background gas is not much of a problem. For a background pressure dominated by Kr, the mean free path is $\geq 10m$ even for background pressures as high as $1.0 \times 10^{-4} Torr$, suggesting minimal scattering for typical flight distances of $\sim 10-20cm$. Instead,

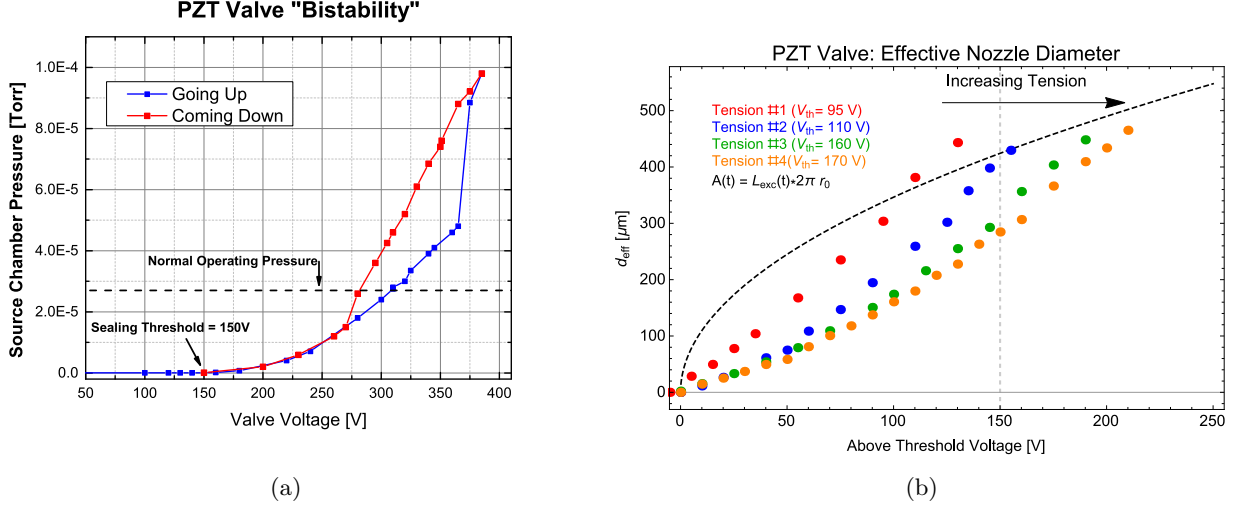


Figure 3.7: (a) PZT valve Bistability or Hysteresis. For details, see text. (b) Effective nozzle diameter as a function of above threshold valve voltage for 4 different poppet tensions and nominal pulse durations of $100\mu\text{s}$. Measured data (colored circles) are derived from measurements of the gas load in the source chamber. The dashed curve is the expected value, calculated using Eqs. 3.12 and 3.13

the maximum permissible gas load is set by molecular trapping experiments, which require a very low background pressure in the (differentially pumped) downstream part of the vacuum chamber. Ultimately a pulse duration of $100\mu\text{s}$ was chosen as a compromise between maximizing d_{eff} and limiting the overall gas load ($P_0 \approx 2200\text{Torr}$). This duration seems to be significantly shorter than that used in the chemistry community (see [114] for example) where restrictions on the gas load are not so great

3.4.2 Distribution of Molecular Velocities in a Supersonic Beam

Translational motion in a collimated supersonic beam is typically described by two effective temperatures; one for the parallel (longitudinal) direction, T_{\parallel} , and one for both perpendicular directions, T_{\perp} . The corresponding parallel (v_{\parallel}) and perpendicular (v_{\perp}) velocities are described by modified Maxwellian (Gaussian) distributions of the form

$$f(\mathbf{v})d\mathbf{v} = n\sqrt{\frac{m}{2\pi k_B T_{\parallel}}}\left(\frac{m}{2\pi k_B T_{\perp}}\right)e^{-\frac{m}{2k_B T_{\parallel}}(v_{\parallel}-u)^2}e^{-\frac{m}{2k_B T_{\perp}}v_{\perp}^2}d\mathbf{v} \quad (3.15)$$

In Eq. 3.15 u is the central longitudinal velocity, and n is the molecular number density [$\#/cm^3$]. The

spread in velocities is given in terms of the standard deviation, $\Delta v_i = \sqrt{\frac{2k_B T_i}{m}}$. Note that the longitudinal velocities are centered around the terminal flow velocity while the transverse velocities are centered around zero. Eq. 3.15 reduces to the well-known Maxwellian distribution function when $T_{\parallel} = T_{\perp}$ and $u = 0$.

3.4.2.1 Beam Velocity Measurements by TOF Measurements

The transverse velocity distribution in Eq. 3.15 is difficult to measure experimentally, but can be easily estimated based on geometric parameters for a skimmed or collimated beam. However, the longitudinal velocity distribution can be easily measured by time-of-flight (TOF) measurements. The velocity of a single isolated particle is easily determined from a measurement of the flight time, t and the flight distance, L through the relation $v = \frac{L}{t}$. For an ensemble of particles, the *distribution* of flight times can be used to determine the distribution of molecular velocities (provided the flight distances are accurately known). What is measured experimentally with the TOF technique is the longitudinal velocity distribution which from Eq. 3.15 is given by⁵

$$f(v_{\parallel})dv_{\parallel} = n\sqrt{\frac{m}{2\pi k_B T_{\parallel}}} e^{-\frac{m}{2k_B T_{\parallel}}(v_{\parallel}-u)^2} dv_{\parallel} \quad (3.16)$$

This distribution is obtained by converting the measured time of flight (TOF) signal, $g(t)$, from the time domain to the velocity domain. This is accomplished by noting that $v_{\parallel} = L/t$ from which the relevant Jacobian is calculated as

$$dv_{\parallel} = \frac{L}{t^2} dt \quad (3.17)$$

The TOF distribution can then be expressed as

$$\begin{aligned} g(t)dt &= f(v_{\parallel})dv_{\parallel} \\ &= -\frac{L}{t^2} f\left(v_{\parallel} = \frac{L}{t}\right) dt \end{aligned} \quad (3.18)$$

⁵ More rigorously we would need to include a factor of v_{\parallel}^2 in Eq. 3.16, which makes the normalization factor enormously more complicated. Fortunately, in the limit of fast, cold beams, the deviation of Eq. 3.16 from this rigorous result is negligible (see [115], page 123). For buffer gas beams, where the velocity width is comparable to the central velocity, this factor would have to be included.

Dropping the minus sign and using Eq. 3.16 gives

$$g(t)dt = \sqrt{\frac{m}{2\pi k_B T_{\parallel}}} \frac{L}{t^2} e^{-\frac{m}{2k_B T_{\parallel}} \left(\frac{L}{t} - u\right)^2} dt \quad (3.19)$$

Since it is difficult to obtain the pre-factor on an absolute scale, it is often dropped. Furthermore, the TOF data are often referenced to some “clock” that sets the initial time, which may be well before the molecules are created/released from the valve. To account for this time delay, we denote the time of creation of the molecules by t' so that Eq. 3.19 becomes

$$g(t)dt \propto \frac{L}{(t - t')^2} e^{-\frac{m}{2k_B T_{\parallel}} \left(\frac{L}{t - t'} - u\right)^2} dt \quad (3.20)$$

The situation is complicated somewhat in a molecular beam because the starting times (and thus total flight times) of the particles are not identical. For pulsed beams, the window of possible start times is narrowed by the finite shutter function of the valve, or, for radicals, the firing time of the photolysis laser pulse (duration $\sim 10ns$) or a brief discharge pulse (duration $\approx 20\mu s$). The velocity measurement is greatly simplified if 1) the flight time is long compared with the shutter function and 2) the flight time is long compared with the spread in arrival times of molecules with different velocities, i.e.: $t - t' \gg L/\Delta v$. Both of these limits are satisfied for the velocity measurements of OH radicals made at the end of our decelerator.

3.4.3 Skimmers

Generally, a molecular beam *skimmer* is used to extract the central, coldest portion of a molecular beam. (See Fig. 3.8a for a photograph of a skimmer). There can be several reasons for doing this, and the specific purpose that a skimmer serves in a given experiment will vary. Historically, the first supersonic beams were continuous and generally operated in a regime of high background pressure. As the beam enters the vacuum chamber, a shock wave forms due to compression of the background gas. This shock wave is called the *Mach disk shock* [29] and is shown schematically in Fig. 3.8b. These shock waves profoundly disturb the isentropic flow conditions and lead to significant degradation of the beam. For these beams, a skimmer could be used to “pierce the Mach disk shock” and sample the molecular beam in the “zone of silence” [116].

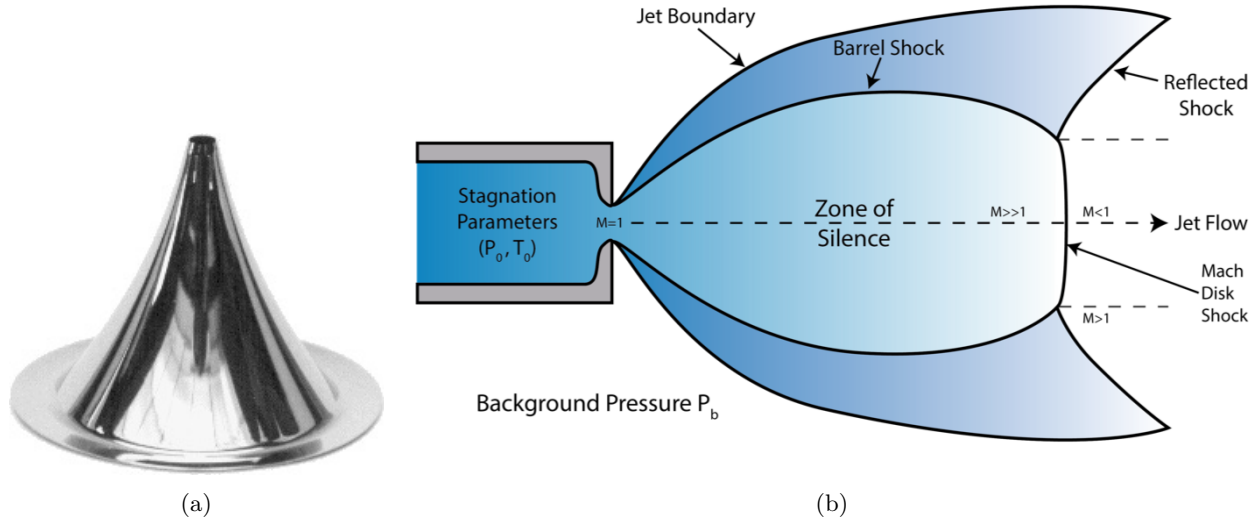


Figure 3.8: (a) Photograph of a molecular beam skimmer, (b) shock fronts formed due to compression of background gas in a supersonic expansion. For the most part, the various shock fronts described in this figure and thousands like it are actually irrelevant for pulsed supersonic beams operated with low background pressure. Figure taken from [10] (where these parameters were relevant).

The location of the Mach disk scales with the ratio of the stagnation pressure to the background pressure in the vacuum chamber via

$$\frac{x_M}{d} = 0.67 \left(\frac{p_0}{p_b} \right)^{1/2} \quad (3.21)$$

For pulsed beams the ratio p_0/p_b can be as large as 10^7 - 10^8 , which for a geometric nozzle diameter of $d = 1\text{mm}$, places the Mach disk shock several meters or more from the nozzle (beyond the end wall of the vacuum chamber). At these large distances, the beam has transitioned to the effusive regime and the Mach disk shock, a property of continuous fluid, is absent. Instead, in modern pulsed molecular beams, the skimmer primarily serves 1) as a collimating agent and 2) to facilitate differential pumping.

The *ideal skimmer* would be one that achieves these tasks without otherwise altering the beam. Unfortunately, this notion of the skimmer as a neutral device is a bit of a fantasy. Real skimmers are known to degrade a beam's angular spread, temperature and intensity. This phenomenon known as *skimmer interference* can generally be ascribed to unskimmed molecules being reflected off of the skimmer and

re-colliding with undisturbed molecules in the beam. Reflection of unskimmed molecules back onto the beam is minimized by using long, slender skimmers (small exterior angle) with an extremely sharp tip (lip radius $< 5\text{-}10\mu\text{m}$). However, if the skimmer is too narrow, molecules will build up inside the skimmer. To prevent this “skimmer clogging” the interior angle should be made large. It has been found empirically that optimal performance is obtained with total exterior and interior included angles of 30° and 25° [117] [118]. The trumpet-shaped skimmer manufactured by Beam Dynamics [119], ($\theta_{int} = 25^\circ$ and $\theta_{ext} = 30^\circ$) is a compromise between these last two effects.

There is a general theoretical [120] [87],[88] and experimental [121], [122],[87], [88] consensus that the onset of skimmer interference occurs as the Knudsen number at the skimmer entrance approaches unity (in this case flow is not collisionless). Definition of the Knudsen number relevant to skimmer interference requires some care. Clearly the collisions that will contribute most to skimmer interference, are not those between gas molecules at the local beam temperature, T but are instead between undisturbed molecules in the beam and those reflecting off of the skimmer. This latter type of collision is characterized better by the temperature of the skimmer, which is typically the same as the reservoir $T_0 \approx 300\text{K}$ (for unheated/cooled reservoirs or uncooled skimmers). The relevant modified mean free path at the skimmer entrance is given by [121], [29]

$$\lambda_s = \frac{1}{n_s} \left[5.3 \left(\frac{C_6}{k_B T_0} \right)^{1/3} \right]^{-1} \quad (3.22)$$

where the term $5.3 \left(\frac{C_6}{k_B T_0} \right)^{1/3}$ is proportional to the classical integral cross section of two rare gas atoms in a binary collision and n_s is the number density at the skimmer. To minimize skimmer interference the mean free path at the skimmer entrance should be at least twice the skimmer entrance diameter d_s [120]. Physically, this corresponds to the situation of collisionless flow where the molecules traverse the skimmer entrance (where the skimmer is the most constricted) without striking the skimmer. This theoretical result has been shown to be in good agreement with experimental results [121] [122], including those presented in this thesis (see Sec. 3.9.2).

The mean free path at the skimmer entrance (Eq. 3.22) can be approximated for an effective nozzle

diameter of d_{eff} using the results of the continuum model of Appendix B (see in particular Sec. B.1.1). Fig. 3.9 plots the mean free path as a function of the valve-to-skimmer distance for the rare gases at an effective nozzle diameter of $d_{eff} = 400\mu m$ and a stagnation pressure of $P_0 = 2000Torr$ for the rare gases. The lower horizontal dashed line is the geometric diameter of a standard skimmer ($2.0mm$) and the upper dashed line is the condition to neglect skimmer interference of Ref [120]. The key idea of Fig. 3.9 is that the heavier, more polarizable rare gas atoms with a larger C_6 coefficient have the largest collision cross section and are thus more susceptible to skimmer interference [123], [87] [88]. Heavier carrier gases generically require larger nozzle-skimmer distances compared with helium beams operated at the same value of $p_0 \cdot d$.

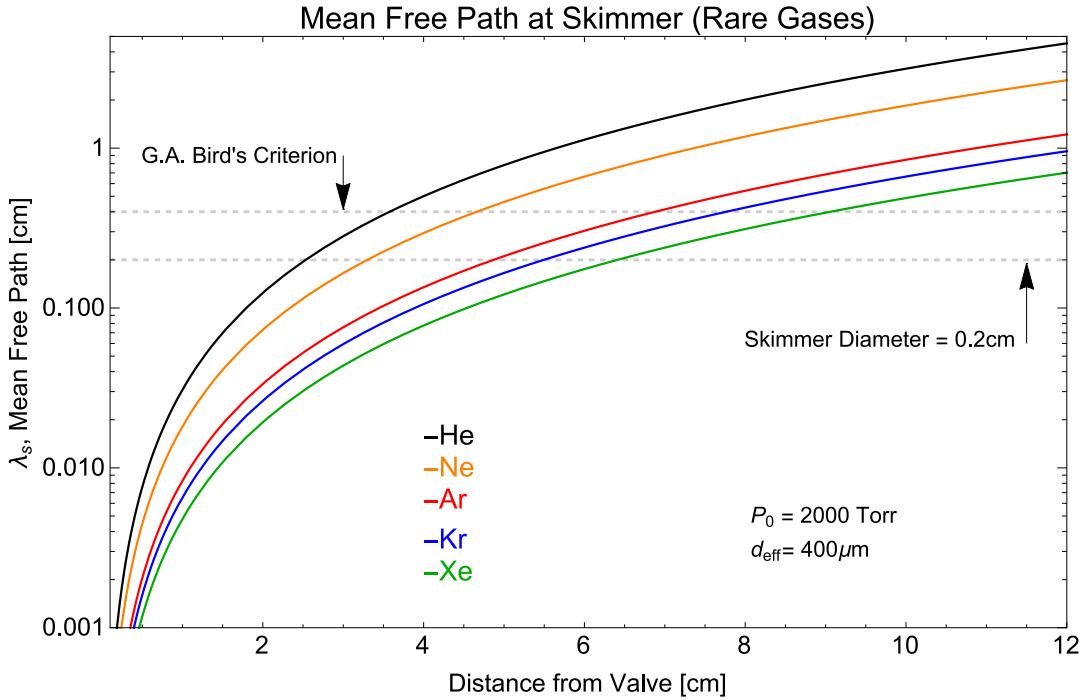


Figure 3.9: Mean free path of at the skimmer entrance for the rare gases at nominally equal beam intensities ($p_0 d = 80[Torr \cdot cm]$).

Anticipating Stark deceleration experiments, which require heavy gases, we focus our attention on Kr. Eq. 3.22 is plotted for different stagnation pressures (Fig. 3.10a) and effective nozzle diameters (Fig. 3.10b). These calculations indicate that, for a krypton carrier gas, valve-skimmer distances in the range of 7-12 cm will be necessary.

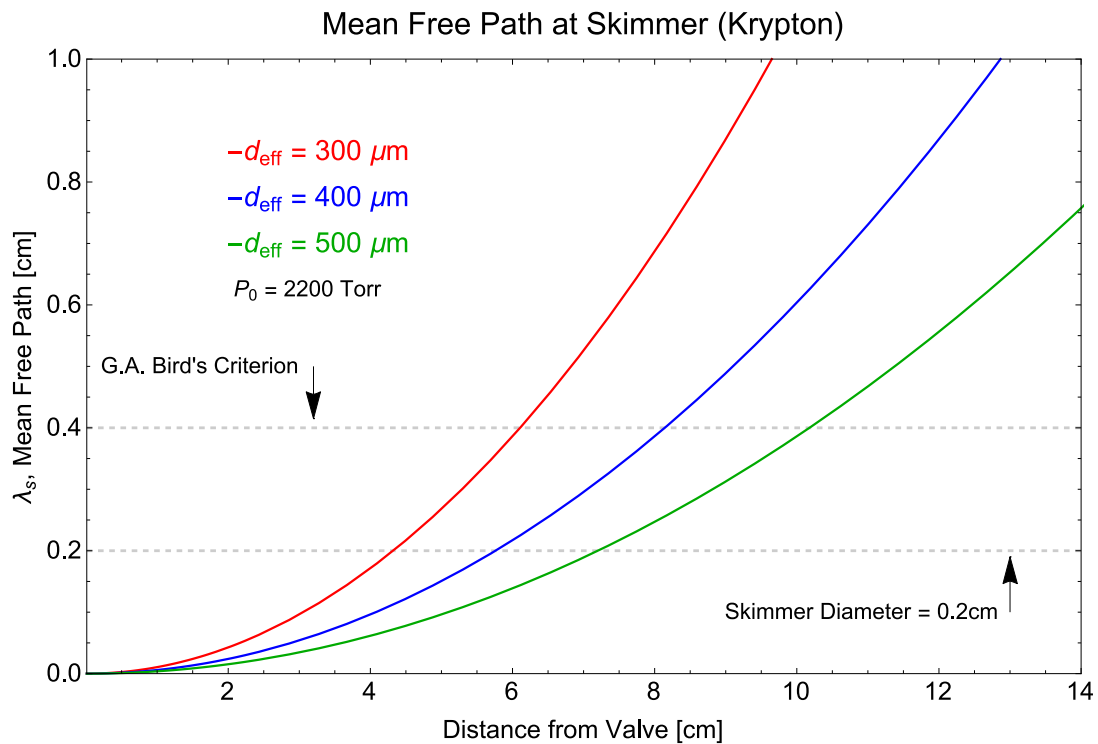
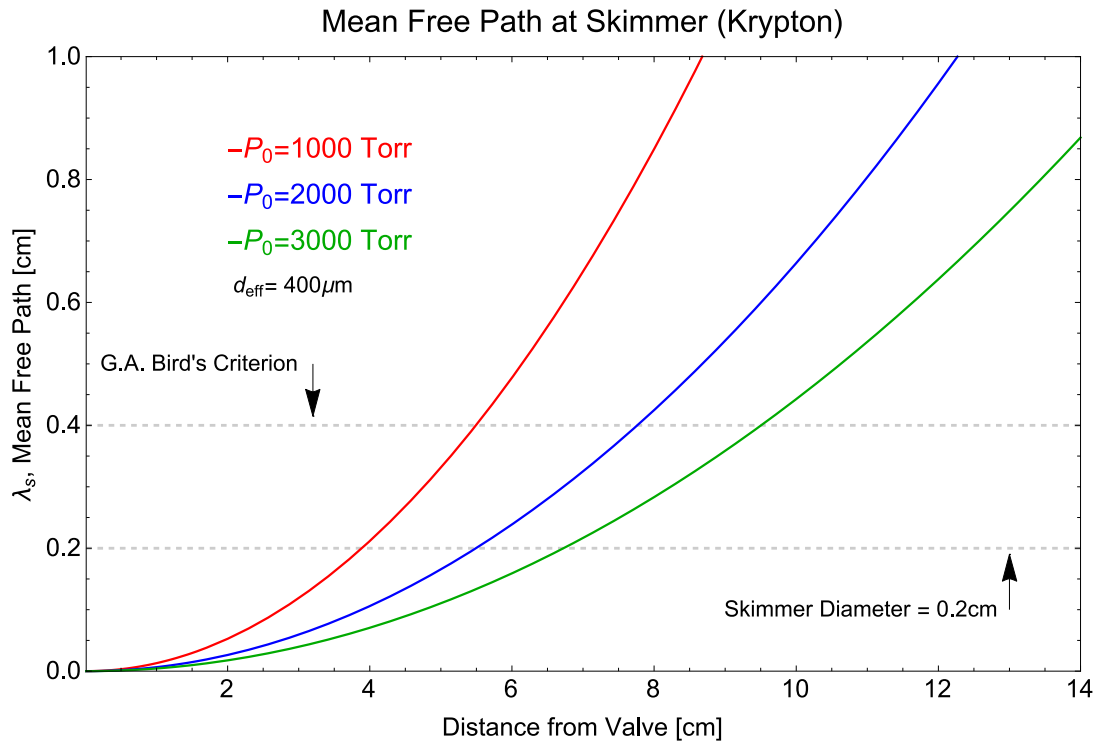


Figure 3.10: Kr mean free path at skimmer entrance for varying stagnation pressures (a) and nozzle diameters (b). Panel (a) is for $d_{eff} = 400\mu\text{m}$ and krypton stagnation pressures of 1000, 2000, and 3000 Torr and (b) is for a fixed stagnation pressure of $P_0 = 2200\text{ Torr}$ and nozzle diameters of $d_{eff} = 300\mu\text{m}$, $d_{eff} = 400\mu\text{m}$, and $d_{eff} = 500\mu\text{m}$.

3.5 Radical Sources: Beyond the Gas Bottle

Supersonic beams of chemically stable molecules such as ND_3 can be produced by preparing a low mole ratio (few %) mixture in a rare gas *directly in the reservoir*. The wide variety of gases commercially available in a pressurized gas bottle makes this “seeded” beam method especially convenient. Experiments requiring species that are highly chemically reactive, such as open shell diatomic radicals or those in a metastable state, must be produced with a different method since neither of these species can be stored in a container for any appreciable period of time. Instead, these species must be introduced directly into the vacuum chamber where collisions will be low. The production of NH radicals for Stark deceleration must satisfy *both* of these requirements as only the metastable $a^1\Delta$ state has an appreciable Stark shift.

This method of *post nozzle seeding* takes various forms but generally requires the fragmentation of a stable precursor molecule. Laser ablation of a solid precursor, pioneered by Richard Smalley [124], [125], [126], [127] for the production of metal cluster beams, finds some use in the cold molecule community for the production of rather exotic molecules such as ThO [51], SrF [50], HfF [128] and YO [41]. For the production of more “traditional” gas phase free radicals [129], [130], however, precursor molecules are typically introduced in the gas phase where they can be fragmented through laser photodissociation (photolysis), thermal dissociation (pyrolysis), chemical processes, and electrical discharges.

3.6 Radical Beams via UV Photolysis

Early on, significant time was spent on making a beam of NH radicals in the metastable $a^1\Delta$ state via photolysis of one of two precursors, either HNCO or NH_3 . The next section presents a brief discussion of the the dynamics of HNCO photolysis and concludes with a comparison of estimated radical yields and experimental data comparing photolysis of NH_3 and HNCO .

3.6.1 Photolysis of HNCO

Isocyanic Acid, HNCO , is a surprisingly well studied molecule due to the fact that it (and its isomers[131]) are the simplest molecules containing the four basic building blocks of organic matter. Its

photodissociation dynamics in particular have received considerable experimental and theoretical attention due to the relatively complicated dissociation mechanisms for a simple four-atom molecule. In large part the complications arise from a large change in molecular geometry. The $S_0(^1A')$ ground state consists of a predominantly linear NCO segment ($\angle NCO$ 172.6°) with the H atom at an angle of $\angle HNC$ 123.9°. Excitation out of the ground state to the $S_1(^1A'')$ electronic induces a severe conformational change, where the NCO segment is bent from 172.6° to 120-130° (see Fig. 3.12b for structure). This change in structure is partly responsible for the considerable breadth of the $S_1(^1A'') \leftarrow S_0(^1A')$ absorption band, which extends from 260 to 182.5 nm [132], [11] with a peak near 200 nm.

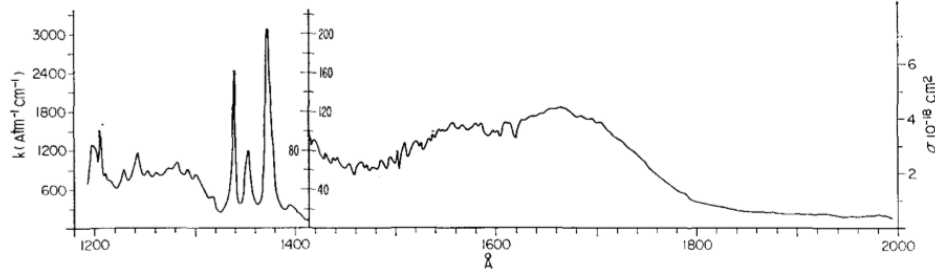
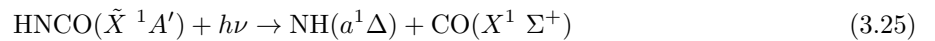
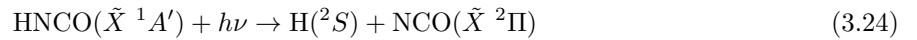
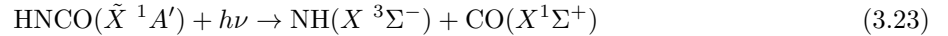


FIG. 1. Absorption coefficient of HNCO in the region 1200–2000 Å with a resolution of 0.8 Å; light source, a hydrogen lamp; scanning speed, 20 Å/min; k is defined by $I_0 = I \exp(-kpl)$, $\sigma(\text{cm}^2) = 4.06 \times 10^{-20} k$ ($\text{atm}^{-1} \cdot \text{cm}^{-1}$).

Figure 3.11: Figure from [11]

Decomposition of HNCO out of the $S_1(^1A'')$ excited state proceeds predominantly along one of three channels:



The first of these channels producing $\text{NH}(X^3\Sigma^-)$ is not spin allowed. Many experimental studies ([133], [134], [135], [136], [137], [12], [138]) have shown that the third process (Eq. 3.25) which yields NH

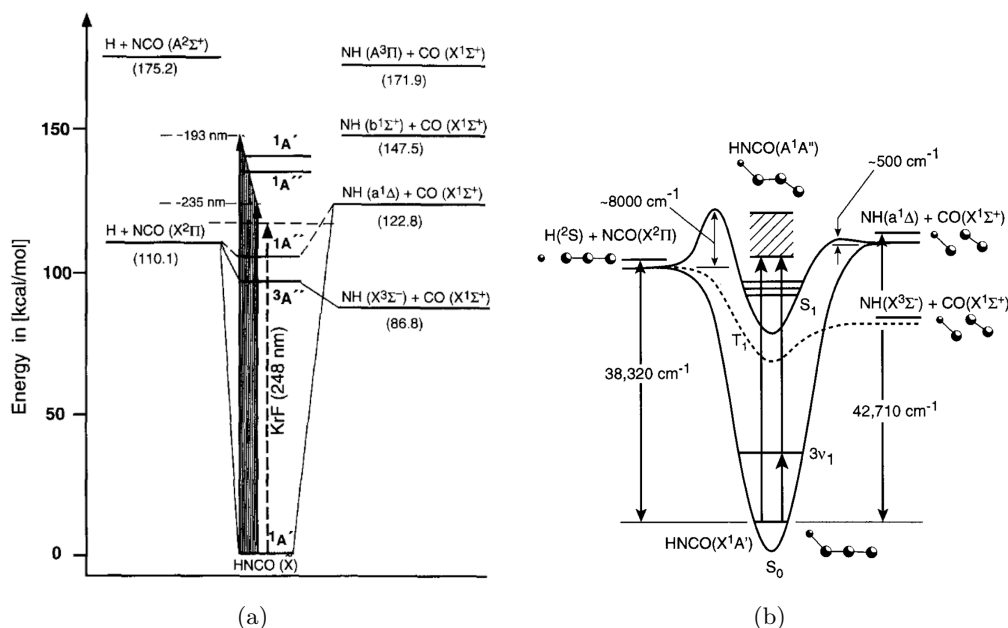


Figure 3.12: Energy level diagram of the photolysis products of HNCO at 193 nm. (a) from [12] and (b) from [13].

($a^1\Delta$), is the dominant decomposition pathway for photon energies above the formation threshold for the products ($\approx 230nm$).

3.6.2 Estimated Radical Yields

Molecular photodissociation pathways (such as Eqs 3.23-3.25 for HNCO) are typically described in terms of their *quantum yield*, γ_{pd} , defined as the number of generated radicals (of interest) per absorbed photon.⁶ The quantum yields give the relative probability of the different processes provided a photon has already been absorbed but says nothing about the probability of the initial photoabsorption event, which is described in terms of the absorption cross-section, $\sigma_{abs}[cm^2]$.

The rate of radical production is given by

⁶ It is useful to consider the mindset of chemists when reading papers about laser photolysis. Unless explicitly stated otherwise, the goal of a chemical dynamicist performing photolysis experiments is not necessarily the production of intense radical beams. Scattering experiments investigating the state-to-state dynamics of bimolecular reactive collisions are incredibly complex [139], [140]. Photolysis experiments offer an alternative and much simpler avenue to study the nature of chemical bonds. Instead of looking directly at bond formation, photolysis experiments watch molecules as they fall apart (breaking of bonds), which can be considered “chemistry in reverse.” Fortunately for those interested primarily in the production of radical beams, absolute absorption cross-sections (as well as quantum yields and rate constants for secondary processes) for a wide variety of molecules have been compiled to facilitate accurate modeling of complex photochemical dynamics in the atmosphere [141], [142] [143].

$$\frac{dN_{rad}}{dt} = \gamma_{pd}\sigma_{abs}\frac{\Phi}{A}, \quad (3.26)$$

where Φ is the laser flux in [$\#photons/s$] and A is the laser beam's cross-sectional area in [cm^2]. From Eq. 3.26, the effective cross-section for radical production can be identified as $\sigma_{eff} = \gamma_{pd}\sigma_{abs}$. The important quantity for generating radical beams is then the *absolute* dissociation probability at a given laser photon flux. This is more easily described in terms of the total fluence in $\#photons/pulse$, Φ_p , so that the relative dissociation probability per pulse, \mathcal{P}_{pd} , is given by

$$\mathcal{P}_{pd} = \sigma_{eff} \times \frac{\Phi_p}{A} \quad (\text{Dissociation Prob/Pulse}) \quad (3.27)$$

At $193nm$, every mJ consists of $\approx 9.6 \times 10^{14}photons/pulse$. Typical pulse energies available from our excimer laser (GAM, Model *EX10*) are not greater than $10mJ$ limiting the available photon fluence to $\approx 10^{16} \#/pulse$. Due to the poor beam quality of ArF Excimer lasers, the cross-sectional area of the focused beam isn't expected to be smaller than $\approx 0.1cm^2$ giving a peak intensity of $\approx 1 \times 10^{17} [\#/cm^2]$.

For photolysis sources of radicals, the laser is focused just outside of the nozzle (typically a capillary tube). We can estimate the properties of the precursor molecules as a function of reservoir properties by using the results of the continuum model described in Appendix B. To simplify matters, we assume that the precursors are photolyzed at the throat of the expansion, where the flow velocity is equal to the local speed of sound. Here the number density and temperature of the gas are very similar to the reservoir conditions ($n_{th} = 0.65 \times n_0$, see Fig. B.3, and $T_{th} = 0.75 \times T_0$, see Fig.B.2). This suggests that measured absorption cross-sections in relatively dense (many Torr) samples of gas at $T = 300K$ should give reasonably accurate descriptions of photoabsorption by the precursors. Assuming precursor molecules are seeded in the carrier gas at a 1% mixture, the precursor densities at the focus of the laser are not expected to be greater than $\approx 0.01 \times n_0$. Values of absorption cross-section, σ_{abs} , and the quantum yield, γ_{pd} , for precursors, NH_3 , $HNCO$, and HN_3 taken from the literature are tabulated in Table 3.1 at various UV wavelengths. The quoted rotational temperatures in the last column are derived from measurements in a gas cell. In a supersonic beam the rotational temperature will be less than this due to expansion cooling, but the values display the

non-thermal nature of the photolysis process. The dissociation probabilities calculated in the next to last column assume a net laser fluence of $\frac{\Phi_p}{A} = 10^{17} [\#/cm^2]$.

The foregoing analysis assumes that the every molecule in the gas pulse sees the same laser intensity. This is a reasonable assumption for an optically thin sample of gas. Assuming that the precursor molecule is mixed into the carrier gas (Ar, Kr or Xe) at a 1% mole ratio, the density of precursors at the throat of the expansion will not be greater than $0.01 \times n_0$. For a total stagnation pressure of $P_0 = 1000 - 2000 Torr$, the density of the precursor molecules is estimated to fall in the range of $n_0 = (3-6) \times 10^{17} [\#/cm^3]$. For simplicity, we assume that the absorption path length is equal to the geometric nozzle diameter of $d_{geo} = 0.1cm$. Taking a relatively large value for the absorption cross-section of $\sigma_{abs} = 10^{-17} cm^2$, then the quantity $n * \sigma * L < 0.1$ for all cross sections considered above. This allows us to neglect any significant attenuation of the excimer laser beam.

The simple estimate of radical yield presented here neglects any subsequent kinetic processes that could deplete radicals from the beam. To some extent, the radicals will be shielded by the buffer gas with a $\sim 100 \times fold$ higher density. As such, the yields estimated using Eq. 3.27 and tabulated in Table 3.1 serve only to provide a rough upper limit of radical yields. These secondary processes are known to be especially relevant for NH ($a^1\Delta$). For radical production with HNCO for instance, the secondary reaction,



between NH($a^1\Delta$) and HNCO to produce NCO and NH₂ is known to be fast [133]. In fact, this reaction and the photodissociation process directly generating NH($a^1\Delta$) (see Eq.3.25) have actually been used a *source* of NCO radicals in combustion studies. With these caveats in mind, the results of Table 3.1 indicate that despite nearly two orders of magnitude difference in the quantum yield of HNCO and NH₃, both precursors are expected to have comparable radical yields due to a nearly complete offset by the vast difference in the absorption cross-sections. This fact is supported by experimental measurements of an unskimmed beam in a small vacuum chamber of NH($a^1\Delta$) beams from both NH₃ and HNCO, which showed essentially identical yields (Fig. 3.13).

Note that for HNCO even at $10mJ/pulse$ the dissociation probability to make NH $a^1\Delta$ is only $\approx 3.5\%$.

Table 3.1: NH $a^1\Delta(\nu = 0)$ radical photolysis yields from various precursors. Values of γ_{pd} for HNCO at 193nm are based on measurements of the H/NCO channel which imply a range of values from 0.95-0.64. A value of 0.7 is given in the table as a reasonable lower bound, which is in reasonable agreement with absolute measurements at 221.9nm. Dissociation probabilities in the next to last column are calculated assuming a laser fluence at 193nm of $\frac{\Phi_p}{A} \approx 1 \times 10^{17} [\#/cm^2]$.

Precursor	$\lambda [nm]$	$\sigma_{abs} [cm^2/\#]$	QY, γ_{pd}	$\sigma_{eff} [cm^2/\#]$	Diss. Prob.	$T_{rot} [K]$
NH ₃	193.3	1.25×10^{-17} [144]	≤ 0.0056 [144]	7×10^{-20}	7×10^{-3}	1035 ± 90 [144]
HNCO	193.3	5×10^{-19} ¹ [11]	≈ 0.7 [133][138][137][136]	3.5×10^{-19}	3.5×10^{-2}	≈ 1100 [145][146]
	221.9	-	$= 0.77 \pm 0.12$ [13]	-	-	-
	225	-	≈ 0.3 [147]	-	-	-
	248	-	< 0.01	-	-	-
HN ₃	193	2.8×10^{-18} [148]	0.40[148]	1.12×10^{-18}	0.11	3150 ± 750 [148]
	248	6.9×10^{-20} [148]	1 [148]	6.9×10^{-20}	6.9×10^{-3}	1180 ± 150 [148]
	266	-	1[149][148]	-	-	-

Assuming HNCO is seeded in a carrier gas at a $\sim 1\%$ ratio this amounts to an effective NH $a^1\Delta$ seeding ratio of 0.035%. Fully realizing the benefit of the large quantum yield of HNCO, where the effective seed ratio of NH $a^1\Delta$ in the carrier gas is on the order of the precursor seed ratio (i.e., every HNCO molecule is dissociated/absorption probability = 100%), would require a photon flux on the order of the inverse cross absorption cross-section, or $\Phi/A \approx 2 \times 10^{18} [\#/cm^2/pulse]$. For a focused beam cross-sectional area of $A = 0.1cm^2$, this would require $200mJ/pulse$.

For completeness, analogous parameters for the production of OH radicals are presented in Table 3.2. The yields are generally comparable to those for NH except for photolysis of nitric acid (HNO₃) at 193nm. We note that this is the source preferred by the G. Meijer group [150] (and subsequently also that used by S. van der Meerakker [151] [152]) for Stark deceleration experiments and used by the M. Lester [28], [27] group at the University of Pennsylvania.

Table 3.2: OH $X^2\Pi$ radical photolysis yields from various precursors.

Precursor	$\lambda[nm]$	$\sigma_{abs}[cm^2/\#]$	QY, γ_{pd}	$\sigma_{eff}[cm^2/\#]$	Diss. Prob.	$T_{rot}[K]$
HNO ₃	193.3	1.3×10^{-17}	(0.47 ± 0.06) [153]	6.1×10^{-18}	0.611	-
	248	1.98×10^{-20} [154]	(0.75 ± 0.1) [153]	1.5×10^{-20}	1.5×10^{-3}	-
H ₂ O ₂	193.3	6.1×10^{-19}	(1.22 ± 0.13) [153]	7.4×10^{-19}	7.4×10^{-2}	-
	248.3	9.0×10^{-20}	(1.58 ± 0.23) [153]	1.4×10^{-19}	1.4×10^{-2}	-
H ₂ O	193	1.75×10^{-21}	1 [155]	1.75×10^{-21}	1.8×10^{-4}	-

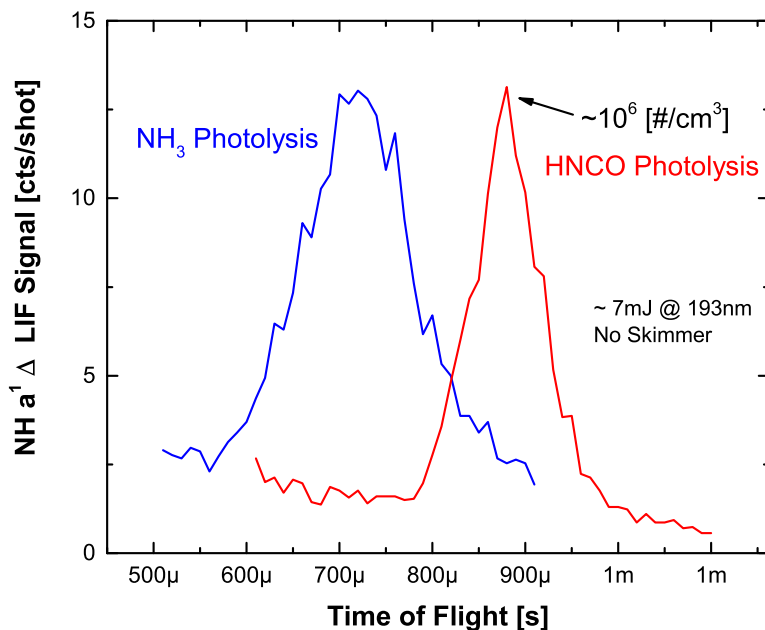


Figure 3.13: Experimental measurements of unskimmed $\text{NH } a^1\Delta$ beams generated by photolysis of HNCO and NH_3 under similar conditions in a test chamber.

Finally, we address the costs associated with photolysis based radical beams. The results of Tables 3.1, 3.2 indicate that high radical yields from photolysis-based sources will require very high pulse energies. Unfortunately, photons become progressively more expensive as the wavelength decreases. The high cost of commercial excimer at 193nm of $\sim \$3k/mJ$ can present significant obstacles. This problem is compounded for simultaneous operation of multiple radical sources. Electric discharges, however, offer a very simple and inexpensive method of dissociating precursors.

3.7 Basic Physics of Gas Discharges

Before discussing our discharge source in detail, we briefly review the basic physics of discharges. A gas discharge is characterized by the transition of a neutral, electrically insulating gas to a conducting state consisting of a partially ionized gas or plasma. The basic features of an electrical gas discharge can be understood by considering the simple case of a steady (DC) voltage applied to two parallel electrodes separated by a distance D with a gas of pressure P between them. The operating regime of the resulting discharge is classified by the current-voltage characteristic curve, which is shown schematically in Fig. 3.14.

Even at very low voltages, rare ionization events due to cosmic rays or natural radioactivity will generate electron-ion pairs which will be collected by the electrodes. If the electron encounters a neutral atom during transit across the electrode gap, the neutral atom is likely to be ionized, generating an ion and a second electron. This process repeats many times, resulting in an avalanche process (Townsend avalanche). Breakdowns consisting only of these primary avalanche electrons have very low currents ($\sim 10^{-15}[A]$) and exist only for brief moments (non-self-sustaining). This regime corresponds to the first region of Fig. 3.14. Stable operation of discharges requires a source of secondary electrons to start new avalanches.

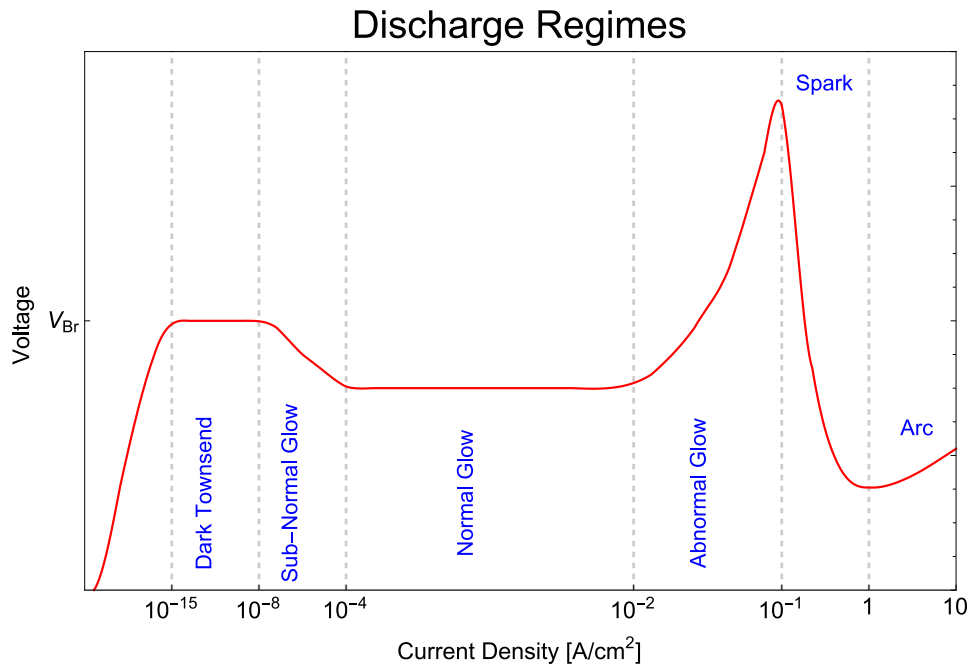


Figure 3.14: A schematic IV curve of a gas discharge showing different regimes of operation. Adapted from [14] [15].

When the voltage across the electrode gap reaches the *breakdown* voltage, V_{Br} , the rate of electron-ion pair generation equals the loss, and the discharge becomes sustained (breakdown). For $P \sim 1Torr, D \sim 1cm$, the breakdown voltage will typically be a few hundred volts. At this point, the ionization fraction is so small that no detectable light is emitted (Townsend dark discharge). If the pressure is kept fairly low, ($P \sim 10-100Torr$), as the bias voltage is raised further a *glow* discharge will develop, which is accompanied by emission of light and a large increase in current ($10^{-4}-10^{-2}[A]$). Because the normal glow region is very

weakly ionized ($f_i \approx 10^{-8}$ - 10^{-6}) the electrons are out of thermal equilibrium with the rest of the gas. While electron temperatures are of order $T_e \sim 10^4 K$, the temperature of the neutrals and the ions will be *much cooler*, around the ambient temperature of $\approx 300 K$.

An interesting feature of the normal glow discharge is a vanishing differential impedance, $\frac{dV}{di} = 0$ (see Fig. 3.14); the discharge current can vary by many orders of magnitude but the electrode voltage stays the same. The normal glow is followed by the abnormal glow characterized by a positive differential impedance (electrode voltage increases with current). At high pressures, the abnormal glow makes an abrupt transition to arcing, where currents can be as high as $i = 0.1$ - $1 A$. The ionization fraction in an arc is much higher ($f_i^{arc} \sim 10^{-3}$ - 10^{-1}), which leads to thermal equilibrium among the electrons, neutrals, and the ions at $T \sim 10^4 K$. Clearly for the production of cold molecules, the low temperatures of the neutral buffer gas in a glow discharge offer significant advantages over the arc discharge.

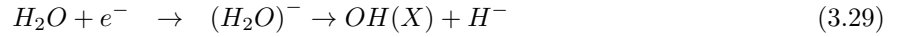
3.7.1 Radical Beams by Discharge

Early experiments showed that a wide variety of radicals could be efficiently generated in discharges contained to gas cells [156] but that coupling radicals to a supersonic beam is more difficult. Furthermore, it is not immediately clear whether the relatively hot conditions in the discharge will be at all effective at producing cold radicals. Engelking's [157] [158] corona discharge ($\sim 15 kV, 100 \mu A$) excitation of a continuous supersonic beam was able to achieve surprisingly low rotational temperatures ($T_{rot} \leq 15 K$) by localizing the discharge *upstream* of the expansion. This is in stark contrast to discharge designs that strike the discharge *across* the expanding gas [159], which effectively limits the extent of expansion cooling. This is a especially important for the production of cold molecular samples since the majority of the collisional cooling occurs fairly early on in the expansion.

Types of discharges used for radical generation fall into either a corona, glow discharges, [18] and dielectric barrier discharges [160]. The comparatively low temperatures of the neutrals and ions in a weakly ionized, low-pressure glow discharge are ideal for efficient radical generation with minimal heating. This factor as well as the simplicity of a DC discharge, led us to choose a glow discharge source for OH radicals.

3.8 Cold OH Beams Generated in Glow Discharge of Kr/H_2O

This section discusses the design and performance of our OH radical source based on a glow discharge of Kr/H_2O . In this setup, OH generation ultimately results from the fragmentation of H_2O in high energy collisions, with either e^- or excited state (neutral) atoms. Relevant processes resulting from a single e^-/H_2O collision [17] include

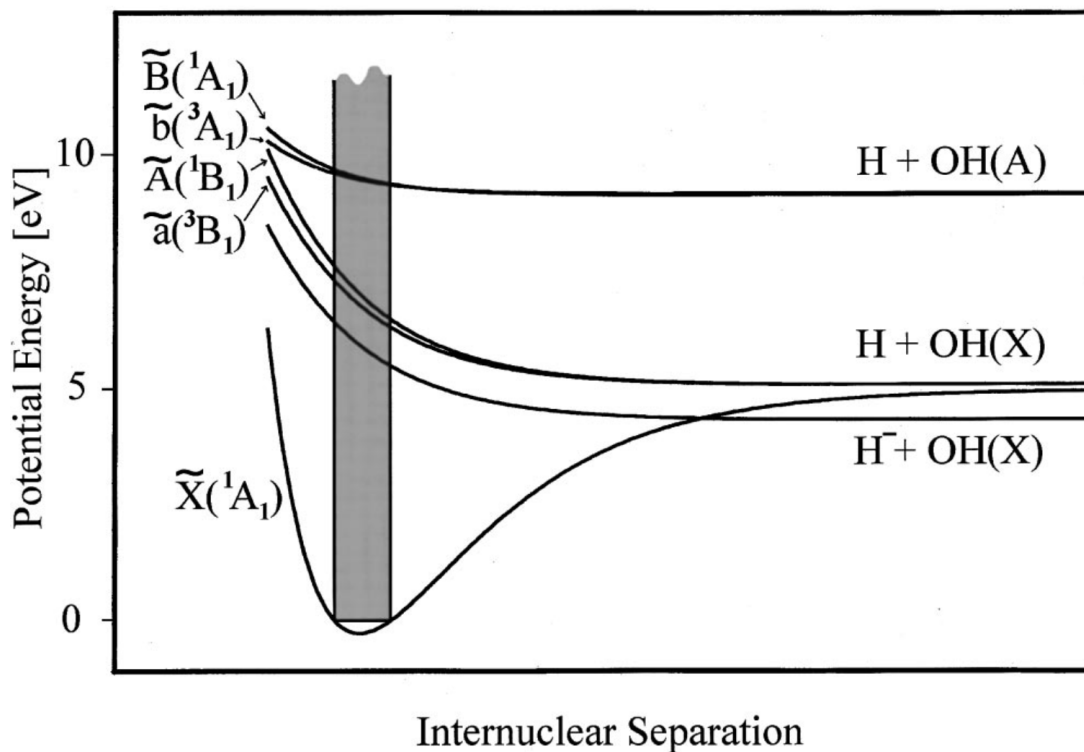


The relevant potential energy curves for fragmentation of water from electron collisions is shown in Fig. 3.15a. The cross-sections for processes Eq. 3.29 - 3.31 are shown in Fig. 3.15b. The first process (Eq. 3.29), known as dissociative attachment, has a very low cross-section and only occurs at very low energies and therefore can be neglected. The second process (Eq. 3.30) is readily observed in high pressure discharges [161] but is not thought to play a significant role in the formation of ground state OH(X)[16]. Thus, the third process is expected to be dominant in the formation of OH(X) from e^-/H_2O collisions.

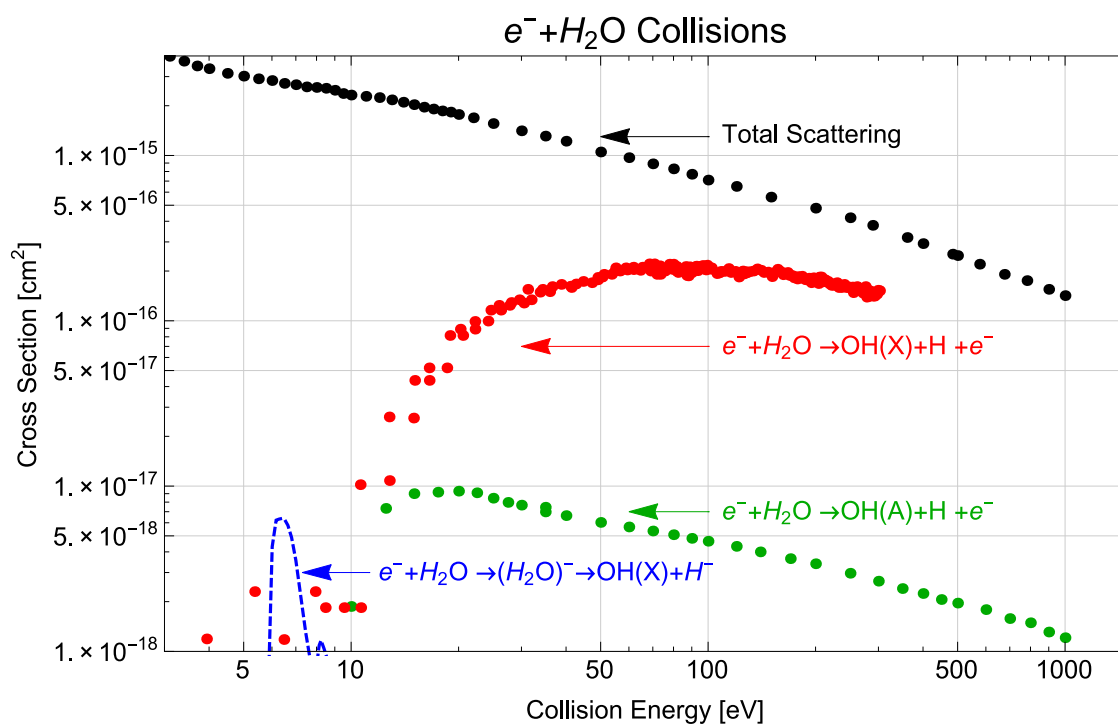
Another possible fragmentation mechanism is Penning dissociation,



In this process, a buffer gas atom, M , is collisionally excited to a metastable state, which then breaks water apart in a second collision. Whatever the exact mechanism for OH production, either mechanism is expected to depend strongly on the electron flux, i.e.: the discharge current.



(a)



(b)

Figure 3.15: e^-/H_2O water collisions. (a) Potential energy curves of H_2O relevant for electron impact dissociation. Figure from [16]. (b) Absolute cross-sections for the electron-water collision processes given by Eq. 3.29-3.31 based on data given in [17] and [16].

3.8.1 Experimental Setup

A simplified schematic of the gas system used for generating OH beams is shown in Fig. 3.16. High pressure Kr is fed into a stainless steel container (“bubbler”) filled with $\approx 25\text{mL}$ of liquid water, which is connected to the valve body. The welded gas manifold is made of electropolished stainless steel tubing (dairy grade) and VCR fittings to minimize contamination which could compete with radical generation. The stagnation pressure is monitored with a high accuracy baratron (10,000 Torr model) which is mounted upside down to prevent water condensation from collecting on the diaphragm. During pump out and supplying Kr, care is taken to ensure that the pressure in the bubbler changes as slowly as possible to prevent large pressure gradients from blowing liquid water throughout the gas system, or pulling liquid water into the scroll pump. As a precaution to protect the pump from coming into contact with liquid water (in case a valve is opened too quickly etc.) the gas lines from the gas system are fed into a trap where any liquid water is pooled at the bottom.

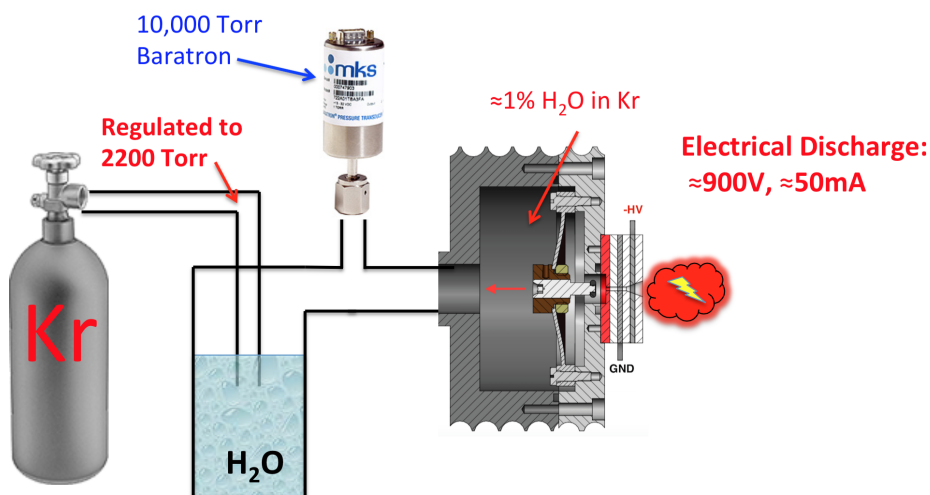


Figure 3.16: Simplified schematic of the gas system used to generate OH beams in a glow discharge of a Kr/H₂O mixture. For details, see text.

The output from the bubbler is then connected to the PZT valve which is described in Sec. 3.4.1.1. The discharge plates are attached to the end of the valve assembly, after the valve-orifice plate. A detailed scale drawing of the discharge plates is shown in Fig. 3.17. The highly polished stainless steel electrodes (1.22mm thick) are separated by a macor insulator (2mm thick). The central hole in the assembly is 1mm

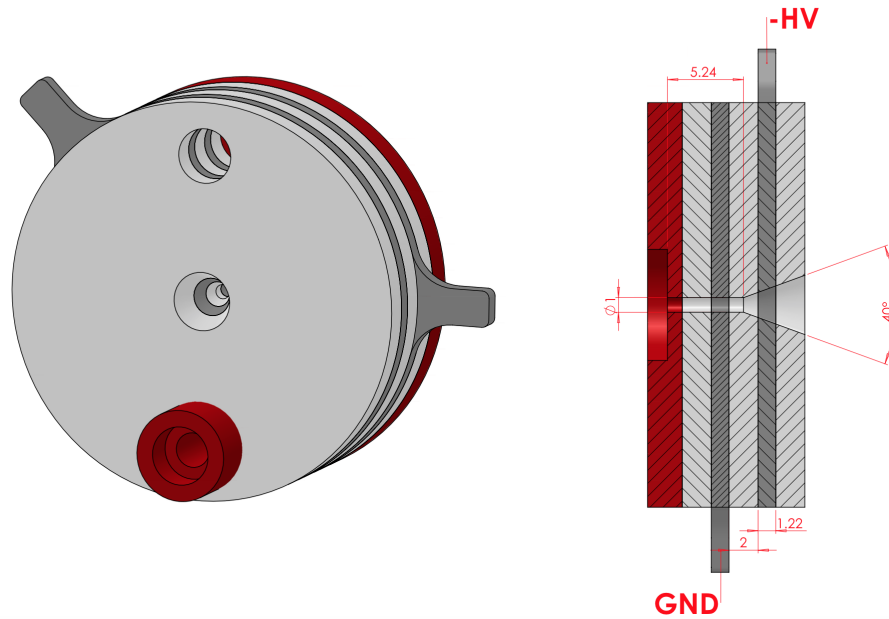


Figure 3.17: Detailed scale drawing of the discharge plate assembly. In the cross-sectional view on the left, lengths are given in [mm] and the full opening angle in degrees.

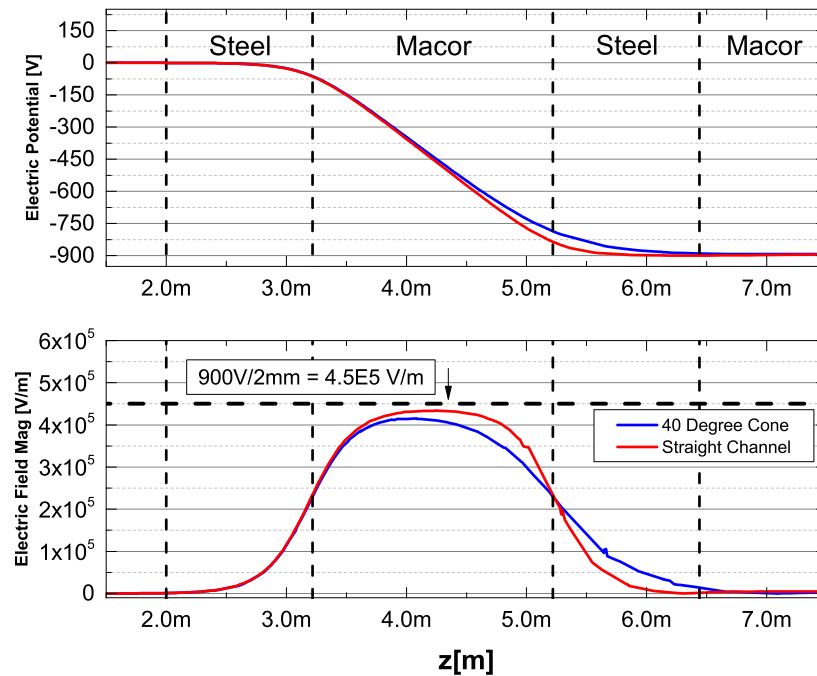


Figure 3.18: Electric field properties of the discharge plates used to generate OH in Kr/H₂O mixture for -900V applied to downstream electrode.

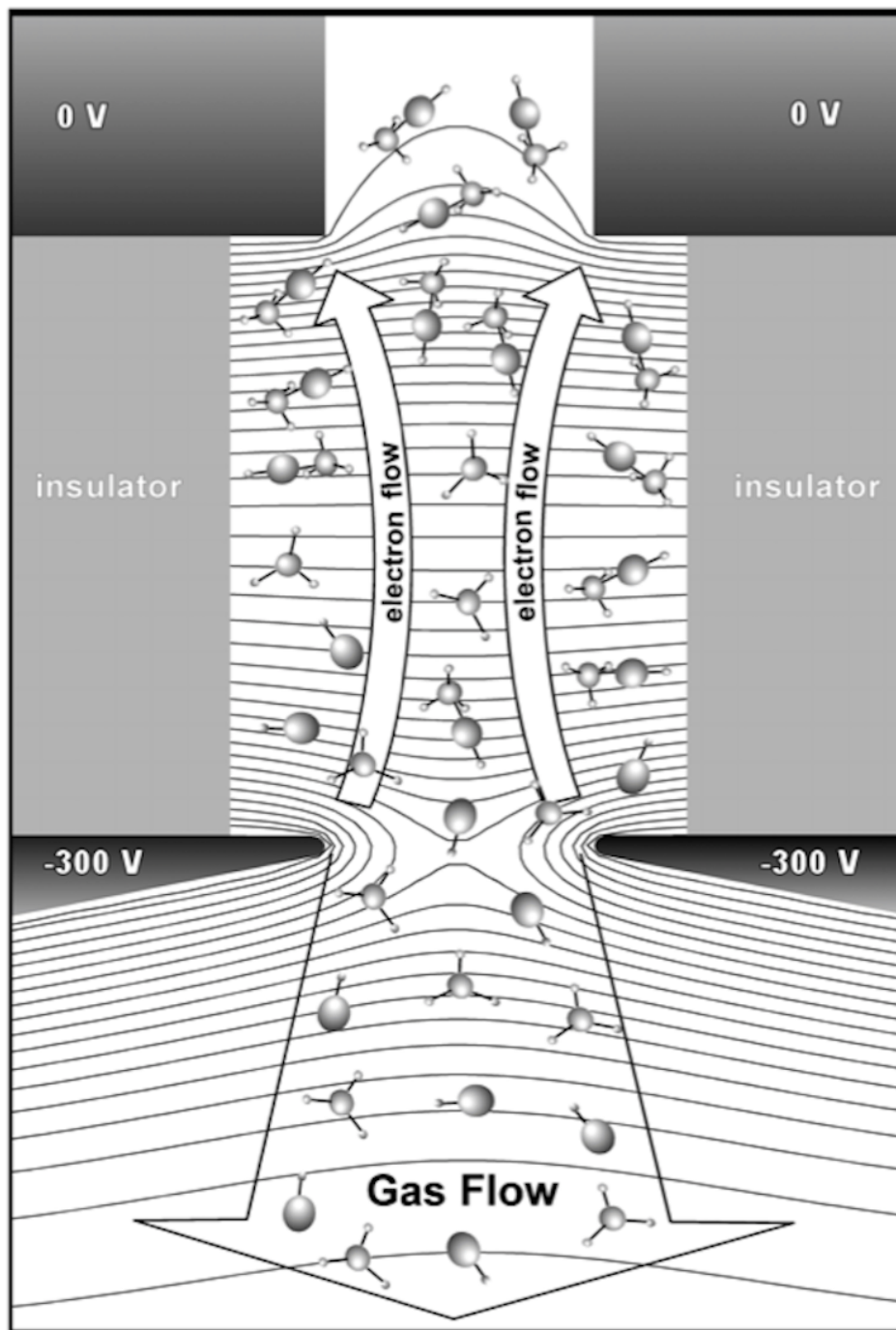


Figure 3.19: Schematic of the asymmetric flow conditions of the electrons and cations in a flowing discharge medium. It is critical that the downstream electrode be biased negatively and the upstream electron be grounded. Figure from [18].

to match the geometric diameter of the valve orifice plate ($1mm$). Midway between the electrodes the $1mm$ diameter channel transitions to cone (full opening angle = 40°).

The polarity of the discharge electrodes is very important. Despite plasma being fundamentally an ionized gas, a stable discharge must be overall electrically neutral. In a flowing discharge media, the motion of the heavy cations can be significantly affected by bulk flow of the gas, while the light electrons are comparatively unaffected. A positively biased discharge, where the the ions move against the neutral gas flow quickly leads to a net buildup of a positive charge and a visibly erratic discharge. As noted in [18] (see also Fig. 3.19), the discharge stability is greatly enhanced by negatively biasing the downstream electrode which causes the cations to be “sped up” by the bulk flow of the gas and helps keep the discharge overall neutral. Finite element analysis of the on-axis electrostatic fields produced by the discharge electrodes indicates that the cone has a minimal effect of the electric field strength (see Fig. 3.18) and that the electric field is largely confined to the upstream region.

3.8.1.1 Measuring the Discharge Current

A simplified electrical circuit diagram of the discharge setup is shown in Fig. 3.20a. A negative HV supply (SRS, PS350) is connected to a TTL-controlled HV switch (Behlke, HTS-151-03-GSM). The HV supply is backed by a storage capacitor ($C = 2\mu F$) to supply the large currents needed during operation of the discharge.

One of the most useful diagnostics of the OH beam is the discharge current, which can be measured with either of two methods. The first method is depicted in Fig. 3.20b, where the discharge duration has been made longer than the duration of the gas pulse. In this way, the voltage characteristic curve serves to “map out” the shape of the gas pulse. The total applied voltage, $-\mathcal{E}$, is split between the ballast resistor and the discharge electrodes. The degree of partitioning will depend on the impedance of the discharge which will vary with the density of gas between the electrodes. The topmost arrow, V_b , is a measure of the voltage drop across the electrodes and the bottom arrow is the drop across the ballast resistor. The discharge current is then $i_{disc} = \frac{V_b}{R}$.

If the discharge pulse is short compared to the valve duration (as is the case for optimized OH beams)

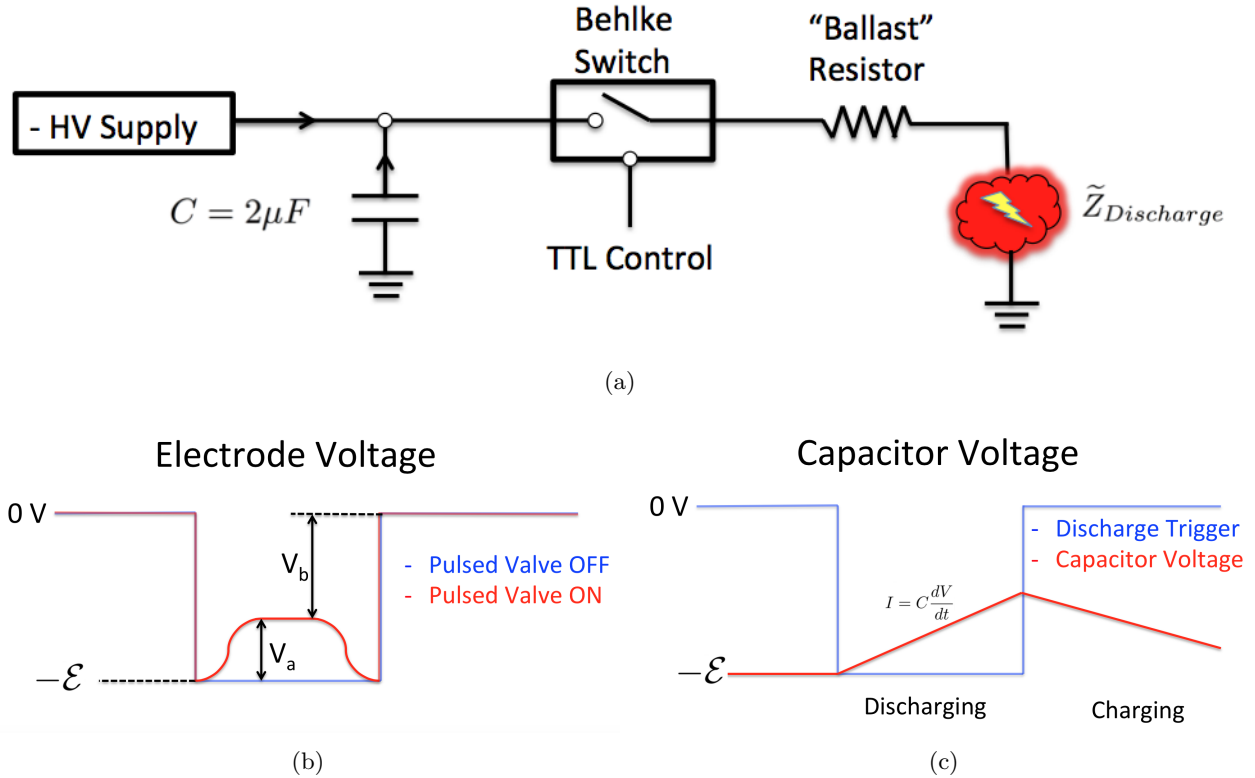


Figure 3.20: (a) shows a simplified electrical circuit diagram for the pulsed glow discharge. (b) and (c) depict two different ways to measure the discharge current based on directly measuring the voltage on discharge electrodes (b) and monitoring the voltage slew rate off the storage capacitor (c). For details, see text.

a better way to measure the discharge current is to monitor voltage slew rate of the discharging storage capacitor (see Fig. 3.20c). We note that the high currents and high voltages associated with the storage capacitor make this method inherently more dangerous than the other method (though neither should be done alone). The two methods give similar results as shown by the direct comparison in Fig.3.21 for nominal valve durations of (a) $50\mu s$, (b) $100\mu s$, and (c) $150\mu s$. Because the coldest OH beams are those created in a pulsed discharge [162], the method of Fig. 3.20b doesn't turn out to be as useful as the method in Fig. 3.20c, which is well suited to μs pulses.

Measurement of the discharge current yields diagnostics of the valve itself in that it maps out the time profile of the gas pulse that is emitted from the valve. Fig. 3.23a shows gas pulses emitted by the valve for a stagnation pressure of $\approx 2200\text{ Torr}$ for three different valve durations. For a $100\mu s$ valve duration (used for subsequent experiments) we observe a overall delay between the trigger of the HV pulse and the

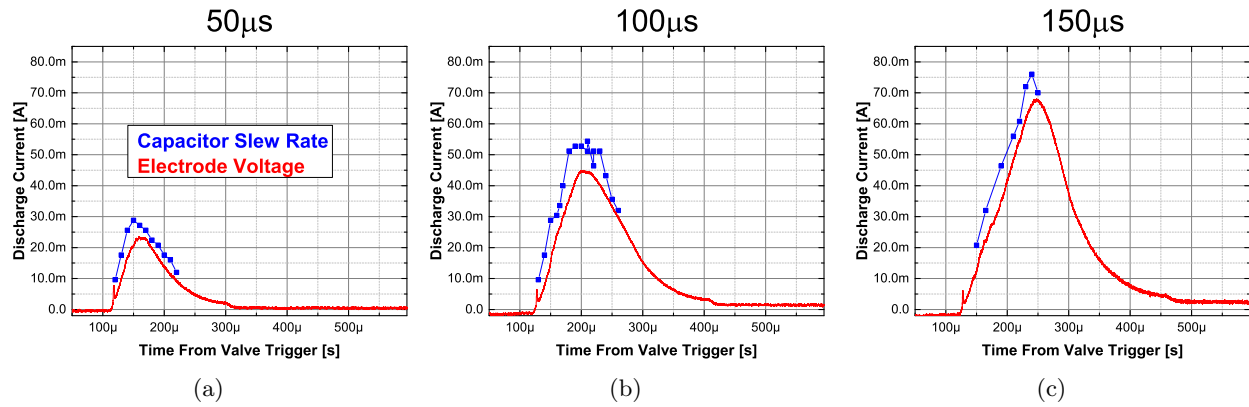


Figure 3.21: Comparison of the two different methods used to measure the discharge current for three different valve durations (a) $50\mu s$, (b) $100\mu s$, and (c) $150\mu s$. For all three, the capacitor slew rate data (blue squares) has been shifted forward by $10\mu s$ to be in the center of the $20\mu s$ discharge pulse. For the measurements of the electrode voltage (red line) the bias is applied continuously, so that the measured current would map out the gas pulse as it exits the valve.

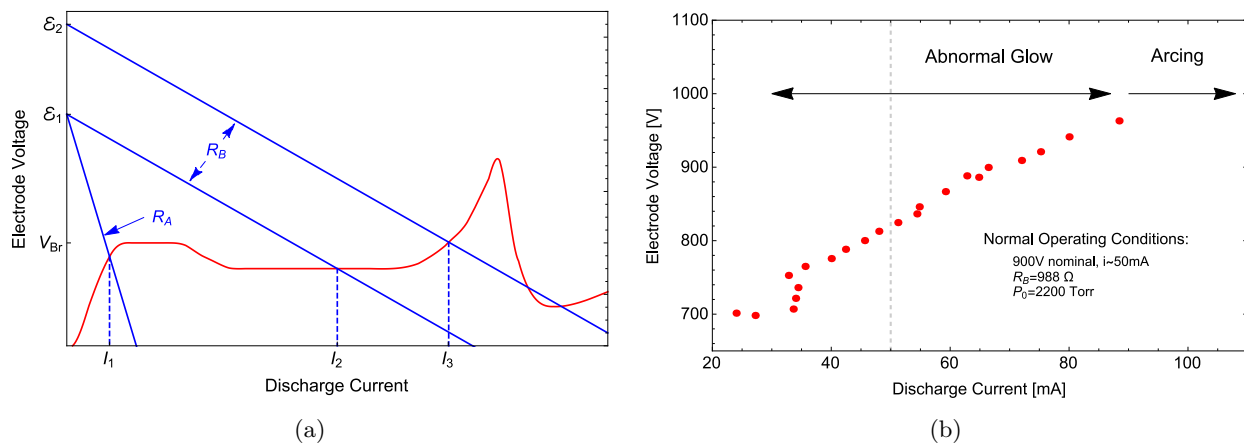


Figure 3.22: (a) Schematic of a discharge IV curve including the details of the electronic circuit showing two different ballast resistors R_A and R_B and two different power supply voltages \mathcal{E}_1 and \mathcal{E}_2 . (b) Measured IV curve indicating operation in the abnormal glow regime. The vertical dashed line in (b) indicates the normal operating value of the discharge current of $\approx 50mA$.

time of peak conductance of about $125\mu s$. This delay ($\approx 125\mu s$) is the same across pressure ranges from 1000 - 2000 Torr and for valve durations in the range 50 - $150\mu s$. Accurate knowledge of this delay is crucial for determining the velocity distribution of a molecular beam for deceleration experiments.

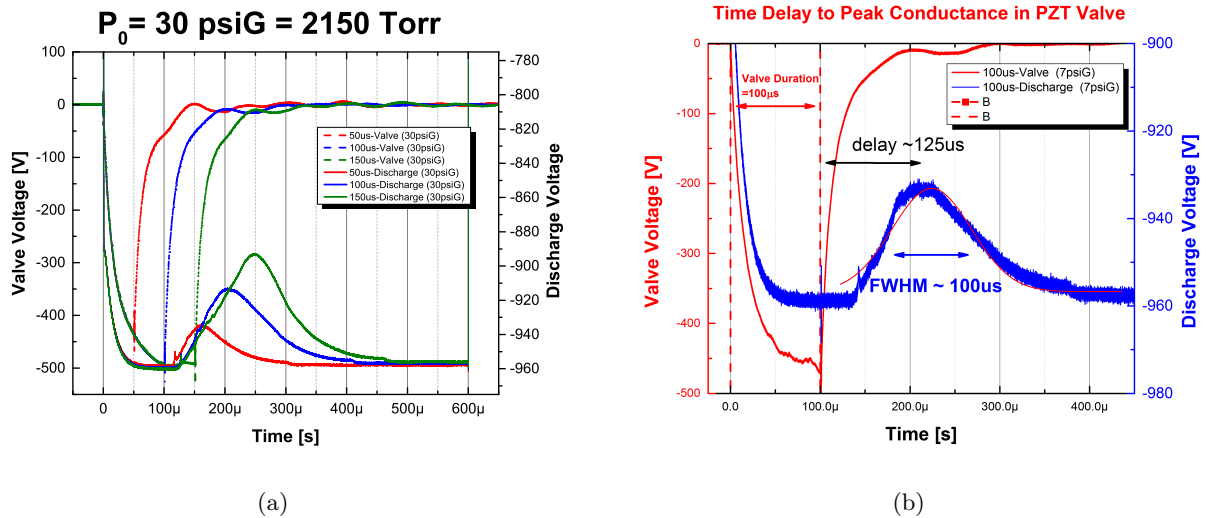


Figure 3.23: Relation between voltage applied to PZT valve and resulting gas pulse measured by monitoring the discharge current. (a) shows the general dependence for nominal valve durations of $50\mu\text{s}$ (red), $100\mu\text{s}$ (blue) and $150\mu\text{s}$ (green). In each case, the delay between the end of the PZT valve pulse and the time of maximum discharge current (maximum Kr density between the discharge plates) is approximately $125\mu\text{s}$. This dependence is highlighted for the case of $100\mu\text{s}$ nominal valve duration (which is used for all OH deceleration data presented in this thesis) in panel (b).

3.8.2 Glow Discharge Stability: Discharge Current and “Ballast” Resistor

Here we analyze the voltage-current characteristic of a discharge from the perspective of stability. Consider the case where the applied voltage is increased from zero. Once the threshold is reached, the avalanche becomes sustained forming a low-resistance current path. As the current increases, the avalanche grows, producing more charge carriers, which increases the electrical conductivity. As a consequence, increases in current are accompanied by a decrease in the electrode voltage, which is effectively a negative differential impedance. (See the “sub-normal glow” region in Fig. 3.14). When the voltage drops below the threshold for sustained avalanche, the discharge will cease. If only a power supply is used to operate a discharge, it will oscillate between below threshold behavior and the sub normal glow. To make the discharge stable, the circuit must have an overall positive differential impedance, which is accomplished with a simple resistor in series with the discharge. As the current through the resistor increases, the voltage drop across it will increase, limiting the total voltage that is applied to the electrodes.

The IV curve shown in Fig. 3.22a emphasizes the role of the electrical circuit (power supply voltage \mathcal{E} , and ballast resistor R) in determining the stability of the discharge. The equation for the electrode voltage during operation, $V = \mathcal{E} - i * R$, is known as the load line (shown as straight blue lines in Fig. 3.22a). Upon switching on the power supply, the discharge voltage and current is set by the intersection of the load line and the discharge IV curve. If the power supply voltage (\mathcal{E}_1) is low and/or the ballast resistor very large (R_A) the electrode voltage will be below threshold and the discharge will not fire (bottom most blue line). By reducing the load resistor (R_B) and keeping the power supply voltage at \mathcal{E}_1 the discharge can be stably operated in the normal glow regime. If the power supply voltage is then increased keeping R_B fixed, the discharge will eventually transition to the abnormal glow regime (top-most blue line).

The interplay between the ballast resistor and the bias voltage should be carefully considered. Larger bias voltages increase avalanche formation, which tends to stabilize the discharge but also increases the probability of an undesired transition from abnormal glow to arcing. In the end, a ballast resistor of $R = 988\Omega$ and a bias voltage of $900V$ was chosen. The measured IV curve of our discharge shown in Fig. 3.22b indicates that it is in the abnormal glow regime, which is in agreement with the findings of [163] [164]. This situation is qualitatively similar to the topmost blue line in Fig. 3.22a. The high operating currents make it necessary to continually monitor the discharge (both visually and with electrical measurements) to ensure it does not transition to an arc.

3.9 Production of Cold OH Beams Optimized for Loading Stark Decelerator

As mentioned in Ch. 1, Stark deceleration is best classified as a “slowing” or “filtering” technique because it preserves phase space density. As such, any decrease in the temperature (or velocity width) of an ensemble of decelerated molecules is always accompanied by a decrease in number density, n . It is therefore advantageous to start with a the largest phase space density possible.

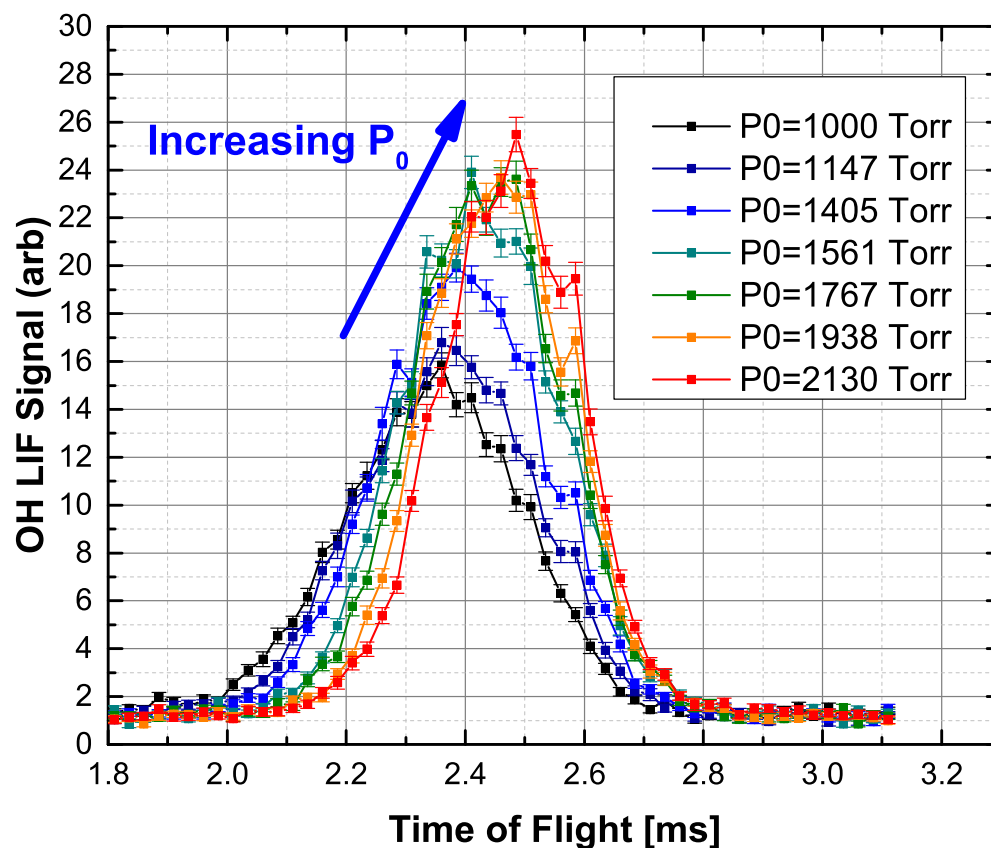
3.9.1 Effect of Stagnation Pressure, P_0

The value of stagnation pressure of Kr behind the valve plays an important role in the resulting OH beam phase space density. TOF measurements of OH beams created with varying values of p_0 and fixed valve parameters ($20\mu s$ discharge pulse fired $200\mu s$ after valve trigger, $900V$ nominal voltage) are shown in Fig. 3.24. As seen in Fig. 3.24a, a modest increase in the stagnation pressure from 1000 to $2200Torr$ results in striking changes to the OH TOF profiles; not only does a higher pressure result in an increased peak signal, but also narrower profiles that are delayed in time (valve-skimmer distance fixed at $11.3cm$). The latter two effects suggest that the beam is colder and slower, both of which are important for Stark deceleration.

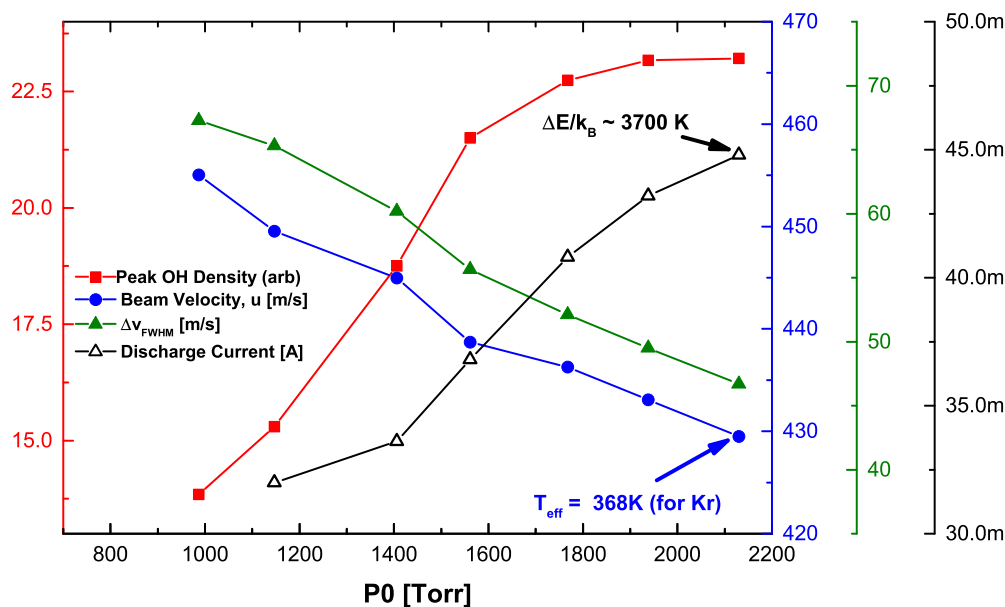
The increase in 2-body collisions (see Sec. 3.4) at high pressures provides a reasonable explanation for the decrease in beam temperature (for a fixed reservoir temperature, T_0) but cannot explain the reduced final velocity. As described in Sec 3.3, the terminal velocity of a supersonic beam is determined by conversion of thermal energy in the reservoir to kinetic energy associated with bulk flow. The observed velocities are already significantly in excess of the flow velocity of Kr from a $300K$ reservoir ($u \approx 385m/s$) suggesting an elevated source temperature due to heating from the discharge. Apparently, the effect of the high pressures is to reduce the effective temperature of the reservoir, $T_0^{(eff)}$ [165]. If we assume that the measured OH beam velocities are the same as those for the Kr beam, then the minimum velocity of $u \approx 430m/s$, implies an effective stagnation temperature for Kr of only $T_0^{(eff)} \approx 368K$.

This is somewhat surprising considering the increased stagnation pressure is accompanied by an increase in the discharge current, and thus in the total electrical energy injected into the gas. At $45mA$ and electrode voltages of $\approx 900V$ the peak power is $\approx 40W$ amounting to a total of energy of $\approx 800\mu J$ during the $20\mu s$ discharge pulse. For nominal valve durations of $100\mu s$ and stagnation pressures of $P_0 = 2200Torr$, typical fluxes are $\sim 7 \times 10^{16} \#Kr/Pulse$. The $20\mu s$ discharge fired at peak valve conductance only interacts with $\approx 15\%$ of the pulse (see Fig. 3.25). Distributing the $800\mu J$ equally between the $N \sim 10^{16}$ Kr atoms in the pulse ($U_{int} = \frac{3Nk_B T}{2}$) would amount to an *added* average energy of $\sim 3700K$.

The order of magnitude difference in the two estimates of the reservoir temperature can be attributed



(a)



(b)

Figure 3.24: OH beams as a function of stagnation pressure, p_0 , for fixed valve parameters ($20\mu s$ discharge pulse fired $200\mu s$ after valve trigger, $900V$ nominal voltage). (a) Raw TOF data (b) Beam properties extracted from TOF fits. Vertical axis labels are suppressed to minimize cluttering of figures (see legend). From left, axes are peak OH density (red squares), beam velocity (blue circles), velocity width (FWHM) (green triangles), and discharge current (black hollow triangles). For details, see text.

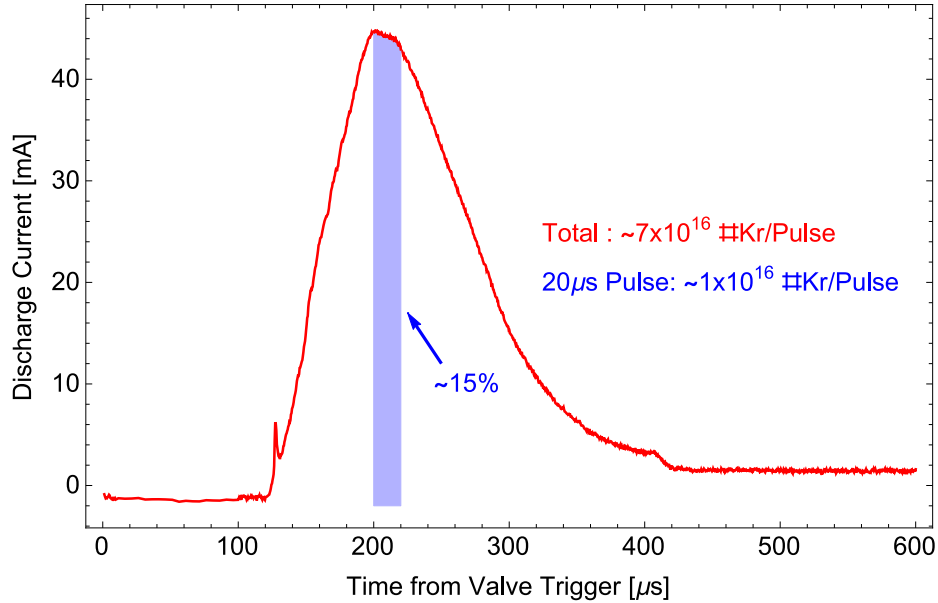


Figure 3.25: Typical gas pulse from the PZT valve (nominal duration = $100\mu s$) mapped out using discharge current. The blue-shaded band indicates the $\sim 15\%$ fraction of the total gas pulse which the $20\mu s$ discharge pulse actually interacts with.

to the favorable non-equilibrium properties of a glow discharge mentioned at the beginning of Sec. 3.7. At $45mA$ the density of electrons between the discharge plates is estimated to be $n_e \sim 10^{15}cm^{-3}$. By striking the discharge in the upstream high-pressure region, the ionization fraction is kept low and heating to the ions and neutrals is minimized, which leads to a slower OH beam. At $7 \times 10^{16}\#Kr/pulse$ and assuming the plasma is overall neutral then this suggests an ionization fraction of order $f_i \sim 10^{-4}-10^{-5}$, which is typical for a non-equilibrium glow discharge. This is in contrast to OH discharge design used in [166], which produced OH beams with central velocities of $\sim 885m/s$.

3.9.2 Skimmer Interference

Here, we present experimental measurements of the degradation of OH beams as a result of interactions with the skimmer. The skimmer used in this and all experiments presented in this thesis has a 2mm entrance diameter with exterior/interior angles of a $25^\circ/30^\circ$ (Beam Dynamics, Model 2).

As mentioned in Sec 3.4.3, skimmer interference can generally be attributed to the interaction of the molecular beam with the “cloud” of molecules that have scattered off the skimmer [122]. The collisions

of the undisturbed beam with the cloud will be best characterized in terms of the skimmer temperature and not the local beam temperature. For a low density cloud, beam molecules will typically undergo only a single collision. This regime can be considered the *onset* of skimmer interference since it will result in Beer’s law attenuation of the beam but will leave the velocity distribution unaffected. To affect the velocity profile, a beam molecule scattered off the warm cloud must undergo a *second* collision that redirects it back towards the beam. Since multiple collisions would require a smaller mean free path, this (more deleterious) regime of skimmer interference is expected to occur at higher beam intensities than the simple Beer’s law type scattering/attenuation. If the second collision occurs past the skimmer entrance the molecule “rattles around” inside the skimmer, leading to a “skimmer choking/clogging” effect, which can completely block the beam.

In more extreme cases of skimmer interference the temporal pulse shape may actually be asymmetric. In this case, the leading edge of the gas pulse gets through the skimmer largely unscathed while the center of the pulse undergoes many collisions within the interior of the skimmer, which can completely block the transmission of the tail end of the pulse. This effect can be very important for the production of cold beams since it is most problematic at high intensities where the beam is expected to be the coldest.

The two stages of skimmer interference are visible in the TOF measurements with OH beams at varying valve-skimmer distances, as shown in Fig. 3.26. Raw TOF data is shown in Fig. 3.26a and beam properties extracted from TOF fits are summarized in Fig. 3.26b; the longitudinal velocity width (FWHM) is plotted as green triangles, the flow velocity as blue circles, and the beam intensity (amplitude of TOF distribution) is shown as red squares. As expected, the flow velocity is unaltered by the presence of the skimmer, but the intensity and velocity distribution show a strong dependence on valve-skimmer distance. The longitudinal velocity width reaches a plateau at distances of 11 *cm*, but the beam intensity appears to be linearly increasing even at distances as large as ≈ 13.5 *cm*. These distances are significantly larger than the ≈ 8 *cm* predicted for our nominal operating conditions of $p_0 \approx 2200$ *Torr* and $d_{eff} \approx 400$ μm (see Fig. 3.10b). This could be due in part to the estimated value of d_{eff} being derived from the average properties of the gas pulse, which underestimates the peak value of d_{eff} where the discharge is actually struck. In any case, these large distances are in reasonable agreement with the data presented in [88] were a high-intensity

Ne beam required valve-skimmer distances as large 15 *cm* ($x/d \sim 750$).

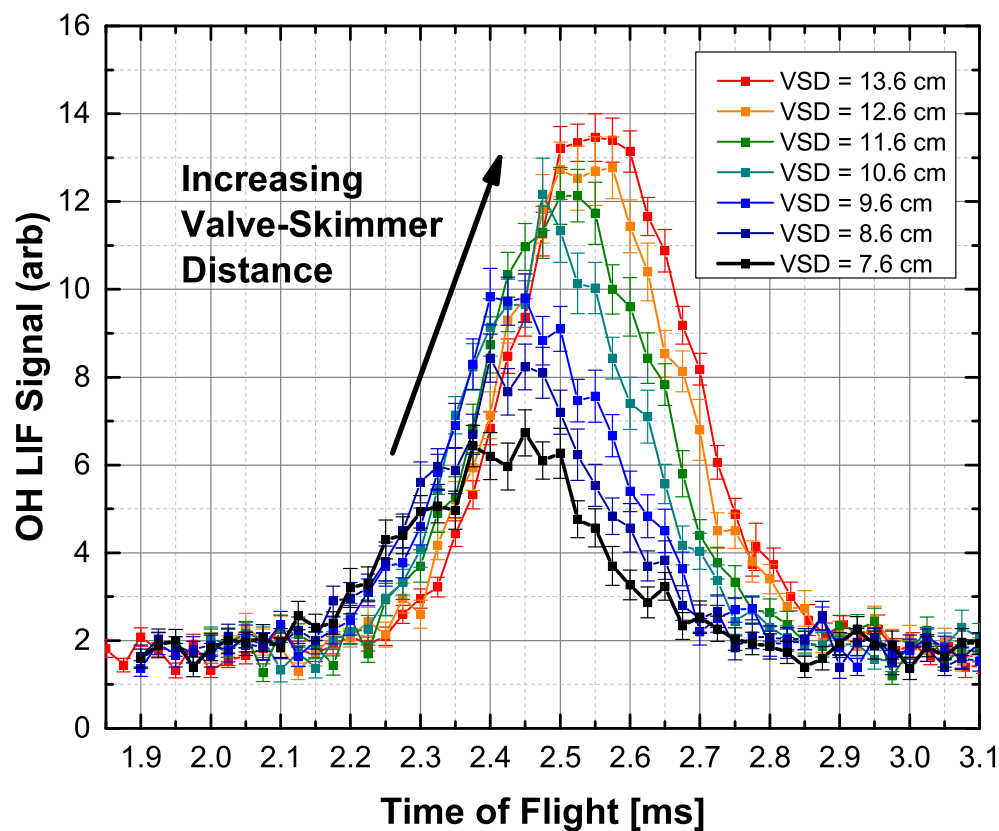
3.9.3 Dependence on Ignition Time

As described in Sec. 3.4.1, the application of valve pulse durations comparable to the intrinsic response time of the valve invariably results in a commensurate decrease in the effective valve diameter, d_{eff} (provided the gas flow out of the valve was not already choked). In this limit, where the motion of the valve piston never stabilizes, flow properties will be different in different parts of the gas pulse, due to a time-dependent value of $p_0 \cdot d_{eff}(t)$. Various experiments have reported that the center of the gas pulse where d_{eff} is largest (and thus $p_0 \cdot d$ is largest) is the coldest part of the pulse and region of the most intense clustering [167], [100].

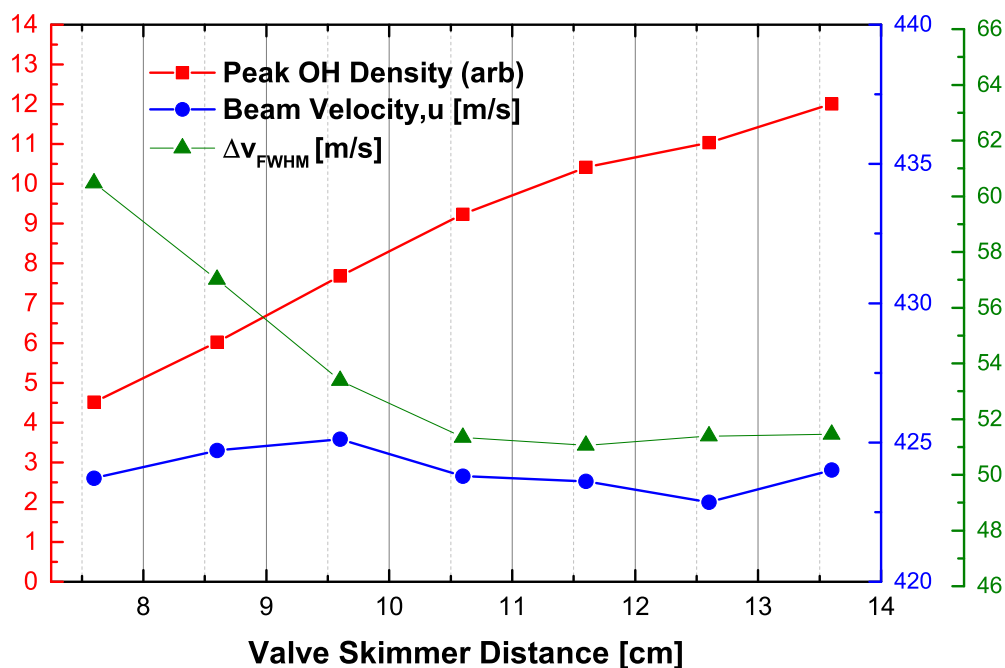
This basic concept can be applied to a discharge source of OH radicals by localizing the HV pulse to the time of the peak valve diameter. Fig. 3.27 shows summarized properties of OH beams created in a 20 μs discharge pulse at various ignition times (different values of d_{eff}) for nominal valve durations of 50 μs , 100 μs , and 150 μs . Due to the sluggish response time of our valve, all three valve durations have different peak values of d_{eff} . The velocity distributions of the fitted OH TOF profiles generally have a minimum near the center of the valve pulse, where $p_0 * d_{eff}$ is largest, and rising at the trailing ends of the pulse.

3.9.4 Total OH Yield?

Finally we consider the effective dissociation yield of the discharge source. For the production of cold OH beams, typical discharge currents are $i_{disc} \approx 50 \text{ mA}$, which corresponds to a peak current density of $\sim 3 - 6 \text{ [A/cm}^2\text{]}$ across the 1mm channel/cone between the discharge electrodes. This amounts to a peak electron flux of $(1 - 4) \times 10^{19} \text{ [e}^- \text{/}(s * \text{cm}^2\text{])}$ or a peak fluence of $(2 - 8) \times 10^{14} \text{ [e}^- \text{/cm}^2\text{]}$ integrated over the 20 μs discharge pulse. If OH was generated only by direct electron impact dissociation (Eq. 3.29) then taking the cross-section for formation of OH ($X^2\Pi$) to be $\sim 10^{-16} \text{ cm}^2$ would imply a water dissociation probability of $\sim (2 - 8)10^{-2}$ or $\sim 1\%$. At a stagnation pressure of 2200 Torr, the 23 Torr vapor pressure of water amounts to an effective seed concentration of $\approx 1\%$. An upper limit to the actual dissociation yield can then be found by assuming that the discharge electrons interact with $\sim 10^{14}$ water molecules (see Fig.



(a)



(b)

Figure 3.26: Representative behavior of OH beams for varying valve-to-skimmer distances (VSD) and fixed valve ($100\mu s$, $p_0 = 2200 Torr$) and discharge parameters ($20\mu s$, $900V$). (a) shows raw TOF data and (b) shows summarized beam properties extracted from TOF fits. (Vertical axes are as in Fig. 3.24b.) The data displayed here show pronounced skimmer interference where the beam central velocity is unaffected (blue circles), but the beam intensity (red squares) and velocity width (green triangles) show increasing degradation as the valve-skimmer distance is decreased. For details, see text.

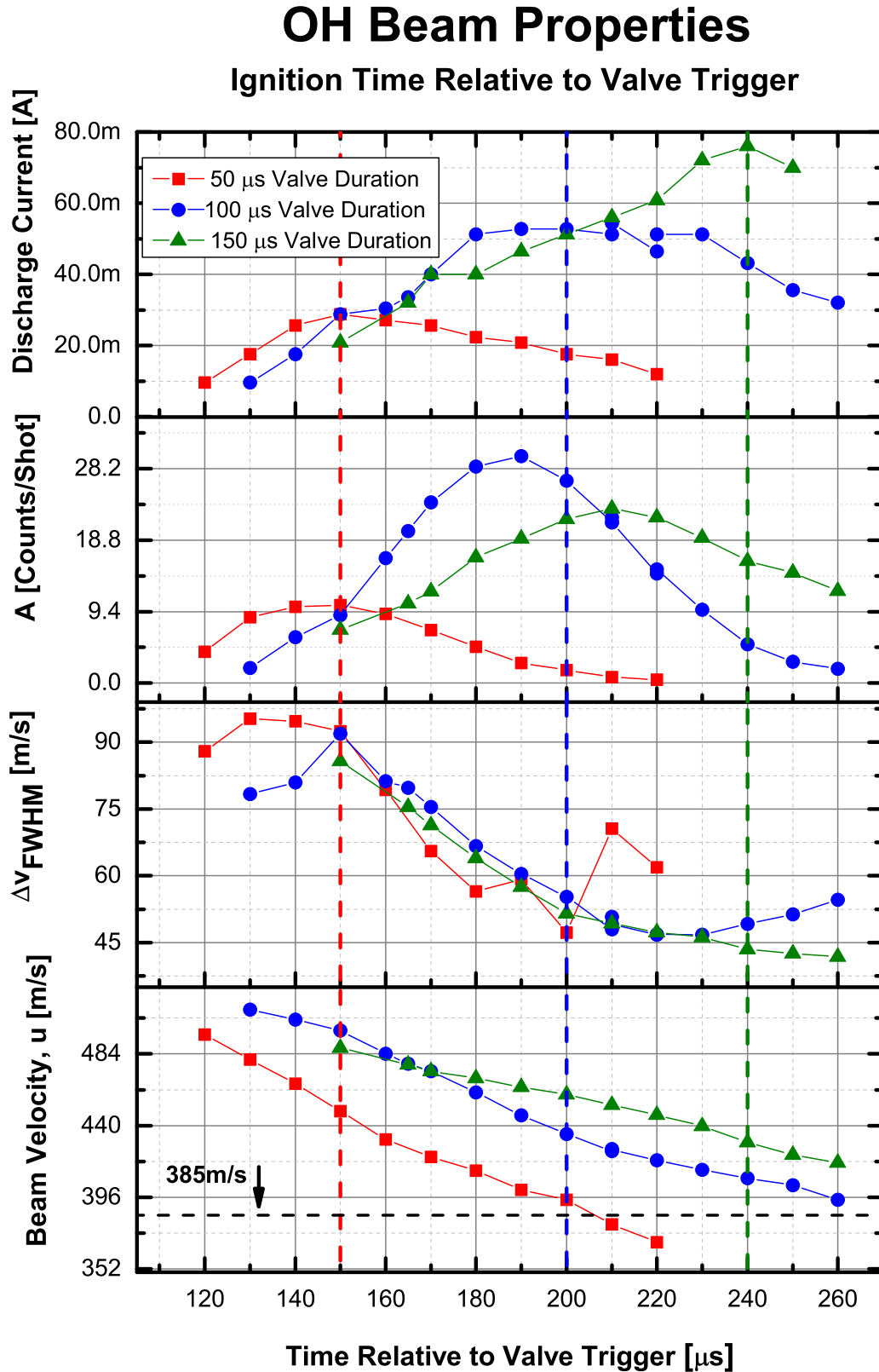


Figure 3.27: Properties of an OH beam created from a $20\mu\text{s}$ discharge pulse for varying discharge ignition times. The central velocity u and width Δv_{FWHM} are obtained by fitting TOF data to the functional form given in Eq. 3.20. Colored dashed vertical lines indicate the approximate time of the peak valve diameter and consequently largest gas density. In the bottom panel the horizontal dashed line corresponds to the expected terminal velocity for a Krypton beam at a reservoir temperature of 300K of $u = 385\text{m/s}$ (Eq. 3.8).

3.25) to yield of order 10^{12} molecules.

The estimated yield of 1% is in reasonable agreement with absolute density measurements of OH (X) in a pulsed slit jet discharge of 0.1% H₂O water vapor in a carrier gas of 70%Ne/30%He [18]. Here the density at the throat of the gas expansion was extrapolated to be $\approx 2 \times 10^{14}$ radicals/cm³ ($p_0 = 400Torr$). It should be noted that the authors of [18] concluded that dissociation resulting from direct electron impact did not have a large enough cross section to explain 1% fragmentation yields. This seems to have been the result of incorrectly assigning the cross sections of Ref [168] to formation of OH (X) when it was really the emission cross section to produce electronically excited OH (A).

Stark Deceleration and Trapping

4.1 Introduction

As described in Ch. 3, supersonic expansion is a general technique to produce dense samples of cold molecules. However, the large forward velocity of these beams presents a problem for experiments in which the end goal is the production of molecules at rest in the *lab frame*. Electromagnetic beam deceleration techniques [169] [78], such as Stark deceleration [60] [170], allow the high phase-space density in the beam's moving frame to be translated to the lab frame. As discussed in Sec. 4.2, the process is conservative so that the phase-space density is constant. In this regard, beam deceleration is best classified as a “slowing/filtering” technique rather than “real cooling” (see also Sec. 1.1).

The manipulation of neutral particles with static and time-varying electric and magnetic fields has a long history [171] [172] [173] [174] [175] [78]. The forces exerted on the neutral species arises from the interaction between the neutral's dipole moment and the externally applied field,

$$U_{dip} = -\boldsymbol{\mu}_i \cdot \mathcal{F} \quad (4.1)$$

where $\boldsymbol{\mu}_i$ represents either an electric or magnetic dipole moment and \mathcal{F} represents either \mathbf{E} or \mathbf{B} . The semi-classical force on the dipole is

$$\mathbf{F} = -\nabla U_{dip} = \nabla (\boldsymbol{\mu}_i \cdot \mathcal{F}) = \boldsymbol{\mu}_i^{(eff)} \nabla |\mathcal{F}| \quad (4.2)$$

where $\boldsymbol{\mu}_i^{(eff)}$ is the effective dipole moment, which accounts for precessional averaging as well as the effects of

angular momentum coupling and mixing of parity states in electric fields. As a consequence of Eq. 4.2, the force on a dipole is non-vanishing only for spatially inhomogeneous fields ($\nabla |\mathcal{F}| \neq 0$). Species with negative values of $\mu_i^{(eff)}$ are termed low-field seekers and those with positive values of $\mu_i^{(eff)}$ are high-field seekers. Classically, the low- (high-) field seekers can be regarded as the dipole aligning (anti-aligning) with the local field, such that the potential energy is minimized by moving towards regions where $|\mathcal{F}|$ is a minimum (maximum).

Application of these basic ideas to deceleration of a molecular beam is fairly straightforward. The basic configuration of a pulsed decelerator [60] [62] consists of pairs of electrodes, spaced longitudinally by a distance L (Fig. 4.1a), which are alternately charged up to $\pm HV$ or are grounded. (See Fig. 4.1b for a photograph of our pulsed decelerator.) A large electric field is then generated between the electrodes, which low-field seeking molecules see as a longitudinal potential barrier. As the molecules enter this section of the decelerator and “climb the hill,” their kinetic energy is reduced. If the fields were applied continuously, the molecules would regain this kinetic energy as they roll down the back side of the hill. This is avoided by switching off the current stage and switching on the next stage when the molecules are near the top of the hill. The net effect is to make the molecules “constantly go up hill.”

For a molecular dipole moment of $d = 1$ Debye and reasonable laboratory fields of $|\mathbf{E}| \approx 50 - 100 \text{ kV/cm}$, the interaction energy is $\sim 1\text{-}2K$, so that removal of the $\sim 300K$ of forward energy takes ~ 150 stages. A notable exception is Stark deceleration of atoms and molecules excited to Rydberg states with principal quantum numbers on the order of $n \sim 30$. The dipole moments of these states scale as n^2 [176] so that the effective electric dipole moment is on the order of $\sim 10^3$ Debye. This technique has allowed the deceleration of $\approx 500 \text{ m/s}$ beams of atomic [177] and molecular hydrogen [178] with only a *single* stage.

4.2 Liouville’s Theorem and Phase-Space

Before discussing the details of Stark deceleration and trapping of molecules, it is useful to discuss the general features of the dynamics of particles in conservative potentials formed by electromagnetic fields. Our primary interest is the motion of light molecules, such as OH ($m_{OH} = 17 \text{ amu}$) and ND₃ ($m_{ND_3} = 20 \text{ amu}$), at temperatures around $\approx 1K$. Under these conditions, the de Broglie wavelength ($\lambda_{dB} \sim 5 \text{ \AA}$) is much

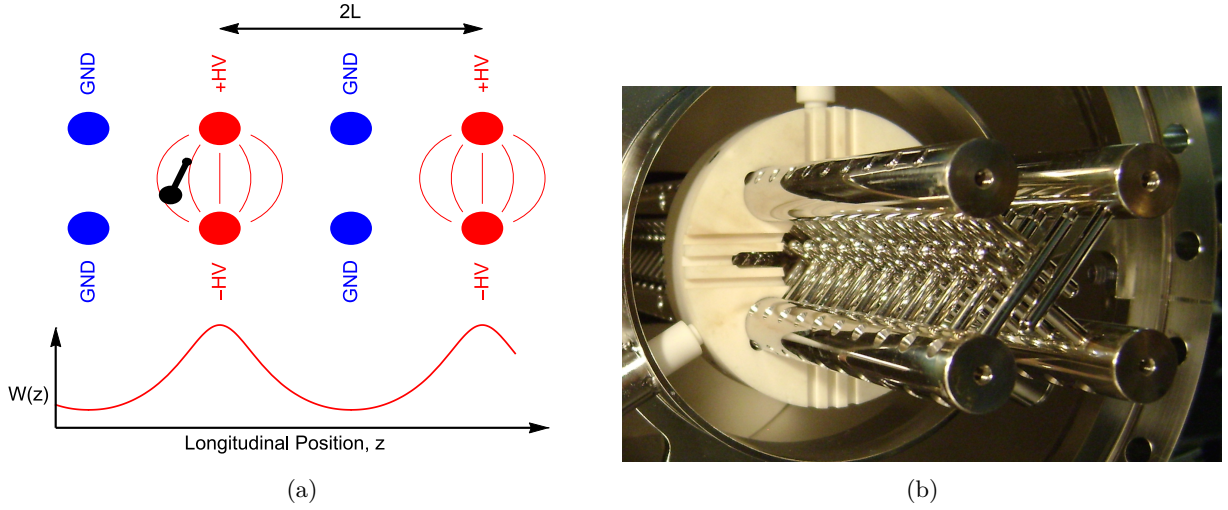


Figure 4.1: Panel (A) shows a schematic of the configuration of the potentials $W(z)$ formed. A stick and ball model of a polar diatomic molecule (such as OH) is shown in black. (b) A photograph of our pulsed decelerator (from the trap end). The four larger rods form a skeleton that holds the smaller rod electrodes [solid circles in (a)], which create the potential used to decelerate molecules.

smaller than the characteristic length over which the potential varies ($\sim 1mm$). As a result, quantum interference effects regarding the center of mass motion of the molecule are completely negligible. The classical motion can be described in terms of the Hamiltonian, \mathcal{H} , and Hamilton's equations [179] [180] [181] for the generalized velocities, \dot{q} , and forces, \dot{p} ,

$$\dot{q} = \frac{\partial \mathcal{H}}{\partial p} \quad \dot{p} = -\frac{\partial \mathcal{H}}{\partial q} \quad (4.3)$$

For an N -particle system there will be $3N$ - pairs of equations given by Eq. 4.3. Provided \mathcal{H} is known, the classical trajectory is uniquely determined by specification of the two initial conditions: $q(t = 0)$ and $p(t = 0)$. Furthermore, from the time-reversal symmetry of classical systems (invariance with respect to the substitution, $t \rightarrow -t$), these initial conditions also serve to completely specify the past history of the particle. As a consequence, two different trajectories in phase-space (q, p) cannot cross since this would violate the uniqueness property.¹

¹ In other words, specification of the conditions at the crossing point has apparently failed to specify future motion because it diverges on either side.

For conservative systems, in which the only forces are those derivable from a potential $\mathbf{F} = -\nabla U$, the Hamiltonian is constant and equal to the total energy E ,

$$H(q, p, t) = \frac{p^2}{2m} + U(q) = E, \quad (4.4)$$

where m is the mass of the particle. Since the total mechanical energy of the system is conserved, the phase-space trajectories are constrained to lie along a 6D-surface of constant E . For systems confined to one spatial dimension (two dimensions in phase-space) the surface is reduced to a curve. The motion of a particle in an idealized 1-dimensional potential is shown in Fig. 4.2. The potential, $U(q)$, is shown in the upper panel, and the phase-space trajectories for three different values of the total energy are shown in the lower panel. The lowest energy, E_B corresponds to bounded orbits such that the particle is confined to the potential well for all times (trapped). The trajectories of particles with an energy equal to the maximum of the potential, E_C , serve as the boundary between bound and unbound orbits. In the context of trapping experiments, E_C is commonly referred to as the *trap depth* and the corresponding trajectory in phase-space is termed the *separatrix*. The contour of the separatrix is termed the *acceptance* of the potential well. Particles with energies greater than the trap depth, E_U , lead to unstable orbits and are consequently not trapped.

The most powerful applications of the idea of phase-space is to large ensembles of particles. The distribution in phase-space of an N - particle ensemble at any given time is described by a swarm of $3N$ - points in phase-space (phase points). The *phase-space density*, ρ_Ω , is defined as the number of such points² per unit spatial volume, V , and momentum volume V_p ,

$$\rho_\Omega = \frac{N}{VV_p} = \frac{N}{\prod_i^N dq_i^3 dp_i^3} \quad (4.6)$$

Since phase space trajectories do not cross, the time evolution of the phase points in the ensemble is similar to laminar fluid flow with each particle being represented by a streamline. This means that rather than dealing explicitly with all $6N$ - degrees of freedom of an N - particle system, one may instead look only

² In a quantum picture, the classical phase points become quantum states that are no longer localized to infinitesimal points. Using semiclassical Bohr-Sommerfeld quantization, the phase-space volume occupied by a single state is equal to h^3 where h is Planck's constant. In other words, the density of quantum states, or occupancy, is given by

$$\frac{\rho_\Omega}{h^3} = \# \text{particles} / \text{quantum state} \quad (4.5)$$

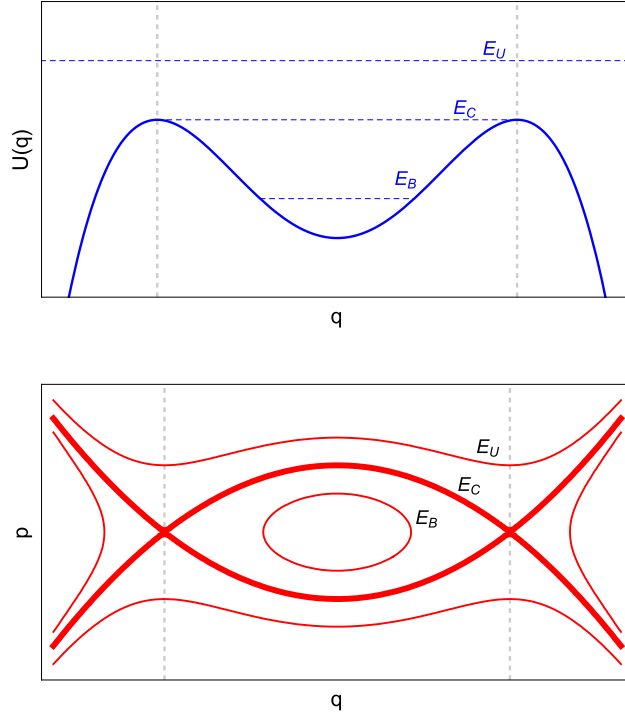


Figure 4.2: Idealized motion in a 1-dimensional potential well. The potential, $U(q)$, is shown in the upper panel, and the phase-space trajectories for three different energies, E_B , E_C , and E_U , are shown in the lower panel. The trajectory at the critical energy, E_C , separates bound and unbound trajectories is indicated by a heavy line. For details, see text.

at the trajectories of particles on the outer edge of phase space as a representation of the motion of the ensemble. These ideas are depicted in the “cartoon” shown in Fig. 4.3 for generalized potential (no relation to the potential shown Fig. 4.2). Here a contour, C_1 , that bounds a group of particles at a time, t_1 , smoothly transforms into a boundary C_2 at a time t_2 , that encloses the same group of particles [182].

The evolution of these contours is constrained by Liouville’s theorem to keep the phase-space density constant [182] [183]. For a fixed total number of particles, N , conservation of phase-space density is equivalent to keeping the area enclosed by contours, C_i , fixed in the 1D example shown in Fig. 4.3 . Mathematically, Liouville’s theorem can be expressed by

$$\frac{d\rho_\Omega}{dt} = \{\rho_\Omega, \mathcal{H}\} + \frac{\partial\rho_\Omega}{\partial t} = 0 \quad (4.7)$$

where $\{\rho_\Omega, \mathcal{H}\}$ is the Poisson bracket (the classical analogue of a commutator) [179]. The analogous form of

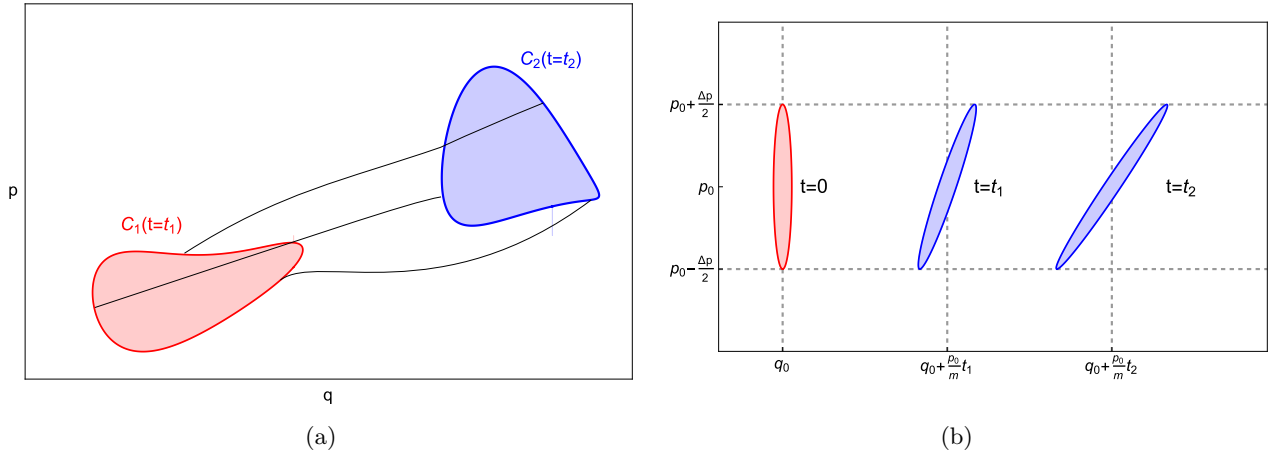


Figure 4.3: Time evolution of the phase space density ρ_Ω for an N -particle system. Panel (a) shows generalized contours $C_1(t = t_1)$ and $C_2(t = t_2)$ illustrating that although the shape of the contours may change, Liouville's theorem requires the enclosed area to stay constant (for $N = \text{fixed}$). A concrete example of this behavior is shown in panel (b) for the special case of vanishing external potential which is analogous to the evolution of a gas pulse from the pulsed valve to the decelerator. For details, see text.

Eq. 4.7 with the continuity equation in hydrodynamics leads to the idea that phase space density acts as an incompressible fluid.

For a concrete, and extremely relevant example, consider the free evolution ($U(q) = 0$) of a distribution characterized by a positive central velocity $v_0 = \frac{p_0}{m}$ and position and momentum widths of Δq and Δp . Contours corresponding to widths $\Delta q(t)$ and $\Delta p(t)$ at three different times are shown in Fig. 4.3b. The elongation of the distribution results from faster molecules moving ahead of molecules at the center of the distribution, and slower molecules falling behind. The position spread $\Delta q(t)$ is increasing for all times, but the momentum spread is fixed at $\Delta p(t) = \Delta p$. This behavior is in agreement with Liouville's theorem because the free evolution has correlated position and momentum such that only a certain velocity class is located at a given position (and time).

Loading this distribution of molecules into a potential well results in an immediate problem since the potential wells formed by electromagnetic elements (electrodes, current coils, permanent magnets, etc.) are of limited spatial extent and hence have a finite phase-space acceptance. Particles that are outside the phase-space acceptance of the potential well upon loading will remain untrapped for all times. Liouville's

theorem still applies to these untrapped molecules, but these molecules end their life in a turbo pump and do not contribute to the slowed fraction of a beam³. Thus, one is led to the idea that despite constant phase-space density ensured by Liouville's theorem, portions of phase-space can nonetheless be rendered *useless*.

It is tempting to view the time-dependent potential inherent to beam deceleration as a violation of Liouville's theorem. As shown in Ref [184], using general results based on information entropy, an increase in phase space density requires an irreversible process, which is absent for Stark deceleration. In conventional laser cooling, the irreversibility comes from the velocity-dependent *molasses force* [183] arising as a result of spontaneous emission. Thus, as a result of Liouville's theorem, the phase-space density of the sample of molecules can at best stay constant throughout the deceleration and trapping process.

4.3 Determining Longitudinal Motion in a Stark Decelerator

We begin our discussion of Stark deceleration with two equivalent methods to describe the longitudinal motion in a Stark decelerator. The first of these is based on direct numerical integration of Newton's laws, and the second is based on conservation of energy principles outlined in Sec. 4.2. The second method is simpler and more easily extendable to other types of deceleration such as continuous wave deceleration.

4.3.1 First Order Approximations

A schematic of the electrodes and the potential hill seen by low-field-seeking molecules within the decelerator is shown Fig. 4.4. A deceleration stage is formed by a pair of electrodes charged to $\pm HV$ which are flanked on each side by a pair of grounded rods, as indicated by the gray boxes in Fig. 4.4. The initial configuration of the decelerator electrodes is shown in the upper portion, and the other configuration is shown in the lower half.

The translational symmetry of W , which has a period of $2L$, leads to the description of longitudinal position in terms of a reduced position θ defined by

³ or a publication record.

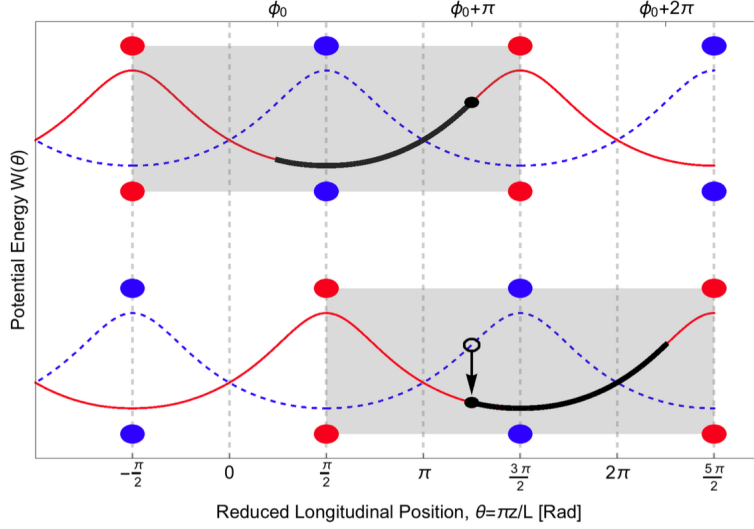


Figure 4.4: Diagram of potentials formed within a Stark decelerator for both electrode configurations. The reduced longitudinal position is shown on the lower horizontal axis, and the phase angle is shown on the upper horizontal axis.

$$\theta = \pi \frac{z}{L}. \quad (4.8)$$

Here, we follow the convention in Ref [185] to define the reduced position such that $\theta = 0$ is midway between adjacent pairs of electrodes with a charged electrode pair at $\theta = -\pi/2$ [maximum of $W(\theta)$] and a grounded electrode at $\theta = +\pi/2$ [minimum of $W(\theta)$] (see Fig. 4.1a).

The simplest mode of operation of a Stark decelerator is actually to not decelerate at all. In this mode, called *bunching*, the electrode configuration is switched synchronously with the speed of the molecule, v_0 , such that each stage lasts for a time equal to $\Delta t = L/v_0$. Since the average velocity of the molecule is unchanged in this mode, the amount of time going up hill (deceleration) and downhill (acceleration) are equal. From the schematic of the potentials in Fig. 4.4, we can see that for bunching, the fields must be switched when the molecule is midway between an electrode pair. The reduced position θ of the molecule at the time when the electrodes are switched is defined as the *phase angle*, ϕ . Molecules that are at the same position, ϕ at every switch time are termed *synchronous*. Thus, bunching corresponds to a phase angle of $\phi = 0$.

To decelerate molecules, one must use phase angles such that the net effect of switching is a decrease

in kinetic energy. From Fig. 4.4 it can be seen that the change in the kinetic energy⁴ of the synchronous molecule as a function of phase angle is given by

$$\Delta K(\phi) = -\Delta W(\phi) = W(\phi) - W(\phi + \pi). \quad (4.9)$$

The final kinetic energy of a synchronous molecule (mass m) after n deceleration stages is given by,

$$E_n(\phi) = \frac{1}{2}mv_i^2 + n\Delta K(\phi) \quad (4.10)$$

where $\Delta K(\phi)$ is a negative quantity. The final velocity is then

$$v_f(\phi) = \sqrt{v_i^2 + \frac{2n\Delta K(\phi)}{m}} \quad (4.11)$$

where n is the total number of stages. Eq. 4.11 is plotted in Fig. 4.5 for ${}^2\Pi_{3/2}$ OH molecules in our decelerator.

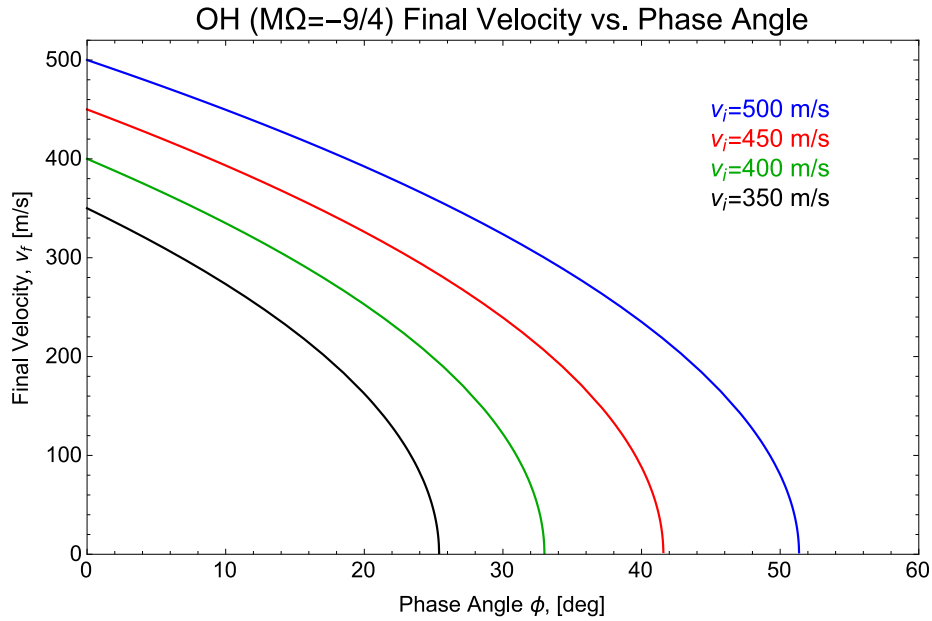


Figure 4.5: Final velocity of OH molecules as function of phase angle, ϕ , for various initial velocities (Eq. 4.11). $\Delta K(\phi)$ was evaluated using a numerical fit to $W(\theta)$. The potential corresponds to the geometry of the decelerator in the Lewandowski lab and assumes $n = 149$ deceleration stages.

⁴ If the charged rod pair were located at $\pi/2$ (instead of at $\theta' = -\frac{\pi}{2}$ as shown in Fig. 4.4), one would have the inconvenient result that positive values of $\Delta K(\phi)$ correspond to deceleration, which is clearly nonsensical.

4.3.1.1 First Order Approximation to Longitudinal Equation of Motion

To develop realistic models of the deceleration process, a functional form for the potential $W(\theta)$ is necessary. The general shape of $W(\theta)$ is shown in Fig. 4.4 for the two basic configurations of the electrode voltages. This periodic translational symmetry suggests that $W(\theta)$ can be expressed by a Fourier series. The different harmonics in the expansion should reflect the translation symmetry (period of $2L$) as well as the fact that the $W(\theta)$ is symmetric about a charged rod pair. The expansion that satisfies this condition for the red potential in Fig. 4.4 is given for $W_R(\theta)$ by

$$\begin{aligned} W_R(\theta) &= \frac{a_0}{2} + \sum_{n=1}^{\infty} a_n \cos \left[n \left(\theta + \frac{\pi}{2} \right) \right] \\ &= \frac{a_0}{2} - a_1 \sin(\theta) - a_2 \cos(2\theta) + a_3 \sin(3\theta) + a_4 \cos(4\theta) - a_5 \sin(5\theta) - a_6 \cos(6\theta) + \dots \end{aligned} \quad (4.12)$$

where the signs of the terms alternate as $-, -, +, +, -, -, +, +, \dots$. The coefficients themselves are defined to be positive. To illustrate the scaling of the potentials inside the decelerator for different molecules, the maximum value of the potential, $W(\theta = -\pi/2) = W_{max}$, can be factored out. Then, Eq. 4.12 can be written in a form to emphasize the relative magnitude of the coefficients,

$$\begin{aligned} W(\theta) &= W^{(max)} [c_0/2 - c_1 \sin(\theta) - c_2 \cos(2\theta) + c_3 \sin(3\theta) \\ &\quad + c_4 \cos(4\theta) - c_5 \sin(5\theta) - c_6 \cos(6\theta) + \dots] \end{aligned} \quad (4.13)$$

where $c_n = \frac{a_n}{W_{max}}$. The normalized coefficients c_i are shown in Table 4.1 for $|\mathbf{E}|$ as well as the potential seen by OH and ND₃ molecules in our decelerator. The similar magnitude of the normalized coefficient for a given harmonic, both to each other and to the expansion for $|\mathbf{E}|$, is a reflection of the fact that both molecules are in the linear Stark-shift regime. For instance, the c_1 coefficient is ≈ 0.46 , for all three columns in Table. 4.1.

Upon switching the electrode potential (from red to blue in the upper portion of Fig. ??), the new potential can be expressed by a translation of π [rad], so that

Table 4.1: Relative Fourier coefficients (See Eq. 4.13) of the electric field magnitude $|\mathbf{E}|(\theta)$ and the potential energy $W(\theta)$ for OH and ND₃ molecules.

	$ \mathbf{E}(\theta) $	$W_{ND_3}(\theta)$	$W_{OH}(\theta)$
$W^{(max)}$	1.063×10^7 [V/m]	1.876 [K]	2.487 [K]
c_0	8.0372×10^{-1}	7.7166×10^{-1}	7.7808×10^{-1}
c_1	4.6324×10^{-1}	4.6406×10^{-1}	4.6377×10^{-1}
c_2	1.1302×10^{-1}	1.1507×10^{-1}	1.1426×10^{-1}
c_3	3.3390×10^{-2}	3.2880×10^{-2}	3.3070×10^{-2}
c_4	1.0520×10^{-2}	1.1000×10^{-2}	1.0820×10^{-2}
c_5	3.0100×10^{-3}	2.8000×10^{-3}	2.8800×10^{-3}
c_6	1.0300×10^{-3}	1.1600×10^{-3}	1.1100×10^{-3}
c_7	3.0000×10^{-4}	2.4000×10^{-4}	2.6000×10^{-4}
c_8	1.1000×10^{-4}	1.4000×10^{-4}	1.3000×10^{-4}

$$\begin{aligned}
W_B(\theta) &= W_R(\theta + \pi) \\
&= \frac{a_0}{2} + \sum_{n=1}^{\infty} a_n \cos \left[n \left(\theta + \frac{3\pi}{2} \right) \right] \\
&= \frac{a_0}{2} + \sum_{n=1}^{\infty} a_n (-1)^n \cos \left[n \left(\theta + \frac{\pi}{2} \right) \right]
\end{aligned}$$

The change in the potential energy of a synchronous molecule is given by

$$\Delta W(\phi) = W_f - W_i = W(\phi_0 + \pi) - W(\phi) \quad (4.14)$$

The kinetic energy lost by the synchronous molecule (Eq. 4.9) is given by

$$\begin{aligned}
\Delta K(\phi) &= W(\phi) - W(\phi + \pi) = W_R(\phi) - W_B(\phi) \\
&= \left[\frac{a_0}{2} + \sum_{n=1}^{\infty} a_n \cos \left[n \left(\phi + \frac{\pi}{2} \right) \right] \right] - \left[\frac{a_0}{2} + \sum_{n=1}^{\infty} a_n (-1)^n \cos \left[n \left(\phi + \frac{\pi}{2} \right) \right] \right] \\
&= \sum_{n=1}^{\infty} a_n [1 - (-1)^n] \cos \left[n \left(\phi + \frac{\pi}{2} \right) \right]
\end{aligned} \quad (4.15)$$

Clearly, the quantity $[1 - (-1)^n]$ vanishes for $n \in \text{even}$ and is equal to 2 for $n \in \text{odd}$. Then we have

$$\begin{aligned}
\Delta K(\phi) &= 2 \sum_{n=1,3,5\dots}^{\infty} a_n \cos \left[n \left(\phi + \frac{\pi}{2} \right) \right] \\
&= -2a_1 \sin(\phi) + 2a_3 \sin(3\phi) - 2a_5 \sin(5\phi) + \dots
\end{aligned} \tag{4.16}$$

The description of the final velocity after n stages for a phase angle ϕ , only applies to the synchronous molecule. The most efficient decelerator is one where a large fraction of molecules in the vicinity (in phase-space) of the synchronous molecules are also successfully decelerated and make it to the end of the decelerator. Within a given stage, the potential energy experienced by a molecule depends only on the spatial coordinates. As a first order approximation we can account for the temporal variation of the potential $W(\phi)$ on a “stage-by-stage” basis using the idea of a time-averaged force. In the limit that the change in the velocity per stage is small compared with v_0 , the average force, $\bar{F}(\phi)$, can be approximated by

$$\begin{aligned}
\bar{F}(\phi) &\simeq \frac{-\Delta W(\phi)}{L} = \frac{\Delta K(\phi)}{L} \\
&\simeq \frac{-2a_1 \sin(\phi) + 2a_3 \sin(3\phi) - 2a_5 \sin(5\phi) + \dots}{L} \\
&\approx \frac{-2a_1 \sin(\phi)}{L}
\end{aligned} \tag{4.17}$$

where, in the last line of Eq. 4.17, terms above $n = 1$ in the expression for $\Delta K(\phi)$ (Eq. 4.16) have been dropped.

Non-synchronous molecules with phase angles $\phi' = \phi + \Delta\phi$, but at the synchronous velocity v_0 feel an average force given by

$$\begin{aligned}
\bar{F}(\phi + \Delta\phi) &\simeq -\frac{\Delta W(\phi + \Delta\phi)}{L} \\
&\simeq \frac{-2a_1 \sin(\phi + \Delta\phi)}{L}
\end{aligned} \tag{4.18}$$

The force on the non-synchronous molecule *relative to the synchronous molecule* is,

$$\begin{aligned}
\bar{F}_{rel}(\phi, \Delta\phi) &= \bar{F}(\phi + \Delta\phi) - \bar{F}(\phi_0) \\
&= \frac{-2a_1}{L} [\sin(\phi + \Delta\phi) - \sin(\phi)]
\end{aligned} \tag{4.19}$$

The relative position of a non-synchronous molecule, Δz , is related to the relative phase angle, $\Delta\phi$, by $\Delta z = \frac{L}{\pi} \Delta\phi$. The equation of motion for the non-synchronous molecule relative to the synchronous molecule can be found from $m \frac{d^2 \Delta z}{dt^2} = \frac{mL}{\pi} \frac{d^2 \Delta\phi}{dt^2} = \bar{F}_{rel}(\phi, \Delta\phi)$. This is conventionally written as

$$\frac{mL}{\pi} \frac{d^2 \Delta\phi}{dt^2} + \frac{2a_1}{L} [\sin(\phi + \Delta\phi) - \sin(\phi)] = 0 \tag{4.20}$$

where m is the mass of the molecule. This is analogous to the equation for a pendulum driven by a constant torque. When $\Delta\phi$ is small, $\sin(\phi + \Delta\phi) \simeq \sin\phi + \Delta\phi \cos\phi$ and the equation of motion becomes

$$\frac{mL}{\pi} \frac{d^2 \Delta\phi}{dt^2} + \frac{2a_1 \cos(\phi)}{L} \Delta\phi = 0. \tag{4.21}$$

Eq. 4.21 is equivalent to a harmonic oscillator with a resonant frequency of

$$f_z = \omega_z / 2\pi = \sqrt{\frac{a_1 \cos\phi}{2\pi mL^2}}. \tag{4.22}$$

The equation of motion Eq. 4.20 can be numerically integrated to determine the separatrices for a given molecule and phase angle, ϕ , as shown in Fig. 4.6 for OH.

4.3.2 Time Averaged Effective Potential

If the average relative force on non-synchronous molecules for a given phase angle ϕ (Eq. 4.19) is viewed as being derived from an effective potential, $U_{eff}(\phi)$, such that

$$m \frac{d^2 \Delta z}{dt^2} = - \frac{dU_{eff}(\phi, \Delta z)}{d\Delta z}, \tag{4.23}$$

then, Eq. 4.23 can be put in terms of phase angle using $\Delta z = \frac{L}{\pi} \Delta\phi$ and $d\Delta z = \frac{L}{\pi} d\Delta\phi$ to give

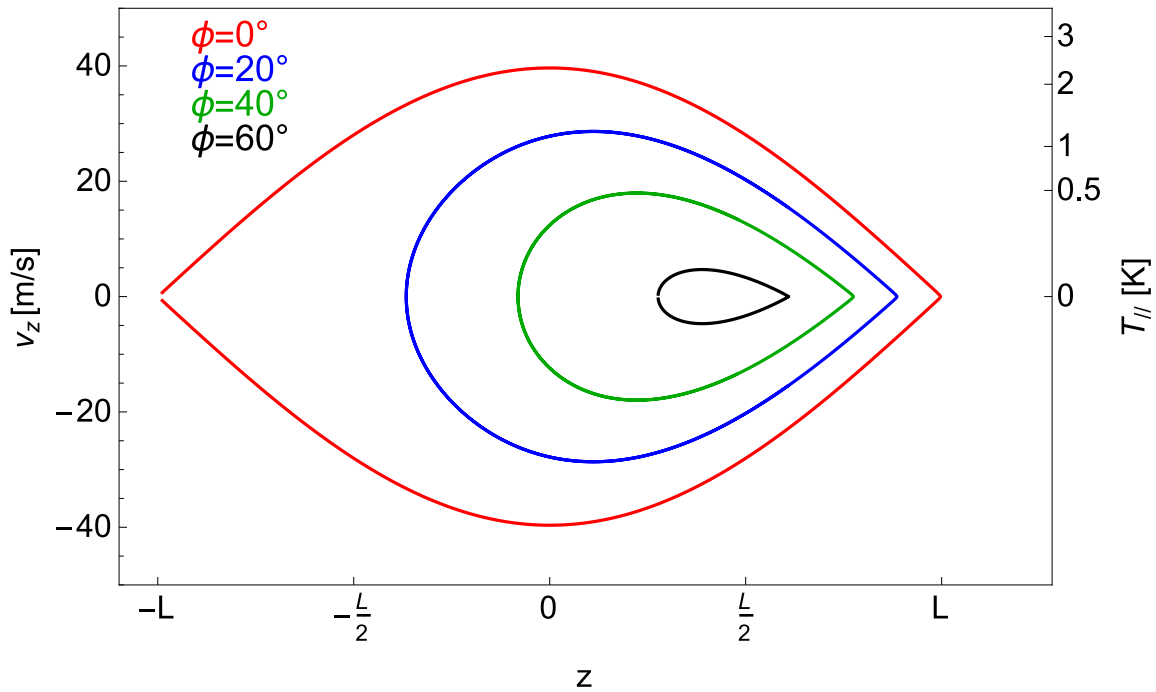
${}^2\Pi$ OH: $M_J\Omega = -9/4$


Figure 4.6: Longitudinal separatrices for ${}^2\Pi$ OH molecules at various phase angles calculated by numerically integrating Eq. 4.20.

$$m \frac{L}{\pi} \frac{d^2 \Delta\phi}{dt^2} = -\frac{\pi}{L} \frac{dU_{eff}(\phi, \Delta\phi)}{d\Delta\phi} \quad (4.24)$$

Setting the right-hand side of Eq. 4.24 equal to Eq. 4.19 yields

$$\frac{-2a_1}{L} [\sin(\phi + \Delta\phi) - \sin(\phi)] = -\frac{\pi}{L} \frac{dU_{eff}(\phi, \Delta\phi)}{d\Delta\phi} \quad (4.25)$$

or

$$\begin{aligned} U_{eff}(\phi, \Delta\phi) &= -\frac{L}{\pi} \int F(\phi, \Delta\phi) d\Delta\phi \\ &= \frac{2a_1}{\pi} \int [\sin(\phi + \Delta\phi) - \sin(\phi)] d\Delta\phi \\ &= \frac{-2a_1}{\pi} [\cos(\phi + \Delta\phi) + \sin(\phi)\Delta\phi] \\ &= \frac{-2a_1}{\pi} \left[\cos\left(\phi + \frac{\pi}{L}\Delta z\right) + \sin(\phi)\frac{\pi}{L}\Delta z \right]. \end{aligned} \quad (4.26)$$

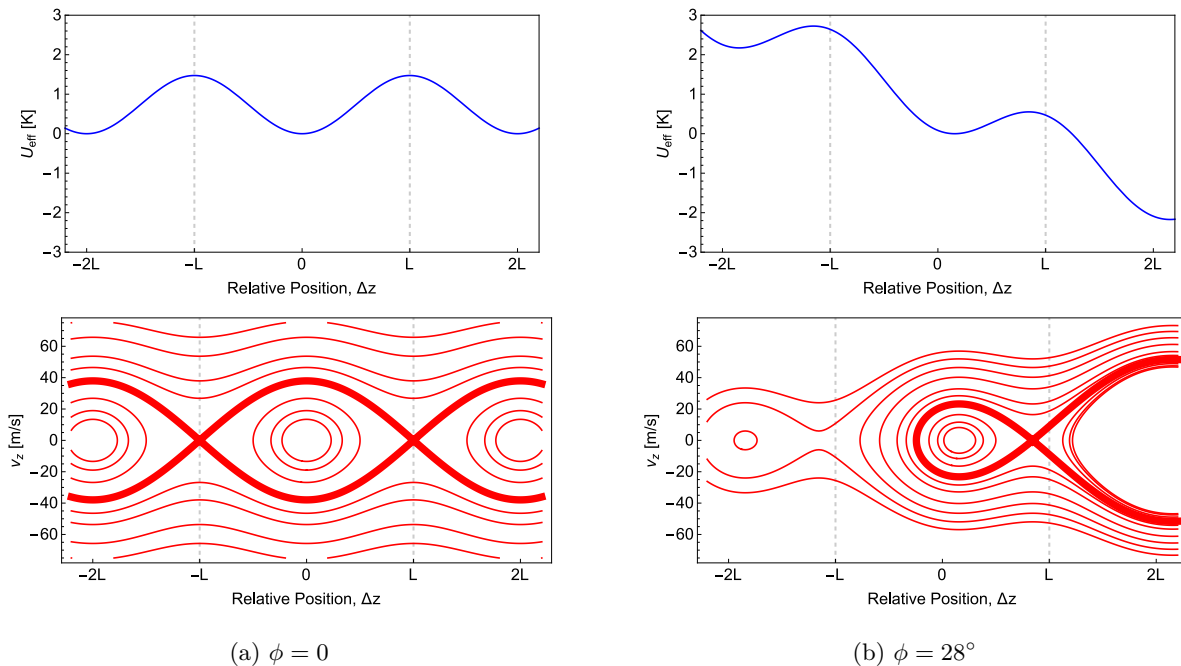


Figure 4.7: Effective potentials for OH at $\phi = 0^\circ$ and $\phi = 28^\circ$. As a result of nonzero phase angles as in (b), the potential well is tilted, which reduces the overall depth causing molecules spill out the front.

Eq. 4.26 can be written relative to the phase angle ϕ of the synchronous molecule by making the substitution $\Delta\phi \rightarrow \Delta\phi - \phi$.

$$U_{eff}(\phi, \Delta\phi) = \frac{-2a_1}{\pi} [\cos(\Delta\phi) + \sin(\phi)(\Delta\phi - \phi)] \quad (4.27)$$

Finally, addition of an offset term equal to $\frac{2a_1}{\pi} \cos\phi$ keeps the minimum of the potential located at zero energy for all phase angles to give

$$U_{eff}(\phi, \Delta\phi) = \frac{-2a_1}{\pi} [\cos(\Delta\phi) - \cos(\phi) + \sin(\phi)(\Delta\phi - \phi)]. \quad (4.28)$$

The benefit of this approach is that the separatrices for a given phase angle can be described using the perspective of energy conservation as outlined in Sec. 4.2. The effective potential $U_{eff}(\phi, \Delta\phi)$ given by Eq. 4.28 and corresponding separatrices are plotted Fig. 4.7 for $\phi = 0^\circ$ and $\phi = 28^\circ$. The local maximum of $U_{eff}(\phi, \Delta\phi)$ is located at $\Delta\phi_{max} = 180 - 2\phi$. (or $\Delta z_{max} = \frac{L}{180} \Delta\phi_{max} = \frac{L}{180} (180 - 2\phi)$).

4.3.3 Calculating the Timing Sequence

4.3.3.1 Linear Approximation (Constant Force)

A consequence of the concept of phase stability is that each deceleration stage (length = L) removes an equal amount of energy, $\Delta K(\phi)$. Then, the simplest approximation to the decelerator timing sequence assumes that the force acting on the molecule is constant with a magnitude equal to $F = \frac{-\Delta W(\phi)}{L} = \frac{\Delta K(\phi)}{L}$. This average force is related to the change of velocity within a single stage Δv and the time spent in that stage Δt by

$$F = \frac{m\Delta v}{\Delta t} = \frac{-\Delta W(\phi)}{L} \quad (4.29)$$

Then for the k^{th} stage, we have $\Delta v = v_k(\phi) - v_{k-1}(\phi)$. This definition is consistent with the notation of Eq. 4.11 so that $v_{k=1} = v_i$ where v_i is the velocity of the molecular beam. The time spent in the k^{th} stage is given by

$$\Delta t_n = \frac{mL}{-\Delta W(\phi)} [v_n(\phi) - v_{n-1}(\phi)] \quad (4.30)$$

In this case Eq. 4.30 is basically equivalent to Eq. 9 of Ref [186], although there is a slight (trivial) difference in the definition of the z-axis.

4.3.3.2 A More Accurate Analytic Expression for Timing Sequence

Within a given stage, the potential experienced by a molecule is a function of only its position. As a molecule rides across the potential $W(z)$, its velocity as a function of position is given by

$$v(z') = \frac{dz'}{dt} = \sqrt{v_i^2 - \frac{2}{m}W(z')} \quad (4.31)$$

where v_i is the initial velocity upon entering the stage at position $z' = z_i$. (The exit of the stage is located at $z' = z_i + L$.) The time spent in that stage is given by integrating the following equation

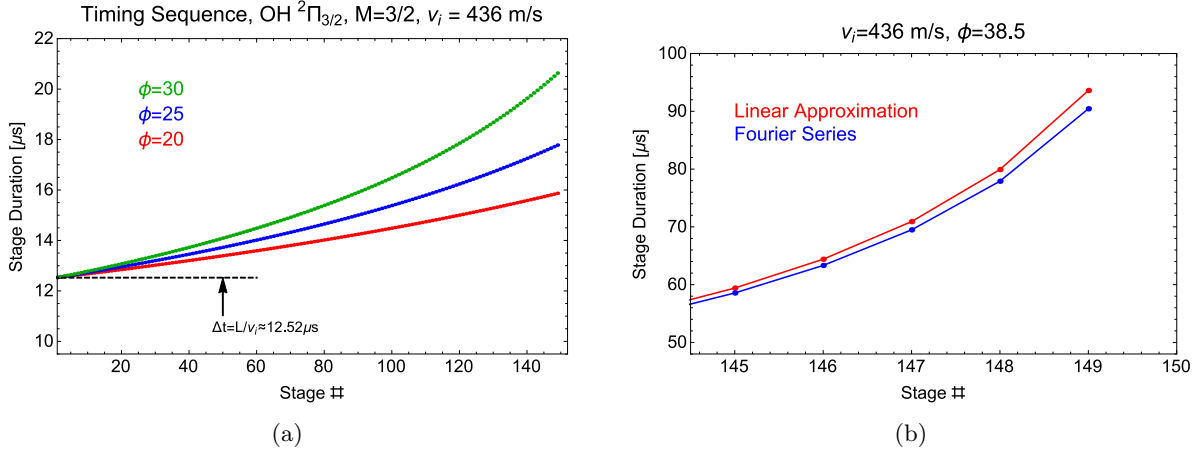


Figure 4.8: Stark deceleration timing sequence for ${}^2\Pi_{3/2}$ molecules in the stretched ($M = 3/2$) state and with an initial velocity of $v_i = 436\text{m/s}$. Sequence was calculated using Eq. 4.33 and the Fourier coefficients in Table 4.1. In the early stages, the velocity is not significantly changed and the stage durations are nearly same, equal to $L/v_i = 12.52\mu\text{s}$ (for this particular example).

$$\begin{aligned}
 dt &= \frac{dz'}{\sqrt{v_i^2 - \frac{2}{m}W(z')}} \\
 &= \frac{L}{\pi} \frac{d\theta'}{\sqrt{v_i^2 - \frac{2}{m}W(\theta')}}
 \end{aligned} \tag{4.32}$$

Integrating Eq. 4.32 from $\theta' = \phi$ to $\theta' = \phi + \pi$ gives the time spent in the k^{th} stage as,

$$\Delta t_k = t_k - t_{k-1} = \frac{L}{\pi} \int_{-\pi+\phi}^{\phi} \frac{d\theta'}{\sqrt{v_{k-1}^2(\phi) - \frac{2}{m}W(\theta')}} \tag{4.33}$$

where $v_{k-1}(\phi_0)$ is the initial velocity at the beginning of the k^{th} stage (i.e., final velocity at stage “ $k - 1$ ”).

As shown in Fig. 4.8b the linear approximation and the Fourier series representation are essentially the same until the the end of the deceleration process when the molecules are moving the slowest.

4.4 Experimental Setup

The decelerator used for all experiments presented in this thesis consists of 150 rod pairs (3.175mm diameter), which are spaced longitudinally by $L = 5.461\text{mm}$. (See Fig. 4.1b for a photograph and Fig. 4.9 for CAD drawing.) From Fig. 4.4, the 150 rod pairs amount to 148 complete deceleration stages. The first

stage is taken to be between the first two electrode pairs (before the first gray box in the upper half of Fig. 4.4). An additional stage, formed by the first two electrode pairs, can be used, although the fields at this point are not as well defined.

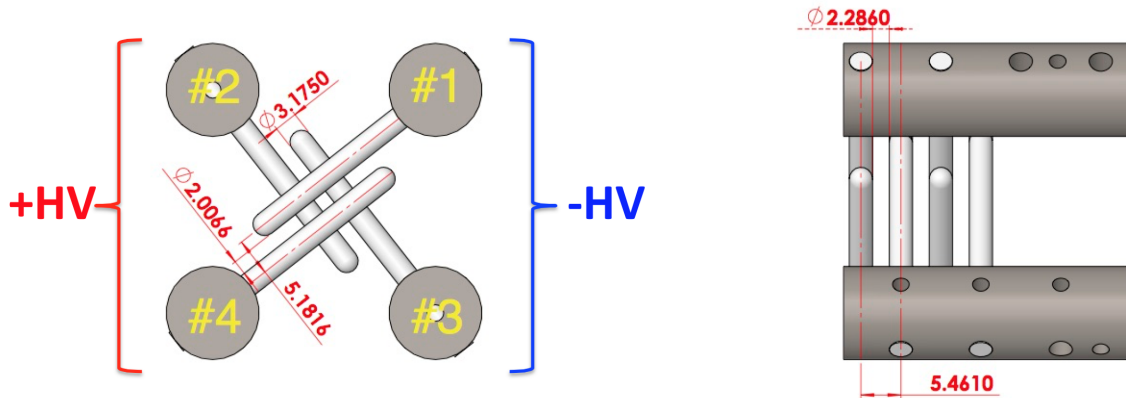


Figure 4.9: CAD drawing showing the dimensions of our decelerator as well as the labeling scheme used in the lab. On the right, only four rod pairs are shown.

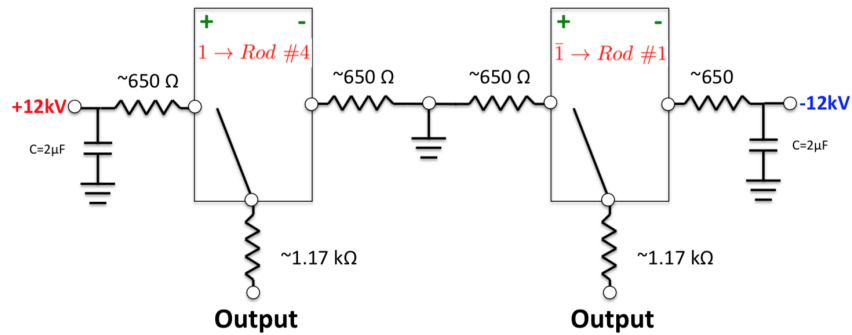
The HV potential applied to the electrodes is controlled with commercial TTL-controlled HV switches (Behlke, HTS-151-03-GSM). A simplified electrical circuit diagram is shown in Fig. 4.10. To provide the high currents required to rapidly swing the high voltages, the switches are connected to $C = 2\mu F$ capacitors.

4.5 Coupling a Supersonic Beam to a Stark Decelerator

Efficient deceleration of a molecular beam requires that the beam be optimally coupled to the potential wells formed by the Stark decelerator. Due to the considerations discussed in Sec. 4.2, poor coupling at this initial loading stage sets an upper limit on the phase-space density in the final decelerated beam. Unfortunately, the spatial extent of the gas pulse is usually significantly larger than the spatial width of the potential well in the decelerator. As a result, only a fraction of the molecules in the molecular beam can actually be decelerated. The geometry with the relevant distances is shown in Fig. 4.9

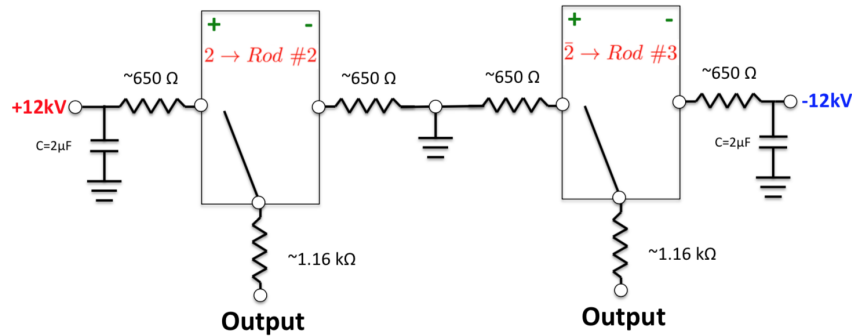
At the entrance of the decelerator, the gas pulse will have a finite spatial extent due to both the velocity distribution (dispersion) as well as the spread in the initial times the molecules leave the valve. As described in Ch. 3, the temporal and velocity distributions are somewhat correlated because different parts of

Rods #1 and #4



(a)

Rods #2 and #3



(b)

Figure 4.10: Simplified diagram of electrical connections for the Behlke switches for (a) rods #1 and #4, (b) rods #2 and #3. The resistors shown are recommended by the manufacture for impedance matching and to minimize EMF noise.

the gas pulse have different temperatures. However, for the purposes of making rough estimates, we assume that the two distributions are separable Gaussian functions. The initial temporal distribution is assumed to be described by a Gaussian with a FWHM equal to the nominal shutter function of the pulsed source ($\Delta t = 20\mu s$ for OH pulsed discharge). The OH velocity distribution is based on the TOF measurements presented in Sec. 3.9 (see in particular Fig. 3.27). For the optimal OH beam produced in our laboratory (largest phase-space density), the velocity distribution is described by a Gaussian with velocity width of $\Delta v \approx 50 m/s$ centered on the central velocity $u \approx 436 m/s$.

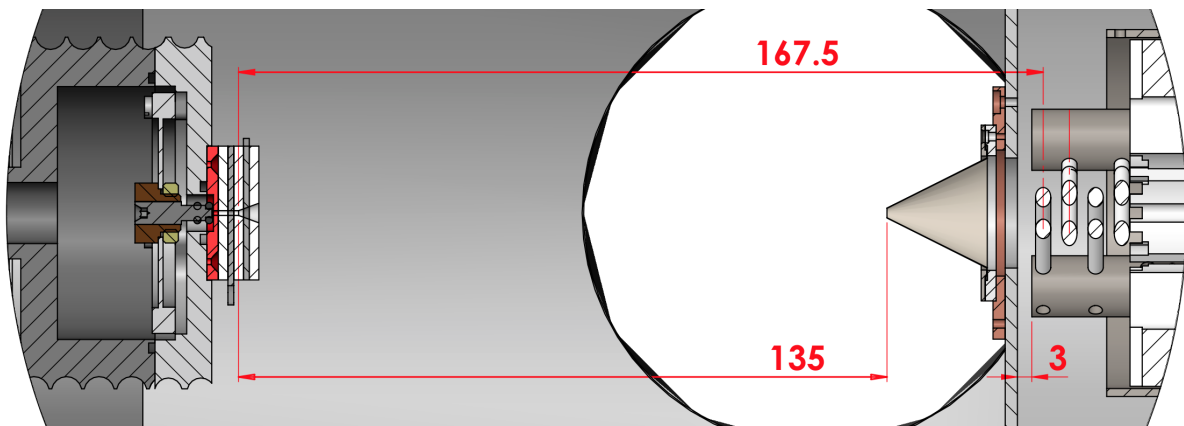


Figure 4.11: Relevant distances (in $[mm]$) regarding flight of the molecules to the decelerator. These distances correspond to the valve translation stage being located at a nominal position of $z = 0$. When the decelerator is installed, the four larger rods are kept $3.0mm$ from the interior surface of the skimmer mounting “can” to prevent discharges.

As the molecules fly from the valve to the decelerator, the spatial extent of the molecules increases as a function of total flight distance (see Fig. 4.3b). The spatial spread due to the velocity distribution (dispersion) can be approximated by

$$\Delta z_v = \Delta v * t_0 = \Delta v * \frac{d}{u} \quad (4.34)$$

where d is the flight distance from the valve to the decelerator and $t_0 = d/u$ is the average flight time from the valve to the decelerator. From Eq. 4.34 it is easy to see that cold beams (Δv small) and short propagation distances (d) are advantageous for loading a Stark Decelerator (or any trap). Estimation of the spatial spread due to the finite shutter function, Δz_0 , is somewhat subtle. Even though all molecules in the gas pulse originate from the same location (the pulsed valve), they can be considered to come from an extended source (along z) due to the temporal spread over which they are created. This equivalent spatial spread is approximately

$$\Delta z_0 = u * \Delta t_s \quad (4.35)$$

The process of loading the Stark decelerator is depicted in Fig. 4.12. The flight distance from the valve to the center of the potential well for a phase angle of ϕ is

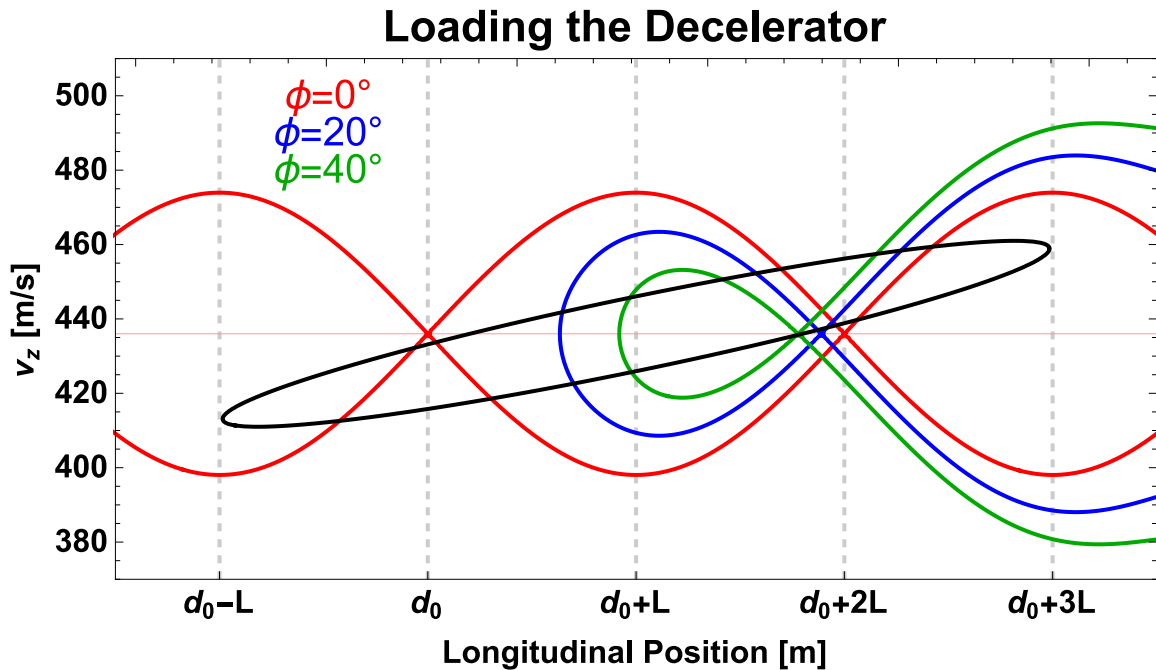


Figure 4.12: Loading the Stark decelerator. The full width half max of the OH distribution is shown by a heavy black curve, and the separatrices at $\phi = 0^\circ$, $\phi = 20^\circ$, and $\phi = 40^\circ$ are shown in red, blue, and green, respectively.

$$d = d_0 + L/2 + \phi \frac{L/2}{90^\circ} \quad (4.36)$$

where d_0 is the distance from the valve to the first electrode pair. Due to the problems of skimmer interference discussed in Secs. 3.4.3 and 3.9.2, the flight distances from the valve to the decelerator are fairly large, so that $d_0 \approx 17 \text{ cm}$. At these distances, $\Delta z_v \approx 1.95 \text{ cm}$, which is comparable to $\Delta z_0 = 436 \text{ m/s} \times 20 \mu\text{s} \approx 0.87 \text{ cm}$. The total spatial extent upon reaching the decelerator can be approximated by assuming that the actual width is due to the convolution of both Gaussian functions, with the widths added in quadrature,

$$\Delta z_{tot}^2 = (u * \Delta t_s)^2 + \left(\Delta v * \frac{d}{u} \right)^2 \quad (4.37)$$

The total width is then $z_{tot} \approx 0.211 \text{ cm} \approx 3.8L$, indicating that the OH packet should extend over roughly four deceleration stages.

4.6 Deceleration

As an introduction to the dynamics of the deceleration process, we discuss the results of numerical 3D simulations for the deceleration of an OH beam shown in Fig. 4.13. The upper portion of both panels shows the longitudinal velocity, v_z , plotted against the time of flight. Integrating the velocity distribution for a given time gives the TOF profile plotted in the lower half of the figure. In the bunching simulations (Fig. 4.13a) the structure in the velocity distribution is composed of two dominant features. The overall downward slope is an artifact of the free flight distribution from the valve (fastest molecules arrive first, etc.), which is modulated by the potentials within the decelerator. In the center of the distribution, the molecules become trapped in the moving time-averaged potential well. In Fig. 4.13b, in which the phase angle is increased to 28° , the molecules trapped in the average well are decelerated from $436 \text{ m/s} \rightarrow 234 \text{ m/s}$. (See in particular the upper panel of Fig. 4.13b.) In the next two subsections, deceleration data is presented for OH as well as ND_3 molecules.

4.6.1 Experimental Results of ND_3 and OH Deceleration

Deceleration of an ND_3 beam is shown in Fig. 4.14. The full range of TOF data is shown in Fig. 4.14a and a zoom of low velocity packets (high phase angles) is shown in Fig. 4.14b. In both (a) and (b), measured data are shown in the upper portion and the results of a 3D numerical simulation are shown in the lower portion (plotted negative). The input parameters for the simulated ND_3 distribution is based on measured longitudinal velocity distributions and transverse distributions estimated from the geometry of the skimmer aperture and flight distance. Aside from these input parameters, the simulation results contain no free parameters. The agreement between the experimental measurements and the simulations is quite remarkable.

As seen in both the ND_3 (Fig. 4.14) and OH data (Fig. 4.15) Show a pronounced drop in molecular signal at low velocities (larger phase angles). This originates from two primary effects. The first of these is a “shrinking” of the phase-space acceptance at larger phase angles (see also, Fig. 4.6). This “first order” effect can be estimated by calculating the area enclosed by the separatrix (the acceptance) as a function of phase

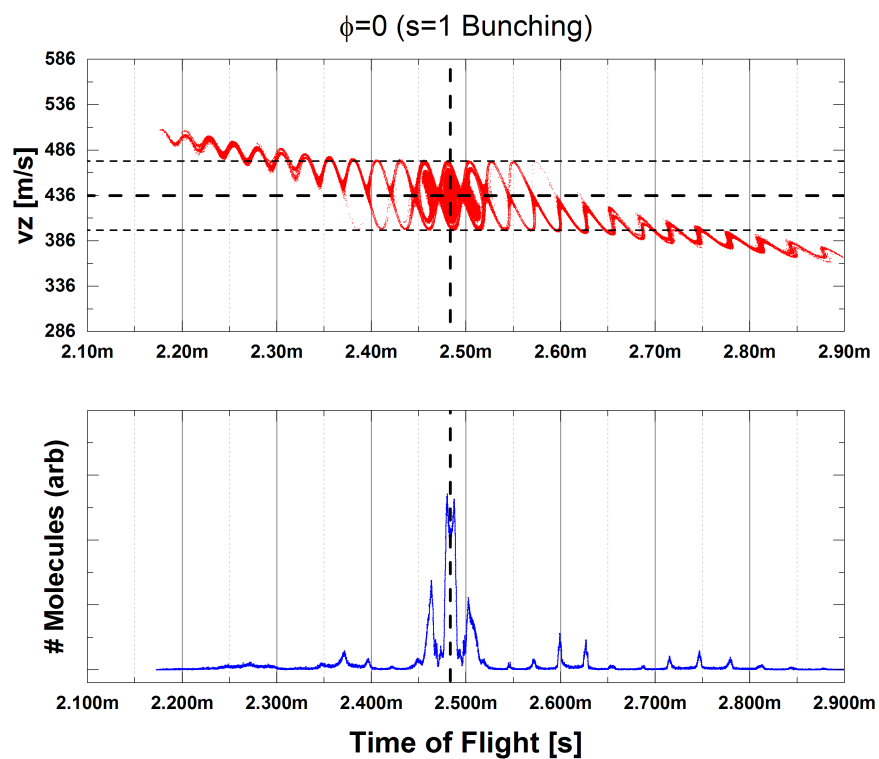
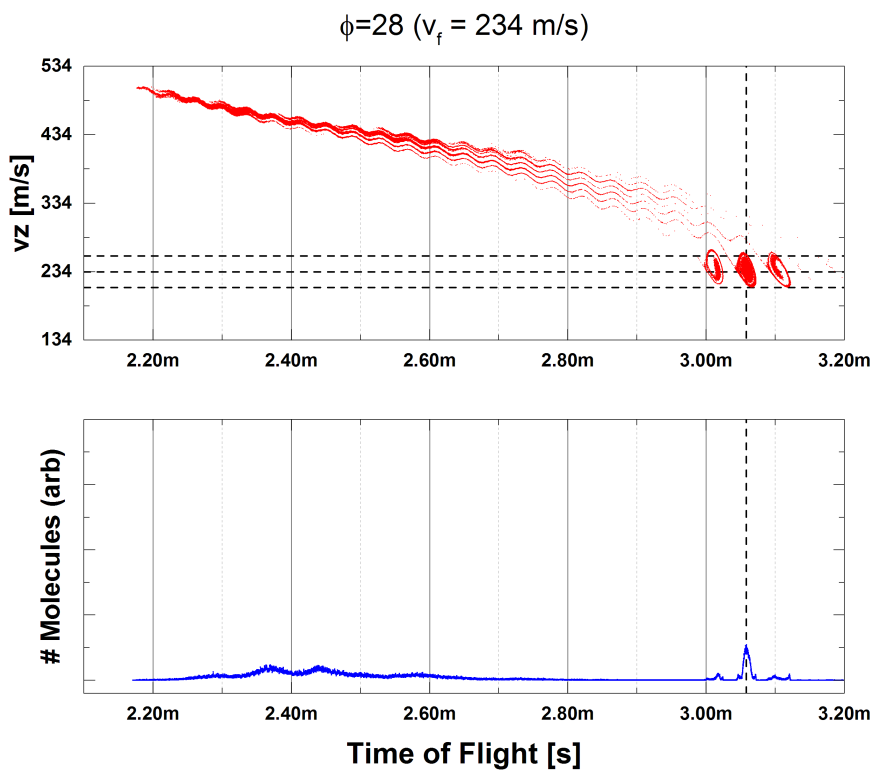
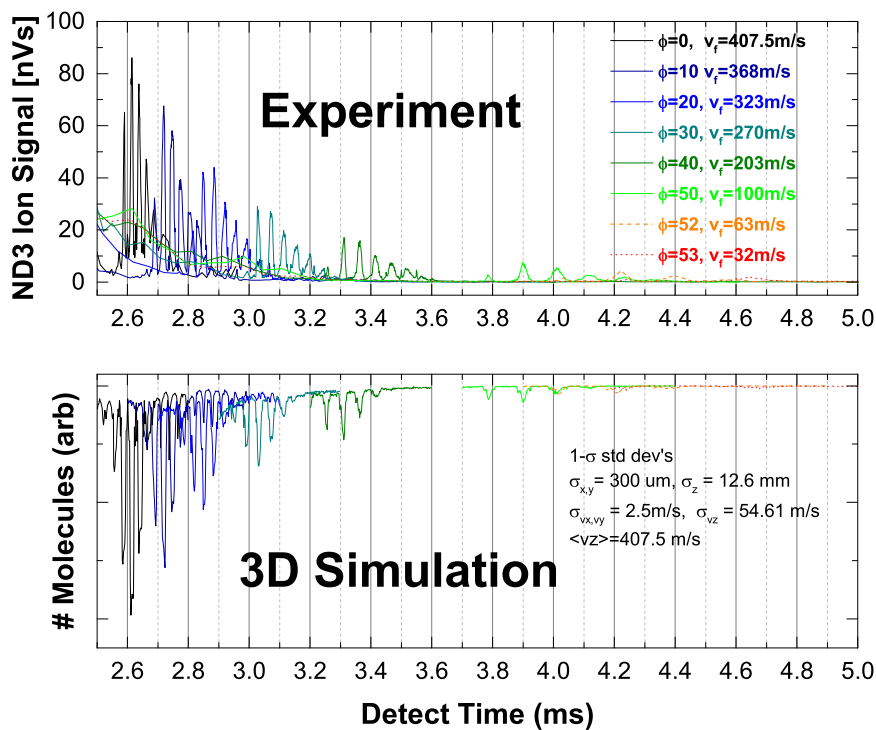
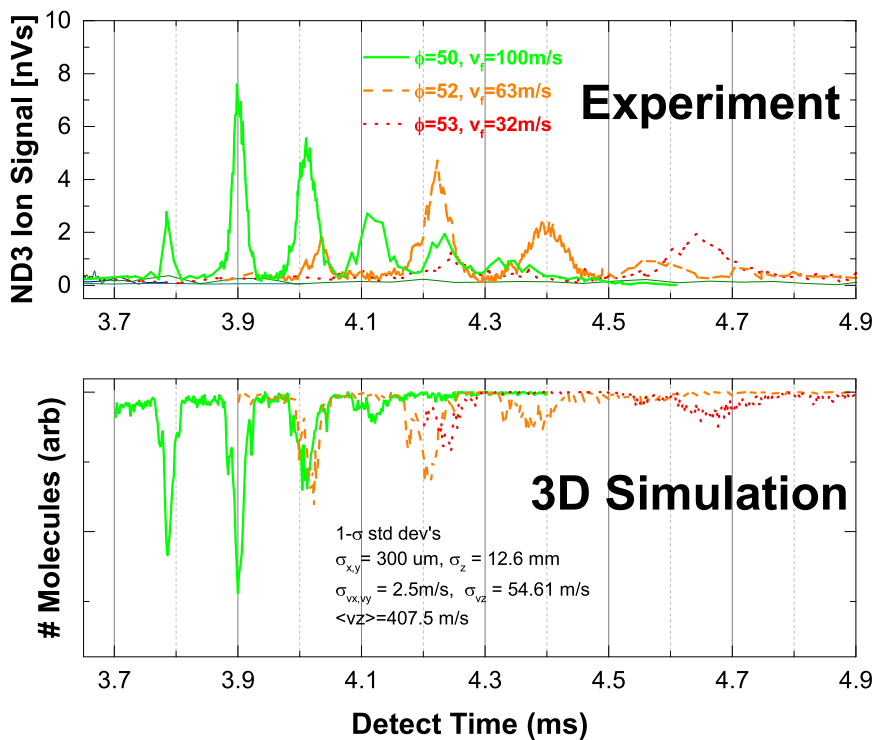
(a) $\phi = 0^\circ$ (b) $\phi = 28^\circ$

Figure 4.13: 3D numerical simulation of the deceleration of OH radicals for a phase angle of $\phi = 0$ and $\phi = 28^\circ$. In the upper panels, the intended final velocity is shown by a thick, dashed horizontal line and the bounds of the separatrix are shown as thinner horizontal lines. The vertical lines correspond to the arrival time of the central packet.

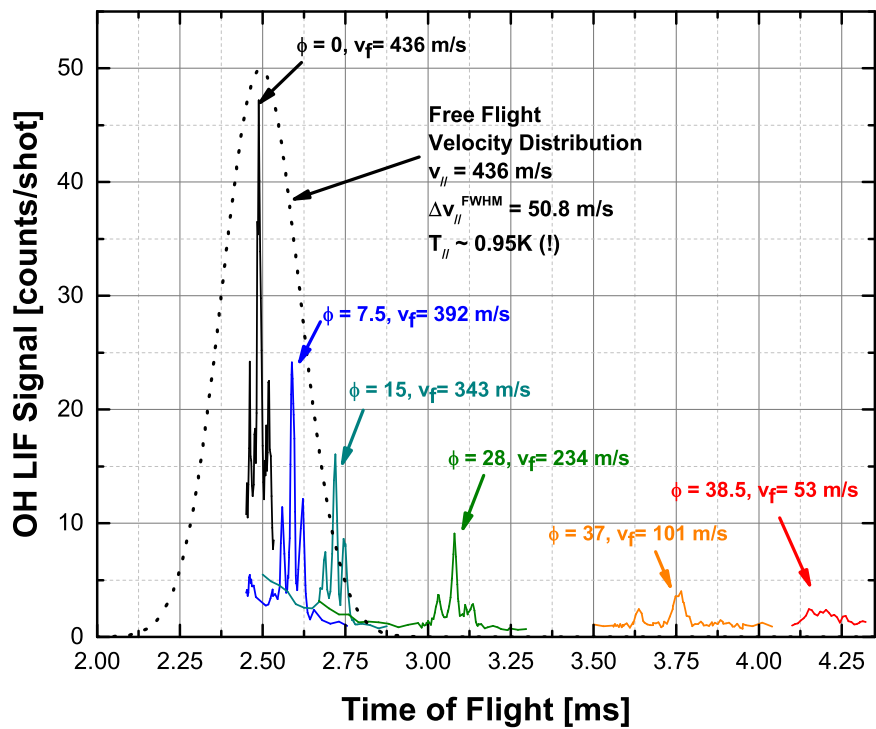


(a)

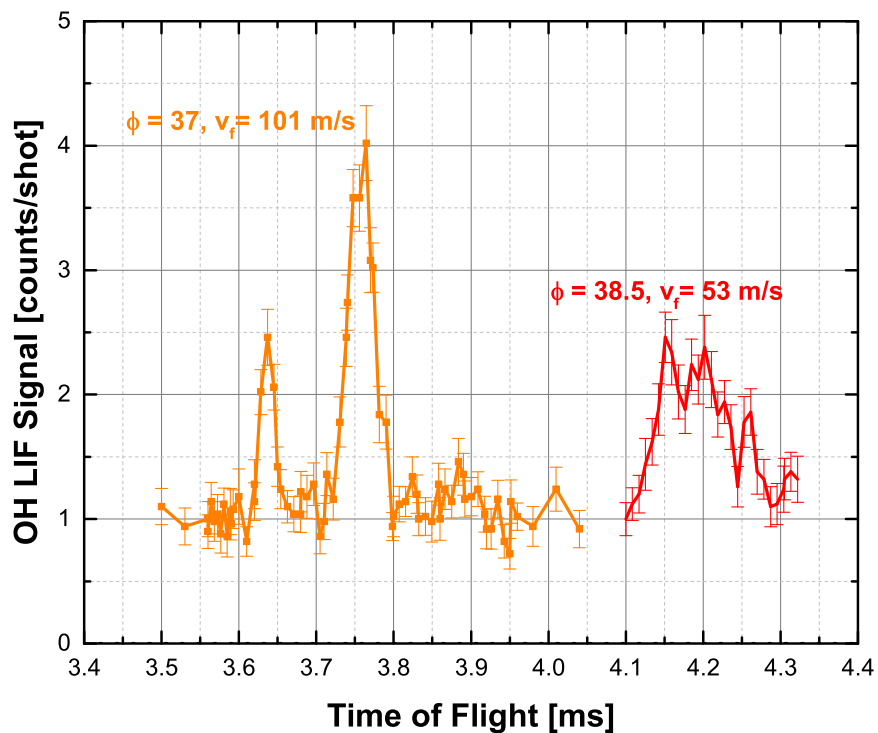


(b)

Figure 4.14: Deceleration of $|1, 1, 1\rangle$ ND_3 molecules. (a) shows the full data set and (b) shows an enlargement of the low velocity data. In both panels, the experimental data are shown in the upper portion and the results of 3D simulations are shown in the lower portion (plotted negative).



(a)



(b)

Figure 4.15: Deceleration of $X^2\Pi_{3/2}, M_J = 3/2$ OH molecules. Initial velocity $u = 436\text{m/s}$ and $T_{\parallel} = 0.95\text{K}$.

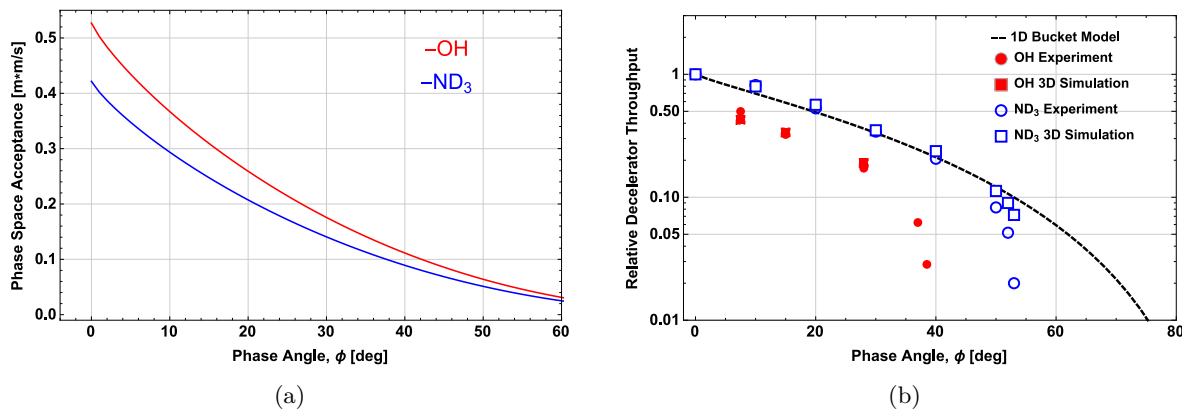


Figure 4.16: Shrinking phase space acceptance vs. phase angle, ϕ . (a) Absolute phase space acceptance for OH and ND₃. The larger phase space acceptance for OH relative to ND₃ molecules is due to the larger Stark shift to mass ratio of OH. (b) Relative phase space acceptance normalized to that at $\phi = 0$. Note the logarithmic vertical scale. The relative phase space acceptance is identical for both molecules (separately normalized). See also, Eq. 4.28

angles. In general, molecules with a larger Stark shift:mass ratio will have larger phase-space acceptances. This is reflected in Fig. 4.16 for OH and ND₃ molecules. The *relative* phase-space area (independently normalized) is the same for any molecular species. This is reflected in the dashed black line in Fig. 4.16b and is referred to as the “1D bucket model”. Agreement with the bucket model is quite good up for ND₃ until final velocities of $\approx 50\text{m/s}$ ($\phi_{OH} \approx 38^\circ$ and $\phi_{ND_3} \approx 55^\circ$) where the second loss mechanism, transverse over focusing [187] takes over. This deviation is reasonably well captured by complete 3D numerical simulations shown as red and blue squares for ND₃ and OH respectively. The overall drop in the throughput for OH (relative to the bucket model) is not well understood, but is present in both the data and 3D numerical simulations. The OH simulations are somewhat preliminary, and at the time of this writing results were not available for $\phi_{OH} \approx 37^\circ$ and $\phi_{OH} \approx 38.5^\circ$.

4.7 Electrostatic Trapping

The ultimate goal of a cold molecule experiment is to create samples of molecules at rest in the lab frame, which can be confined to electromagnetic potential wells. The relatively warm temperatures ($T \sim 1\text{K}$) of molecules produced by direct cooling methods such as Stark deceleration, require traps with similar depths. This can be routinely achieved with either electrostatic [61] [188] [189] and magnetostatic

traps (with permanent magnets) [190]. AC traps [191] [192] have the appeal that they can confine molecules in the absolute ground state [192] but suffer from relatively weak trap depths $\approx 1\text{-}10$ mK [78].

4.7.1 Model Fields for Quadrupole Trap

Analytic expressions for the trapping fields with minima located at $r = 0$ can be expressed in terms of multipole moments [175] [193] [78]. The potential with the steepest field gradient, and thus the most tightly confining, is the quadrupole. To make a pure quadrupole field, all three electrodes are shaped to follow equipotential curves of the analytic quadrupole field. This is the same trap configuration used in original RF ion traps [171]. These traps are composed of a central ring electrode with inner radius, R , and two endcap electrodes located at in axis positions $z' = \pm R/\sqrt{2}$. The analytic expression for the electrical potential in the interior region of the electrodes is [172],

$$\Phi_{quad}(x, y, z) = \Delta V \frac{x^2 + y^2 - 2z^2}{2R^2} \quad (4.38)$$

where R is the inner radius of the ring electrode and ΔV is the potential *difference* applied to the electrodes (i.e., for $\pm 11\text{kV}$ applied to the trap, $\Delta V = 22\text{kV}$). The magnitude of the electric field is then calculated from $\mathbf{E} = -\nabla\Phi$,

$$|\mathbf{E}(\rho, z)|_{quad} = \Delta V \frac{\sqrt{\rho^2 + 4z^2}}{R^2} \quad (4.39)$$

where, $\rho = \sqrt{x^2 + y^2}$ is the radial distance. Thus, $|\mathbf{E}|$ increases linearly from the trap center, reaching a maximum value of $|\mathbf{E}|_{max} = \frac{\Delta V}{R}$ at the trap electrodes. The electric field gradient in the longitudinal direction is larger than in the transverse direction by a factor of 2. Clearly, the electric field maximum, and thus the trap depth and phase-space acceptance, increases with applied voltage, ΔV . Similarly, the field decreases as the electrode separation is increased. Realistic values for applied voltages and spatial dimensions are $\Delta V = 2 \times 11\text{kV}$ and $R \approx 5\text{mm}$, which gives peak fields of $|\mathbf{E}|_{max} = \frac{\Delta V}{R} = 44 \text{ kV/cm}$. The potential depths and gradients of this model trap for ND_3 and OH molecules are summarized in Table 4.2.

Table 4.2: Calculated parameters for a hypothetical perfect quadrupole trap charged to $\Delta V = 2 \times 11kV$, with a single ring electrode of inner radius $R = 5.0mm$ and end cap electrodes at axial positions $z' = R/\sqrt{2}$. Note that the depth is the same in the transverse and longitudinal directions. To facilitate comparison with other types of traps (for instance magnetostatic traps from permanent magnets or optical dipole traps), the depths and associated potential gradients ($\frac{\partial}{\partial z}$ or $\frac{\partial}{\partial \rho}$) are expressed in units of temperature.

Perfect Quadrupole			
	<i>Depth</i>	$\frac{\partial}{\partial \rho}$	$\frac{\partial}{\partial z}$
 E 	44 [kV/cm]	880 [kV/cm ²]	1244 [kV/cm ²]
ND ₃	0.744 [K]	149 [$\frac{mK}{mm}$]	210 [$\frac{mK}{mm}$]
OH	0.996 [K]	199 [$\frac{mK}{mm}$]	281.6 [$\frac{mK}{mm}$]

4.7.2 Trap Design and Loading Strategies

The closed electrode geometry of the pure quadrupole trap does not allow direct access to the trapped molecules. A small hole can be introduced into the trap electrodes to pass a collimated laser beam through it [62] [150] that minimally affects the trapping potentials. However, for our experiments, in which we are also interested in co-locating ultracold Rb atoms for collision experiments, a more extreme modification is required.

To efficiently load magnetically trapped Rb atoms we require a clear aperture of $\sim 5.0mm$. In previous experiments [19] the central ring electrode was split into two distinct ring electrodes (separated by 5.0 mm) so that magnetically trapped ultracold Rb atoms could be loaded from the side (see Fig. 4.17). Additionally, the front electrode electrode had a 2.0mm diameter hole for loading molecules and the back electrode had a 2mm wide slit across it so that the vertical profiles along the trap could be imaged. Both of these modifications significantly reduced the depth and gradient of the trapping potential.

The basic geometry and coordinate system relevant to trapping are shown in Fig. 4.18. The numbering scheme used to label the electrodes is also shown in Fig. 4.18. The two endcaps are formed by electrodes #1 and #4. The role of the ring electrode is filled by electrodes #2 and #3. z_1 is the distance from the center of the last electrode pair and the outside surface of the first electrode #1. The trap center is located at $z_1 + z_2$. ΔL is the remaining distance the molecules travel within the decelerator from the moment the last stage turns off. It is given by,

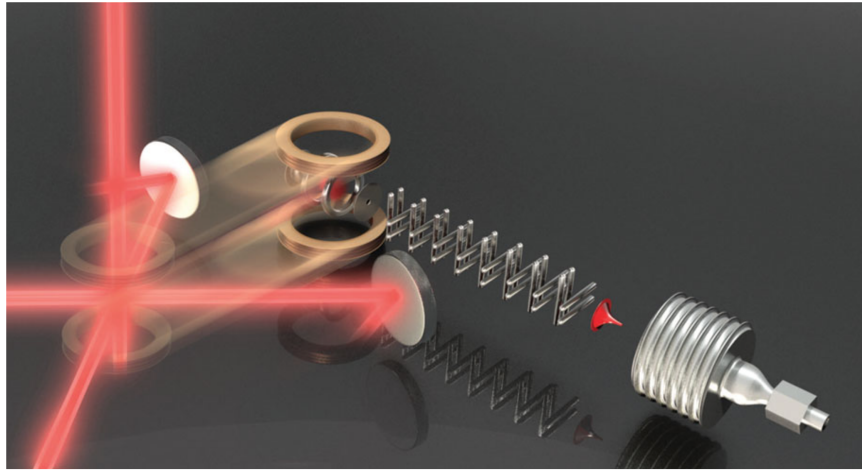


Figure 4.17: Cartoon depicting the sequence for co-trapping cold ND_3 molecules with ultracold Rb atoms. To facilitate loading Rb into the central trapping region, the ring electrode was split into two distinct electrodes separated by 5.0mm. Figure from [19].

$$\Delta L = L - L/2 - L \frac{\phi_0}{180} \quad (4.40)$$

For phase angles of $\phi \approx 55^\circ$ this extra distance is $\Delta L \approx 1.06\text{mm}$.

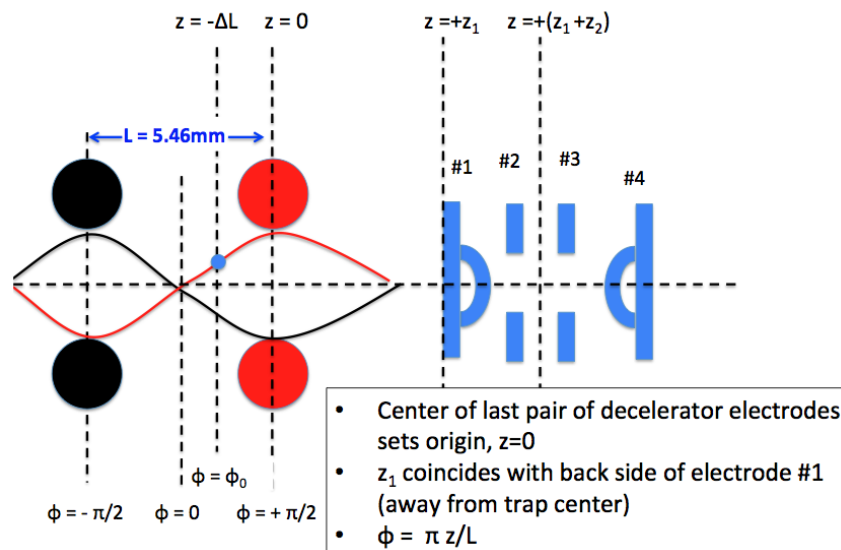


Figure 4.18: Definition of distances relevant to trap loading.

The two primary areas considered in optimization of the trap were 1) enlarging the initial loading aperture to prevent “irising” of incoming molecules, and, 2) moving the two ring electrodes closer together

(and thus also the two endcap electrodes) to increase the strength of the trapping potential. Moving the electrodes closer together meant that an alternative strategy to “side-loading” of Rb must be considered. The solution we chose was to load Rb atoms through a hole drilled in the back electrode. (Electrode #4 would still contain a slit). An additional limitation of the trap used for the Rb-ND₃ experiment [19] was the relatively small electric potential applied to the trap electrodes ($\pm 8kV$). In the end, careful polishing of each of the titanium electrodes allowed the applied voltage to be increased to $\pm 11kV$ with virtually no current draw.

To weigh the relative advantages and disadvantages of a given trap modification, it is crucial to understand the phase-space distributions at the exit of the decelerator. The details of the distribution will depend on the specific phase angle and the final velocity of the decelerated molecules. However, for the range of final velocities that can be loaded into a trap, the widths characterizing the distributions do not vary widely. As such, the phase-space distributions of an ND₃ beam decelerated from $v_i = 415 \text{ m/s}$ to $v_f = 27.6 \text{ m/s}$ ($\phi = 55.1783^\circ$), shown in Fig. 4.19, can be taken as representative values to make rough estimates of the trap loading process. The probability density of all 6 degrees of freedom, obtained by integrating over the conjugate coordinate, are overlaid in gray on each axis. In each case, the distribution can be reasonably described by a Gaussian function with the width indicated in Fig. 4.19. These widths will be important for rough estimates of trap loading, since we can use the results that $\approx 76\%$ (98%) of the molecules are within one (two) FWHM.

Simultaneously with optimization of the trap depth and gradient, one must also consider the loading strategy to be used. From the general principles outlined in Sec. 4.2, the ideal trapping scenario consists of an ensemble of molecules with zero average velocity that are spatially distributed symmetrically about the trap center. If the molecules are loaded into the potential well with a finite velocity, v_0 , such that the $\frac{1}{2}mv_0^2$ is less than the trap depth, the molecules will remain trapped but will subsequently not be located, on average, at the center of the trap. Instead they will orbit around the edges of the trap. Consequently, decelerating all the way to $v_f \approx 0$ will not be successful since these molecules will not actually make it out of the decelerator and into the trap.

Trapping molecules with zero average velocity in the trap center, thus requires that the trap itself

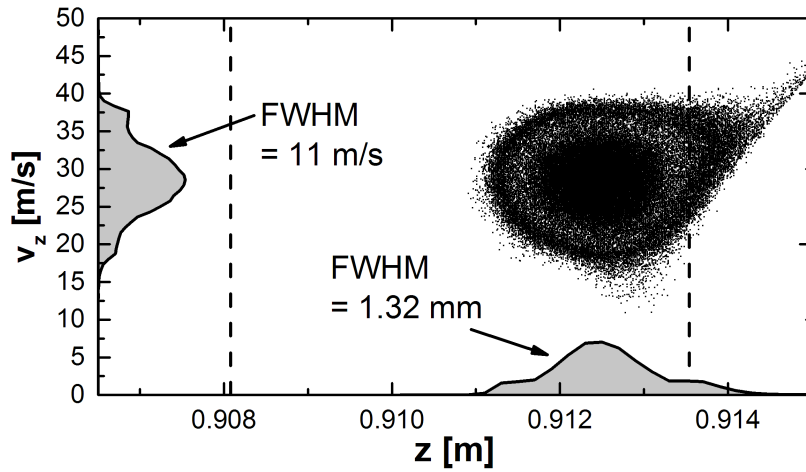
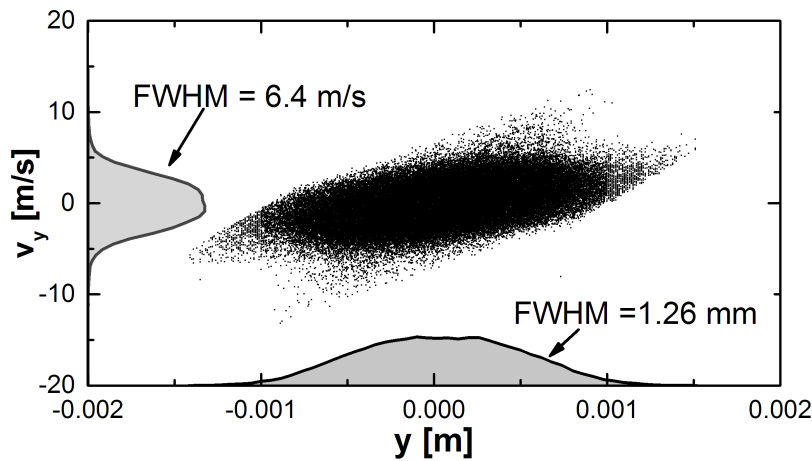
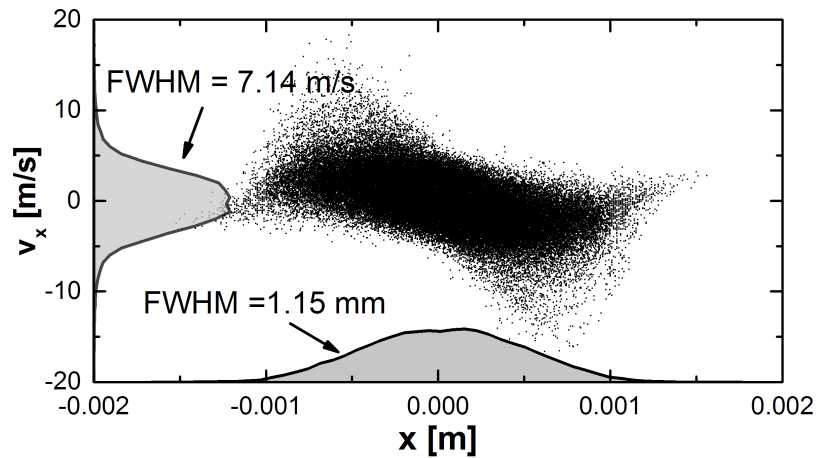
(a) Longitudinal (z)(b) Transverse (y)(c) Transverse (x)

Figure 4.19: Simulated phase-space distributions of an ND_3 beam decelerated from 415 m/s to 27.6 m/s ($\phi = 55.1783^\circ$) at the moment the decelerator turns off. Panel (a) shows the distribution for the longitudinal coordinate, z . Locations of the rod pairs are indicated by dashed vertical lines. (b) and (c) show the distributions in the transverse directions (y and x). In each panel, the probability density for the spatial coordinate and conjugate velocity are overlaid in gray on the respective axis.

serve as the final deceleration stage. The basic idea is to configure a “loading” stage, such that the molecules come to rest at the location of the trap potential minima, and then to quickly switch the configuration to trapping. The different electrode configurations for loading and trapping are shown in Fig. 4.20. The different voltages applied to trap electrodes are indicated in Fig. 4.20a, and a qualitative depiction of the form of the the potentials that can be used to remove energy are shown in Fig. 4.20b.

If only potentials ΔV_2 and ΔV_3 are used, the scheme is referred to as “two hill” trapping. The configuration where the potential energies ΔV_1 , ΔV_2 , and ΔV_3 are used is referred to as “three hill” trapping. The third potential hill (ΔV_1) is formed between trap electrode #1 and the grounded decelerator rods. Significant time and effort were spent investigating the possibility of using this extra barrier to remove energy (which had not been used previously [19]). A summary of the potential heights formed for the trap used in the final design for both ND_3 and OH is given in Table 4.3 in Sec. 4.7.3.

To estimate any “irising” effects molecules in the wings of the distribution experience upon loading, we can estimate the transverse spatial spread as a function of longitudinal distance as

$$\begin{aligned}\Delta x^2 &= \Delta x_0^2 + (\Delta v_x t_f)^2 \\ &= \Delta x_0^2 + \left(\Delta v_x \frac{d}{v_z} \right)^2\end{aligned}\tag{4.41}$$

where $t_f = \frac{d}{v_z}$ is the flight time of the synchronous molecule from the moment the Stark decelerator turns off until it reaches a point downstream a distance d away. Estimates for the transverse and longitudinal spatial spread for trappable velocities are plotted in Figs. 4.21a and 4.21b for the case of zero applied field. Clearly, loading a fast packet has the advantage that it arrives at the trap center faster, and thus has less time to spread out. The basic results shown in Fig. 4.21a and 4.21b can be used to make estimates of the gains that can be had by increasing the diameter initial loading aperture for the “two hill” trapping sequence. The velocities that can be stopped with this scheme are close to $\approx 25\text{m/s}$. Based on the calculations shown in Fig. 4.21a, it appears that large gains can be had by increasing the diameter of the loading aperture from $2.0 \rightarrow 3.0\text{mm}$. Going from, $3.0 \rightarrow 4.0\text{mm}$ should pass still more molecules, but the relative gains are not as great.

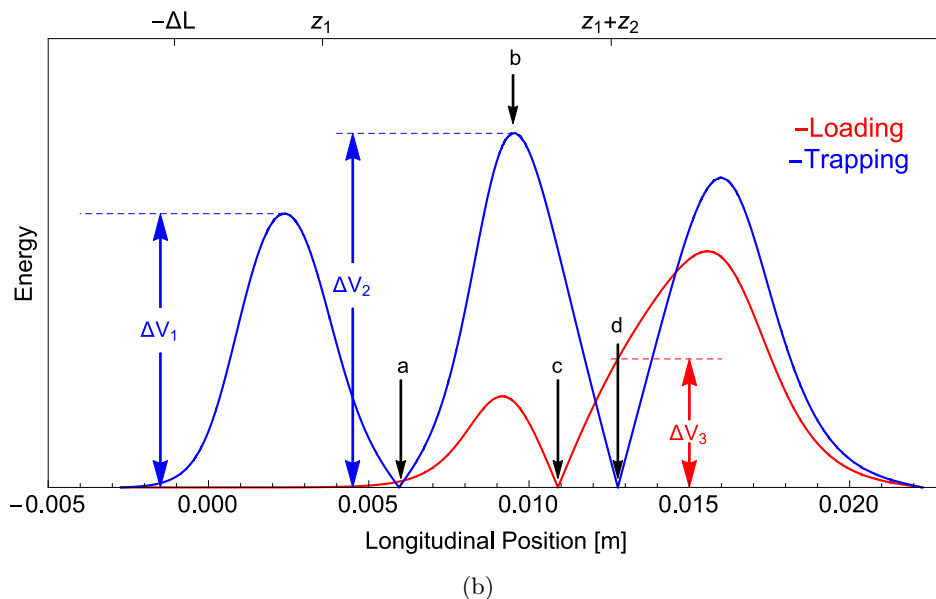
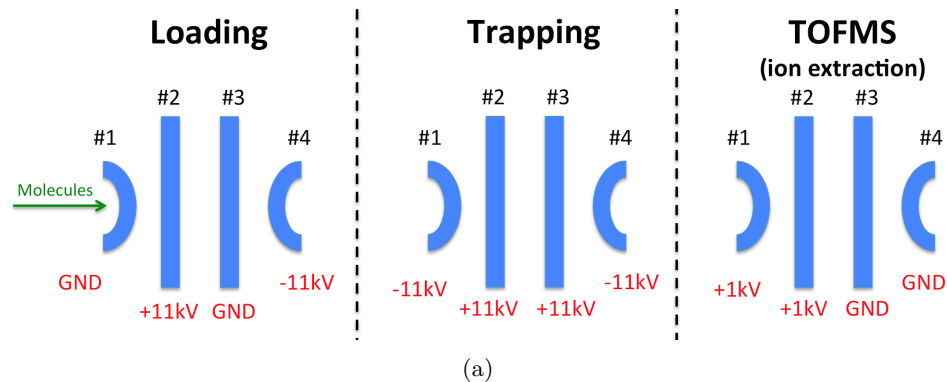


Figure 4.20: (a) Voltages applied to trap electrodes in different configurations and (b) general form of the potentials formed in the trapping and loading configurations.

Numerical simulations of trap loading efficiency for different loading aperture diameters, longitudinal gaps, and trap loading sequences are shown in Fig. 4.22. The different trap geometries are labeled with a series of three numbers: the first is the diameter of the loading aperture in mm, the second is the separation of the two ring electrodes in mm, and the third is the diameter of the new hole drilled in the back electrode (#4) to facilitate loading of Rb. For example, “435” (the trap design we eventually settled on) corresponds to a 4 mm loading diameter, a 3 mm longitudinal gap, and 5 mm diameter hole to load Rb. The trap configuration used in Ref [19] had only a slit cut into electrode #4 and is labeled with a zero for the last

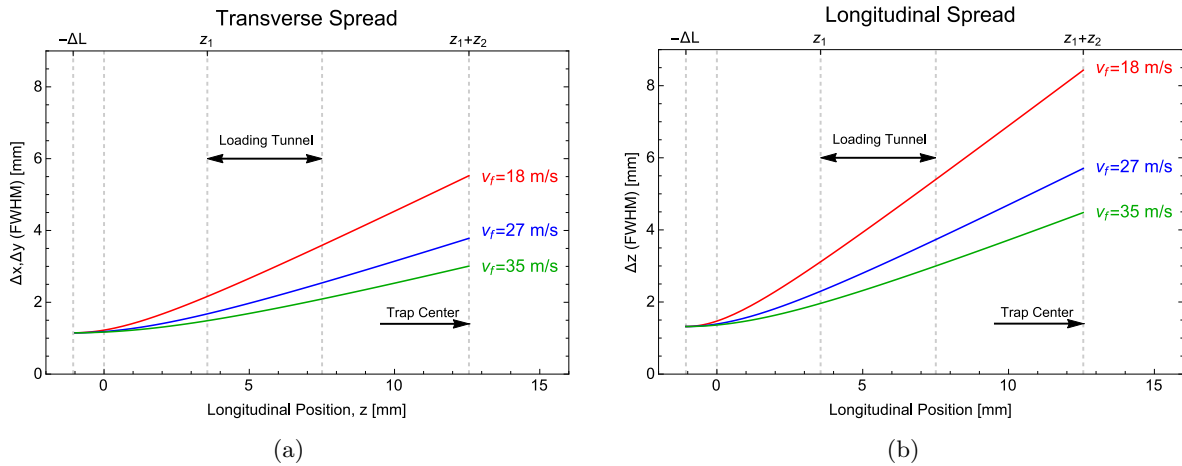


Figure 4.21: Position spreads of slow ND_3 packets if they were allowed to free flight to trap center. Note that the widths given here are the full widths at half max (FWHM) and not the half-width (1-sided). The horizontal axis has zero corresponding to the center of the last rod pair in the decelerator.

number (this trap is 250). In the two panels of Fig. 4.22, the percent of molecules remaining in the simulation, are plotted in Fig. 4.22a (Fig. 4.22b) as a function of the position (velocity) of the synchronous molecule for which the loading sequence was designed.

The simulation results in Fig. 4.22 are colored in a suggestive way. Visually, configurations are grouped into pairs according to the nearest neighbor (most similar curves) and plotted with similar colors. For instance, for the simulations of the 4mm aperture and 3 hill sequence, “reddish” colors are used. If we look at the data during the loading tunnel, the results for different trap configurations with the same loading diameter are essentially the same. As can be seen by comparing the different diameters, we obtain a $\sim 3\text{-}4\times$ increase in the number of molecules passing through the first electrode by increasing the loading diameter from $2.0 \rightarrow 4.0\text{mm}$.

The difference between the $4x5\text{-}3$ Hill (red) and the $4x5\text{-}2$ Hill (green) results can be attributed to the basic idea presented in Fig. 4.21. Due to the higher velocity in the 3 hill scheme, the transverse position spread at tunnel (and thus the loss) is smaller due to the packet having had less time to diverge. The difference in the $4x5\text{-}3$ Hill (red) and the $3x5\text{-}3$ Hill (blue) curves is due to irisring. This confirms the basic idea presented earlier that a fast packet loaded through a large aperture is the ideal scenario.

After the initial loading (passing through the tunnel) the loss is determined by the loading scheme

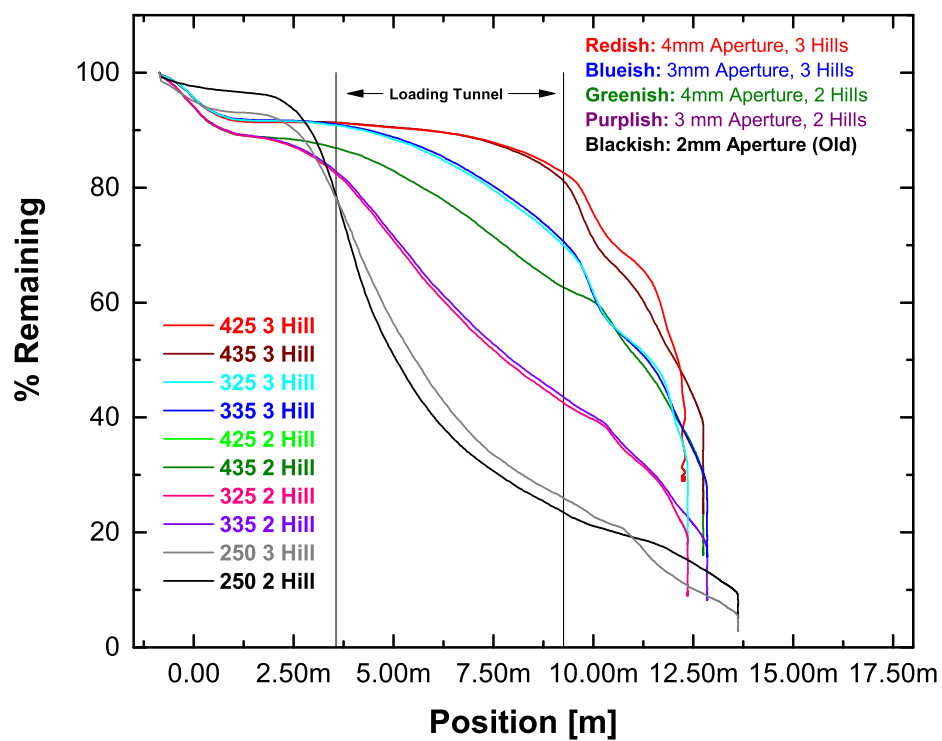
used. To investigate these data, it is useful to look at the data plotted versus velocity (Fig. 4.22b). The sharp falloffs that occur at a single velocity here, happen in a region where the synchronous molecule is in a force-free region but in the wings of the distribution, find themselves in unbound regions of the potential and are lost. Unfortunately, most of the big gains obtained by increasing the loading aperture “wash out” during the final trapping stage. At the end of the each trapping sequence, the “cliff jumpers” are due to high loss at the trap center at the moment the final trap configuration is switched on. By looking at the loss versus velocity graph (Fig. 4.22b), it is clear that at each stair case is corresponds to the next “slowing stage” of the trap loading process. Molecules that are outside of the phase space acceptance at this final trapping stage spill over the top of the trapping potential. Basically, we trap the small fraction of molecules that are in our phase space acceptance and throw everything else away.

4.7.3 Experimental Results of Trap Optimzation

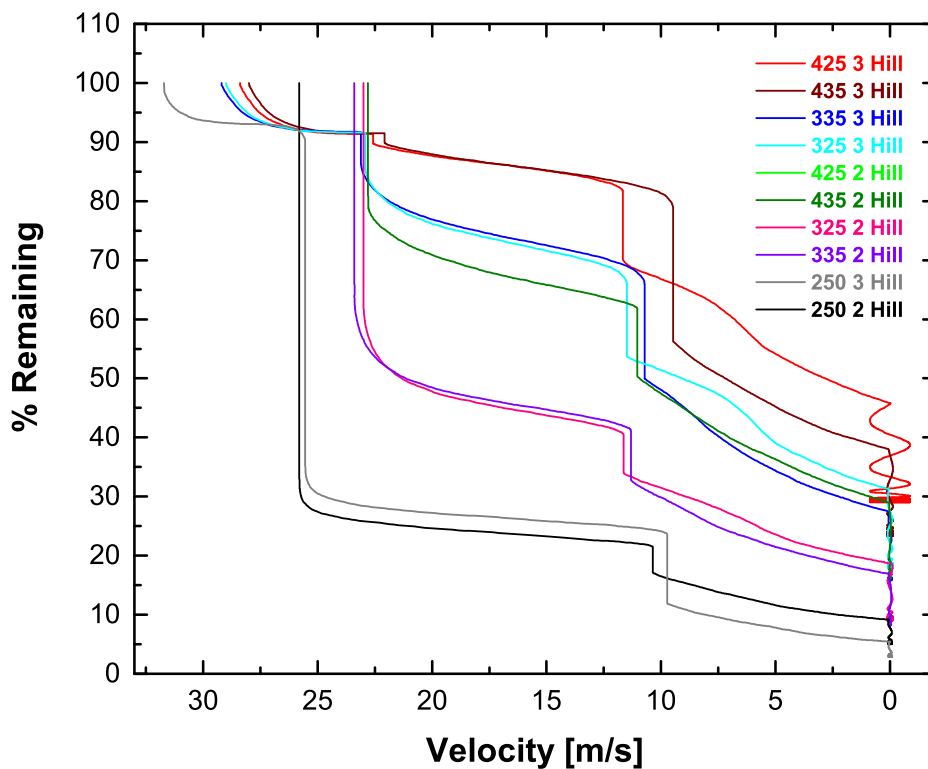
Based on the numerical simulations shown in Fig. 4.22, we chose the 435 configuration. The 425 configuration trapped a slightly larger number of molecules but the added complication of aligning a high peak power UV dye laser through a 2mm gap, was deemed to outweigh this small advantage. A CAD drawing of the final trap is shown in Fig. 4.24a and the calculated electric fields of this trap are shown in Fig. 4.23b. The calculated fields for the 435 trap are compared to those from the analogous “perfect” quadrupole. The reduction in the field strength (depth and gradient) in our actual trap is a result of the removal of electrode surfaces to admit laser beams and Rb molecules. The electric field properties of the original trap design (250) and the final design (435) are summarized in Fig. 4.23.

The separatrices for ND_3 and OH molecules confined in the trapping potentials formed by this trap when charged to $\pm 11\text{kV}$ are shown in Fig. 4.25. The potential heights defined in Fig.4.20b are summarized in Table 4.3 for ND_3 and OH molecules. The corresponding required final velocities and phase angles required for trap loading are given in Table 4.4. A simplified electrical circuit used to hook up the trap electrodes is shown in Fig. 4.24b.

Experimental data on the results of the trap loading optimizations are shown in Fig. 4.26, Fig. 4.27, and Fig. 4.28. The equivalence between two-hill and three-hill trapping sequences is confirmed by the data



(a)



(b)

Figure 4.22: Simulations of different trap configurations and loading strategies used in the trap optimization process. The two panels plot the survival fraction as a function of the position (a) and velocity (b) of the synchronous molecule for which the sequence was designed. The longitudinal oscillations seen in the red trace (425, 3 Hill) were caused by a slight error in the timing sequence that caused the synchronous molecule to be trapped with a nonzero average velocity.

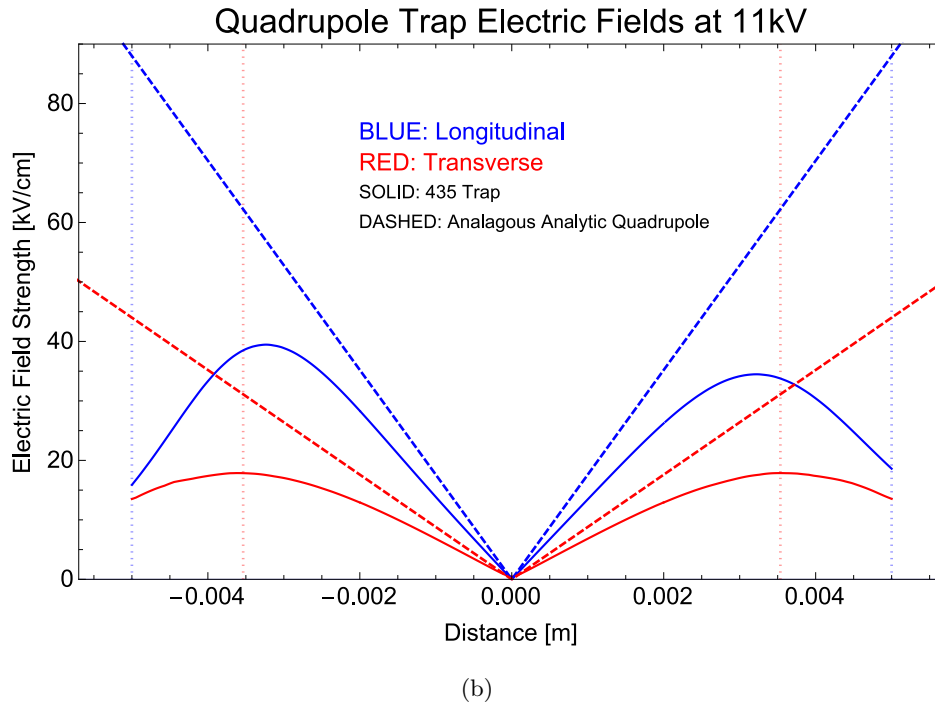
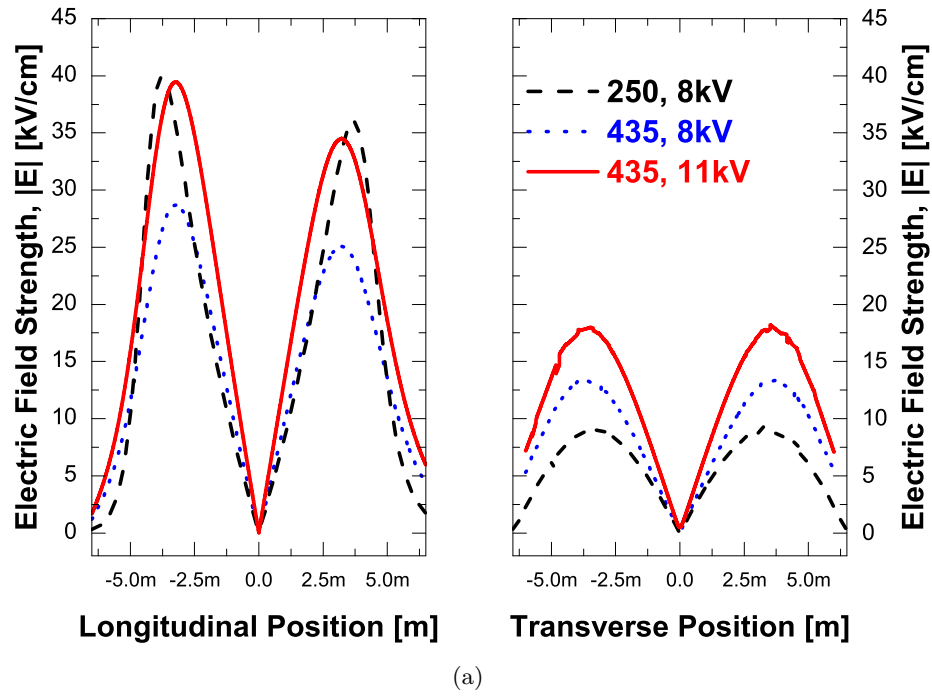
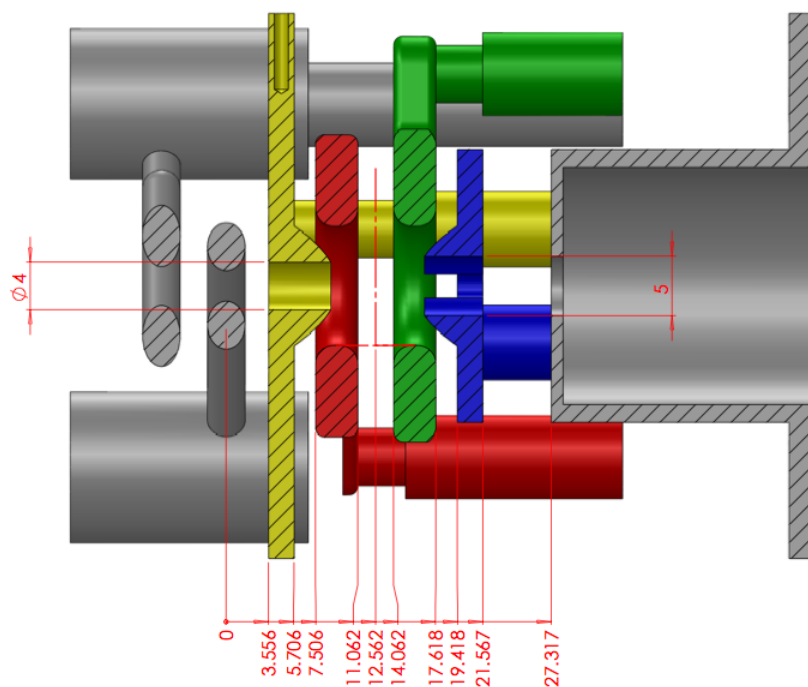
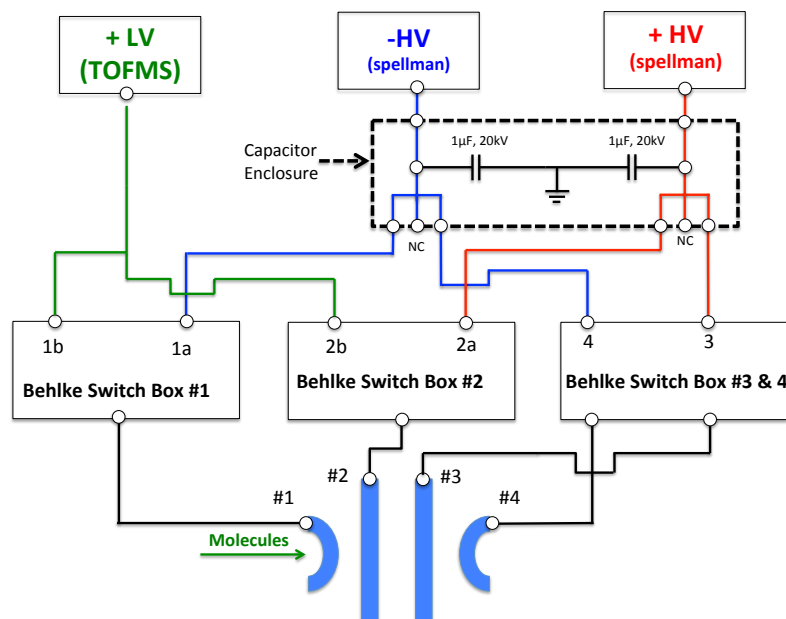


Figure 4.23: (a) Comparison of generated electric fields at 8kV and 11kV of original (250) and modified (435) trap. (b) Electric fields in our electrostatic trap. The calculation for the analogous analytic quadrupole trap assumes $R = 0.005$ and that the endcaps are separated by $2R/\sqrt{2} \approx 7.07\text{mm}$. In the actual configuration, the separation is $\approx 7.8\text{mm}$.



(a)



(b)

Figure 4.24: (a) CAD drawing of the final design of our 435 electrostatic quadrupole-like trap. (b) Electric fields in our electrostatic trap. The calculation for the analogous analytic quadrupole trap assumes $R = 0.005$ and that the endcaps are separated by $2R/\sqrt{2} \approx 7.07\text{mm}$. In the actual configuration, the separation is $\approx 7.8\text{mm}$. (b) Simplified electrical circuit diagram used to hook up the electrostatic trap. The setup is slightly more complicated than that used for the pulsed decelerator due to the requirement of have two distinct HV configurations for trap loading (“Trapping” and “Loading”) as well as a configuration required for extracting ions from the trap. Under typical operating conditions, the $|HV| = 11\text{kV}$ and $LV = 1\text{kV}$.

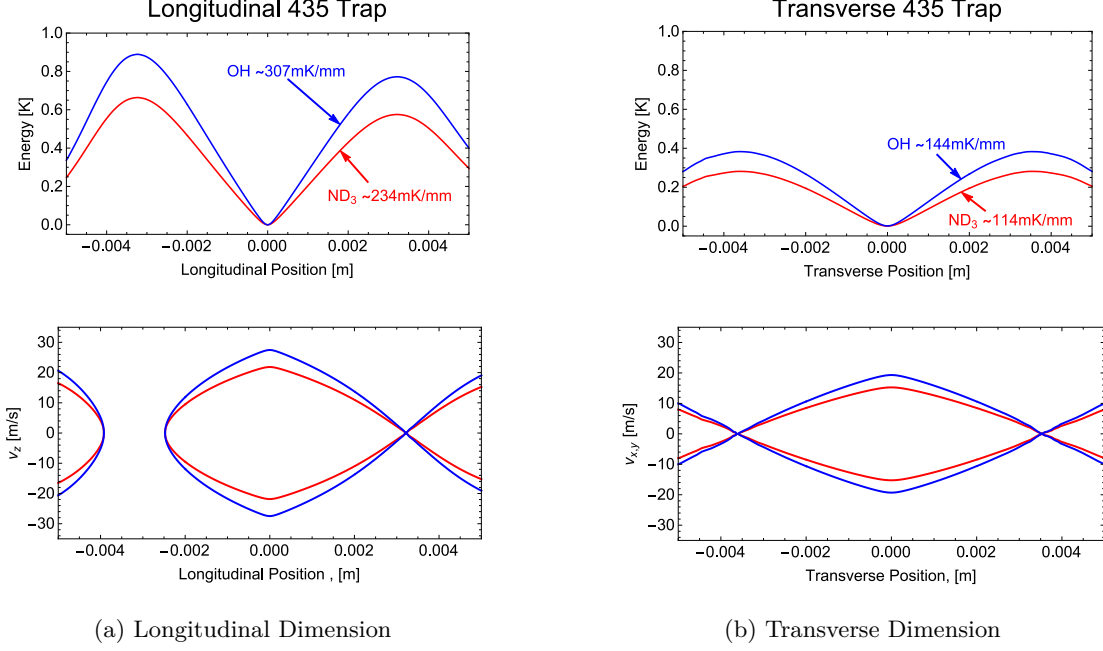


Figure 4.25: Longitudinal and transverse potentials and separatrices for our 435 trap charged to $\pm 11kV$. The smaller hump in the longitudinal dimension occurs at 3.225mm. The max in the transverse direction occurs at 3.528mm.

Table 4.3: 435 Trap Parameters for Nominal Voltage of 11kV

	$\Delta V_1 [K]$	$\Delta V_2 [K]$	$\Delta V_3 [K]$	$\Delta V_2 + \Delta V_3 [K]$	$\Delta V_1 + \Delta V_2 + \Delta V_3 [K]$
<i>OH</i>	0.676	0.889	0.300	1.189	1.865
<i>ND₃</i>	0.503	0.664	0.219	0.883	1.385

shown in Fig. 4.26. Typical trap loading performance for the optimized trap is shown in Fig. 4.27. By trapping the center (position and velocity) of the molecular ensemble distribution at rest in the center of

Table 4.4: Summary of decelerator parameters for coupling to 435 Trap at 11kV. The calculation for the required phase angle assumes an ND₃ with an initial velocity of 415m/s and an OH beam with $v_i = 436m/s$. The first phase angle is for $n = 149$ stages and the second number in parentheses is for $n = 148$ stages. The choice between these is determined by whether or not the first deceleration stage with only *two* pairs of electrodes is used. (See discussion in Sec. 4.4.)

	Two Hill		Three Hill	
	$v_f^{max} [m/s]$	$\phi [deg]$	$v_f^{max} [m/s]$	$\phi [deg]$
OH	34.10	38.8314 (39.0891)	42.70	38.6981 (38.9549)
ND ₃	27.06	55.1884 (55.5868)	33.90	55.0455 (55.4423)

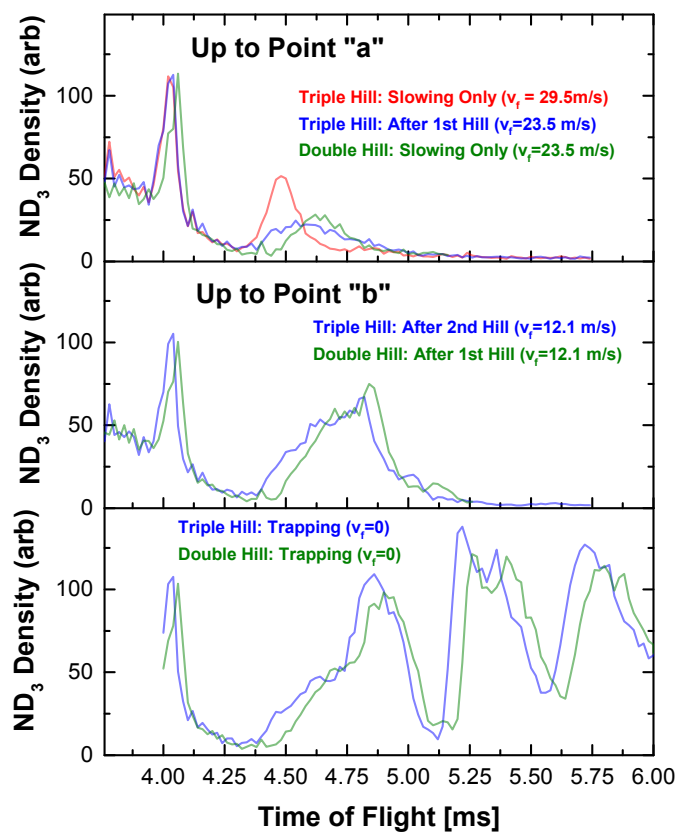


Figure 4.26: Comparison of “two hill” and “three hill” trap loading schemes for the 435 Trap charged to $\pm 8kV$. The top panel is three different scenarios to for sequence progressions to point “a”. The “peaked” red curve in the top panel, has the same is faster than the other two packets and has correspondingly had less time to spread out.

the trap, the longitudinal oscillations are minimized. Fig. 4.28a show the nearly linear increase in trapped molecular signal as a function of increase bias voltage (emphasizing the importance of working at as large a trap depth as possible). The observed transverse spatial distribution of trapped molecules with a FWHM of 1.48mm shown in Fig. 4.28b are consistent with an effective sample temperature of 168mK, based on the separatrices shown in Fig. 4.25.

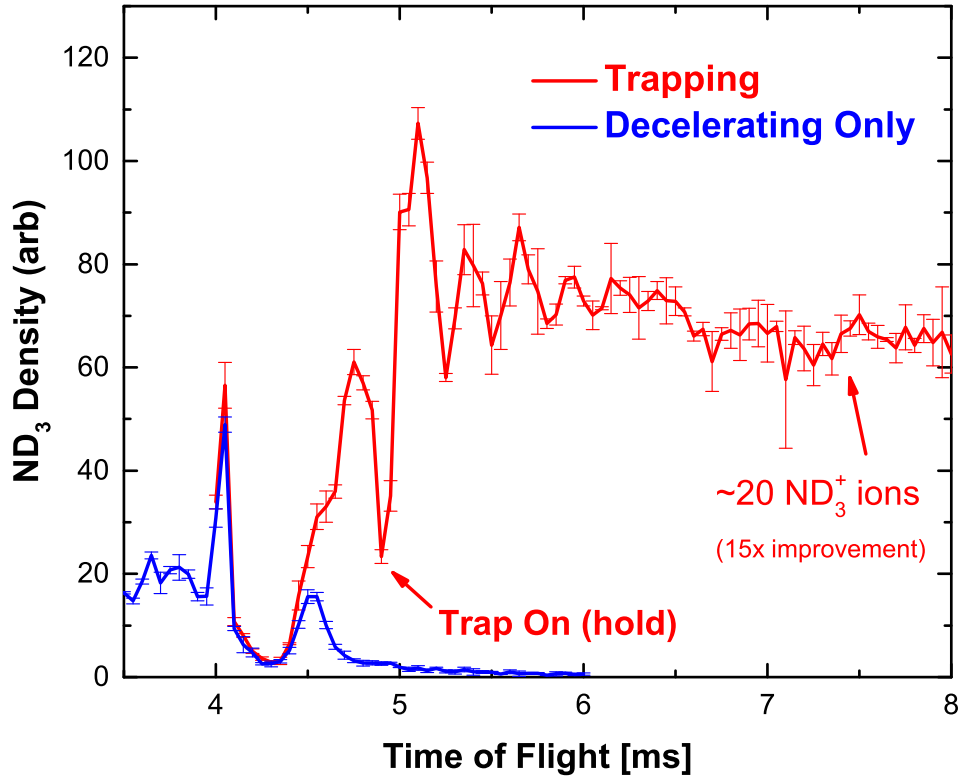


Figure 4.27: ND₃ 2Hill 11kV Trap Loading Data

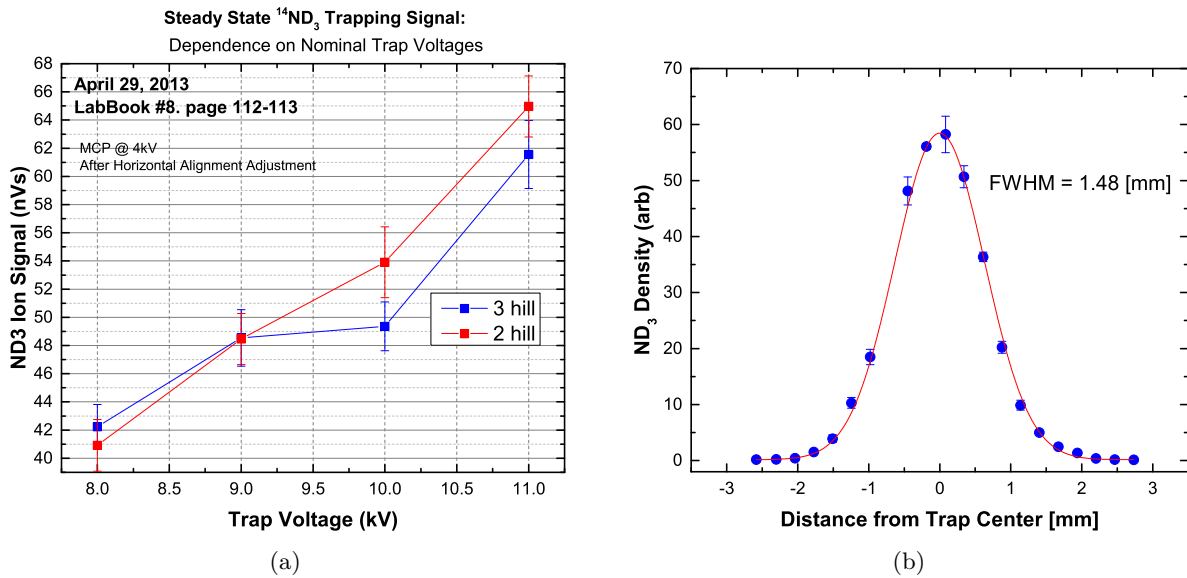


Figure 4.28: ND₃ Trapping.

118nm Generation

5.1 Introduction

Vacuum ultraviolet (VUV) light sources [22] [194] [195] have important applications in a wide variety of atomic physics and physical chemistry experiments. Examples include molecular spectroscopy for the elucidation of the nature of chemical bonds [196] [197] as well as high resolution studies [198] [199] [200] with fascinating possibilities for metrology [201] [202]. Additional applications include their use as a universal ionization source in mass spectrometry. Universal photoionization methods using VUV [197] light have been shown to be much more efficient at ionizing molecules than direct electron impact ionization (on a per-photon to per-electron basis).

Very high fluxes of VUV light are available from synchrotrons, but the complexity (and inconvenience) of these sources makes tabletop VUV sources very desirable. With the exception of Excimer lasers, which operate at only a few wavelengths, tabletop sources of VUV light must resort to nonlinear techniques. Nonlinear optical frequency mixing [203] [204] [205], of which harmonic generation is a special case, is a powerful technique for producing coherent radiation at wavelengths where traditional laser sources do not operate. The generated light originates from a nonlinear polarization, which is induced in the presence of intense optical electric fields. For nonlinear frequency mixing with *ns*-pulsed lasers, where the peak intensity is $< 10^{13} \text{ W/cm}^2$, a perturbative treatment of the nonlinear susceptibility is appropriate. Expanding the polarization in powers of the electric field E gives

$$\mathbf{P}(t) = \epsilon_0[\chi^{(1)}\mathbf{E}(t) + \chi^{(2)}\mathbf{E}^2(t) + \chi^{(3)}\mathbf{E}^3(t) + \dots] \quad (5.1)$$

where ϵ_0 is the permittivity of free space and $\chi^{(n)}$ is the macroscopic n^{th} -order nonlinear susceptibility. The nonlinear terms in Eq. 5.1, $P^{(NL)} = \epsilon_0[\chi^{(2)}\mathbf{E}^2(t) + \chi^{(3)}\mathbf{E}^3(t) + \dots]$, become a source term in the nonlinear wave equation, which can be interpreted as oscillators radiating into a medium of refractive index, $n = \sqrt{1 + \chi^{(1)}}$.

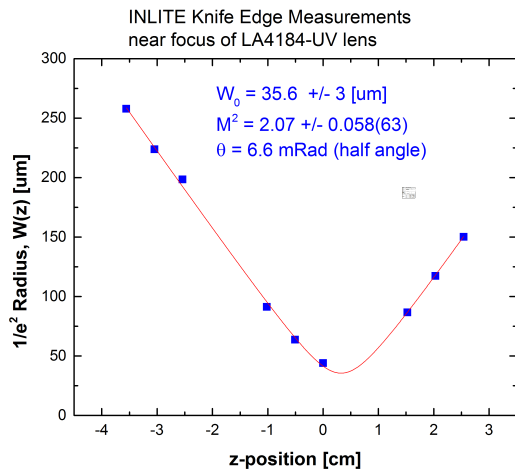
Anisotropic crystals with very large second-order nonlinear optical susceptibilities ($\chi^{(2)}$) and a wide optical transparency range (such as β -barium borate, BBO, and potassium dihydrogen phosphate, KDP) can be very efficient at producing visible, near-infrared, and soft UV, light with efficiencies as high as $\eta \approx 30\text{-}40\%$ in favorable cases [206] [207]. The short wavelength cutoff for generation of light by second-order nonlinear processes in these crystals is around 200 nm, below which all known nonlinear crystals are opaque. Thus, the generation of vacuum ultraviolet (VUV: $\lambda \approx 200\text{-}100$ nm) and extreme ultraviolet (XUV: $\lambda \leq 100$ nm) light via nonlinear optical frequency mixing generally requires gaseous nonlinear media. The distinction between VUV and XUV is somewhat elastic, but generally XUV is reserved for the windowless region below 100 nm where no transparent optical materials exist. The structural symmetry of isotropic media such as gases means that only odd-order nonlinear susceptibilities are non-vanishing [208], leaving the third-order, $\chi^{(3)}$, as the first nonzero term. Thus, one of the most important applications of $\chi^{(3)}$ nonlinear interactions is the generation of VUV radiation in gases.

5.2 Experimental Setup for Third-Harmonic Generation

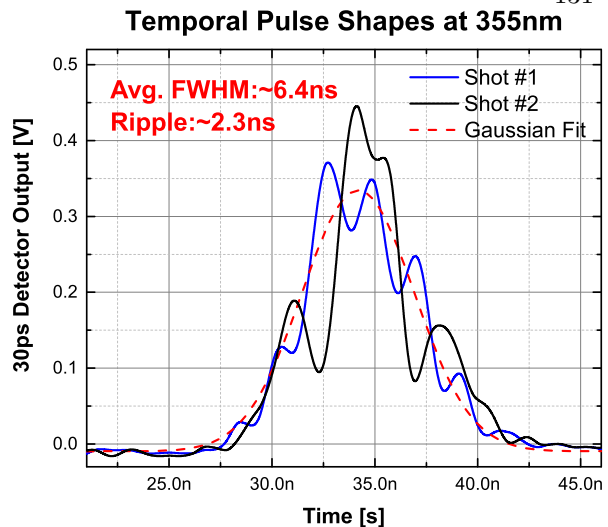
This section describes the experimental apparatus used to generate the VUV light. Different strategies/experimental setups for the production of VUV light with ns-pulsed lasers has been reported in several places [209] [210] [211] [212] [213] [214].

5.2.1 355 nm Laser

The light used for the experiments described here is derived from a Q-Switched industrial Nd:YAG (fundamental at 1064 nm) laser designed for large peak powers (Continuum: Inlite III-10). Light at the third harmonic (355 nm) is generated by $\chi^{(2)}$ interactions in two sequential nonlinear crystals. The large-diameter



(a)



(b)

Figure 5.1: Measurements of the 355 nm Laser. (a) Knife edge measurements of the spatial profile of the 355 nm beam when focused by a $f = 48.3$ cm lens (focal length measured at 355 nm). The divergence angle of $\theta \approx 6.6$ mRad indicates an underlying Gaussian beam with a confocal parameter of $b \approx 1.08$ cm. (b) Measurements of the temporal pulse shape with a $\tau_{rise} = 30$ ps photodetector (Newport, Model D-30) and a 1GHz oscilloscope.

gain media employed to realize these high-energy pulses supports oscillation on multiple transverse spatial modes. Without a seed laser, these modes will not have a fixed phase relationship, so that the output pulse consists of an incoherent superposition of many transverse spatial modes oscillating on different longitudinal modes. This incoherence is evident in the fairly erratic temporal pulse profiles shown in Fig. 5.1b. The average pulse duration is approximately, $\Delta t_{FWHM} \approx 6.5$ ns but shows significant ripple of 2.5 ns, implying a beat frequency of 400 MHz. Neglecting the refractive index of the YAG rod, this value is in reasonable agreement with the longitudinal mode spacing for the 55 cm cavity ($f_{sr} = c/2L \approx 273$ MHz). Lack of coherence in the spatial mode shows up as fast oscillations (hot spots) across the transverse mode.

Despite the lack of coherence, all of the modes oscillate in the same laser cavity; thus the geometrical cavity parameters of the lowest order mode will also serve to characterize the higher order modes [215]. The laser has an unstable resonator with a flat end mirror and a Gaussian variable reflectivity mirror (VRM) as an output coupler with a radius of curvature of ~ 197 cm. The measured far field diffraction half angle of $\theta_{1/e} \approx 0.2$ mRad indicates an underlying beam waist of $w_0 = \frac{\lambda}{\pi\theta_{1/e}} = 564$ μm and a confocal parameter of

$b = 2z_R = 563$ cm. These values are in reasonable agreement with ABCD matrix calculations of the cavity mode at 1064 nm for these geometrical cavity parameters ($w_0 = 547$ μm , located at the flat mirror).

Fig. 5.1a shows knife edge measurements of the beam spatial profile when focused by a $f = 48.3$ cm lens. This lens was used for the majority of the data presented in later in this chapter. The measured effective $1/e^2$ radius is $w_f \approx 35.6$ μm and a divergence half-angle of 6.6 mRad ($M^2 \approx 2.07$). This divergence angle indicates an underlying gaussian beam waist of $w_0 \approx 25.6$ μm ($b \approx 1.08$ cm). Neglecting any nonlinear effects such as self-focusing, we can expect that a peak intensity for a 6.5ns pulse focused to a beam waist of $w_f \approx 35.6\mu\text{m}$ has a peak intensity of $I_{pk} = \frac{\Delta E}{\Delta t \times \pi w_f^2} = 3.9 \times 10^9$ W/cm² per mJ.

5.2.2 Xe/Ar Cell

The xenon/argon cell is made of standard 304 SS conflat vacuum parts with an overall length of $\approx 40\text{cm}$. The Xe/Ar cell is sealed on the input end by a high-quality UV fused silica window. The output side is sealed with a MgF₂ lens, which separates the Xe/Ar generation cell from the rest of the vacuum chamber.

5.2.2.1 Xe/Ar Convective Mixing Cell

The small spatial extent of the generating regions requires gas mixtures (with homogeneity/ to be homogeneous) on a length scale $\ll b$. In the absence of thermal convection currents or turbulence upon adding gas, mixing will occur by diffusion alone (which can be very/unintuitively slow). Even a relatively "dilute gas" of 1-1000 Torr is surprisingly congested. Taking xenon and argon to have the same nominal diameter of $\sim 0.5\text{\AA}$, the hard sphere collision cross section is given by, $\sigma_{hs} = \pi(r_a + r_b)^2 = \pi d^2 \approx 8 \times 10^{-17}$ cm². The mean free path at 100 Torr is only ≈ 40 μm . In this limit, the time required for homogeneous mixing over the length of the cell can be estimated by finding the time required to travel an RMS distance of $L = 40\text{cm}$, which turns out to be $\sim 24\text{hours}$. This surprisingly long time required for mixing can lead to very large errors in measurements for the optimum pressure ratios. (See, for instance, the erratum of Ref [216].) In our experimental setup, gas mixing was facilitated by a fast mixing turbine (qty=4, $2 \times 1[\text{cm}^2]$, $\sim 1\text{kHz}$) and by introducing large temperature gradients via a cold slush bath at -40°C to drive convection currents.

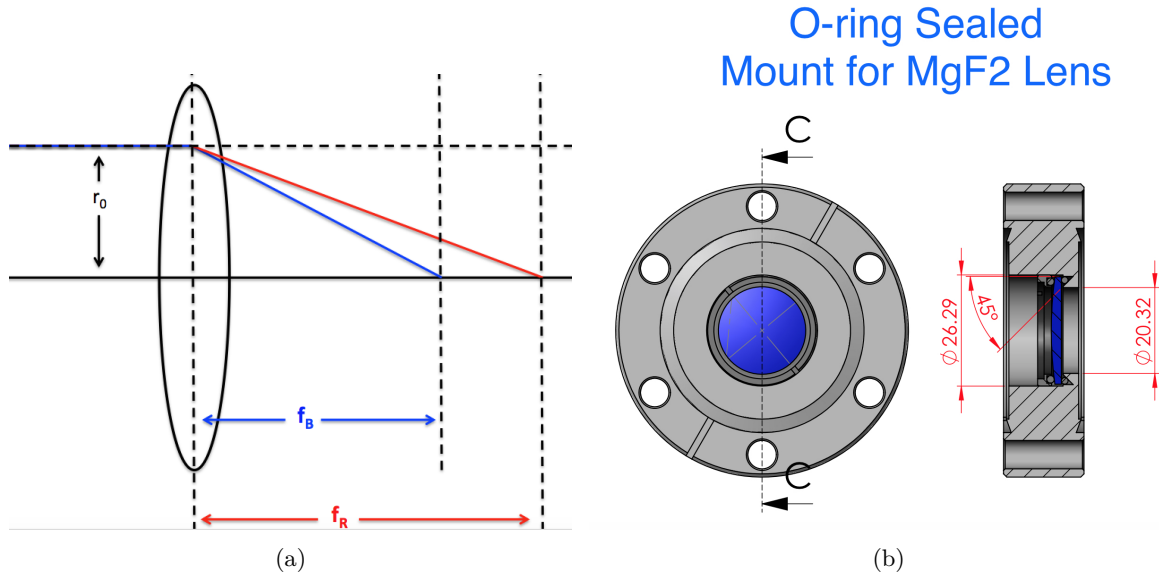


Figure 5.2: MgF₂ lens used as output window of Xe/Ar cell. (a) Spatial separation of beams due to very different focal lengths for red (f_R) and blue (f_B) light. (b) A 0-20 O-ring is used in the V-shaped groove. Lens tube threads not shown.

5.2.3 MgF₂ Lens Holder

There are few optical materials that can be used for lenses and windows in the VUV spectral region. Magnesium Fluoride (MgF₂) and Lithium Fluoride (LiF) have the deepest UV transparency cutoffs: at 115 nm, and 105 nm, respectively. While LiF has higher transmission near 118 nm (than MgF₂), MgF₂'s mechanical hardness and durability, resistance to forming color centers in the VUV [217], [218], and hydrophobic properties make it the preferred material for light near 118 nm. The transmission of MgF₂ near 118 nm has been measured to be $\approx 40\%$ for a 3 mm thick sample [218], which is very nearly the center thickness of the lens used for the majority of the experiments considered here.

The large positive dispersion in MgF₂ ($n_{355} = 1.39307$ [219], $n_{118} = 1.67283$ [220]) results in very different focal lengths in the UV/VUV. Using the standard expression for the focal length of a plano-convex lens with a radius of curvature, R , $f = \frac{R}{n-1}$, the lens focal length at 118nm is about $\approx 58\%$ of that at 355nm. This property can be exploited to minimize the intensity of 355nm (prevent multi-photon processes) at the interaction region by defocusing the 355nm light, or by striking the lens off-axis to obtain spatially separated beams [213] [210] [221] [212] [214] where the 355nm light may be dumped altogether.

A laser beam striking a thin lens at a distance r_0 from the optical axis will be deflected by an angle of

$$\Delta\theta = \left[\left(\frac{dr}{dz} \right)_{out} - \left(\frac{dr}{dz} \right)_{in} \right] = -\frac{r_0}{f} \quad (5.2)$$

For the optical system shown in Fig. 5.2a, the deviation angles of the red (UV) and blue (VUV) light rays are given by

$$\Delta\theta_R = -\frac{r_0}{f_R} \quad \Delta\theta_B = -\frac{r_0}{f_B} \quad (5.3)$$

Then, using $f = \frac{R}{n-1}$ for a plano-convex lens gives the deviation angle at a given wavelength as

$$\Delta\theta = -(n-1) \frac{r_0}{R} \quad (5.4)$$

The deviation angle between the red and blue beams (again, explicit expression here is for a plano-convex lens even though the Fig. 5.2a is biconvex) is given by

$$\begin{aligned} \delta\Phi &= \Delta\theta_B - \Delta\theta_R \\ &= r_0 \left(\frac{1}{f_R} - \frac{1}{f_B} \right) = \frac{r_0}{R} (n_R - n_B) \end{aligned} \quad (5.5)$$

The MgF₂ lens is held in a modified double-sided 2-3/4 CF flange mount and sealed with an O-ring. (See Fig. 5.2b for a drawing.) The central portion of the flange is bored out to leave a 0.8" diameter clear aperture. Standard lens-tube threads were cut into the interior of the bore using a lathe and the lens was secured with a rubber-tipped retaining ring. A sealing O-ring (Viton, size 0-020) is placed into a v-shaped groove to makes a robust, vacuum-tight seal for positive pressures above $\geq 60 Torr$.

5.2.4 Vacuum Level and Gas Purity

It is well recognized that a VUV optical system should be clean and free of contaminants, in particular, hydrocarbons. The level or vacuum and gas purity required for lossless transmission through a vacuum chamber/gas cell can be estimated using measured 295K absorption cross-sections [222] [223]. In the VUV

spectral region, 1-photon absorption cross-sections are typically not greater than $\sigma^{(1)} \approx 10^{-17} \text{cm}^2$. Application of Beer's law gives the rule of thumb that a quantity of $\sim 3 \text{Torr} * \text{cm}$ gives a $1/e$ absorption loss. This keeps the required level of vacuum rather modest; for background pressures of $\sim 1 \text{mTorr}$ and a $L = 50 \text{cm}$ path length, transmission will not be less than $\sim 98\%$. The Xenon and Argon used in these experiments was research grade, 99.999. At 100 Torr of Gas, then this suggests the contaminants are still only at the 1mTorr level (or $1 \text{mTorr}/100 \text{Torr}$). Before supplying gas to the Xe/Ar cell, the gas lines and regulator bodes were flushed with this pure gas $3\times$ to minimize the possibility of contamination. This point will be addressed again in the context of optical breakdown in Sec. 5.4.4.

5.2.5 VUV Detection

The VUV light is detected/measured with two different techniques described in Ch. 6.

5.3 Theory of Non-Resonant Third-Harmonic Generation

The basic experimental setup for third harmonic generation (THG) is depicted in Fig. 5.3. The pump beam, which is assumed for the moment to be a lowest order Gaussian beam, is focused into a gas cell of length, L , (shown as a gray box) with confocal parameter $b = \frac{2\pi w_0^2}{\lambda}$. The total generated third-harmonic power, $\mathcal{P}_{3\omega}$, is given in SI units as

$$\mathcal{P}_{3\omega} = \frac{3\pi^2}{\epsilon_0^2 c^2 (3\lambda)^4} \left| \mathcal{N} \chi_a^{(3)} \right|^2 \mathcal{P}_\omega^3 |F_1(b\Delta k)|^2 \quad [SI] \quad (5.6)$$

where λ is the third-harmonic wavelength in $[\text{cm}]$, \mathcal{N} is the atomic number density of the gas in $[\#/ \text{cm}^3]$, $\chi_a^{(3)}$ is the atomic third-order nonlinear coefficient, and \mathcal{P}_ω is the incident power in Watts. $F_1(b\Delta k)$ is a dimensionless function describing phase matching [224] and accounts for all effects of focusing and dispersion. Δk is the wave vector mismatch between the driving polarization and generated waves, given by

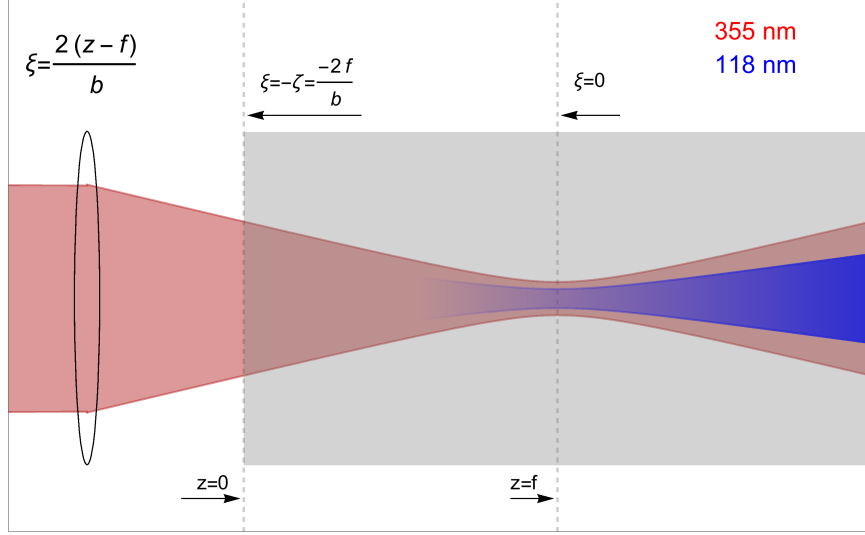


Figure 5.3: Definition of coordinates for THG in a semi-infinite nonlinear media (gray box). Traditional longitudinal coordinates (z) are defined at the bottom of the figure and the reduced longitudinal coordinate, $\xi = \frac{2(z-f)}{b}$, is defined in the upper part of the figure.

$$\begin{aligned}
 \Delta k &= k_{3\omega} - 3k_{\omega} \\
 &= 2\pi \left[\frac{n(\lambda)}{\lambda} - 3 \frac{n(3\lambda)}{3\lambda} \right] \\
 &= \frac{2\pi}{\lambda} [n_1 - n_3]
 \end{aligned} \tag{5.7}$$

In this notation, λ is the wavelength of the third-harmonic in vacuum, and $n_1 = n(\lambda)$ and $n_3 = n(3\lambda)$ are the index of refraction at the third-harmonic wavelength λ and the fundamental wavelength 3λ , respectively. The atomic third-order nonlinear coefficient, $\chi_a^{(3)}$, given in Eq. 5.6 has units of m^5V^{-2} . For historical reasons,¹ susceptibilities are more commonly given in CGS units so that $\chi_a^{(3)}$ has units of *esu*. The two different units of measurement can be related via $\chi_{SI}^{(3)} = \frac{4\pi}{9} \times 10^{-14} \chi_{esu}^{(3)}$. With $\chi_a^{(3)}$ in *esu*, the third harmonic power can be expressed as [225]

$$\mathcal{P}_{3\omega} = \frac{8.215 \times 10^{-2}}{(3\lambda)^4} \left| \mathcal{N}_{Xe} \chi_a^{(3)} \right|^2 \mathcal{P}_{\omega}^3 |F_1(b\Delta k)|^2 \tag{5.8}$$

¹ Discussions of units in nonlinear optics are given in Appendix C of Ref [203] and Appendix A of Ref [205].

The phase matching function, $F_1(b\Delta k)$, is given by the integral,

$$F_1(\xi', \xi, b\Delta k, b/L) = \int_{-\zeta'}^{\xi} \frac{e^{-i\frac{b\Delta k\xi''}{2}}}{(1+i\xi'')^2} d\xi'' \quad (5.9)$$

In Eq. 5.9, $\xi = \frac{2(z-f)}{b}$ is a reduced longitudinal coordinate measured in units of b and the nonlinear medium (gas cell) is taken to extend from $-\zeta'$ to ξ as shown in Fig. 5.3. In the standard convention [224], f is the distance from the input window to the focus, not the distance from the lens to the focus (i.e., lens focal length is not given by f). In general, Eq. 5.9 must be evaluated numerically. In the tight-focusing limit, where the nonlinear medium is much longer than the confocal parameter of the focused fundamental beam ($b \ll L$), the limits of integration can be replaced by $\zeta' = \xi = \infty$. In this case, the integral can be evaluated analytically with value [224]

$$|F_1(b\Delta k)|^2 = \begin{cases} \pi^2(b\Delta k)^2 e^{b\Delta k} & \Delta k < 0 \\ 0 & \Delta k \geq 0 \end{cases} \quad (5.10)$$

$|F_1(b\Delta k)|^2$ has a width of $b\Delta k \approx 3.4$ and peaks at $b\Delta k = -2$, with value $F_{max} = \frac{\pi^2 4}{e^2} \approx 5.34$ (see Fig. 5.4). The most significant result of Eq. 5.10 is that the integral vanishes for perfect phase matching, $\Delta k = 0$, and for all positive values of $b\Delta k$. The shape and peak value of $|F_1(b\Delta k)|^2$ is relatively insensitive to the exact value of b/L provided $b \ll L$, [224], [226].

The electric field of the pump wave, and thus the nonlinear polarization, is clearly largest in the region around $-b \rightarrow b$, which serves to define the 10-90% generating regions [224]. In the tight focusing limit ($b \ll L$), the ends of the medium make a negligible contribution to the total yield. A related and often misunderstood feature of the tight focusing limit is that the total harmonic flux is independent of how tightly the beam is focused (provided $b \ll L$ still satisfied). Thus, at least in the limit that the first order theory is valid, this allows for a great degree of freedom in the choice of lens used to focus the pump light (since the conversion efficiency is independent of the intensity but instead only on the power).

The physical origin of the requirement of negative values of $b\Delta k$ originates from the so called Guoy phase shift. The Guoy phase shift describes the phase shift a gaussian beam goes through at a focus. The

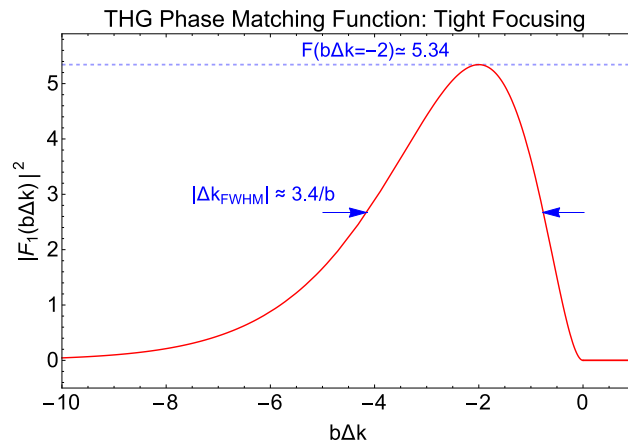


Figure 5.4: Phase matching function, $|F_1(b\Delta k)|^2$, (Eq. 5.10) in the tight-focusing limit, $b \ll L$. The tolerable mismatch in Δk is inversely proportional to confocal parameter, b , with the full width half maximum given approximately by $(\Delta k)_{FWHM} \approx 3.4/b$.

total on-axis phase variations of a TEM_{mn} gaussian beam is given by $e^{i[kz - \Phi_{mn}^G(z)]}$ where, $\Phi_{mn}^G(z)$ is the Guoy phase shift, given by

$$\Phi_{mn}^G(z) = (n + m + 1) \tan^{-1} \left(\frac{z}{z_R} \right). \quad (5.11)$$

From a momentum perspective, the Guoy phase shift can be thought of as reducing the effective wave vector in the vicinity of the focus (where harmonic generation is most significant). For a medium without dispersion ($n_1 = n_3$), where phase matching would be perfect, $b\Delta k = 0$, the harmonic radiation generated on one side of the focus is out of phase with the radiation on the other side of the focus. A negatively dispersive medium introduces an additional phase shift that cancels the Guoy phase shift to keep radiation on both sides of the focus in phase.

5.3.1 Phase Matching Techniques

The requirement of an overall negative value of Δk (Eq. 5.7) is satisfied only in media that exhibit negative/anomalous dispersion, i.e.: $n_3 > n_1$. At frequencies below a gas' first resonance, the dispersion is usually *normal* (index increases with frequency). Above the first resonance, regions of *negative* or *anomalous* dispersion can be found due to the cumulative contributions of many resonances (see Fig. 5.5 for a plot of a generalized resonance structure). For a gas, the effective macroscopic index of refraction, n , is tied to the

number density, \mathcal{N} [$\#/cm^3$], by

$$n(\lambda) = 1 + \mathcal{N}\chi_a^{(1)}(\lambda), \quad (5.12)$$

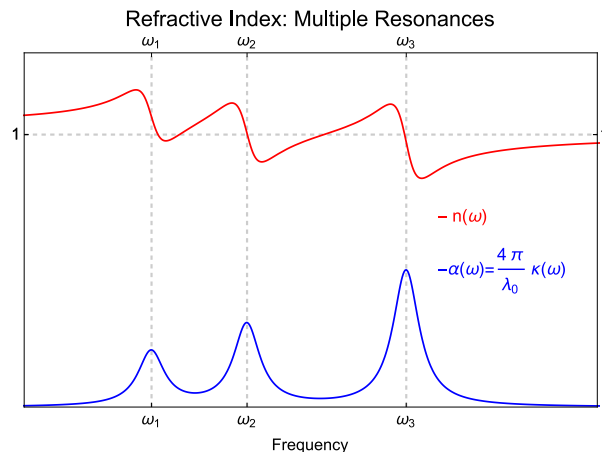


Figure 5.5: Outside of the FWHM of a resonance the index of refraction increases with increasing frequency (see extreme left and right portions of above). Within a resonance width, the index of refraction decreases with increasing frequency.

where $\chi_a^{(1)}$ is the *atomic linear susceptibility* at wavelength λ . Using Eq. 5.12, Δk (Eq. 5.7) can be expressed on a “per atom” basis by

$$\Delta k = C\mathcal{N} \quad (5.13)$$

where $C = \frac{2\pi}{\lambda} [\chi_a^{(1)}(\lambda) - \chi_a^{(1)}(3\lambda)]$ is a constant describing the microscopic dispersive properties of the atoms/molecules comprising the gaseous medium. C can then be thought of as the effective wave-vector mismatch per atom. This affords a convenient “knob” for phase matching, since Δk can be adjusted simply by varying the number density (pressure) of the gas. In a sense, this pressure adjustment is analogous to varying a crystal angle/orientation in birefringent phase matching of second-order processes. Values of C_i have been calculated by Mahon *et al*, [21] for the rare gases, argon, krypton and xenon. For xenon and argon at 118.2 nm they give $C_{Xe}(118.2 \text{ nm}) = -6.12 \times 10^{-17} [cm^2]$ and $C_{Ar}(118.2 \text{ nm}) = +5.33 \times 10^{-18} [cm^2]$.

5.3.1.1 Xenon Only Phase Matching

Experimentally, there are three parameters that can be varied to optimize the third-harmonic power (Eq. 5.8): 1) optimizing phase matching by setting $b\Delta k = -2$ so that $|F_1|^2$ maximizes, 2) maximizing the macroscopic nonlinear coefficient, $\chi_{eff}^{(3)} = \mathcal{N} \times \chi_a^{(3)}$, and, 3) using large peak powers in the fundamental. For a single-component gas, however, simultaneous/independent maximization of the nonlinear optical susceptibility while maintaining phase matching is impossible because both $\chi_{eff}^{(3)}$ and the refractive index/wave-vector mismatch $\Delta k = C_i \mathcal{N}_i$ are both tied to \mathcal{N} .

Thus, for a single-component gas a compromise is made since it is the product $\chi_{eff}^{(3)} |F(b\Delta k)|^2 \propto \mathcal{N}^2 |F(b\Delta k)|^2$ that must be maximized [224]. The relative yield of the third harmonic when phase matching with a single-component-gas is described by the dimensionless function, $G(b\Delta k) = (b\Delta k)^2 |F(b\Delta k)|^2$, which peaks at $(b\Delta k)_{opt} = -4$ [224]. Using Eq. 5.13 and the relation $\mathcal{N} = \beta \times P_{Torr}$ where $\beta \approx 3.27 \times 10^{16} \#/(cm^3 \cdot Torr)$ at $T = 295 K$, the optimum pressure for maximum 118 nm yield is inversely proportional to the confocal parameter, b , of the focused fundamental beam, i.e.,

$$P_{Xe}^{(opt)} = \frac{4}{\beta |C_{Xe}| b_f} \quad (\text{xenon only}) \quad (5.14)$$

Fig. 5.6 shows a pure Xenon phase matching curve with a $f = 48.3cm$ lens (blue) and a $f = 25.7$ cm lens (red) under otherwise identical conditions (17 mJ/pulse). As expected, when the beam is focused more tightly with the $f = 25cm$ lens, (smaller values of b_f and thus w_f), the optimum xenon pressure is moved to larger values.

5.3.1.2 Phase Matching with Two-Component Gas Mixtures

One of the primary limitations of phase matching with a single-component gas is that the effective nonlinear coefficient $\chi_{eff}^{(3)}$ is limited to relatively small values due to constraints imposed by $G_1(b\Delta k)$. Δk and $\chi_{eff}^{(3)}$ can be decoupled by adding a positively dispersive buffer gas with negligible nonlinearity to the “active” gas. For 355 nm tripling in xenon, argon is typically used as the positively dispersive buffer gas. For a mixture of two gases, the total wave vector mismatch at the nominal third-harmonic wavelength λ_0 is

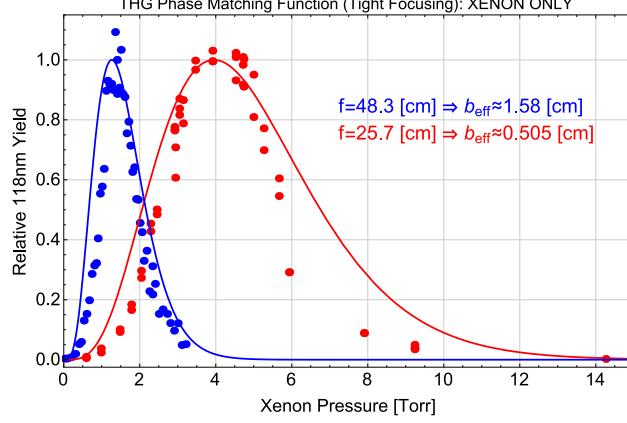


Figure 5.6: Xenon-only phase matching for two different lenses. The effective confocal parameters obtained from fitting the normalized data to $G_1(b\Delta k)/G_1(-4)$ are also indicated.

given by summing over the partial pressures of each gas,

$$\begin{aligned}\Delta k(\lambda_0) &= \mathcal{N}_{Xe}C_{Xe}(\lambda_0) + \mathcal{N}_{Ar}C_{Ar}(\lambda_0) \\ &= \mathcal{N}_{Xe}[C_{Xe}(\lambda_0) + RC_{Ar}(\lambda_0)]\end{aligned}\quad (5.15)$$

where $R = \frac{\mathcal{N}_{Ar}}{\mathcal{N}_{Xe}}$ is the pressure ratio of the two gases. Optimum phase matching in the tight-focusing limit requires $\Delta k(\lambda_0)_{opt} = -\frac{2}{b}$. Simple manipulation of Eq. 5.15 yields the optimum gas ratio that achieves this value of Δk . The optimum ratio is given by

$$\left(\frac{\mathcal{N}_{Ar}}{\mathcal{N}_{Xe}}\right)_{opt} = \frac{-2}{b} \frac{1}{\mathcal{N}_{Xe}C_{Ar}(\lambda_0)} - \frac{C_{Xe}(\lambda_0)}{C_{Ar}(\lambda_0)}\quad (5.16)$$

Eq. 5.16 gives the optimum partial pressure/number density ratio of the active gas (in this case xenon) to the buffer (phase matching) gas, argon. For large xenon pressures the optimum ratio of the two gases approaches a constant value that is independent of the value of b , i.e.: $R = \frac{\mathcal{N}_{Ar}}{\mathcal{N}_{Xe}} \rightarrow \left|\frac{C_{Xe}}{C_{Ar}}\right|$. The fact that the optimum pressure ratio is independent of the value of b (for a lowest order Gaussian beam) may initially seem surprising, but it can be rationalized by considering that, for any lowest order Gaussian beam, the net Guoy phase shift has the same value, but simply requires different distances to undergo the full π phase shift. Using Mahon *et al*'s calculated values for C_{Ar} and C_{Xe} (provided here at the end of Sec. 5.3.1)

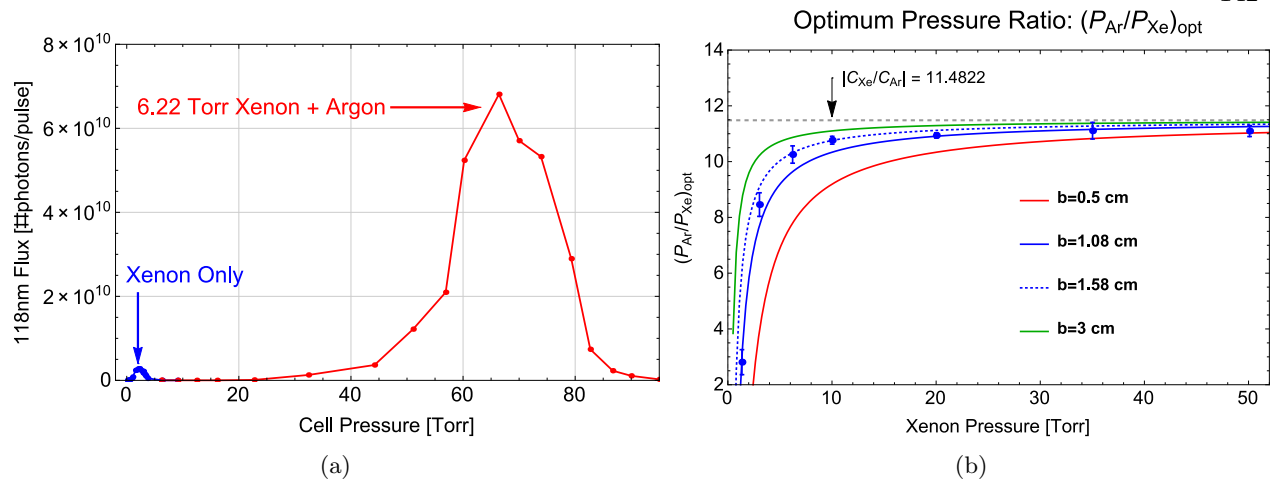


Figure 5.7: Phase matching with xenon and argon. (a) Sample measurement obtained by adding a fixed amount of xenon (6.22 Torr in this case) and then adding argon. (b) Measured optimum pressure ratios P_{Ar}/P_{Xe} for several different xenon pressures (blue circles) with a $f = 48.3$ cm lens (at 355 nm). The four colored curves are Eq. 5.16 for $b = 3$ cm (green), $b = 1.58$ cm (blue,dotted), $b = 1.08$ cm (blue, solid) and $b = 0.5$ cm (red). The error bars in this plot are a reflection of the small number of points used to infer the peak pressure ratio. The dotted, blue curve, corresponding to $b = 1.58$ cm is the effective value obtained from a fit to xenon only data (see Fig. 5.6). The dashed blue curve, corresponding to $b = 1.08$ cm, is based on the knife-edge measurements presented in Fig. 5.1a. For details, see text.

gives a theoretical optimum ratio of $R_{opt} = 11.48$.

Fig. 5.7 shows the experimentally measured optimum ratios (355nm beam focused with $f \approx 48.3$ cm lens to $b_f \approx 1.5$ cm). The agreement between the experimentally measured data (blue circles) and the behavior expected based on the theory curves is quite reasonable. The maximum pressure ratio (obtained at $P_{Xe} \approx 50$ Torr) has value $\mathcal{N}_{Ar}/\mathcal{N}_{Xe} \approx 11.10$. If the data given in 5.7b is fitted to extract the effective confocal parameter, a value of $b_{eff} \approx 1.03$ cm is obtained. Interestingly, this value is nearly the same as the confocal parameter of the underlying Gaussian beam determined from knife edge measurements, $b = 1.08$ cm (see Fig. 5.1a), and is distinct from the value determined from the xenon-only fits shown in Fig. 5.6, $b = 1.58$ cm.

5.3.2 Conversion Efficiency

According to the basic theory laid out in Sec. 5.3, the *power* efficiency of third-harmonic generation (see Eq. 5.8) is

$$\eta \equiv \frac{\mathcal{P}_{3\omega}}{\mathcal{P}_\omega} = \frac{8.215 \times 10^{-2}}{(3\lambda)^4} \left| \mathcal{N}_{Xe} \chi_a^{(3)} \right|^2 \mathcal{P}_\omega^2 |F_1(b\Delta k)|^2. \quad (5.17)$$

Thus, the efficiency should scale quadratically with the effective nonlinear coefficient $\chi_{eff}^{(3)} = \mathcal{N}_{Xe} \chi_a^{(3)}$ (xenon pressure) and the pump power (total yield scaling as $\propto P_\omega^3$). Measurements of the nonlinear susceptibility in xenon at 118.2 nm have been reported by Kung and colleagues [216] [20] to have a value of $\chi_{Xe}^{(3)}(-3\omega; \omega, \omega, \omega) = 5.6 \times 10^{-35} \text{ esu}$. Zych and Young reported [227] a value less than half of Kung's value, at $\chi_{Xe}^{(3)}(-3\omega; \omega, \omega, \omega) = 2.3 \times 10^{-35} \text{ esu}$. Ref [227] appears to be the only place in the literature where the value of $2.3 \times 10^{-35} \text{ esu}$ appears. Given inconsistencies in Zych and Young's value for $\Delta k/b$ as pointed out in [21] we use Kung's value for all theoretical calculations.

Measurements in our laboratory (Fig. 5.8) indicate that the conversion efficiency in pure xenon begins to roll off around peak powers of 1 MW, for beam waist of $w_0 \approx 35 \mu\text{m}$ and peak intensities of $\sim 3 \times 10^{10} \text{ W/cm}^2$. For xenon only, the measured efficiency never rises above $\approx 2 \times 10^{-5}$.

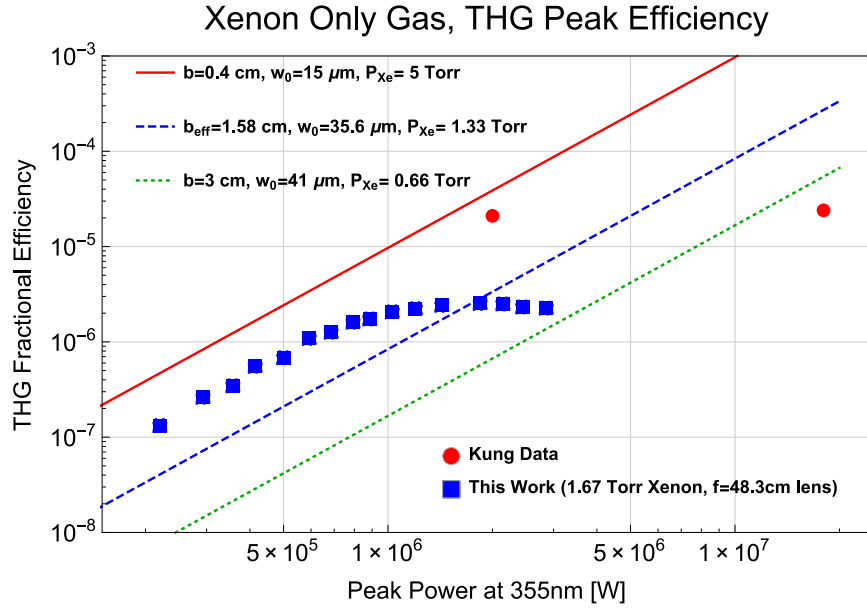


Figure 5.8: Conversion efficiency of xenon only phase matching vs incident pump power. The Kung data, shown by red circles, are taken from [20]. Solid lines are theoretical conversion efficiencies predicted by Eq. 5.17 for different focusing conditions.

As discussed in Sec 5.3.1.2, using gas mixtures allows the dispersion to be decoupled from the nonlinearity. In the limit that the first-order theory is valid, $\chi_{eff}^{(3)}$ can be made arbitrarily large provided that

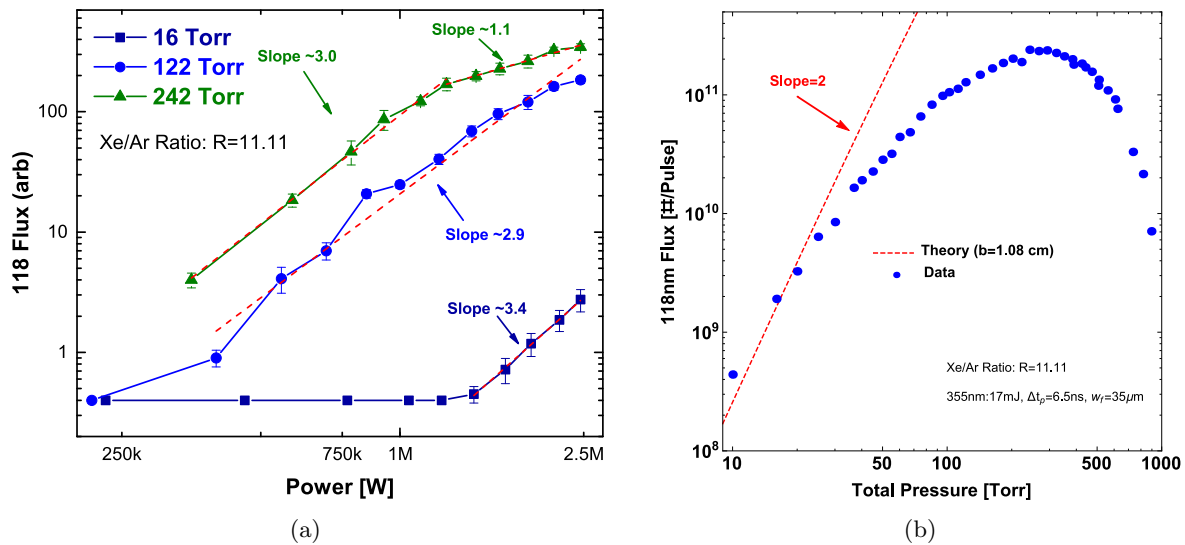


Figure 5.9: Limitation to the total conversion efficiency for phase matched ($R=11.11$) Xe/Ar mixtures at high powers and high total pressures. The total yield is plotted in (a) as a function of the pump power for total pressures of 16 Torr (squares), 122 Torr (circles), and 242 Torr (triangles). In (b), the 118nm flux is plotted as a function of the total pressure for a fixed pump power of $P_\omega \approx 2.6 MW$ ($I_\omega \approx 6.6 \times 10^{10} W/cm^2$).

an appropriate amount of buffer gas is used to phase match. To estimate the theoretical peak conversion efficiency for phase matched gas mixtures, we assume that phase matching is optimized at the optimum value of R so that $F1[b\Delta k] = F_1^{(max)} \approx 5.34$ and consider only the dependence on pump power and xenon pressure. The conversion efficiency calculated from Eq. 5.17 approaches $\eta_{THG} \approx 10^{-4}$ for 10 Torr of xenon and 17mJ, $\tau_p = 6.5ns$ pulses.

Measurements shown in Fig. 5.9 indicate significant reductions in the conversion efficiency at high pump powers and high gas pressures. Fig. 5.9a shows the generated 118nm flux as a function of pump power for three different values of total pressure. At low pressures, the yield is approximately $\propto \mathcal{P}_\omega^3$ but as the pressure and power increases the efficiency drops. Fig. 5.9 shows the measured yield at fixed pump power of $\mathcal{P}_\omega = 6.8 \times 10^{10} W/cm^2$ (17mJ, 6.5ns) as function of total pressure for a phase matched mixture, premixed to a ratio of $R = 11.11$. The data is in reasonable agreement with theory for low pressures, but deviates strongly above $\approx 20 Torr$ of total pressure. The rest of this chapter is devoted to investigations of the possible factors responsible for limiting the conversion efficiency.

5.4 Limitations to Conversion Efficiency

Limitations to the conversion efficiency have been reported to arise from (linear) 1-photon absorption [225] [228] [229] as well as other nonlinear processes not considered in the basic theory of Sec. 5.3. Examples of limiting nonlinear processes include the Kerr effect [227], optical Stark shifts [230], self-focusing [231], bandwidth limitations [21], saturation of the nonlinear susceptibility, population changes, multiphoton absorption, and optical breakdown. Depletion of the pump beam can be neglected due to the small conversion efficiencies (small $\chi_{eff}^{(3)}$) of nonresonant THG in gases.

Stark shifts and saturation effects are expected to be most significant for resonant processes. As such, they are not considered here due to the large detuning of the generated 118.2nm light from xenon resonances. For the generation of intense fluxes with *ns* pulse 355 nm lasers, the most likely limiting factors are a Kerr nonlinearity, bandwidth narrowing, linear absorption at 118 nm, multi photon ionization at 355 nm, and optical breakdown due to the intense 355 nm light. The signature of all of these processes except linear absorption can be seen in the power law dependence of the optical intensity.

5.4.1 Kerr Nonlinearity

Large optical intensities can drive other nonlinear processes in addition to third harmonic generation. The dominant interaction in our system (tripling 355 nm in Xe/Ar mixtures) is a mixed-frequency Kerr nonlinearity, where large intensities at 355 nm modify the refractive index at 118nm. Including this Kerr nonlinearity requires changing Eq. 5.15 to

$$\Delta k = \mathcal{N}_{Xe} \left(C_{Xe} + RC_{Ar} + \delta \frac{\mathcal{P}_\omega}{A} \right). \quad (5.18)$$

In this notation,² A is the cross-sectional area of the pump beam in cm^2 and δ is the Kerr-induced wave vector mismatch per xenon atom, with value $\delta = -3.3(478) \times 10^{-29} cm^4 W^{-1}$. Because δ is negative, it acts to increase the effective wavevector mismatch of a given xenon atom by making it more negative. This

² The notation used by the authors of Ref [227] is different from that used here in a number of ways. First, they defined λ to be the fundamental wavelength instead of the generated third-harmonic. Second, the total wave vector mismatch is expressed with an explicit factor of $\frac{6\pi}{\lambda}$ out front, which changes the interpretation of the “per atom” wave vector mismatches. In Ref [227] Δk is expressed as $\Delta k = \frac{6\pi}{\lambda} \left(\alpha + \beta R + \gamma \frac{P}{A} \right) N_{Xe}$. Their value of $\gamma = -6.3 \times 10^{-36} cm^5 W^{-1}$ can be converted into our notation with the relation $\delta = \frac{2\pi}{\lambda} \gamma$.

means that, for large optical intensities, the optimum xenon pressure (for say, xenon-only phase matching) should decrease.

One could in principle calculate the effect a given intensity would have on Δk and prepare the appropriate gas mixture that would be “Kerr shifted to the phase-matched condition.” However, this approach invariably limits the xenon density, and, thus, $\chi_{eff}^{(3)}$. Therefore, the net effect of the Kerr shift, which constrains both the pump power and the effective nonlinear coefficient, is to set an upper limit on the attainable conversion efficiencies. The analysis given in [227] indicates that the Kerr-limited conversion efficiency should plateau around $\eta \approx 9 \times 10^{-3}$.

However, $\delta \frac{P_\omega}{A}$ does not become comparable to C_{Xe} until pump intensities of $\frac{P_\omega}{A} \sim 2 \times 10^{12} [W/cm^2]$. In fact, this pressure shift only became measurable at intensities of $\approx 4 \times 10^{11} W/cm^2$ (see Fig. 1 of Ref [227]). At the peak intensity available in our experiment of $I \sim 1.66 \times 10^{11} W/cm^2$ (43 mJ, $\Delta t_p \approx 6.5 ns$, $w_f \approx 35.6 \mu m$), the shift in the value of the optimum pressure is only $\sim 0.1 Torr$. As the authors of Ref [227] pointed out, the Kerr limited conversion efficiency of $\eta_{THG} = 9 \times 10^{-3}$ was not realized in practice due to other limitations (not identified in Ref [227]), which become important at high pressures. Thus, this Kerr effect is not expected to play a significant role in limiting the conversion efficiency for 118.2 nm light generated with *ns*- pulse lasers at 355 nm.

5.4.2 Bandwidth Considerations

$|F_1(b\Delta k)|^2$ (Eq. 5.10) is increasingly sensitive to variations in Δk , as the focus of the fundamental beam is loosened (b made larger). This means that while $(b\Delta k)_{FWHM}$ is constant (see Fig.5.4), the bandwidth of tolerable wave vector mismatches decreases as the beam is focused more loosely. Physically, the reduction in Δk_{FWHM} for larger values of b results from the increased distance over which phase matching must be maintained (generating region $b \rightarrow -b$). This behavior of $|F_1(b\Delta k)|^2$ is manifested as a pressure sensitivity in the xenon only phase matching data presented in Fig. 5.6. When the pump beam is focused more tightly (going from the $f = 48.3 cm$ lens $\rightarrow f = 25.7 cm$ lens), the corresponding tolerable pressure range increases.

This behavior also shows up in the spectral dependence of $|F_1(b\Delta k)|^2$. For a media without dispersion

(i.e., $n(\lambda)$ and $n(3\lambda)$ different, but flat over the laser bandwidth) $\Delta k_{FWHM} \approx \frac{3.4}{b}$ would directly translate into an *optical bandwidth* of the third-harmonic (for say, white light input). However, the rapid changes in the refractive index near the generated wavelength will limit the optical bandwidth to a somewhat smaller value. If this phase matching bandwidth is reduced below the bandwidth of the laser pulse, the conversion efficiency will be diminished due to a spectral filtering effect. To achieve high conversion efficiencies, Δk must not vary by more than $\approx \frac{\Delta k_{FWHM}}{2}$ over the bandwidth of the pump laser. This variation in wave vector mismatch is amplified at higher gas pressures via $\Delta k = \sum_i C_i \times \mathcal{N}_i$.

This type of bandwidth limitation was addressed in Ref [21] in the context of non-resonant third-harmonic generation of $Ly - \alpha$ radiation at 121.6 nm in Kr. Despite a brief comment in [21] that C_{Xe} was more strongly varying near 118.2 nm than C_{Kr} at 121.6 nm, efficiency limitations due to bandwidth limitations in the 355 nm/118 nm system seems to have been neglected in the literature. For 355 \rightarrow 118.2 nm tripling in Xe/Ar mixtures, almost all of the dispersion is contributed by xenon. The nearest argon resonance [$(^2P_{3/2})4s$ at 11.624 eV = 106.662 nm] is so far away that the C_{Ar} is essentially constant near 118nm. To estimate the limiting effects of dispersion, we make a linear approximation to the three explicitly quoted values of the C_{Xe}^3 near 118.2 nm of Ref [21]

$$C_{Xe}(\bar{\nu}) = C'_{Xe}(\nu_0)(\bar{\nu} - \bar{\nu}_0) + C_{Xe}(\bar{\nu}_0) \quad (5.19)$$

with slope $C'_{Xe} \approx 1.5 \times 10^{-19} [cm^2/cm^{-1}]$. Assuming the gas ratio is set to optimize at the central frequency ν_0 , the deviations from the optimum value $(\Delta k)_{opt}$ over a bandwidth $\Delta \bar{\nu}_L$ is

$$\Delta k(\bar{\nu}) - (\Delta k)_{opt} = \beta P_{Xe} C'_{Xe} \Delta \bar{\nu}_L \quad (5.20)$$

Taking an upper limit of the laser bandwidth to be $\Delta \bar{\nu}_L \approx 3 \text{ cm}^{-1}$, $\Delta k(\bar{\nu})$ is not expected to deviate from $(\Delta k)_{opt}$ by more than $\sim 1 \text{ cm}^{-1}$ until xenon pressures of $\approx 70 \text{ Torr}$. By incorporating the functional form of Eq. 5.20 directly into $|F_1(b\Delta k)|^2$ one can get sense of how the relative yield varies with xenon pressure in real frequency units. To make the expression absolute we consider a trivial modification of Eq. 5.8, given by

³ The three explicitly given values for C_{Xe} in Ref [21] appear to have typographical errors. Based a digitization of their Fig. 3 as well as our own rough Sellmeier calculations of $C_{Xe}(\lambda)$ using oscillator strengths given in Ref [232], the end points of their three values should be swapped. The three correct values are $C_{Xe}(118.295 \text{ nm}) = -6.71 \times 10^{-17} \text{ cm}^2$, $C_{Xe}(118.244 \text{ nm}) = -6.12 \times 10^{-17} \text{ cm}^2$, and $C_{Xe}(118.195 \text{ nm}) = -5.64 \times 10^{-17} \text{ cm}^2$.

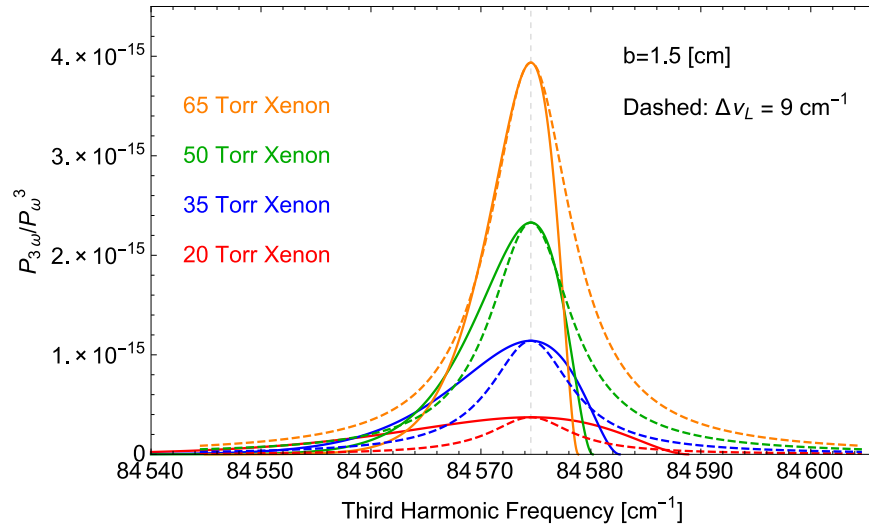


Figure 5.10: Spectral filtering of the generated third-harmonic at 118.2 nm in Xe/Ar mixtures for various xenon pressures. For each xenon pressure the ratio is assumed to be that which perfectly phase matches in the tight focusing limit. The argon wave vector mismatch is assumed to be constant in this region with value $C_{Ar} = +5.33 \times 10^{-18} \text{ cm}^2$. For xenon, a 2^{nd} order interpolation to the three explicitly quoted values in Ref [21] are used. Range of interpolation is 118.295 nm (84534.4 cm^{-1}) \rightarrow 118.195 nm (84605.9 cm^{-1}). This plot was made absolute by taking Kung's value for the nonlinear coefficient in xenon of $\chi_a^{(3)} = 5.6 \times 10^{-35} \text{ esu}$. Scaled, Lorentzian laser lineshapes ($\Delta\bar{\nu} = 3 \text{ cm}^{-1}$) are shown for each xenon pressure. Though the bandwidth of the generated radiation is expected to undergo some “narrowing” it does not become significant until xenon pressures in excess of 50-70 Torr.

$$\frac{\mathcal{P}_{3\omega}}{\mathcal{P}_{\omega}^3} = \frac{8.215 \times 10^{-2}}{(3\lambda)^4} \left| \mathcal{N}_{Xe} \chi^{(3)} \right|^2 |F_1(b\Delta k)|^2 \quad (5.21)$$

Eq. 5.21 is plotted in Fig. 5.10 for phase matched Xe/Ar mixtures for several different xenon pressures up to $P_{Xe} = 70 \text{ Torr}$. Alongside this scale efficiency curve is a scaled Lorentzian laser lineshape with a width of $\Delta\bar{\nu}_L = 9 \text{ cm}^{-1}$. This value is used in Fig. 5.10 due to the expected relation between the bandwidth of the fundamental light ($\sim 3 \text{ cm}^{-1}$) and the tripled light ($\sim 3 \times 3 \text{ cm}^{-1}$). The results of calculations shown in Fig. 5.10 indicate that spectral filtering will not play a significant role in limiting the conversion efficiency even for unseeded Nd:YAG lasers with bandwidths (at 355 nm) up to $\Delta\bar{\nu}_L \approx 3 \text{ cm}^{-1}$, until $P_{Xe} \approx 70 \text{ Torr}$. In practice, other limitations will set in at lower pressures than these.

5.4.3 Linear Absorption at Third Harmonic

Another possible limitation of the attainable 118.2 nm flux is reabsorption of the generated light by the gas mixture. Compared to resonant THG, the relatively large detuning used in non-resonant THG minimizes direct absorption of either fundamental or third-harmonic light. However, detunings cannot be made arbitrarily large since it is only in the vicinity of a resonance that a gas 1) exhibits negative dispersion and 2) has an appreciable nonlinear coefficient. Therefore, high pressures of gas allow the possibility of absorption from the wings of the absorption line.

According to the discussion in Sec. 5.2.4, absorption from impurities is expected to be very low for the oil-free system used here. Absorption of the generated 118.2 nm (10.48 eV) light by the Xe/Ar mixture itself is expected to be dominated by the Xe ($^2P_{3/2}$)5d [$\frac{3}{2}$] line at 119.203 nm (10.401 eV) with oscillator strength $f_{5d} = 0.379$ [232]. The comparably close Xe ($^2P_{3/2}$)7s line at 117.043 nm (10.593 eV) will contribute less due to its smaller oscillator strength, $f_{7s} = 0.0859$ [232]. The nearest argon line ($^2P_{3/2}$)4s at 106.66 nm (11.624 eV), is 9206 cm^{-1} (1.031 eV) farther away and is neglected. Absorption at 355 nm is neglected for similar reasons.

The resonance lines of the relatively dense ($P_{tot} \approx 1 - 1000$ Torr) and warm ($T \approx 295$ K) gas mixtures of interest here are expected to experience natural, doppler and collisional (pressure) broadening. In the immediate vicinity of the resonance, the line shape is expected to be dominated by the Gaussian doppler profile with FWHM $\Delta\nu_D \approx 2.7$ GHz (for Xe). However, for the large detunings of interest here (for the ($^2P_{3/2}$)5d [$\frac{3}{2}$] line, $\Delta\bar{\nu} = 556$ cm^{-1} or $\Delta\nu = 16.701$ THz $\approx 6185 \times \Delta\nu_D$), any absorption will be found in the wings of the absorption line. Due to the “persistent” character of Lorentzian line shape characterizing collisional broadening compared to the Gaussian profile of doppler broadened lines (see Fig. 5.11), absorption in the wings is expected to be completely dominated by collisional broadening.

If all frequencies are expressed in [cm^{-1}], the frequency-dependent (not yet integrated over frequency) absorption cross-section, $\sigma_{ij}(\bar{\nu})$ can be expressed in terms of the total (frequency integrated) oscillator strength f_{ij} and the lineshape function $g(\bar{\nu})$ by

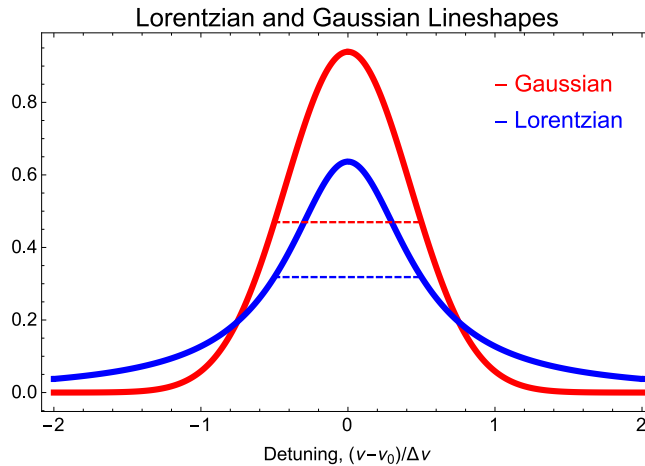


Figure 5.11: Lorentzian (natural, collisional) and Gaussian (doppler) lineshapes with the same FWHM, $\Delta\nu$. As a result of the much slower decay of the Lorentzian lineshape, the wings ($\frac{(\nu-\nu_{ij})}{\Delta} \gg 1$) of the absorption line will be completely dominated by the Lorentzian component of the lineshape.

$$\sigma_{ij}(\bar{\nu}) = \pi r_e f_{ij} g(\bar{\nu}), \quad [cm^2] \quad (5.22)$$

where $r_e \approx 2.817 \times 10^{-13} cm$ is the classical electron radius. For Lorentzian lines, the properly normalized lineshape is given by

$$g(\bar{\nu}) = \frac{1}{2\pi} \frac{\Delta\bar{\nu}}{(\bar{\nu} - \bar{\nu}_{ij})^2 + (\frac{\Delta\bar{\nu}}{2})^2}, \quad (5.23)$$

where $\bar{\nu}_{ij}$ is the resonance frequency and $\Delta\bar{\nu}$ is the FWHM of the absorption line. On resonance, the peak value of the lineshape function is $g(\bar{\nu} = \bar{\nu}_{ij}) = \frac{2}{\pi\Delta\bar{\nu}}$. This gives the peak absorption cross-section as

$$\sigma_{ij}^{(peak)}(\bar{\nu}) = \frac{2r_e f_{ij}}{\Delta\bar{\nu}} \quad (5.24)$$

Far away from the resonance frequency, $\bar{\nu} - \bar{\nu}_{ij} \gg \Delta\bar{\nu}$, the absorption cross-section is approximated by

$$\sigma(\bar{\nu}) = r_e f_{ij} \frac{\Delta\bar{\nu}/2}{(\bar{\nu} - \bar{\nu}_{ij})^2} = \sigma^{(peak)} \left(\frac{\bar{\nu} - \bar{\nu}_{ij}}{\Delta\bar{\nu}/2} \right)^{-2} \quad (5.25)$$

Thus, the magnitude of the absorption cross-section falls off quadratically in the detuning measured in units of $\Delta\bar{\nu}/2$ (i.e., 20dB per decade of detuning). A unique feature of this “continuum-like absorption” is

that high gas pressures/densities not only linearly increase the number of absorbers, but also increase the linewidth (logarithmically), which increases the pressure broadening cross section (on a per molecule basis) at the third harmonic.

If the resonance line were broadened only by the natural lifetime, $\tau_{ik} = 1/A_{ik}$, then the line width of the resonance line in $[Hz]$ would be $\Delta\nu_N = \frac{1}{2\pi\tau_i} = \frac{A_{ik}}{2\pi}$. To estimate the extent this line will be broadened due to collisions, we can consider the collision to simply be an additional deactivation mechanism, that adds linearly to the total relaxation rate, i.e.,

$$A_i = A_{ik} + \kappa_i * \mathcal{N}_b = A_{ik} + a_i * P_b \quad (5.26)$$

where \mathcal{N}_b (P_b) is the density (pressure) of the buffer gas in $[\#/cm^3]$ (Torr) and $a_i = \kappa_i * \beta$ where $\beta \approx 3.27 \times 10^{16} [\#/(cm^3 \times Torr)]$ is the standard conversion factor between number density and pressure at $T = 295K$. Then the total linewidth is expressed by

$$\Delta\nu_{tot} = \Delta\nu_N + \Delta\nu_c = \Delta\nu_N + b_c \times P_b \quad (5.27)$$

This mechanism is successful at providing a conceptual picture for collisional broadening, but in general the observed quenching collision cross-sections are much too low to explain the degree of experimentally measured pressure broadening [233]. (See also the last column of Table 5.1).

Table 5.1: Collisional broadening parameters for Xe lines near 118 nm. The last three columns give the expected width in units of $[cm^{-1}/Torr]$. Quenching rate constants of the Xe (${}^2P_{3/2}$) $5d[\frac{3}{2}]$ state for Xe and Ar buffer gas taken from [1]. Values of κ are given in $\times 10^{-10} [cm^3s^{-1}]$, and values of a_i are given in $\times 10^6 [Torr^{-1}s^{-1}]$. The inferred contribution to the line width due to this collisional quenching $\Delta\nu_c$ is given in $[MHz/Torr]$. The natural lifetime given for Xe (${}^2P_{3/2}$) $5d[\frac{3}{2}]$ is based on the natural lifetime measurement $\tau = 1.4ns$ given in Ref [2]. It has value $115MHz = 0.00379cm^{-1}$.

Resonance	$\lambda[nm]$	$\Delta\nu_N = \frac{1}{2\pi\tau}$	Perturber	Width	Shift	Quenching
$({}^2P_{3/2})5d[\frac{3}{2}]$	119.203	3.79×10^{-3}	Xe	2.73×10^{-2} [234]	1.45×10^{-2} [234]	9.53×10^{-6} [1]
			Ar	-	-	1.67×10^{-7} [1]
$({}^2P_{3/2})7s$	117.043	-	Xe	7.3×10^{-3} [234]	3.8×10^{-3} [234]	-
			Ar	-	-	-

Since the both the 5d and 7s xenon lines have dipole-allowed pathways to the ground state, self-pressure

broadening [235] [236] [234] must be considered. Values of b_c (see Eq. 5.27) for the two most relevant xenon resonances used to estimate self-broadening in xenon are taken from Ref [234] and tabulated in Table 5.1. Even though, all absorption is expected to be due to xenon, the argon buffer gas will contribute to the overall broadening of the line. There do not seem to be experimental measurements foreign gas broadening for Argon perturbers. To estimate this effect, we take the typical value of $5 \text{ MHz/Torr} = 0.000167 \text{ cm}^{-1}/\text{Torr}$ [70]. Calculations of the pressure broadening linewidths and absorption cross-sections are presented in Fig. 5.12. It is not immediately apparent whether the rather large amount of self-broadening ($\approx 790 \text{ MHz/Torr}$ for the 5d line) should really be applicable for the very large detunings of interest here. For this reason, Fig. 5.12 also shows calculations that neglect self broadening and assume that Xe and Ar both broaden the line equally, at 5 MHz/Torr .

For a phase-matched mixture of Xe/Ar ($R = 11.11$) containing 50 Torr of xenon, the total pressure will be ~ 606 Torr. Taking the self-broadened cross-section as $\sigma_{abs}(\nu_{118}) \approx 2 \times 10^{-19} \text{ cm}^2$, the absorbance is $\alpha = n_{Xe} \sigma_{abs}(\nu_{118}) \approx 0.33 \text{ cm}^{-1}$. The VUV light must travel the distance between the generating region and the MgF₂ lens ($L \approx 20 \text{ cm}$), which amounts to a fractional transmission of $\frac{\Phi_{118}(L)}{\Phi_{118}(0)} = e^{-\alpha L} = 1.4 \times 10^{-3}$, which is surprisingly small. However, as shown in Fig. 5.13, even this large amount of absorption is not sufficient by itself to explain the large discrepancy between the first-order theory and the measured 118nm flux.

5.4.4 Optical Breakdown

The final mechanism considered for limiting the conversion efficiency is dielectric breakdown of the Xe/Ar mixture in the presence of intense optical fields. The resulting plasma consists of a very hot, relatively dense ($n_e \sim 10^{17} [e^-/\text{cm}^3]$, Ref [237]) gas of ions and electrons, which amounts to a complete destruction the nonlinear medium. In low-density gases, where the time between e^- -neutral collisions is long compared to the pulse duration, multiphoton ionization is expected to be the dominant source of electrons. At higher pressures, where the mean free time is comparable to pulse duration, electron impact ionization is expected to dominate. In this second process, electrons (whose source is not yet determined) are accelerated by the intense laser field through inverse bremsstrahlung collisions with neutrals. If the electrons are accelerated

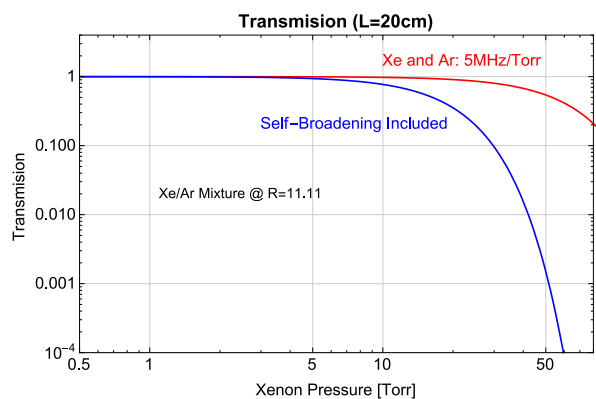
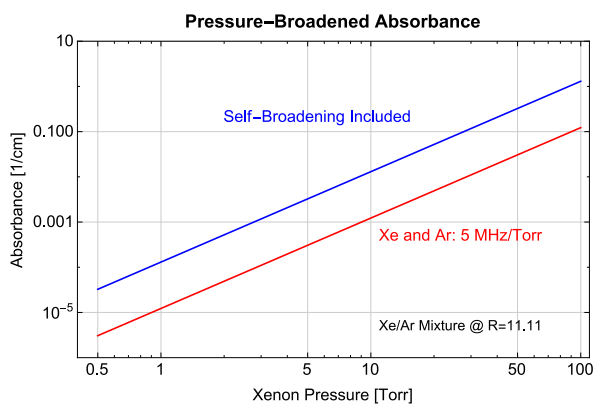
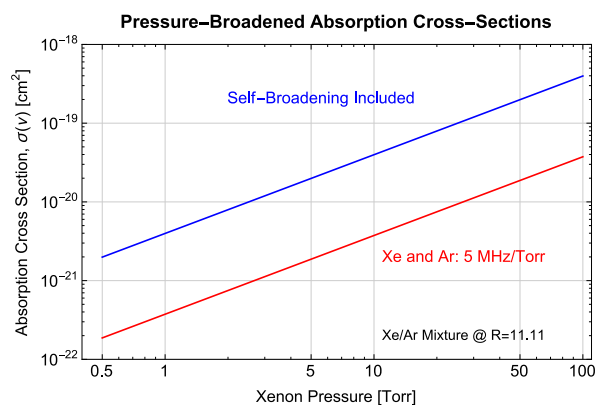
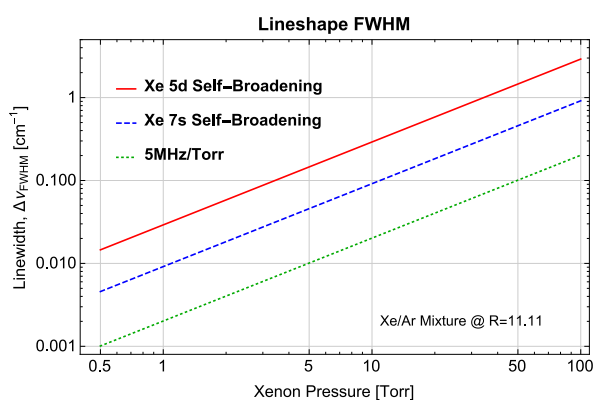
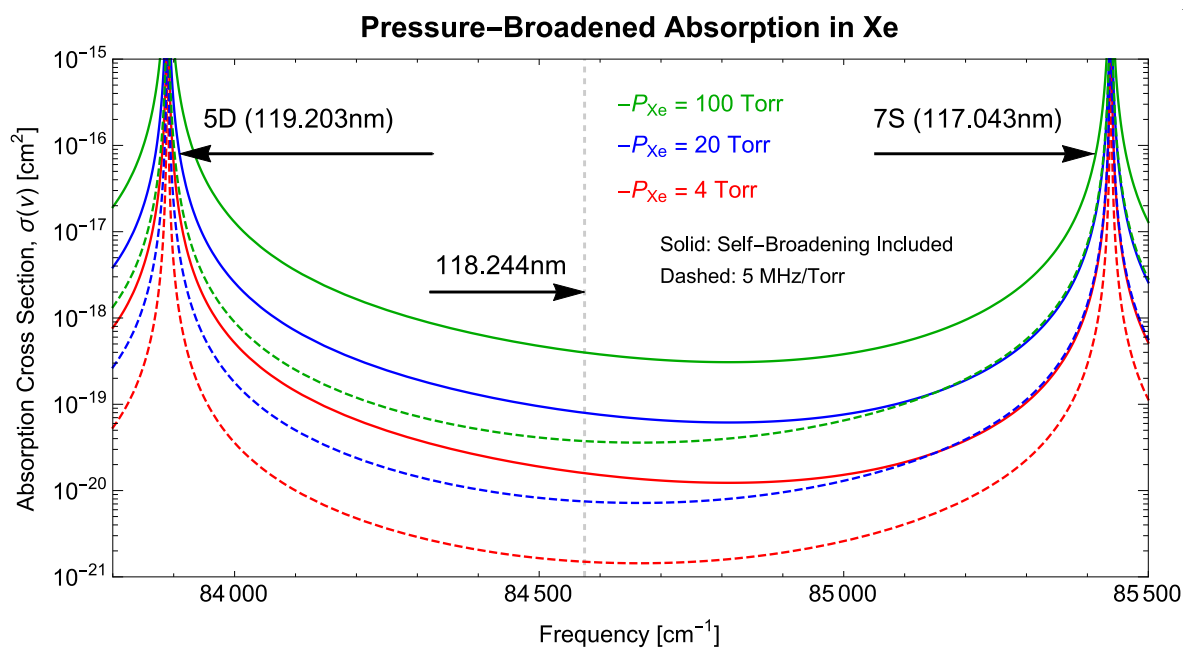


Figure 5.12: Pressure-broadened absorption parameters for the two Xe lines nearest to 118.2 nm. Panel (a) shows the spectral dependence of the absorption cross-section due to both the $5d$ and $7s$ lines as a function of total pressure in phase-matched mixtures. Panel (b) shows the calculated linewidth of the $5d$ and $7s$ Xe lines as a function of xenon pressure. In (c), (d) and (e), parameters are plotted as a function of xenon pressure, but argon is assumed to be present at a $R = 11.11 \times$ higher density.

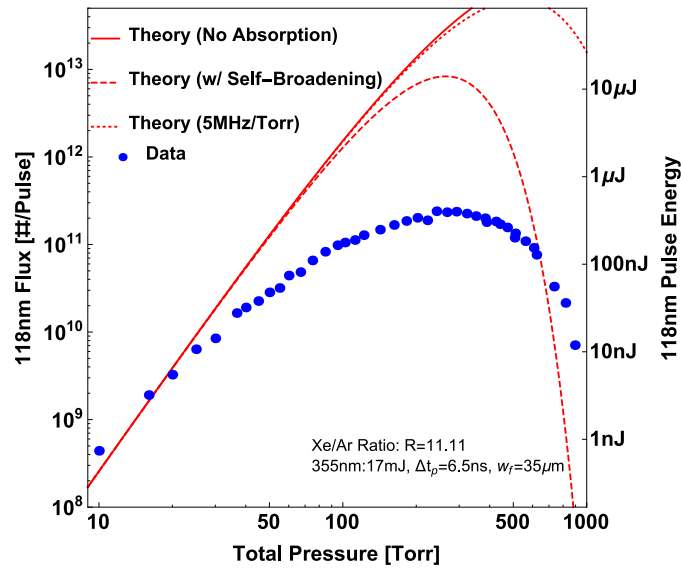
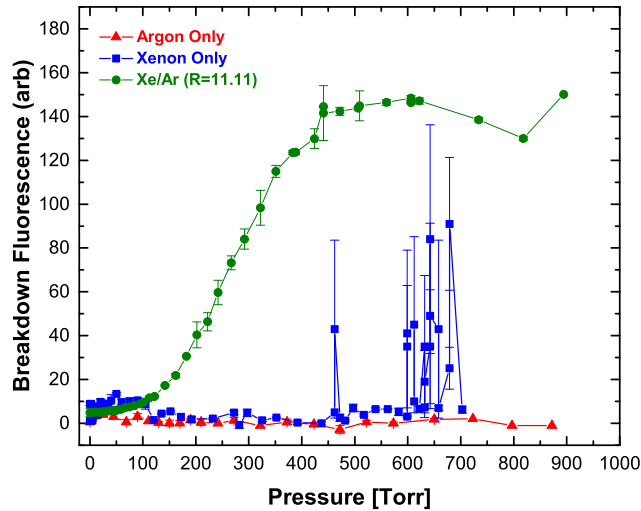


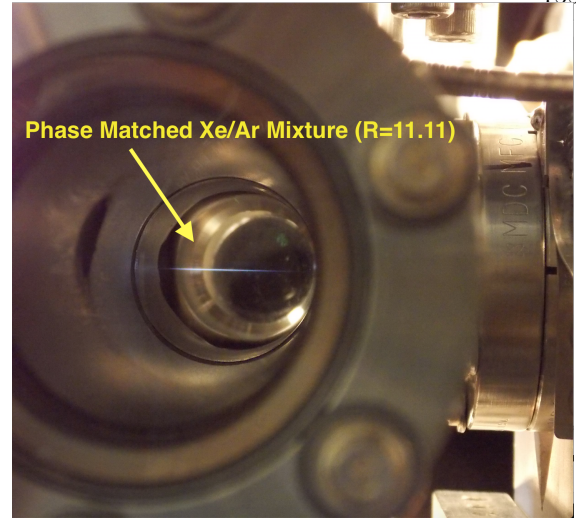
Figure 5.13: Inclusion of absorption into the basic theory given in Sec. 5.3. Even with the inclusion of self-broadening of Xe, for which the fractional transmission can be as small as $\approx 1.4 \times 10^{-3}$ for total pressures of 600 Torr ($P_{Xe} = 50$ Torr), absorption alone is not sufficient to explain the discrepancy between measured flux and that predicted by theory.

to energies above the ionization potential of the atoms in the gas, additional electrons will be generated through electron impact ionization, eventually creating an electron avalanche. This second mechanism of breakdown formation is similar to that of the discharge radical source reported Ch. 3. As long as there are initial seed electrons present, the discharge will be maintained by large electric fields.

Measurements performed in our lab of the onset of optical breakdown in gases are shown in Fig. 5.14a. Fluorescence was spectrally filtered to suppress scattered 355 nm light and imaged onto a photomultiplier tube. Pure argon (ionization potential ≈ 15.76 eV) did not show a detectable breakdown up to intensities of $I \approx 6.8 \times 10^{10}$ W/cm² and pressures of 900 Torr. At this same maximum intensity, xenon (ionization potential ≈ 12.13 eV) began to show signs of breakdown near 600 Torr. The breakdown was highly erratic with only $\sim 1/10$ shots producing a visible breakdown. When breakdown did occur, however, it was very intense flash of light, which John Gray appropriately called “flash bombs”. With room lights only partially dimmed, the interior of the Xe/Ar cell was filled with a blue glow. The data presented in 5.14a were recorded by averaging over many shots, and, as such, underrepresents the intensity of the breakdown that did occur



(a)



(b)

Figure 5.14: (a) Measurements of the intensity of the optical breakdown fluorescence. Data taken at $17\text{mJ}/6.5\text{ns}$ pulse, focused to $35\mu\text{m}$ beam waist. This corresponds to a peak intensity of $6.8 \times 10^{10}\text{W}/\text{cm}^2$. (b) Photograph of optical breakdown in phase matched mixture (green circles in (a)) at total pressure of $\approx 120\text{Torr} \approx 25\text{mJ}$. For the purposes of a photo this was taken at a higher pulse energy than normal.

by a factor of ~ 10 .

These measurements are in reasonable agreement with data presented in Ref [237], the authors of which used a similar multimode laser ($\tau \approx 20\text{ns}$) but with higher intensities. The lowest xenon pressure at which they observed breakdown was $p = 240\text{Torr}$ where the breakdown intensity was $1.29 \times 10^{11}\text{W}/\text{cm}^2$. The p^{-1} scaling of the threshold intensity for breakdown in Xe and Ar at 355nm reported in [237] indicates that the threshold intensity at 355nm is determined by avalanche breakdown rather than by multiphoton ionization. This means that if a secondary source of electrons is present, the breakdown intensity is lowered. Absorbing impurities have been reported to reduce the optical power density at which breakdown occurs [237], [238].

Measurements with a phase-matched mixture of Xe/Ar ($R = 11.11$), however, showed very different behavior. A faint “streak,” somewhat resembling a lightning strike (see Fig. 5.14b for a photograph), could be seen by eye in a dimly lit room beginning around 50Torr total pressure at intensities of $I \approx 6.8 \times 10^{10}\text{W}/\text{cm}^2$ ($17\text{mJ}, 35\mu\text{m}, 6.5\text{ns}$). Thus, one is led to the idea that this form of breakdown, which is absent for pure

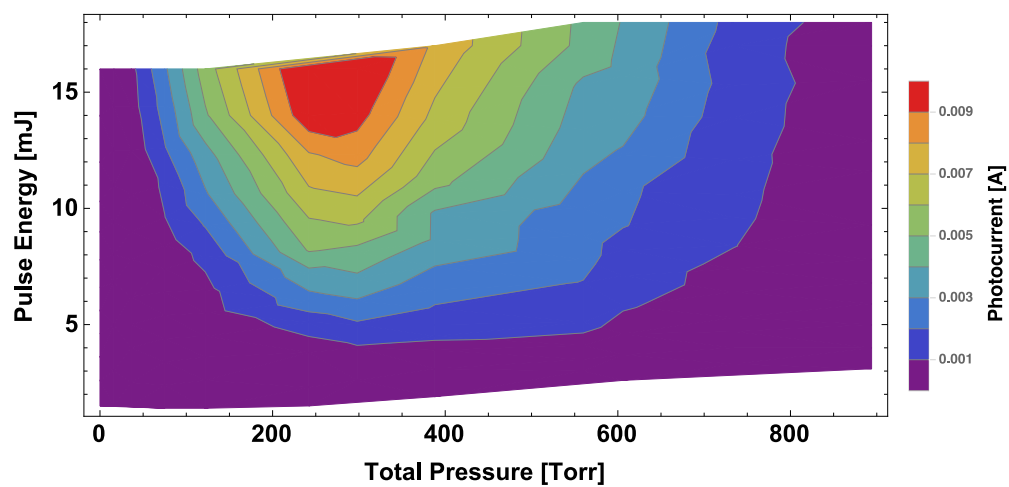
xenon or pure argon, requires 118 nm light to be present.

Simultaneous measurements of the 118.2 nm flux and breakdown fluorescence for phase-matched mixtures (R=11.11) are presented in Fig. 5.15. The maximum 118 nm yield occurs around ≈ 242 Torr of total pressure (≈ 20 Torr xenon) (Fig. 5.15a). The data are plotted on a log-log plot in Fig. 5.16. Up to 100 Torr total pressure, the 118 nm yield increases nearly quadratically ($slope \approx 2.3$) with total pressure as would be expected from the quadratic dependence on $\chi_{eff}^{(3)}$ (see Eq. 5.17 and surrounding discussion). Past this pressure, generation of 118 nm light becomes much less efficient with increasing total pressure ($slope \approx 0.88$), until it reaches a maximum at ≈ 242 Torr.

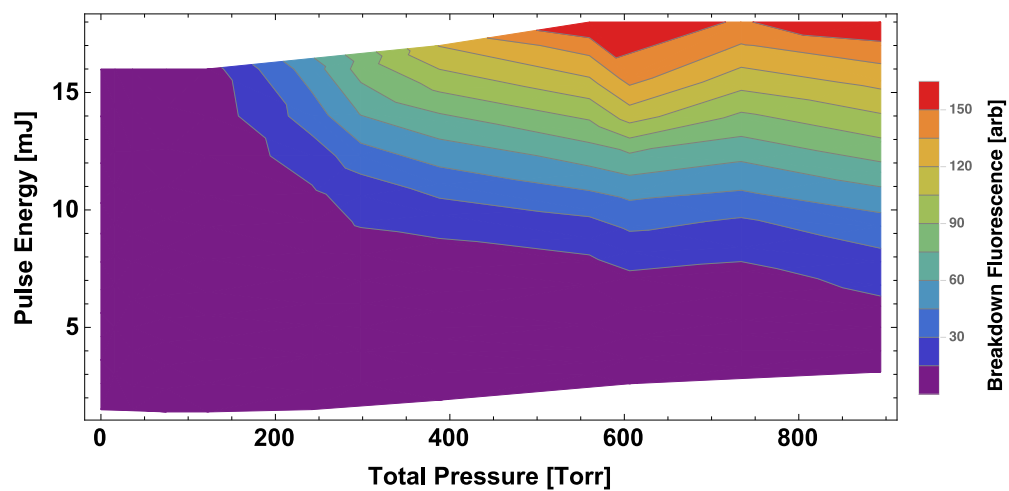
The result of the basic “first order” theory indicates that the third-harmonic yield is independent of the beam intensity and only on the optical power (provided that the tight focusing limit, $b \ll L$ is still satisfied) would seem to indicate that a relatively simple “fix” to the breakdown problem is to simply focus the pump beam less tightly. In practice, however, going to focal lengths much longer than $f = 75$ cm leads to impractically long cells that are incompatible with compact experimental apparatuses. The problems of optical breakdown can be somewhat mitigated by using a longer focal length lens. However, this leads to problems with the laser beam being collimated over a longer distance, which can lead to burns (even from an $\sim 1\%$ back-reflection off of an AR coated windows) of other optics.

5.5 Conclusions

Based on the measurements reported in Sec. 5.4.4, it seems that the dominant mechanism limiting the conversion efficiency of 355 nm \rightarrow 118 nm is dielectric breakdown *initiated* by the 118.2 nm light and *maintained* by the 355 nm light (avalanche breakdown). This emphasizes the critical importance of maintaining a clean, hydrocarbon-free VUV generation system. The attractive feature of 118.2 nm light sources that it is above the ionization potential of the vast majority of organic molecules [197] [223] also turns out to be the origin of the mechanism that limits the attainable VUV flux. For light at energies above $h\nu \approx 10$ eV, this VUV seeded optical breakdown seems unavoidable. It should be noted that harmonic generation with ultrafast pulse durations (ps) that are less than the time required for avalanche to occur (~ 1 ns), is somewhat immune to the avalanche formation at intensities below $\sim 10^{11}$ W/cm² [239].



(a)



(b)

Figure 5.15: Simultaneous measurements of 118nm yield and intensity of optical breakdown fluorescence as a function of a total pressure and pulse energy.

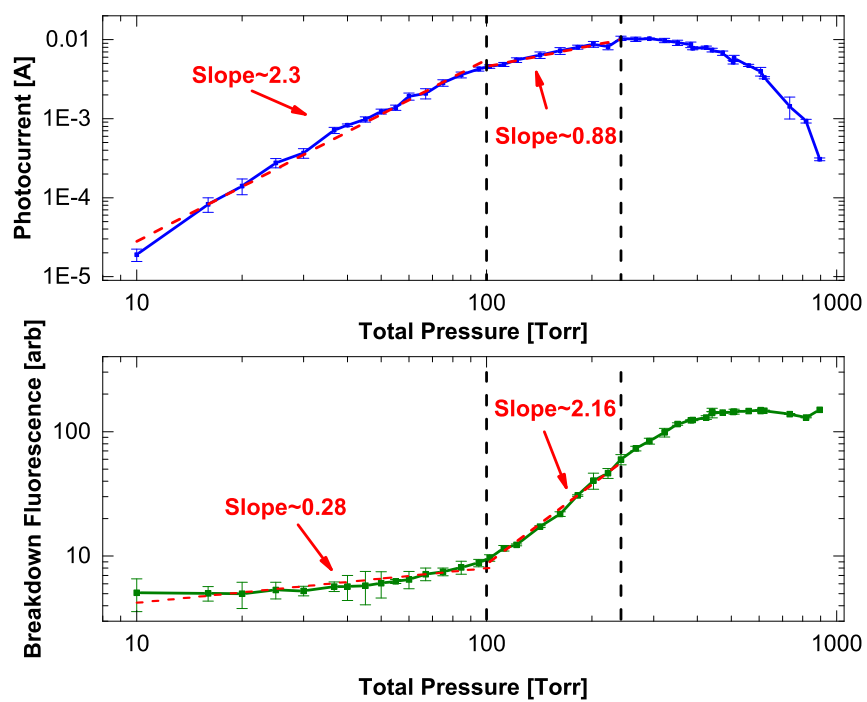


Figure 5.16: Simultaneous monitoring of 118.2 nm flux and optical breakdown fluorescence of phase matched mixtures of the “streak” with a PMT. Vertical dashed lines are located at 100 Torr (the first “knee”) and at 242 Torr, the pressure of maximum yield.

Molecular Detection

6.1 Monitoring Molecular Absorption

A critical aspect of all cold molecule experiments is the sensitivity of the method used to detect the presence of molecules. The various methods are invariably based on the correlation of molecular absorption events (generally quantum-state specific) with the density of the molecular sample. For the most part, these methods are based on driving *electronic* transitions in the absorbing species with lasers in the visible and ultraviolet. Often, this is the practical limitation on the diversity of possible experiments.

The simplest spectroscopic detection method is linear absorption. The basic scenario here is that of an optical beam passing through a sample of gas molecules with an interaction length, L . If the light is resonant with the molecular transitions, some fraction of the optical beam will be absorbed, diminishing the intensity of the beam. From Beer's law, the attenuation factor is given by

$$\frac{I(L)}{I_0} = e^{-\alpha L} \quad (6.1)$$

where α is the molecular *absorbance* in units of $[cm^{-1}]$ and is related to the absorption cross-section, $\sigma [cm^2]$, and the absorber density, $n [#/cm^3]$, by $\alpha = n\sigma$. The “dip” in the transmitted light as the laser is tuned across a resonance is recorded by a photodetector. The sensitivity of this detection method is then determined by the random fluctuations (noise) on the detector output, with the minimum detectable absorption being the absorbance that creates a “dip” on the detector that is larger than the fluctuations from the noise. The minimum detectable absorption in a typical “good” system, can be as low as $(\alpha L)_{min} \approx 10^{-8}$ at 1s

averaging time [240] [241]. Techniques to improve the signal-to-noise ratio of linear absorption methods include bandwidth narrowing techniques [242] such as lock-in detection [243] [244] [245] [246] [247] [240], electronic cancellation of residual intensity noise [248], and using long absorption path lengths enabled by optical cavities [249] [240] [250] [251].

For the detection of molecules in a molecular beam, however, many of these techniques are difficult, if not impossible to implement. In a collimated molecular beam, the absorption path length is typically only ~ 0.1 - 1 *cm*, which seriously limits the overall sensitivity of absorption-based measurements. Mutipass techniques, including cavity ring-down [252], [250], have been succesfully implemented with molecular beams [253] but these experiments are generally aimed at understanding molecular spectra and not diagnostics of the molecular beam. An alternative approach to monitoring the attenuation of the transmitted laser beam, is to directly monitor the absorption itself. There are a number of such techniques (see [241] Sec. 6.3-6.4) but we focus on laser-induced fluorescence and ionization techniques.

A major focus of this chapter is on the detectors themselves, since they represent the first part of a molecular detection method. We follow the advice of P.C.D. Hobbs (Ref [76], 2nd ed, page 91) “The guiding principle of detector system design is this: a photon, once lost, cannot be recovered.” The loss of signal photons/ions before reaching (or failing to be registered by) the detector can never be repaired with electronic post processing. It is thus of critical importance to understand the performance of a given detector, since the signal from it tells you everything about your sample of cold molecules. Indeed, the advantages of fluorescence and ionization methods can largely be attributed to the electron multiplier-based detectors used. For photons, this takes the form of a photomultiplier tube (PMT) and, for ions, a microchannel plate (MCP). Since the noise associated with the electron multiplication process is so low, the detection of single ions or photons is possible with these methods.

The most important detectors used for the experiments in this thesis generate *pulses* of electrons with a time duration of $\tau_p \approx 100$ *ps*- 10 *ns*. The simplest of these are photoemissive detectors which emit large #'s of primary electrons in response to a fast optical pulse. For detection of very low level light (or ions), these photocathodes are coupled to an electron multiplier that generates $G \sim 10^6$ - 10^7 secondary electrons in response to the initial photoemitted electron. In this thesis, PMT's are used to detect single photons and

MCP's are used to detect single ions. Before discussing these two detector types, which are used to detect the molecular absorption events, we discuss a simple, homemade vacuum photodiode used to detect VUV light at 118.2nm.

6.2 A Simple, Compact VUV Vacuum Photodiode

Studies involving the basic physics of VUV generation and/or the ensuing interaction with matter generally require a quantitative description of the VUV photon flux. This task is generally accomplished by a photodetector, i.e., a device whose output signal is proportional to the incident photon flux. The same near universal absorption feature of VUV radiation that makes its production so appealing as a spectroscopic light source also makes it a challenging wavelength to both generate and detect. In this section we describe the design and performance of a low cost VUV detector.

6.2.1 Metal Photocathodes for Detection of VUV Light

In the visible, near IR, and near UV spectral regions, semiconductor-based photodiodes (such as PN junction or PIN) are the detector of choice due to their high sensitivity ($\eta \sim 1$ for Si), long-term temporal stability, compact size, and ease of use. The quantized nature of the photoemission keeps the output signal highly linear which allows the output to be put on absolute terms if the photodetector quantum efficiency, η , is known and stable. Here, η is defined as the number of ejected photoelectrons per incident photon. The high cost and delicate nature of high-sensitivity semiconductor photodiodes (5 nm -254 nm) [254] [255] precludes their use in many laboratories. As a result, rather "old fashioned" detectors based on photoemission from a cathode have remained appealing in the VUV, even though they have been largely supplanted by other types of detectors in other spectral regions.

In principle, the photocathode can be any material with a work function, ϕ , below the photon energies of interest, $h\nu > \phi$ [22] [256]. Unfortunately, the highly sensitive and low-dark-noise alkali photocathodes used in UV-VIS PMT's, including those used for OH, are completely unresponsive below ≈ 165 nm. Alkali iodides and tellurides have a relatively large quantum efficiency [22] in the VUV spectral region (≈ 100 -200 nm) but, unfortunately, are not stable in air. Windowed cesium telluride (CsTe) photocathode detectors

are available for the spectral range of 116nm - 254nm with a peak efficiency of ~ 0.16 near 190 nm . In the windowless VUV region, aluminum oxide, Al_2O_3 (150 \AA Al) (good for $\lambda \approx 5$ - 122 nm) is the preferred material due to its high sensitivity and excellent long-term stability [257]. Calibrated detectors are available from NIST [258] with 2σ uncertainty in the quantum yield between 7-15%.

However, like semiconductor-based VUV photodiodes, the added cost of these ultrastable photocathodes presents a significant barrier for many labs. However, if the photocathode is only to be used in a relatively narrow spectral region near $\sim 120\text{ nm}$ ($\sim 10.5\text{ eV}$), and accuracy within a factor of ~ 2 is all that is required, simple metal cathodes with work functions in the range $\phi \approx 4$ - 6 eV offer a number of appealing features. First, near 120 nm , the quantum efficiency of most metals is \sim few %, which is actually quite competitive with CsTe ($\eta \approx 8\%$) and Al_2O_3 ($\eta \approx 1$ - 2%) [258] photocathodes. Secondly, smooth metal surfaces formed in air are exceptionally stable. The relative uncertainty of the quantum efficiency over the spectral range 20-150 nm is only 30% [259]. In fact, before the development of Al_2O_3 and CsTe photocathodes, metal cathodes were the secondary standard adopted by NIST [259]. The short-term stability at a constant temperature of metal cathodes ($\sim 1\text{ hr}$) is generally acceptable [260]. *In vacuo* heat treating of Cu photocathodes (and other metals in general) was not found to change the quantum yield by more than a factor of ~ 2 [261].

The photoelectric quantum efficiency of polycrystalline copper ($\phi_{\text{Cu}} = 4.65\text{ eV}$ [24]) is shown in Fig. 6.1. These results are typical of metals [261] [262] for which useful photoemission ($\sim 1\%$) starts near $\sim 130\text{nm}$, reaches a maximum of 10 – 20% around 70-90 nm, and decreases to $\sim 1\%$, between 5-20 nm. In the region from 20-130 nm, all metals have quantum efficiencies within 30% of each other [259].

6.2.2 Basic Operating Principles of Vacuum Photodiodes

For high light levels photocathodes can be usefully operated without any form of electron multiplication gain. Such a “bare” detector consists only of a photocathode that emits electrons which are extracted across the vacuum gap by a bias electric field and finally collected by the anode. (See Fig. 6.2a for a cartoon.) These detectors are referred to as *vacuum photodiodes* (VPDs) [263] (sometimes phototubes or simply photoemissive detectors). The photoelectrons moving from the cathode to the anode induce currents

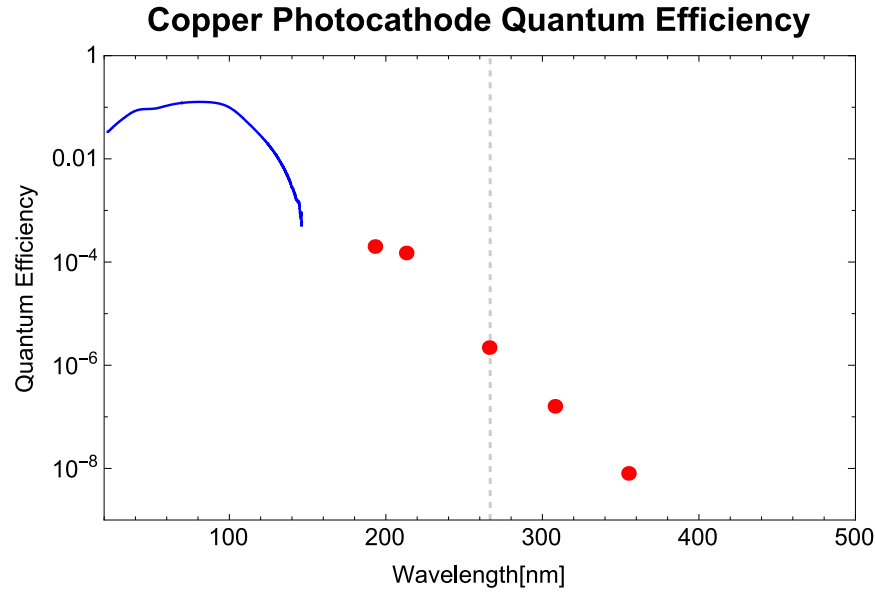


Figure 6.1: Photoelectric Yield, or Quantum efficiency of bulk copper. Blue data is digitized from [22]. The discrete data (red circles) is taken from [23]. From this data we have $\eta_{118} = 0.032$ and $\eta_{193} = 2 \times 10^{-4}$ and $\eta_{355} = 8 \times 10^{-9}$. The vertical dashed line is the work function of copper at $\phi_{Cu} = 4.65$ eV ($\lambda = 266.63$ nm) [24].

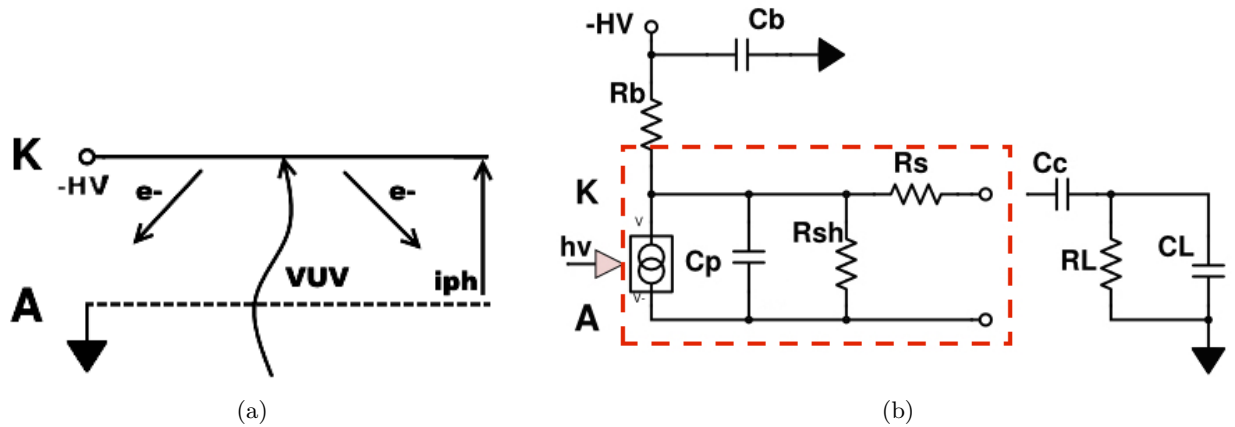


Figure 6.2: (a) Basic setup of a vacuum photodiode and (b) Equivalent circuit used during operation. The components enclosed by the red dashed rectangle, are equivalent elements within the physical detector itself. These include the parasitic capacitance, C_p , the shunt resistance, R_{sh} due to the finite electrical insulation, and the series resistance, R_s . The other elements, including R_b and C_b , for the bias voltage, as well as C_c , R_L and C_L , are discussed in Sec. 6.2.3.2. Thanks to Kevin Loeffler for his help with this figure.

on the cathode(+)/anode(-) given by $i_{ph} = q_e * \eta * \Phi$, where Φ is the incident photon flux in $[\#/s]$. The resulting charge imbalance is discharged through the RC circuit shown in Fig. 6.2b.

For the VPD to provide an accurate representation of the optical signal, the emitted photoelectrons must be successfully collected by the anode. To prevent photoelectron loss due to collisions with background gas, the anode-cathode gap must be evacuated to a level at which the mean free path is much greater than the anode-cathode spacing/distance. In practice, this implies only rather modest vacuum requirements. For example, the total scattering cross-section for electron-N₂ collisions over a wide range of electric fields is not greater than $\sigma_{total} = 10^{-15} \text{ cm}^2$ [264]. (See their Fig. 4.) Thus, for gaps as large as $\sim 0.1 \text{ cm}$, background gases are not expected to be problematic even for vacuum pressures as high as 10 mTorr .

A more serious problem is the space-charge limitations caused by insufficient bias voltages [263]. If the bias voltage is too low, the photo emitted electrons can be reabsorbed into the cathode, setting an upper limit on the total current that can be collected by the anode. To space-charge-limited current density for a given bias voltage can be estimated with the Schottky-Langmuir equation [263],

$$J_a = \frac{4\epsilon_0}{9d^2} \left(\frac{2q_e}{m_e} \right)^{1/2} V_b^{3/2} \quad [A/m^2] \quad (6.2)$$

where d is the anode-cathode spacing and V_b is the applied bias voltage. In general, high photon fluxes and large anode-cathode gaps will require increased voltages. We will return to this point in Sec. 6.2.3.3.

In addition to the photocurrent, the anode also collects the dark current, i_d , and the leakage current due to the finite resistance of the insulation, R_{sh} :

$$i_a = i_{ph} + i_d + V_b/R_{sh}; \quad V_b > V_{sat} \quad (6.3)$$

Ideally, the shunt resistance is sufficiently large that the leakage current is negligible in comparison with the photocurrent. The dark current from a photocathode is predominantly from thermionic emission and can be estimated with the Richardson-Dushman equation [265]

$$i_d = q_e \left(\frac{4\pi m_e}{h^3} \right) (k_B T)^2 A e^{-\phi/k_B T}. \quad (6.4)$$

In Eq. 6.4, A is the area of photoemissive surface, ϕ is the work function of the cathode, and T is the temperature. This current can be extremely small, due to the exponential term in Eq. 6.4. This feature is

exploited in photomultiplier tubes and MCPs for the detection of low light levels but does not play a role in the detection of the high fluxes considered here.

The time response of a VPD can be very fast, in principle limited only by the transit time t_d across the gap [266], [267]. For uniform fields, t_d can be estimated by

$$t_d = d \left(\frac{2m_e}{q_e} \right)^{\frac{1}{2}} V_b^{-\frac{1}{2}} \quad (6.5)$$

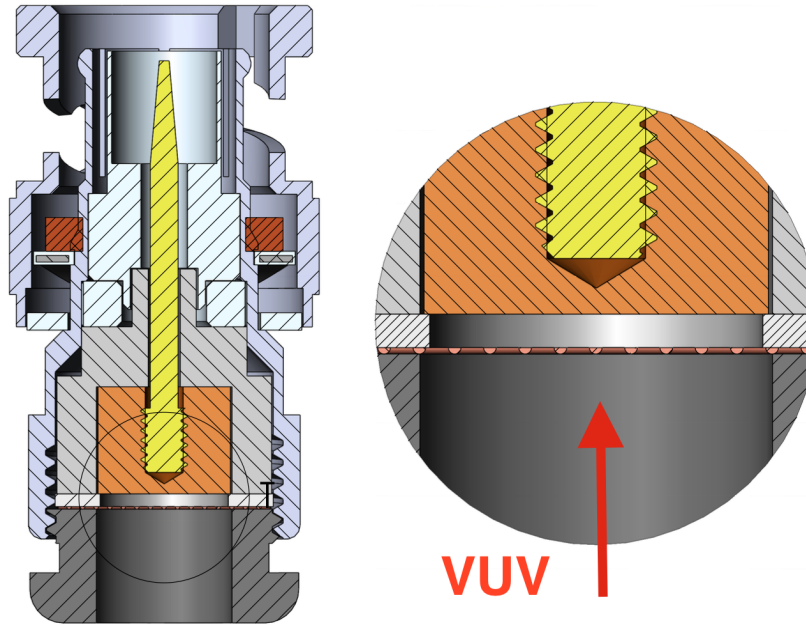
For even modest gap sizes of $d = 500 \mu m$ and voltages of $V_b = 100 V$, $t_d < 0.2 ns$ which is more than adequate time resolution for experiments with ns pulsed lasers. In practice, the measurement circuit (see Fig. 6.2b) will be the limiting factor determining the time-response of the detector.

6.2.3 Design and Performance of Homebuilt Vacuum Photodiode

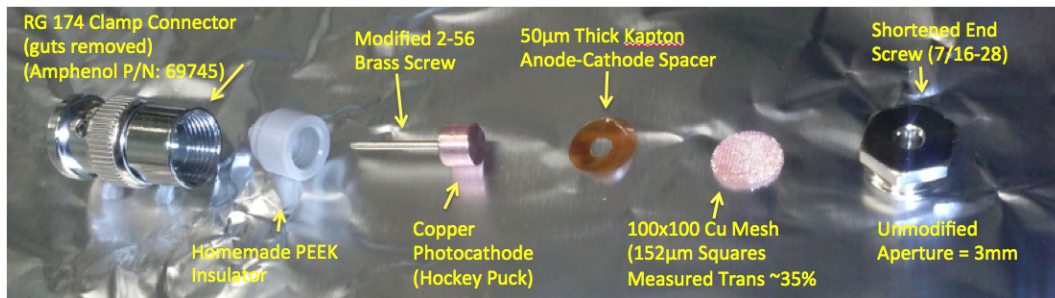
6.2.3.1 Mechanical Design

Our primary design criteria were based on the desire for a low-cost, compact and reasonably accurate (accuracy $\approx 50\%$) VUV detector. The only available vacuum port in a line of sight with the $118 nm$ propagation direction was a 1-1/3 CF flange, which meant that the complete detector assembly had to be less than $\approx 1.5 cm$ in cross-section. Inspired by the design reported in Ref [268], we opted for a design based on a BNC connector that could be easily incorporated into a standard vacuum feedthrough.

The detector shell is a BNC clamp style connector body with all interior “guts” removed. The particular model (Amphenol RF P/N: 69745-RG-174) was chosen for a large interior volume to allow for flexibility in the small parts incorporated into the interior. A cross-sectional view of the final design is shown in Fig. 6.3a. The copper photocathode was machined on a lathe from standard electric-grade copper, and the surface was lightly sanded with 1000-grit sandpaper. A modified brass screw (2-56) forms the center pin of the BNC connector. Details on construction of these parts are given in Fig. 6.4. A plastic insulator securely holds the copper photocathode in a “cup” and electrically isolates the cathode and center pin from the exterior of the BNC connector body. The anode-cathode spacing is set by the $600 \mu m$ insulating PEEK spacer. Details on these insulating parts are given in Fig. 6.5. A fine copper mesh (see Fig. 6.3b) with a



(a)



(b)

Figure 6.3: VUV vacuum photodiode base on BNC clamp plug. Panel (a) shows a cross-sectional view of the final design and panel (b) shows an annotated assembly of the first-generation detector. For the final design the kapton film insulator ($50\ \mu\text{m}$ thick) of the first-generation detector was replaced with a $600\ \mu\text{m}$ thick PEEK insulator (shown in (a)) and the end cap/screw was drilled out to a $6.35\ \text{mm}$ clear aperture and shortened to a final length of $5.3\ \text{mm}$. The order in which the parts are installed is the same as indicated here. Note that the ID of the PEEK spacer is smaller than the OD of the copper photocathode. This is important to keep the photocathode from shifting. Detailed descriptions of the individual parts is given in Fig. 6.4

measured transparency of $\approx 35\%$ forms the anode.

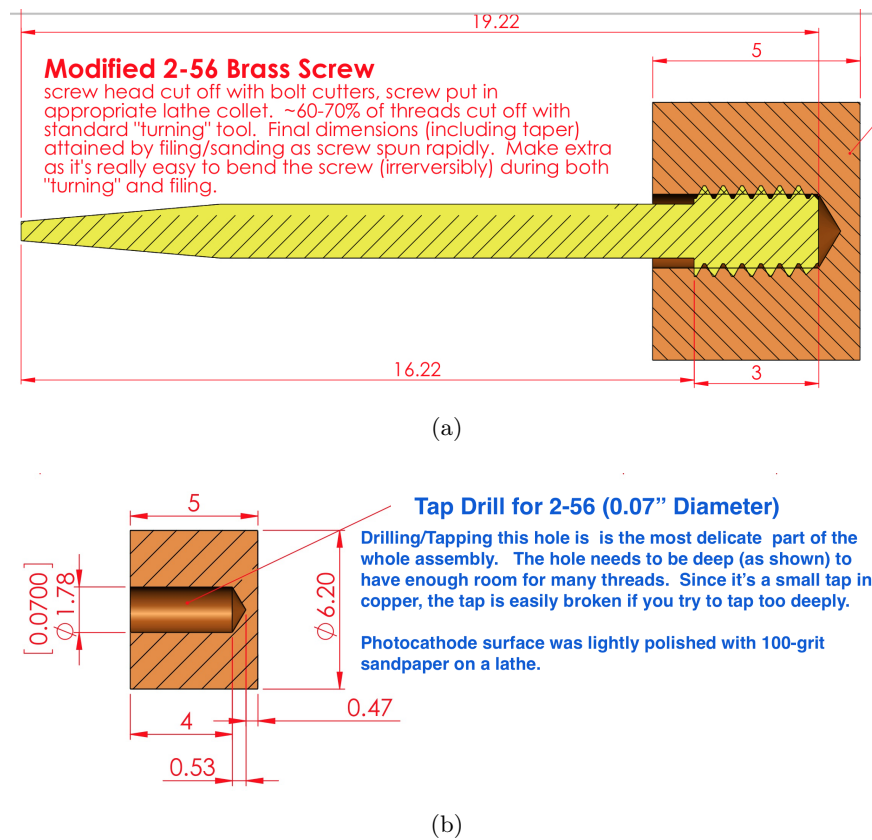


Figure 6.4: Construction details for the Cu photocathode and conducting center pin. (a) Detail of the copper photocathode and the modified 2-56 brass screw which becomes the center pin of the BNC connector. (b) Detailed description of the manufacturing process for the photocathode.

6.2.3.2 Electrical Design

The choice of front end [76],[269] [270] front end for a given detector is dictated by the photon flux, the desired frequency bandwidth and noise. The primary applications here are for the detection of rather intense VUV $\tau_p \approx 5\text{-}10\text{ ns}$ pulses at 193 nm and 118.2 nm light. Using the quantum efficiency data shown in Fig. 6.1, the the detector is expected to be $\sim 160\times$ more sensitive at 118.2 nm than at 193 nm (on a "per photon" basis). At 355 nm , the detector is mostly solar blind¹, being 4×10^6 more efficient at 118 nm than 355 nm .

Taking a reasonable number for a "high" flux at 118.2 nm to be $\approx 10^{11}$ photons/pulse and assuming a photoelectron collection efficiency near unity, this amounts to $3.2 \times 10^9\text{ e}^-/\text{pulse} \approx 5 \times 10^{-10}\text{ C/pulse}$. The

¹ The term "solar blind", is a historical, but ubiquitous, remnant [22] that simply means "unresponsive to visible light."

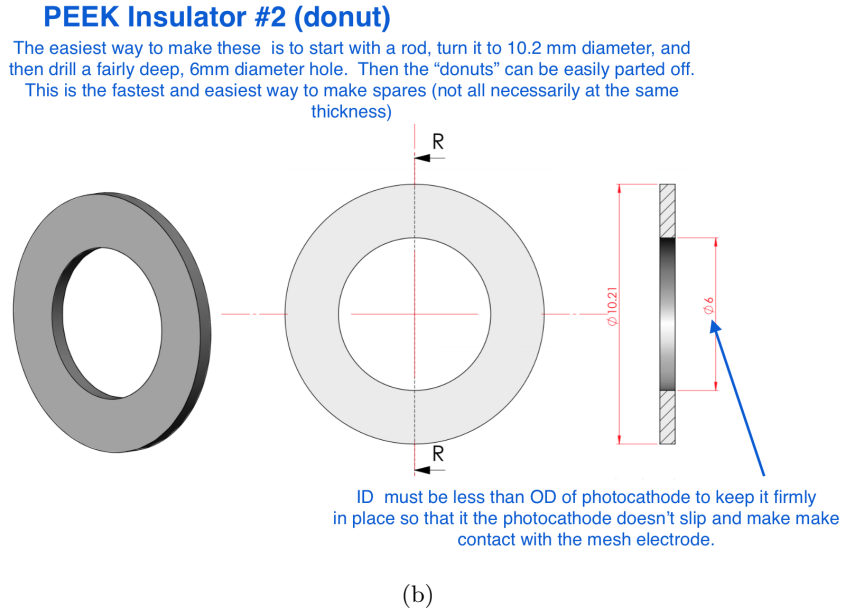
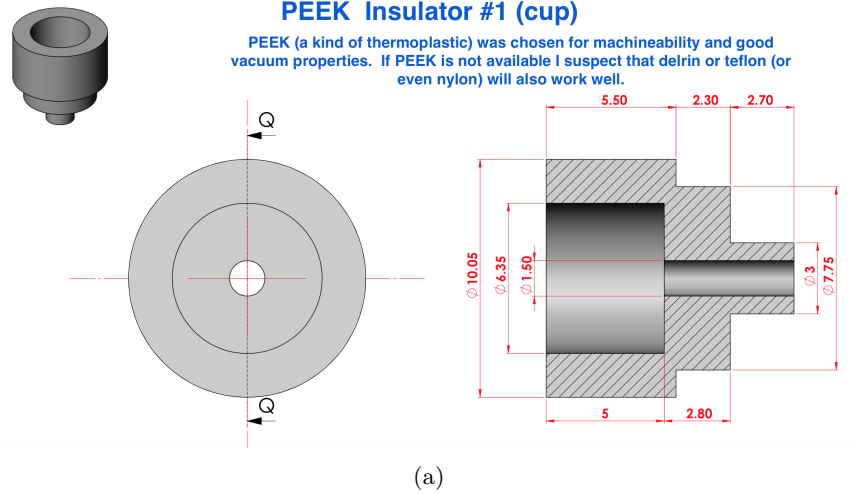


Figure 6.5: Detailed description of plastic (PEEK) insulators for the copper VPD. (a) shows the cup that securely holds the photocathode, insulating it from the body of the BNC connector, and (b) is the insulating “donut” that sets the anode-cathode spacing at $600\mu m$. Thanks to Ian Collet for excellent and expedient craftsmanship on these parts for the second generation detector.

average photoelectron/current rates from a 10Hz laser system are very low ($\approx 3.2 \times 10^{10} e^-/s = 5 \times 10^{-9} A = 5nA$), but the peak currents delivered during the $\tau = 5-10 ns$ pulse are larger by a factor of $\approx 10^7$ (that is, taking a nominal pulse duration to be $7 ns$ this amounts to roughly $4.5 \times 10^{17} e^-/s$ or $73 mA$). These incredibly high currents are easily detected by simply dumping the current across a 50Ω load to generate

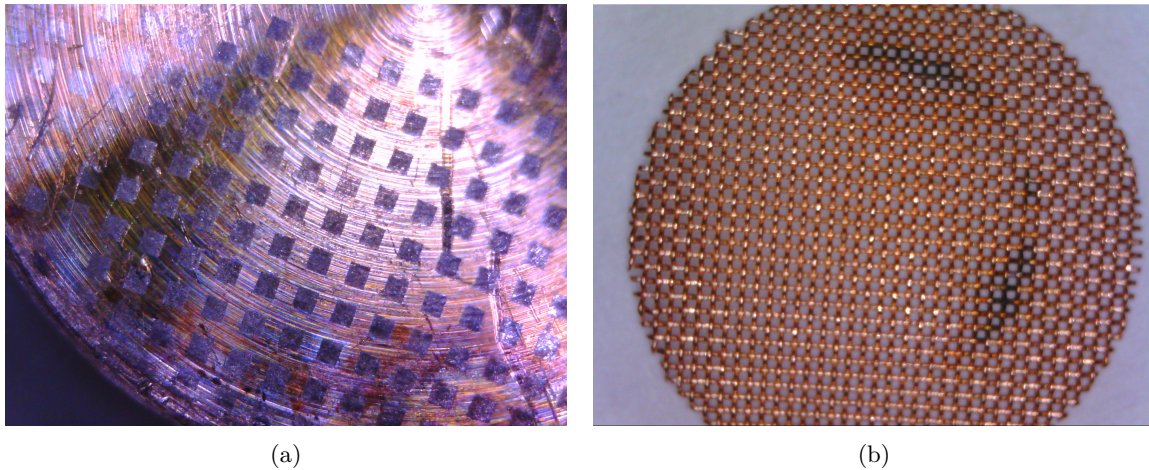


Figure 6.6: Irreversible damage to photocathode (a) and copper mesh (b) due to a short caused by intense 355nm when operated at high voltages. The dark squares on the photocathode (a), corresponds to the open squares in the mesh (b) After this incident, the anode-cathode spacing was increased from $50\mu m \rightarrow 600\mu m$. Since then, the detector has been operated without problems.

peak voltages of near 3.6V. In our lab where technical pickup noise from flash-lamps, Excimer thyratrons, and our Stark decelerator, can be as large as 10 mV on an oscilloscope, the value of $10^9 \# / pulse$ sets a reasonable lower limit for detection of 118.2 nm where the voltage is simply dumped across a 50Ω load.

The details of the detector operating circuit must be carefully considered in order to preserve the photoelectric current collected by the anode. Above the saturation voltage of, $V_b > V_{sat}$, the VPD is well approximated by the standard photodiode equivalent circuit shown in Fig. 6.2b. The circuit elements (equivalent sense) comprising the detector itself (and feedthrough) is indicated in the dashed box in Fig. 6.2b, including the inter electrode capacitance, C_p ; the shunt resistance, R_{sh} , formed by finite electrical insulation; and a series resistance, R_s . Before installing the assembled detector into the vacuum chamber, a HV insulation tester is used to check that $R_{sh} > 2 G\Omega$. For a bias voltage of $\sim 300 V$ and $R_{sh} \sim 2 G\Omega$ the leakage currents will be negligible ($I_{sh} \approx 150 nA$). The contact resistance ($\sim 1\Omega$) can usually also be ignored. The capacitance of the bare detector was measured with an LCR meter to be $C_p \approx 6 pF$ which is reasonably consistent with a parallel plate estimate of $\sim 0.5 pF$ for a $600 \mu m$ gap. With the feedthrough attached, the the total capacitance increases to $C_p \approx 30 pF$.

Supplying the bias voltage through a large resistor, R_b , placed close to the detector prevents reflections

down and back the cable supplying the high-voltage². The resistor value should be chosen so that the charge stored on the detector parasitic capacitance, C_p is prevented from discharging through the RC network formed by R_b and C_p . If the time constant $\tau = R_b C_p$ is kept very long compared with the optical pulse duration, very little of the signal charge is lost before escaping through the coupling capacitor, C_c . The charging time constant $\tau = R_b C_b$ should also be short compared to the repetition rate of the laser system, so that the storage capacitor completely recharges before the next optical pulse reaches the detector. For 10Hz laser systems this is actually a rather modest requirement. For a bias resistor of $1\text{ M}\Omega$, this indicates that to keep the $R_b C_b$ time constant less than 10ms, this suggests a capacitor in the range $C_b < 10\text{ nF}$.

Since in this implementation the high-voltage signal is directed applied to the cathode, it must be AC-coupled with a decoupling capacitor, C_c . To monitor pulse fluctuations of ns - pulsed lasers, a bandwidth of $f_{3dB} = \frac{0.35}{\tau_{rise}} = 35\text{-}350\text{ MHz}$ is required. This indicates that the coupling capacitor should have a low impedance at these frequencies, requiring a large (low ESR) capacitance in the range of $10\text{-}100\text{ nF}$.

6.2.3.3 Performance

The performance of the Cu detector was measured with an ArF excimer at 193nm and with 118nm light obtained by tripling 355nm light in a Xe/Ar cell. The experimental setup for generating 118nm light has been described in detail in Ch. 5.

The choice of the anode-cathode gap spacing is very important. A large spacing keeps the capacitance low, but in principle decreases the e^- collection efficiency, and, thus, the total amount of current collected. A small gap reduces the electron transit times and lowers the bias voltages required to operate the detector in the saturation regime for large photocurrents. Initially, attempts were made to use a very small anode-cathode gap of $d \sim 50\ \mu\text{m}$ (see Fig. 6.3b) determined by the thickness of kapton film insulator. This implementation showed saturation of 20 mA peak current at a bias voltage of only $\approx 20\text{ V}$. However, after a few days of use in the 118 nm system, the detector became irreversibly damaged due to intense residual 355 nm light (see Fig. 6.6). Measurements of the bias voltage saturation behavior for an anode-cathode

² Alternatively, the bias voltage could be supplied through a very long cable ($\sim 3\text{-}5\text{ m}$), so that the transit time down the cable is much longer than the pulse duration, which keeps the reflected pulse from overlapping with the original pulse, thus minimizing the distortion of the signal.

spacing of $600 \mu m$, with and without a copper anode mesh, are shown in Fig. 6.7. Inclusion of a mesh anode (transmission $\approx 30\%$) reduces the absolute signal size by roughly a factor of ≈ 3 but reduces the voltage required to be operated in the saturation regime. Thus, the mesh is recommended for situations where photon fluxes are high but only low bias voltages are available. We have observed that the detector can be used without a mesh at bias voltages of $V_b \approx 300 V$ up to peak currents of $\sim 3-4 mA$. However, including the mesh reduces the required bias voltage required for saturated operation for a given flux. In general, the bias voltages required for actual implementation are significantly larger than those predicted by Eq. 6.2 (by about a factor of 10). This is attributed to a) the field not being truly uniform, and b) deviations in the effective value of d caused by warping of the mesh.

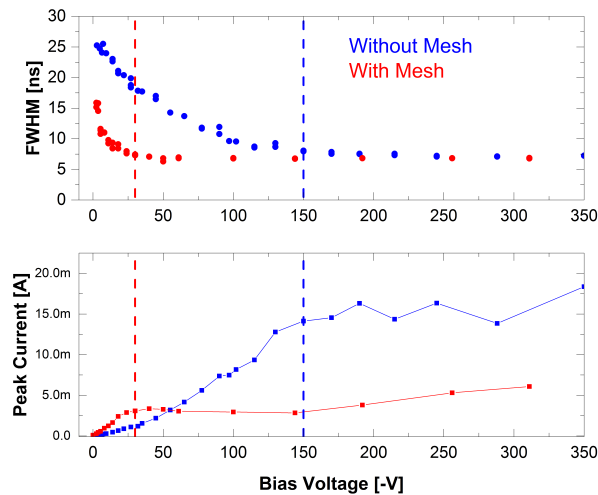


Figure 6.7: Bias voltage saturation behavior at an anode-cathode spacing of $\approx 600 \mu m$ measured with an ArF excimer at $193 nm$. For details, see text.

The linearity of the detector (with an anode-cathode spacing of $50 \mu m$) was measured with a ArF excimer laser at $193 nm$ (reproducible light source) and compared against a calibrated silicon power meter (see Fig. 6.8). The observed deviations are within the factor of 2 of the design criteria for this detector.

6.3 Introduction to Ionization Spectroscopy: Application to ND_3

On a per-ion basis, ionization spectroscopy is an inherently sensitive technique due to the high collection efficiency and the ease of incorporating a charged particle directly into an electronic measurement. The

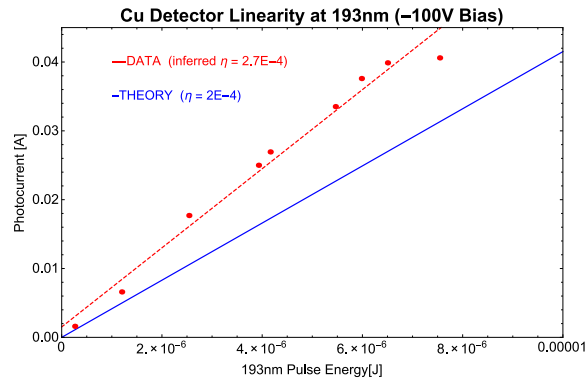


Figure 6.8: Cu VPD linearity measured at 193 nm. These measurements were made with a anode-cathode spacing of 50 μm . Measured signal sizes were within $\sim 50\%$ of the predicted values. Theory calculation assumes $\eta_{193} = 2 \times 10^{-4}$, $\tau_{193} = 7.5 ns$. The horizontal axis corresponds to the pulse energy incident on photocathode. This is based on pulse energy measurements directly outside vacuum with a calibrated Si power meter (optimized for deep UV) and accounts for 80% and 35% transmission of vacuum window and anode mesh, respectively.

majority of laser-based ionization schemes require a step-wise multiphoton process, because a single photon does not typically have enough energy to directly ionize the atom or molecule. The transition rate of an n -photon transition can be calculated using perturbation theory [271] [272] to be of the form

$$W^{(n)} = \sigma^{(n)} \Phi^n \quad [1/s] \quad (6.6)$$

where Φ is the laser photon flux in $[\#/(s * cm^2)]$ and $\sigma^{(n)}$ is the n^{th} order cross section with units of $[cm^{2n} s^{n-1}]$. This simple $\propto I^n$ power law only holds when there are no intermediate steps. Compared with one-photon absorption, multiphoton absorption is inherently improbable. Typical values for 1-photon absorption cross sections are $\sigma^{(1)} \sim 10^{-17} cm^2$, while those for 2- and 3- photon absorption are $\sigma^{(2)} \sim 10^{-51} cm^4 s$ and $\sigma^{(3)} \sim 10^{-82} cm^6 s^2$, respectively.

For the purposes of making rough estimates, suppose that the laser in question has the following characteristics: $\lambda = 300 nm$, 10 mJ/10ns pulses focused to $w_0 \approx 30 \mu m$. This amounts to a photon flux of $\Phi \approx 5 \times 10^{27} [\#/(cm^2 \cdot s)]$ or an optical intensity of $I \approx 3.5 \times 10^9 [W/cm^2]$. These photon fluxes are sufficient to excite a reasonable fraction of the ground state molecules to the excited state through a 2-photon process. Before discussing the results on multiphoton ionization of ND₃ we discuss the detector and experimental setup used for all data presented here.

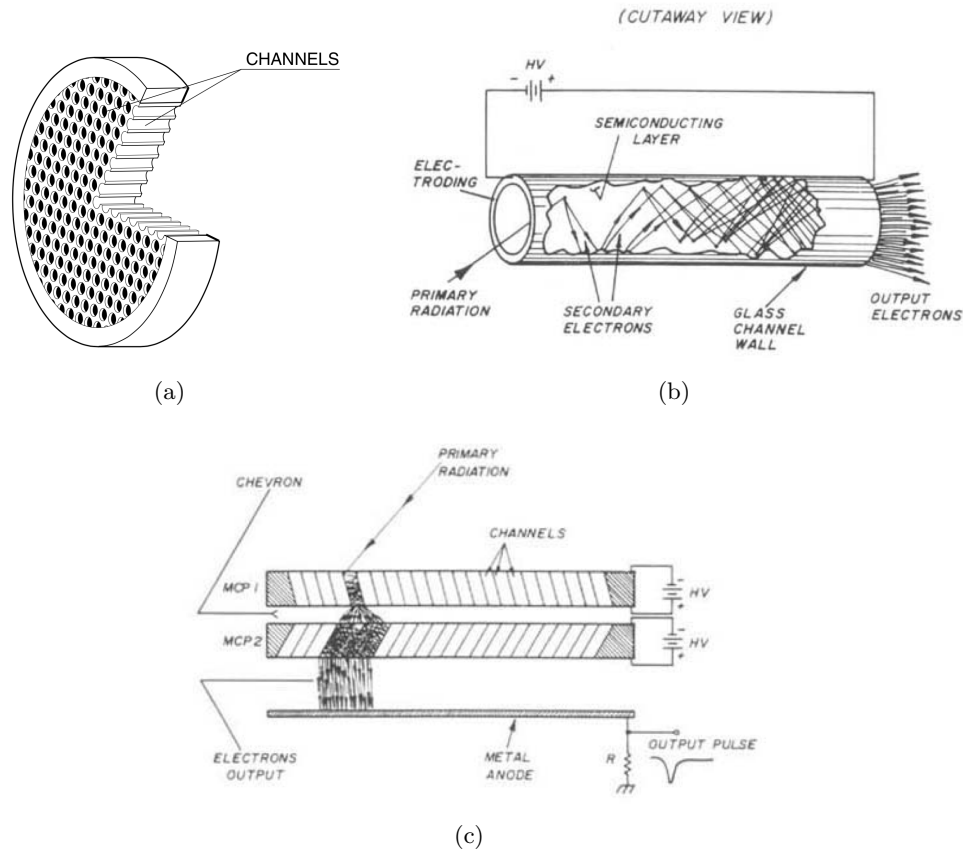


Figure 6.9: Microchannel plate (MCP) electron multipliers. (a) Schematic diagrams of a microchannel plate. (b) Electron multiplication within a single straight channel electron multiplier. (c) Cartoon/schematic of a chevron configuration dual MCP detector. (b) and (c) from Ref [25]

6.4 The Micro Channel Plate

The ion detector used for all experiments described in this thesis is a micro channel plate (MCP), a schematic of which is shown in Fig. 6.9a. The MCP is a two-dimensional array of small glass capillaries (diameter, $d \sim 15\text{-}25 \mu\text{m}$) bundled into a thin disc with metal electrodes (typically Inconel or Ni-Cr) evaporated onto each side.

With a high voltage applied to the electrodes, each capillary acts as an independent electron multiplier, as shown in Fig. 6.9b. If a primary electron strikes the inner wall of the channel, secondary electrons will be emitted. The secondary electrons are accelerated to high energy from the large electric potential applied to either side of the MCP plate, knocking out more electrons. This process, each stage of which is described

by the secondary emission coefficient, γ , results in a very large number of electrons being emitted at the output from a single input electron. Analogously with the dynode stages of PMT's, the overall gain, G , is given approximately by $G = \delta^n$ where n is the effective number of stages. The gain factor is an intrinsic characteristic of the channel wall material and is a function of the electric field intensity inside the channel. For the lead glasses typically used in MCP plates (Corning 8161), secondary emission coefficients are typically not greater than 2. The maximum gain obtainable from a MCP plate depends on the length-to-diameter ratio of the channels, $\alpha = L/d$, by

$$G = e^{\delta * \alpha} \quad (6.7)$$

The maximum gain from a MCP plate is obtained by making α larger, which allows for more collisions with the inner channel walls. Typically, the gain of a single plate cannot be made larger than $\sim 10^4$, because of the noise due to ionization of residual gas molecules in high energy electron collisions. If these ions find their way to the input face of the MCP, they can generate spurious (noise) ion signals. To avoid this, α is usually chosen to be around 40, so that a single MCP provides a gain of about 10^4 at $1kV$. If larger gains are required as for detection of single ions (or photons), larger gains can be obtained by using a cascade of MCPs stacked in close proximity to each other, with alternating bias angles as depicted in Fig. 6.9c. This stacked configuration minimizes the effect of ion feedback because the ions generated from residual gases are absorbed at the junction between each MCP.

In addition to the overall larger gain, dual-stage MCPs have the additional benefit of a peaked pulse height distribution, as opposed to the exponential falloff from a single-stage MCP [273]. This is beneficial in pulse counting applications because the ion signal is well separated from the baseline noise, which allows complete suppression of analog noise sources (such as EMF noise, which is problematic with Q-switched lasers and Stark decelerators) with a voltage height discriminator level.

6.4.1 RM Jordan Dual Chevron Detectors

The MCP assembly used for all experiments described here is a dual/chevron detector from Jordan TOF [99] with a 40 mm diameter and with 25 μm diameter channels spaced center to center by 32 μm .

The open area ratio specified by the manufacturer is ≥ 0.45). HV is applied to the MCP plates through a voltage divider circuit (see Fig. 6.10 for simplified schematic), which allows for operation with a single power supply and precludes the need for a matched set of MCP plates. The voltage drops across the resistor stages indicated in Fig. 6.10 are calculated assuming that the large resistance of the MCP plates ($\approx 300\text{ M}\Omega$) is infinite. At a nominal supply voltage of 3.5 kV (5 kV), the potential difference across each plate is -700 V (-1000 V).

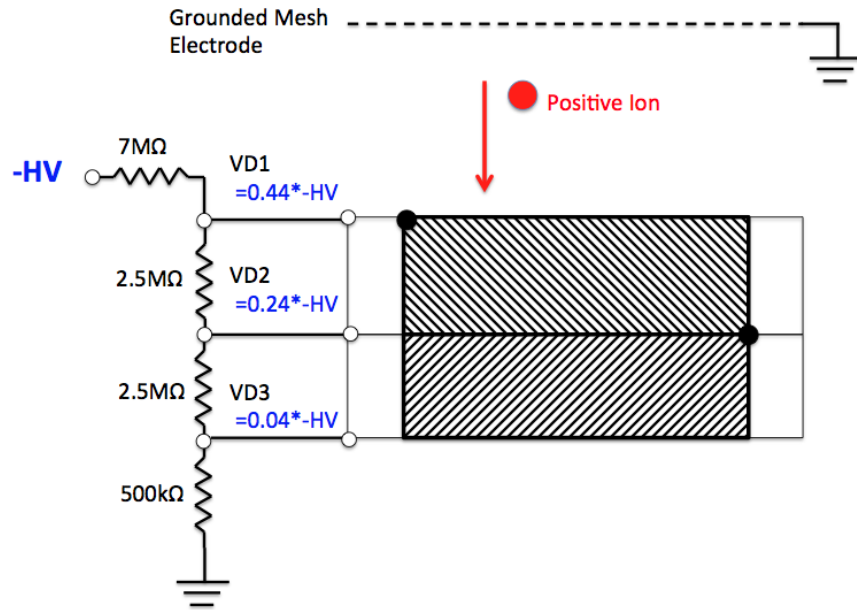


Figure 6.10: Depiction of the standard voltage divider in our Jordan MCP. With this voltage divider in place, nominal voltages up to $-HV = 5\text{ kV}$ ($\Delta V = 0.2 \times HV = 1\text{ kV}$ max per plate). The solid black circles on the diagram of the MCP plates indicate the alignment marks on the plates themselves.

Since the MCP lifetime is shortened by prolonged operation at high voltages (1 kV per plate max), the assembly is typically operated at 700 V per plate. The output is fed into a preamp (Transimpedance, $Tz = 5.1\text{ k}\Omega$, $f_{3dB} \approx 5\text{ MHz}$) for additional amplification. The “peaked” signal distribution under these conditions is shown in Fig. 6.11. Note that this measurement is for the integrated signal and not the more traditional “voltage height” used in pulse counting measurements. This analysis allows the number of detected ions to be known on an absolute scale.

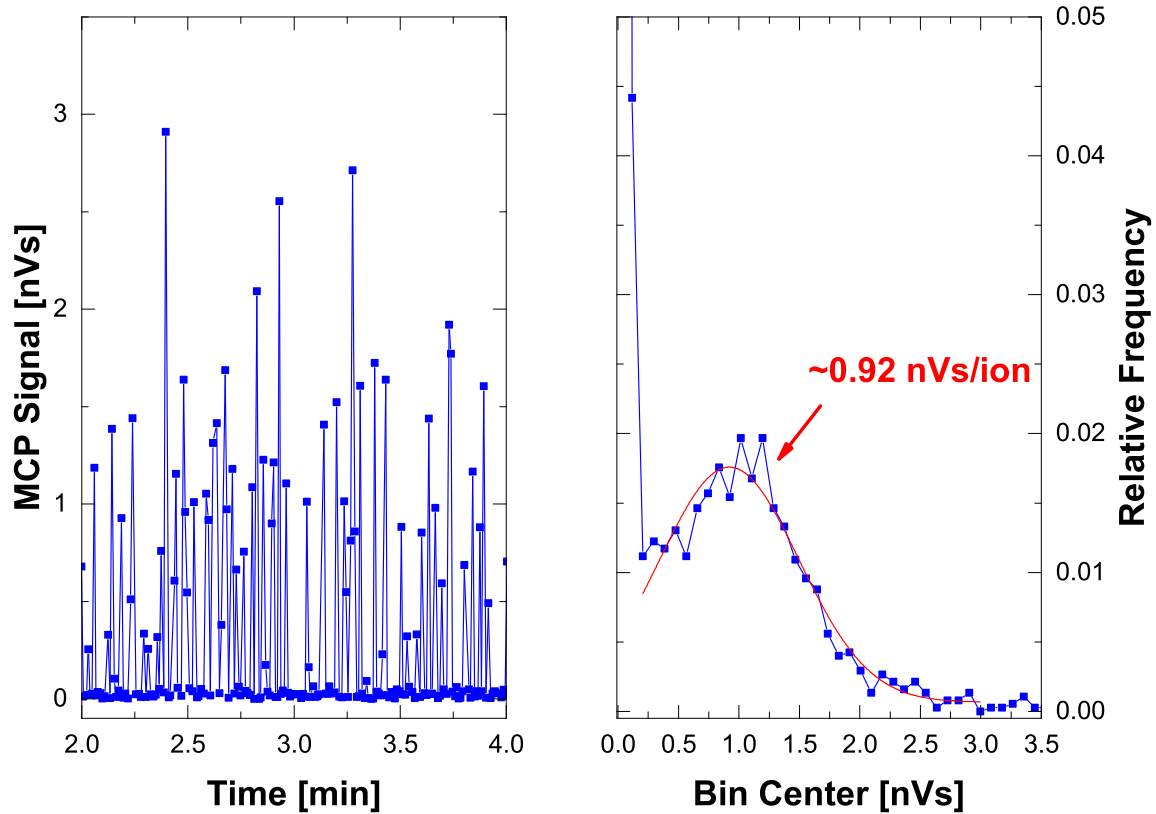


Figure 6.11: Integrated signal from MCP detector (700V/ plate) with preamp ($T_z = 5.1k\Omega$, $f_{3dB} \approx 5 MHz$) vs. time for low count rates. Data were taken by attenuating 118 nm flux (by lowering flux at 355 nm) until it looked “by eye” to be in the single ion/shot limit. The resulting “blinking” seen in the left panel is indicative quantized ions being detected. The panel on the right shows a histogram of the data shown on the left, returning a value of 0.92 nVs/ion.

6.4.2 Time of Flight Mass Spectrometers (TOFMS)



Figure 6.12: Schematic of different regions and voltages used to describe a generic two-electrode TOFMS, the free flight region for mass separation, and a MCP ion detector with a repeller grid.

Here we consider the arrival time of ions in a time of flight mass spectrometer. This flight time depends on mass of the ion, the magnitude of the accelerating fields, as well as the position within the electrodes at which the ion is created (neutral is ionized). The position within the electric field plates where ionization takes place, can be given in terms of the parameter α (see Fig. 6.12). For $\alpha = 1$, the ion is created just to the right of the back ($+\Delta V_1$) plate so that the ion is accelerated through the full potential ($+\Delta V_1$) and $\alpha = 0$ corresponds to the ion being created at the front plate so that it is accelerated through a vanishingly small electric potential.

The time it takes the ion to reach the front surface of the MCP plate after being ionized by the laser pulse at $t = 0$ is

$$t_{tot} = t_1 + t_2 + t_3 \quad (6.8)$$

where the subscripts refer to the amount of time spent in the regions described in Fig. 6.12. For simplicity we assume that the electric field plates/electrodes are large enough that they create a uniform field of magnitude $|\mathbf{E}| = \Delta V_1/L_1$ so that the forces are constant and always in the z -direction. This assumption is good for parallel electrodes and greatly simplifies the analysis. The ions can be assumed to be created at rest, which is valid for large applied voltages. (This is a valid assumption since the velocity imparted to the ions by the ion optics will be vastly larger than the initial velocity of the neutral, even for velocities as high as 450 m/s .)

Working through the simple kinematic equations gives the time spent within the TOFMS plates (region 1), t_1 , as:

$$t_1 = \sqrt{\frac{2m\alpha L_1}{qE_1}} = \sqrt{\frac{2m\alpha L_1^2}{q\Delta V_1}} \quad (6.9)$$

$$t_2 = \frac{L_2}{v_1} = \frac{L_2}{\sqrt{\frac{2q\alpha\Delta V_1}{m}}} \quad (6.10)$$

$$t_3 = \frac{-v_1 \pm \sqrt{v_1^2 + 2\frac{q\Delta V_3}{m}}}{\left(\frac{q\Delta V_3}{mL_3}\right)} \quad (6.11)$$

where $v_1 = \sqrt{\frac{2q_e\alpha\Delta V_1}{m}}$.

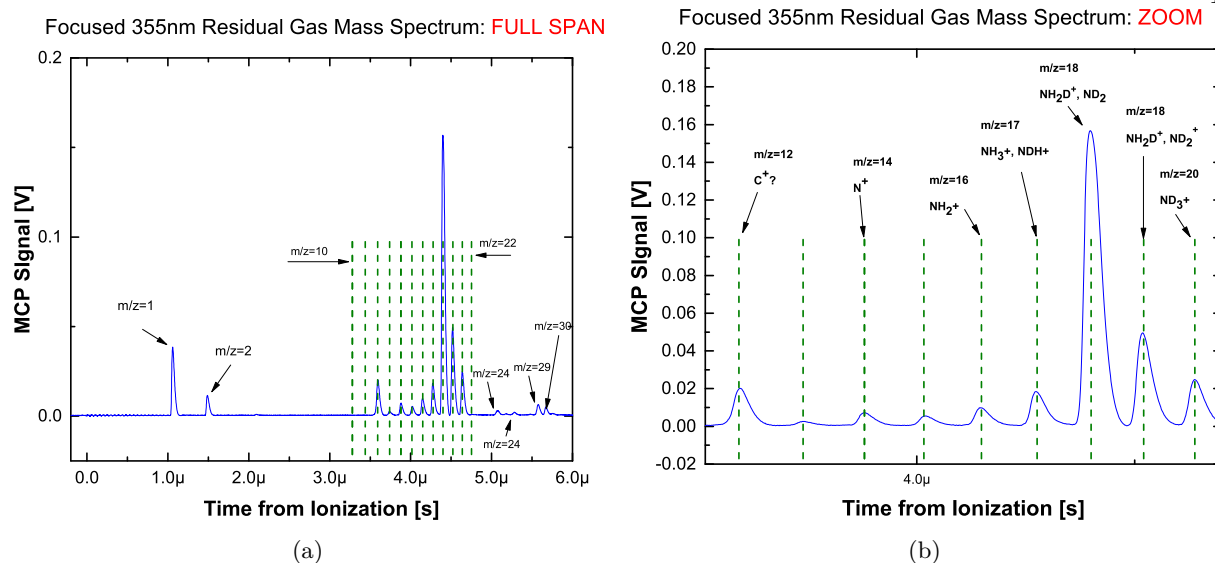


Figure 6.13: Mass spectrum obtained by focusing 355nm light in the center of the extraction plates filled with a residual background gas of ND_3 molecules ($T \approx 295\text{K}$). This measurement was made several minutes after switching off ND_3 gas flow admitted directly into the vacuum chamber. With the gas flow on, the ND_3 peak ($m/z = 20$) is larger by a factor of 20-50). The presence of other mass peaks is attributed to the other isotopomers of ammonia, which presumably originate from a $D \rightarrow H$ substitution upon collisions with the vacuum chamber walls (or the gas supply lines). Possible molecular species assignments are indicated in both (a) and (b) with black arrows. The focused beam waist is estimated at $\approx w_f \approx 30\mu\text{m}$.

By mapping out the arrival time of an ion of known mass, the value of α can be determined, which then allows the determination of the arrival times of other mass ions. This is very useful for the detection of small signals, since you know exactly when to look. Ion TOF distributions calibrated in this way for 355nm light focused into a residual gas of ND_3 are shown in Fig. 6.13.

An additional complication of working with small gaps between HV electrodes and intense UV lasers is damage to the electrodes themselves, and to the MCP, from the HV ions created from ablating the electrodes. Photographs of an MCP damaged in this way are shown in Fig. 6.14.

6.4.2.1 Calibration of 118nm flux with ND_3 ionization

As an introduction to ionizations based methods, we consider an alternative detection method to the vacuum photodiode presented in Sec. 6.2. This technique consists of filling the vacuum chamber with a low flow rate of a gas of known ionization cross-section (in this case ND_3) and recording the resulting ionization

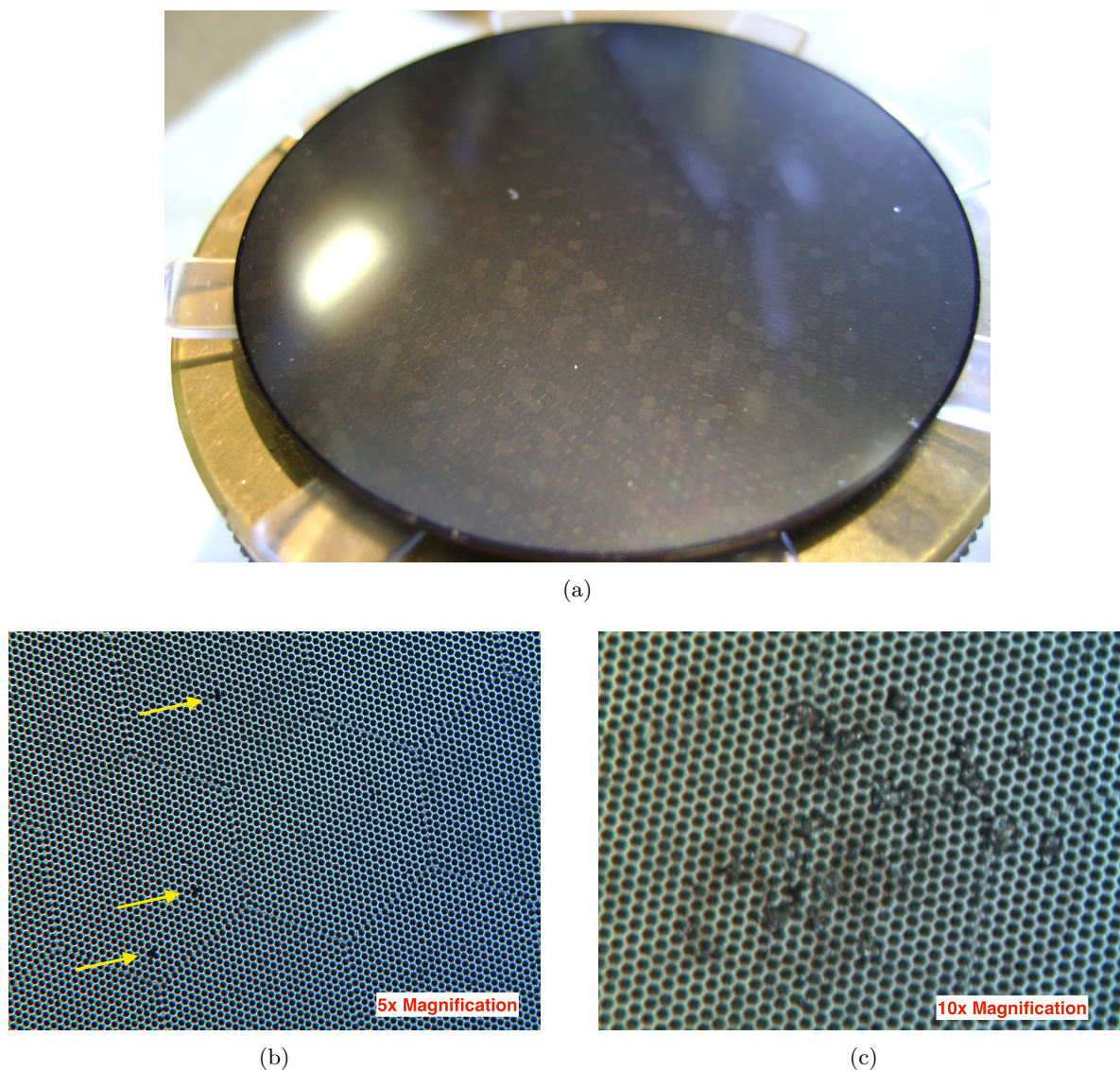


Figure 6.14: Damaged MCP plates. Panel (a) shows a photograph of an MCP taken with a standard camera. The “leopard spots” seen here fill the larger hexagonal subunits of the honeycomb structure. These features seem to be unique to this particular pair of damaged MCP plates, but at present, the origin of the discoloration is not understood. Panels (b) and (c) show images taken in the Keck lab at JILA with an optical microscope at magnifications of $5\times$ and $10\times$ respectively. Channel diameter is $d \approx 25 \mu\text{m}$. The honeycomb structure seen in (a) can also be seen in (b). The “holes” shown in (b) marked by yellow arrows could be the result of manufacturing defects or surface ablation from high-energy ions. The damage seen in (c), however, is almost certainly the result of high energy bombardment for intense ion bunches. (Note: This figure does not print well and is best viewed on a high resolution monitor.)

signal with the standard TOFMS electrodes and MCP. This technique is analogous to ionization chambers [22], which allow absolute calibration of the VUV photon flux; however, this method has the advantage

that it may be done *in situ*, allowing the absolute VUV flux in the interaction region to be measured on a day-to-day basis.

For single photon ionization with 118.2 nm light, the rate of ion production is

$$\frac{dN_i^{(prod)}}{dt} = \sigma_i \frac{\Phi}{A} N_0, \quad [\#ion/s] \quad (6.12)$$

where $\sigma_i = \sigma_{abs} * \gamma$ is the photoionization cross-section in [cm^2], Φ is the laser flux in [$\#photons/s$], N_0 is the number of neutral (ground state/absorbing) molecules within a volume, ΔV , intercepted by the laser beam. If the molecular density is uniform across ΔV , then N_0 is simply, $N_0 = n_0 \Delta V = n_0 A * L_{int}$. Then Eq. 6.12 becomes

$$\frac{dN_i^{(prod)}}{dt} = \sigma_i \Phi n_0 L_{int}, \quad (6.13)$$

which reflects the fact that the 1-photon absorption rate is independent of the beam cross-sectional area. For single photon ionization to the continuum, relaxation can be neglected. Then the number of ions per pulse is simply:

$$\delta N_i^{(prod)} = n_0 \sigma_i \Phi_{pulse} * L_{int} \quad [\#ions \text{ produced/ pulse}] \quad (6.14)$$

Not all of the ions produced will be detected. These losses can be accounted for by including an ion collection efficiency factor, $\eta_{ion} \leq 1$, in Eq. 6.14 such that

$$\delta N_i^{(det)} = \eta_{ion} \times \delta N_i^{(prod)} \quad (6.15)$$

η_{ion} can be partitioned into two parts

$$\eta_{ion} = \chi * \xi \quad (6.16)$$

where χ is the overall detection efficiency of the MCP assembly including losses due to finite open area ratio and ξ is the ion extraction/collection efficiency of the electron optics including the transparency losses of all mesh electrodes (including those on the MCP). The absolute detection efficiencies of low-mass ions

($\leq 40 \text{ amu}$) accelerated to potential energies above $\sim 2.5 \text{ keV}$ have been measured to have absolute detection efficiencies asymptoting to the MCP open area ratio [274] [275], which for our MCP is $\chi \geq 0.45$.

The uniformity of the TOFMS electric fields was investigated using finite element modeling (COMSOL Multiphysics software). Ion trajectory simulations using these field calculations indicate ion collection efficiencies of $\sim 80\%$ across the 13 mm plate separation, with a weak decrease of $3 - 4\%$ for molecules ionized close to the grounded (back plate). Typically, a large extraction voltage is used to make the ion trajectory's insensitive to patch fields downstream of the plates in the drift tube. Including the mesh transparencies which are estimated at 50% and 90% for the TOFMS and MCP respectively, gives the total collection efficiency of $\xi = 0.8 * 0.5 * 0.9 = 0.36$. Then the overall detection efficiency of our MCP is estimated to not be greater than $\eta_{ion} = \chi * \xi = 0.45 * 0.36 = 0.162$.

$$\delta N_i^{(det)} = \eta_{ion} \delta N_i^{(prod)} = 0.45 * 0.36 \delta N_i^{(prod)} = 0.162 \delta N_i^{(prod)} \quad (6.17)$$

The density of neutral ND_3 molecules (for the moment ignoring what specific quantum state they are in) in the vacuum chamber can be inferred from

$$n_0 = \frac{\beta \Delta P_b}{\kappa} \quad (6.18)$$

where $\beta \approx 3.27 * 10^{16} \text{ \#}/(\text{cm}^3 * \text{Torr})$ (for $T = 294.15 \text{ K}$), ΔP_b is the pressure *rise* when the ND_3 gas flow is on, and κ is the ion gauge correction factor [276]. For κ_{ND_3} , we take the value for NH_3 of $\kappa_{\text{NH}_3} = 1.23$ based on the similarity of the electron impact ionization cross-sections for the two species [277] [278]. An additional factor of C_{press} could be included in Eq. 6.18 as a correction factor accounting for a drop in pressure between the detection region (where the density is detected by the laser) and the location of the pressure gauge [279]. However, this factor is neglected here. Since the molecules are not detected in a direct line of sight from the place where the molecules are introduced, it is safe to assume that they will undergo many collisions with the 300 K walls and any expansion cooling will be negligible. (This will be important later in the calibration of state-dependent ionization signals.)

Then, the VUV flux is given in terms of the ND_3 density and the $\#$ of detected ions as

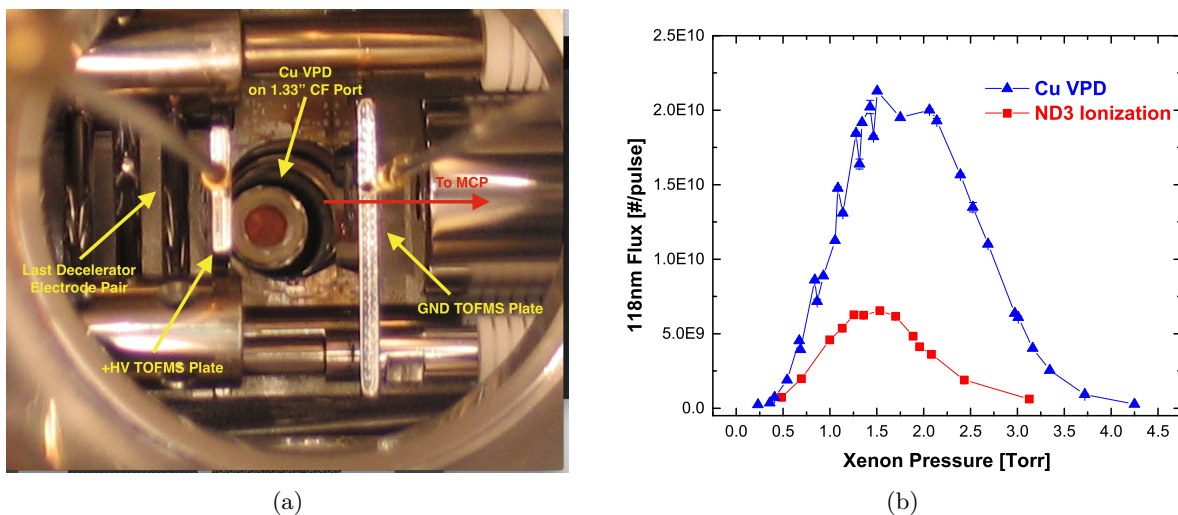


Figure 6.15: Comparison of 118nm flux measurements. (a) Experimental setup for comparison of 118nm flux measurements made with Cu VPD and ND₃ backfill ionization method. Note “spotted” surface damage on the interior of the vacuum chamber walls surrounding the VPD. (b) direct comparison of two completely independent calibration methods to detect 118nm light. The discrepancy between the two methods is approximately a factor of ~ 3 .

$$\Phi_{pulse} = \frac{\delta N_i^{(prod)}}{n_0 \sigma_{ion} L_{int}} = \frac{1}{\eta_{ion}} \frac{\delta N_i^{(det)}}{n_0 \sigma_{ion} L_{int}} \quad (6.19)$$

where n_0 is given by Eq. 6.18. Measurements of the 118 nm flux with this technique are directly compared to those made with the Cu VPD in Fig. 6.15. The agreement between the two is not perfect, but given that the fluxes are calibrated using completely independent methods, the disagreement between them of only a factor of ~ 3 given the spectral region, is satisfactory for our purposes.

6.4.3 2+1 REMPI of ND₃ near 317nm

This section presents an analysis of the sensitivity of resonantly enhanced multiphoton ionization (REMPI) of ND₃. The primary goal this section is to a) provide a comparison to the ionization results of OH presented at the end of this this chapter as well as b) to provide a means of calibrating the density of ND₃ deceleration data. The detection limit of REMPI can be expressed in terms of the minimum density required to reliably generate 1 ion per shot. If all intermediate steps are saturated, then every molecule within the focal volume will give rise to 1 ion. The mode quality of dye lasers is notoriously poor, but,

nevertheless, we can estimate the focal volume by assuming a lowest order Gaussian mode. A collimated beam of waist (radius) w_0 will be focused to a new waist, w_f , and Rayleigh range, z_R , given by

$$w_f \approx \frac{\lambda f}{\pi w_0}; \quad z_R \approx \frac{\pi w_f^2}{\lambda} = \frac{\lambda f^2}{w_0^2} \quad (6.20)$$

Calculated Gaussian beam profiles for a beam focused with $f = 50\text{cm}$ and $f = 75\text{cm}$ lenses are shown in Fig. 6.16. If one is detecting molecules in a decelerated beam, the interaction distance is limited to the space distance between the decelerator rod pairs, $L_{int} \approx 2.0\text{mm}$, to give an interaction volume of $V_{int} = \pi w_f^2 \times L_{int} \approx 6 \times 10^{-6}[\text{cm}^3]$ (or $1.6 \times 10^{-5}\text{cm}^3$ if one is backfilling the chamber with a gas, and the interaction length is the diameter of the hole in the TOFMS plates). If the transition were saturated, then the minimum detectable density for a decelerated beam would be $n_{min} \approx \frac{1}{V_{int}} = 1.55 \times 10^5 [\#/ \text{cm}^3]$.

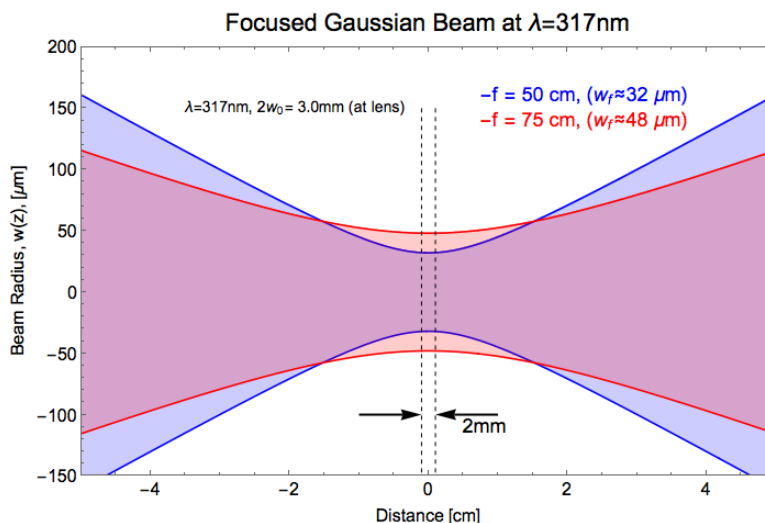


Figure 6.16: Estimated focal volume for a dye laser beam focused with 50cm and 75cm lens. The effective interaction length for detection of a decelerated beam of $L_{int} = 2.0\text{mm}$ is indicated with vertical dashed lines.

However, measurements of the intensity dependence of the ion yield for the 2+1 REMPI scheme exploiting the \tilde{B}^1E'' intermediate state near 317nm^3 show a quadratic dependence on laser intensity (Fig. 6.17a.) This result, which indicates that we are not in the saturation regime, is reasonable considering that one expects the initial 2-photon absorption to be rate-limiting as opposed to the final 1-photon ionization

³ The REMPI transitions are labeled according to $2\nu''$. We will only populate the ground vibrational state, $\nu'' = 0$. The specific v

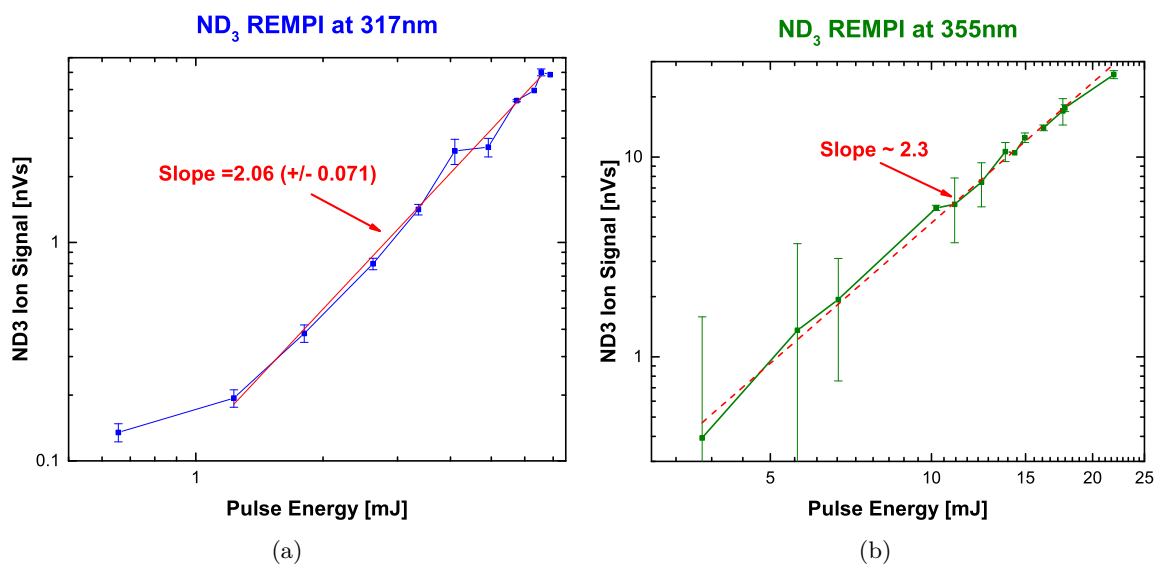


Figure 6.17: Measured power laws for multiphoton ionization of ND₃. Panel (a) shows measurements for the standard 2+1 scheme at $\approx 317\text{nm}$ using the $\bar{B}^1 E''$ state as a 2-photon resonant intermediate. Panel (b) shows measurements made at 355nm. In both panels the relative ion yield is plotted on the vertical axis as a function of the incident pulse energy (horizontal axis). For details on the multiphoton ionization of ND₃ at 355nm shown in (b), see text.

step. Fig. 6.17b shows a similar measurement made by tightly focusing 355nm into the center of the TOFMS plates, and filling the chamber with $T \approx 295\text{K}$ ND₃. The observed power law is closer to 2 than 3, indicating that the 355nm light is coincidentally resonant with a 2-photon transition in ND₃, as opposed to the ion signal being the result of non resonant 3-photon ionization. Very little seems to be known in the literature about this transition, except for a brief comment made in the introduction of Ref [280]. Since this ion signal originates from $T \approx 295\text{K}$ gas, and the laser used is not tunable, it is not known what initial state is being excited. It seems unlikely that the 355nm laser would accidentally resonant with a transition from the $|1, 1\rangle$ state that is amenable to deceleration, but, if so, this could be a very simple detection method for other experiments.

To estimate the absolute sensitivity of these ionization methods, pure is ND₃ introduced to the vacuum chamber (see also Sec. 6.4.2.1). The number of ions detected as a function of the total ND₃ density (inferred from the vacuum pressure rise) is shown in Fig. 6.18a for direct photoionization at 118nm (circles) as well as 2+1 multiphoton ionization at 317nm (squares) and 355nm (triangles). The photon fluxes used for

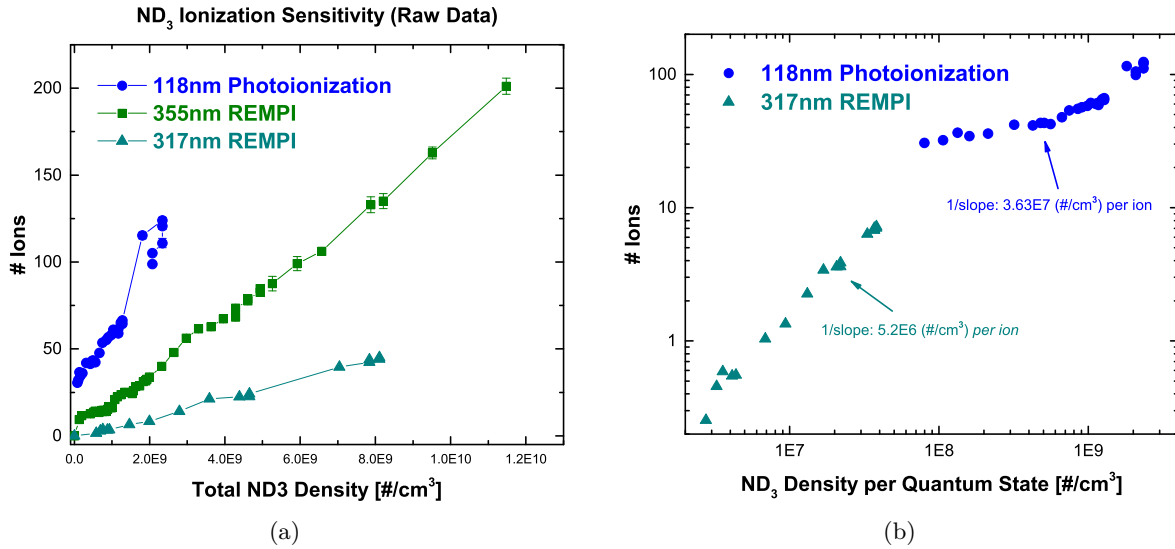


Figure 6.18: Sensitivity of ND_3 ionization schemes. Direct photoionization at 118nm (circles) is compared to 2+1 multiphoton ionization at 317nm (squares) and 355nm (triangles). The photon fluxes used for these measurements were $\approx 10^{11}$ #/pulse at 118nm, 7mJ/pulse or 10^{16} #/pulse) at 317nm, and 17mJ/pulse, 3×10^{16} #/pulse at 355nm. Panel (a) shows the raw data, with the horizontal axis corresponding to the total ND_3 density (ignoring the distribution of quantum states). The horizontal axis in panel (b) has been scaled to correspond to the density *per quantum state* and is thus a direct measure of the sensitivity of the given detection method. The inverse slopes indicated in (b) are approximately, the minimum detectable density to generate 1 ion/shot over an interaction length of $L = 0.5$ cm.

these measurements were $\approx 10^{11}$ #/pulse at 118nm, 7mJ/pulse or 10^{16} #/pulse) at 317nm, and 17mJ/pulse, 3×10^{16} #/pulse at 355nm. All three measurements were made essentially the largest practical flux for each light source (larger fluxes are possible at 355nm, but one begins to rapidly destroy optics at higher fluxes) and as such, the data in Fig. 6.18 presents a reasonable upper limit to the detection sensitivity available in our experiments. To estimate the absolute sensitivity, the important quantity is not the ion yield as a function of the total density, but rather the density *per quantum state*.

The REMPI transition at 317nm is only resonant for ND_3 molecules initially in the $|1, 1\rangle$ excited state. This state is 8.26 cm^{-1} (11.9 K) above the ground state. For a rotational temperature of $T \approx 295$ K, only a small fraction of the ND_3 molecules will be in the $|1, 1\rangle$ state. Calculation of the partition function (using rotational energy levels of ND_3 [281]) and including the nuclear spin degeneracy factors, indicates that this fraction is only $\approx 4.7 \times 10^{-3}$. An additional complication that must be addressed, is the fact that the 295K REMPI spectrum contains a forest of overlapping lines. As a result, the observed ion signal will have false

positives. The same molecular transition and type of laser (SIRAH Precision Scan) is used here as in Ref. [279], and we take their calculated value of $C_{overlap} \approx 0.16$. The sensitivity estimated using both of these corrections is shown in Fig. 6.18b. For direct photoionization at 118 nm, we assume that all rotational levels are ionized with equal probability. Thus we directly use the horizontal axis of Fig. 6.18a. The 355 nm data are not included in this plot due to uncertainty about the initial state.

In Fig. 6.18b, the data is plotted on a log-log plot for visualization purposes only. The slopes indicated for each plot are the result of linear fits on a lin-lin plot. The sensitivity of each ionization method is proportional to the slope of curves (at a fixed photon flux) in Fig. 6.18b. (More ions being generated for a given ND₃ density, amounts to a more sensitive detection method.) Note that since both sets of data are taken under essentially identical conditions, the dependence on ion collection efficiency factors is removed, and the difference in the total yields can be attributed to a difference in the overall ionization rates. As expected from the quadratic dependence in Fig. 6.17a, the measured sensitivity for REMPI at 317 nm, is significantly less than the lower limit estimated from the focal volume.

The observed ionization rates indicate a relative ionization probability of only 1% for 317nm REMPI using 7mJ/pulse. These data are used later to make an absolute calibration of ND₃ deceleration data, except that the conversion factor indicated in Fig. 6.18b of $5.2 \times 10^6 [\#/cm^3]$ per ion, is multiplied by 5/2 to account for the difference in the absorption lengths for the two measurements.

6.5 Detection of OH

The section describes two methods used to detect neutral OH radical at the end of a Stark decelerator. Since both methods are based on the $A \leftarrow X$ electronic transition, we start with a detailed discussion of the energy level structure.

6.5.1 The AX Band

The vibrational sublevels within the $X^2\Pi$ and $A^2\Sigma^+$ potential energy curves (level diagram shown in Fig. 6.19a) can be parameterized by

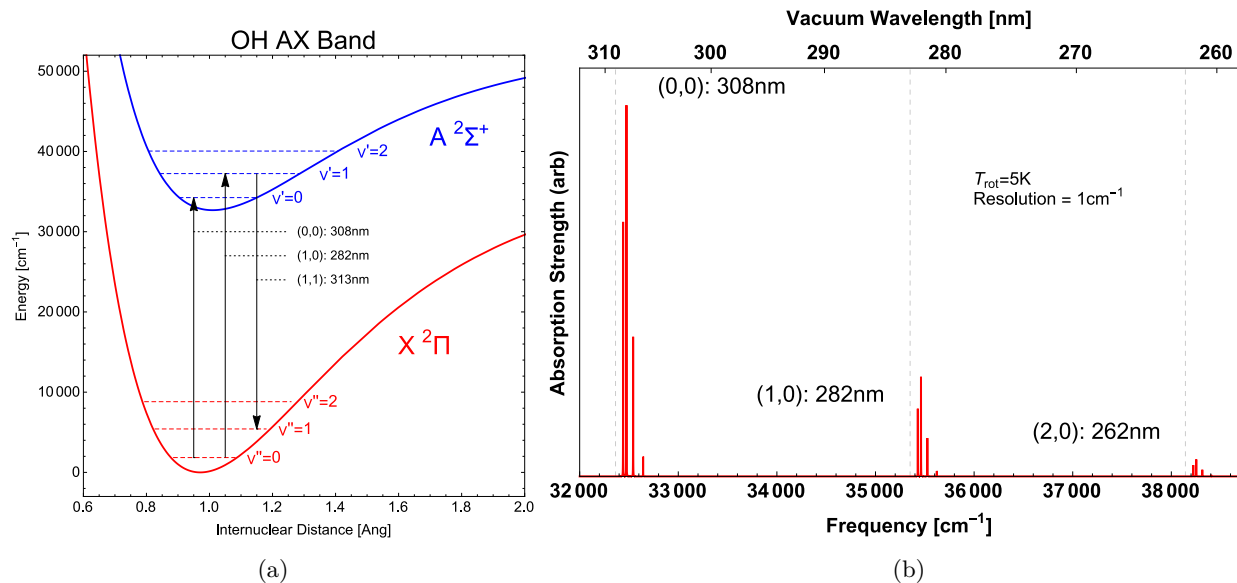


Figure 6.19: Vibrational structure of the OH $AX(\nu', \nu'')$ electronic transition. (a) Morse potentials for the $A^2\Sigma^+$ and $X^2\Pi$ electronic states, calculated using spectroscopic constants given in Ref [3]. The first three vibrational levels for both potentials are shown as horizontal dashed lines. (b) Simulated absorption spectrum [26] of a $T_{rot} = 5\text{ K}$ sample of OH at an instrumental resolution of $\Delta\bar{\nu} = 1\text{ cm}^{-1}$. An expanded view of the rotational structure of the AX (1,0) band [center of panel (b)] is shown in Fig. 6.21.

$$G(\nu) = \omega_e \left(\nu + \frac{1}{2} \right) - \omega_e x_e \left(\nu + \frac{1}{2} \right)^2 + \dots \quad (6.21)$$

The vibrational constants for OH in the $A^2\Sigma^+$ and $^2\Pi$ states are given in Table 6.1. A simulated (relative) absorption spectrum from the $X^2\Pi(\nu'' = 0)$ ground state to the $\nu' = 0, 1, 2$ vibrational levels of the $A^2\Sigma^+$ state is shown in Fig. 6.19b. As discussed in Sec. 2.2, transitions to different electronic states are accompanied by a change in the potential energy curve of the nuclei. Due to the Franck-Condon principle, the $\Delta\nu = 0$ transition is the strongest, with the $\Delta\nu = 1, 2, \dots$ transitions being much weaker. This is seen in the decreasing intensity of the (1, 0) and (2, 0) bands shown in Fig. 6.19b.

Once excited to the $A^2\Sigma^+(\nu' = 1)$ state, radiative decay to the vibrational sublevels within the $X^2\Pi$ ground state will be determined (again) by the Franck-Condon factors. Since $\Delta\nu = 0$ is strongest, decay is expected to primarily be to $X^2\Pi(\nu = 1)$. Using absolute spontaneous emission coefficients A_{ik} for the $AX(\nu', \nu'')$ band [3] tabulated in Table 6.2, the branching ratio to decay to $X^2\Pi(\nu'' = 1)$ is calculated as

Table 6.1: Spectroscopic constants for the OH AX band in units of $[cm^{-1}]$. A more comprehensive list can be found in Ref [3].

	X $^2\Pi$	A $^2\Sigma^+$
T_e	0	32683
D_e	37275	20406.2
ω_e	3737.7941	3178.3554
$\omega_e x_e$	84.91456	92.68141
B_e	18.89638	17.38922
α_e	0.725042	0.858139

Table 6.2: Selected vibrational spontaneous emission coefficients, $A_{\nu',\nu''}$ and oscillator strengths, $f_{\nu',\nu''}$ of the OH AX(ν',ν'') band taken from [3].

(ν',ν'')	$A_{\nu',\nu''} [s^{-1}]$	$f_{\nu',\nu''}$
(0,0)	1.451×10^6	1.036×10^{-2}
(1,0)	4.643×10^5	2.779×10^{-4}
(1,1)	8.595×10^5	6.364×10^{-4}
(1,2)	8.207×10^3	7.62×10^{-6}
...

$$\gamma = \frac{A_{11}}{\sum_i A_{1i}} \approx 0.645 \quad (6.22)$$

Within the AX(1,0) vibrational band, there is additional rotational level structure. An energy level diagram is given in Fig. 6.20, and spectra are shown in Fig. 6.21. The selection rules for electric dipole transitions in diatomic molecules [282] are

$$\Delta J = 0, \pm 1 \quad (J' = 0 \leftrightarrow J'' = 0) \quad (6.23)$$

$$\Delta N = 0, \pm 1, \pm 2, \pm 3 \quad \text{for } \Sigma - \Sigma \text{ transitions : } \Delta N = 0 \quad (6.24)$$

$$\Delta \Lambda = 0, \pm 1 \quad (6.25)$$

$$\Delta S = 0 \quad (6.26)$$

$$\Delta \Sigma = 0 \quad (6.27)$$

$$(+) \leftrightarrow (-) \quad (\text{Parity must change}) \quad (6.28)$$

OH AX (1,0) Band Transitions

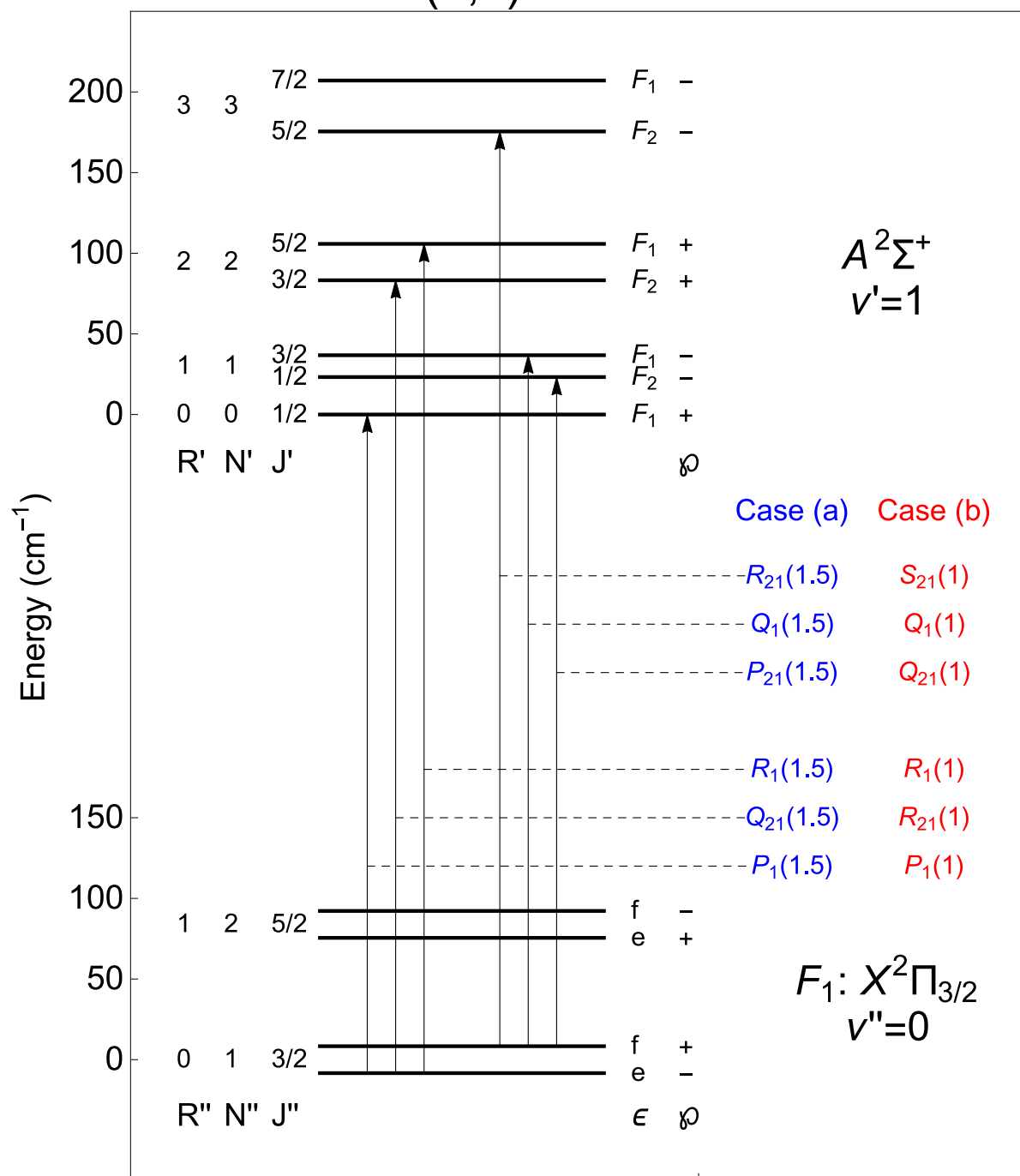


Figure 6.20: OH AX($\nu' = 1, \nu'' = 0$) band electronic transitions observed for cold samples of OH ($T_{rot} \approx 1-5$ K). Spectroscopic labels are given on the right for both Hund's case (a) (blue) and case (b) (red). The splitting between the parity doublet in the $X^2\Pi(\nu'' = 0)$ state is exaggerated by a factor of $100\times$. Similarly, the ρ -doublets in the $A^2\Sigma^+$ state are exaggerated by a factor of $40\times$. In reality, the splitting ($\gamma_{NR} \approx 0.22\text{cm}^{-1}$) is comparable to the linewidth of our pulsed dye laser ($\Delta\bar{\nu}_L \approx 0.15\text{cm}^{-1}$) so that transitions to states of the same final N are only partially resolved. Transitions are grouped by the parity of the initial state due to the parity selecting properties of the Stark decelerator. The spectroscopic notation for labeling the transitions in case (a) and case (b) coupling schemes is $OPQRS \rightarrow -2, -1, 0, 1, 2$ for ΔN and ΔJ , respectively. The subscript labels the initial and final spin-orbit manifolds (either F_1 or F_2). The complete notation is $\Delta J_{F'F''}(J'')$ and $\Delta N_{F'F''}(N'')$ for case (a) and case (b), respectively.

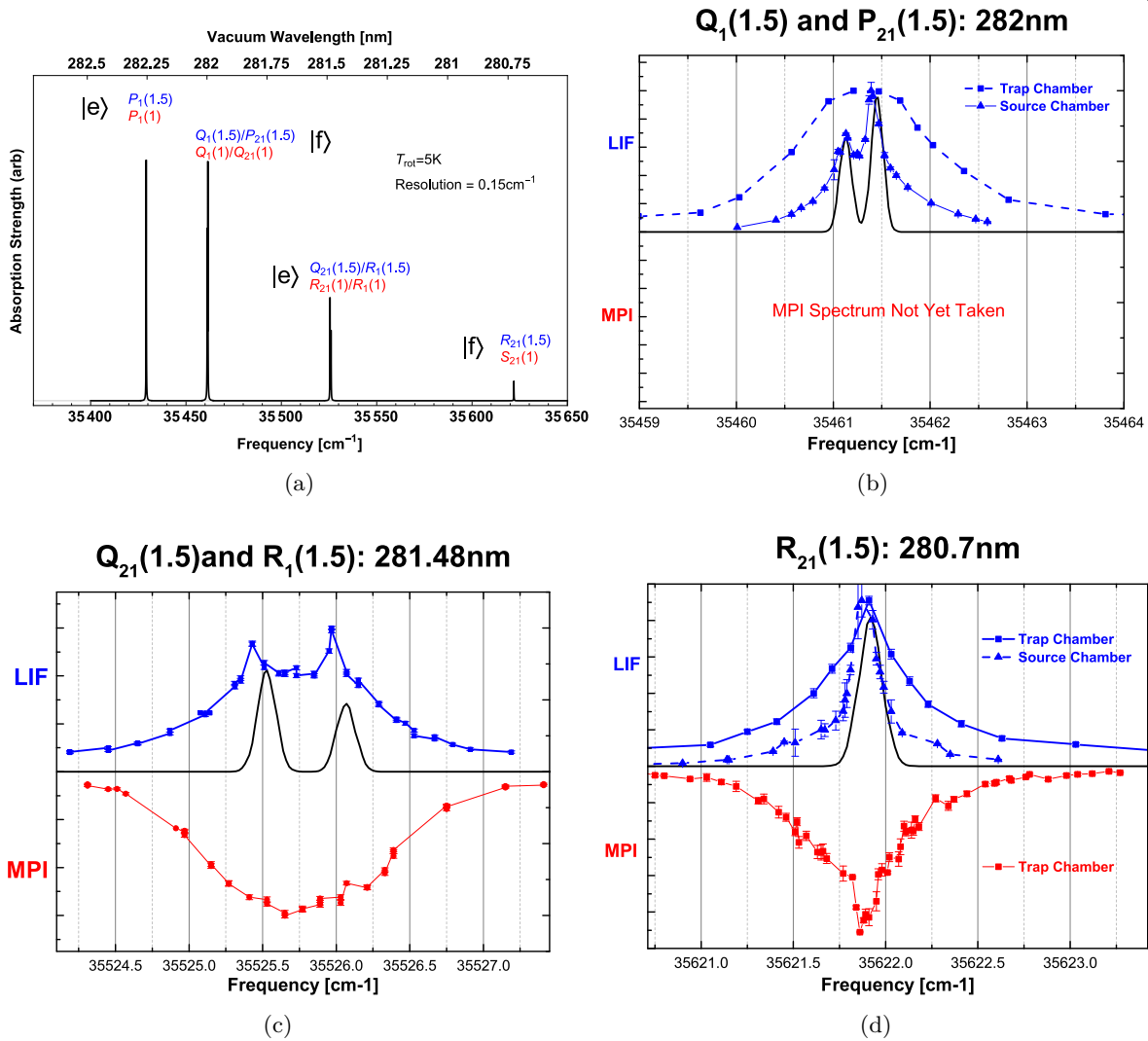


Figure 6.21: Rotational structure of the OH AX($\nu' = 1, \nu'' = 0$) electronic transition band. Panel (a) shows a simulated absorption spectrum [26] for the 6 transitions indicated in Fig. 6.20 ($T_{\text{rot}} = 5\text{K}$, instrumental resolution of $\Delta\bar{\nu} = 0.15\text{cm}^{-1}$). The initial state parities (either $|e\rangle$ or $|f\rangle$) as well as the abbreviated spectroscopic labels in Hund's case (a) (blue, upper) and (b) (red, lower) are also indicated. Enlarged views near 282nm, 281.48nm and 280.7nm are shown in panels (b), (c), and (d) respectively. Experimental data for LIF is shown in the top of each panel by blue symbols and when available, MPI data is shown in the lower portion of each panel in red. The simulated spectra shown in (a) are shown as black solid lines. For the $|f\rangle$ transitions shown in panels (b) and (d), LIF spectra taken in the source chamber (before skimmer) and trap chamber (after exit of decelerator) are shown. In the source chamber, the spectral widths are likely determined by the linewidth of our pulsed dye laser. The broader trap chamber spectra ($\sim 1\text{cm}^{-1}$) is reasonably consistent with Stark broadening from residual electric fields of magnitude $\approx 60\text{kV/cm}$.

$$\Delta F = 0, \pm 1 \quad F = 0 \leftrightarrow F = 0 \quad (6.29)$$

The rules given by Eq. 6.23, 6.28, and 6.29 are independent of the specific Hund's case. The transitions

can be labeled in either a case (a) or case (b) basis. For case (b), the transitions labeled by $OPQRS$ corresponding to $\Delta N = -2, -1, 0, +1, +2$. In a case (a) basis, the same letters are used but with the assignment in terms of J , $OPQRS \rightarrow \Delta J = -2, -1, 0, +1, +2$. For case (b) coupling, there is an additional approximate selection rule: $\Delta = N' - N'' = 0, \pm 1$. Transitions where $\Delta J = \Delta N$, are known as the *main branch transitions*, and those that violate this rule are known as *satellite lines* and have a weaker intensity. The complete notation is $\Delta J_{F'F''}(J'')$ and $\Delta N_{F'F''}(N'')$ for case (a) and case (b) respectively. The subscript labels the initial and final spin-orbit manifolds (either F_1 or F_2). The choice of using only either case (a) or case (b) labels for the OH AX band is not standardized. In the classic AX band reference [283], case (b) labels are used, but in some more recent work [28] [27], case (a) labels are used. It is critical then to note that the assignment of the letter (O,P,Q,R,S) is only the same for the two Hund's cases for transitions to the same spin-orbit manifold (i.e., $F'' = F_1$ to $F' = F_1$).

6.5.2 LIF Detection on the AX(1,0) band

The most popular method for detecting OH, is laser-induced fluorescence (LIF) based on the AX transition [283]. As shown in Fig. 6.19b, the strongest transition out of the $X^2\Pi_{3/2}(\nu'' = 0)$ state is to the $\nu' = 0$ vibrational sublevel of the $A^2\Sigma^+$ (308 nm) state. However, due to the Franck-Condon factor, the decay is primarily along $\Delta\nu = 0$, which means that the fluorescence is at the same wavelength as the excitation, which can result in large amounts of scattered light. The standard technique is to use the AX(1,0) transition at 282 nm, which will predominantly decay to the $\nu'' = 1$ state, which is red-shifted to 313 nm. This allows the fluorescence light to be spectrally discriminated from the excitation light.

6.5.2.1 SIRAH Precision Scan Dye Laser

In the experiments described in this thesis, tuneable light to drive molecular transitions was generated by a SIRAH Precision Scan pulsed dye laser. The resonator in our laser is equipped with dual 2400 l/mm gratings which achieves a nominal linewidth of $\delta\lambda \approx 1.2$ pm at 450 nm. Neglecting the dependence of $\delta\lambda$ on the central wavelength, and taking $\delta\lambda = const$, at 564 nm = 2 * 282 nm (the OH AX(1,0) band) this spectral width is expressed in frequency units as

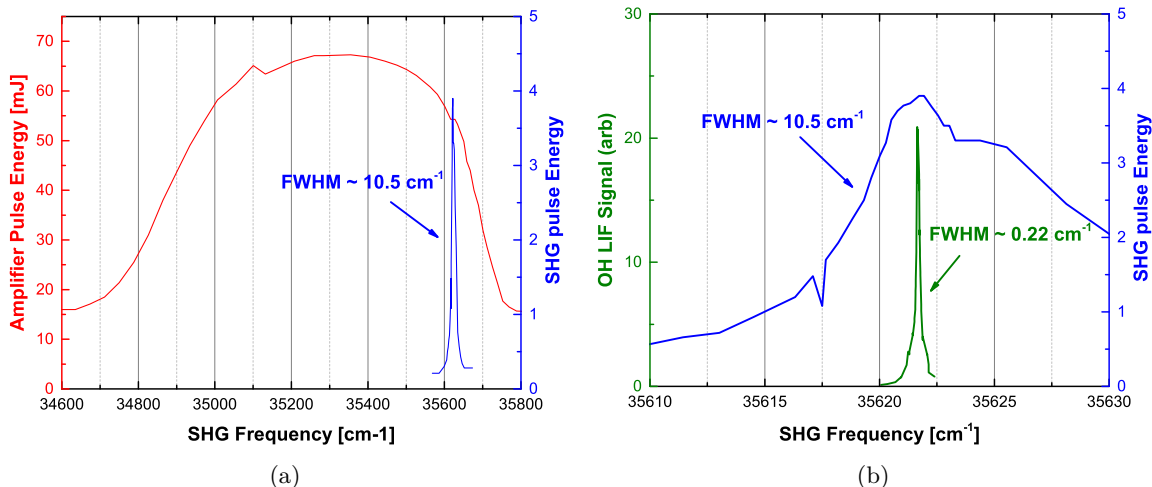


Figure 6.22: (a) Typical spectrum of the output (after final amplifier) of our SIRAH precision scan dye laser with R6G dye dissolved in 100% ethanol. The pulse energy for a fixed crystal position at the doubled wavelength ($\approx 280.7nm$) is plotted on the right axis. The spectral width of the doubled light indicates a phase matching bandwidth of $\approx 10.5 cm^{-1}$. Panel (b) shows the SHG spectrum plotted in (a) (still on the right axis) alongside a measured LIF wavelength scan, plotted on the left axis. The linewidth observed for the LIF transition is $\approx 2\text{-}3\times$ the estimated value predicted by calculations in Sec. 6.5.2.1.

$$\delta\nu = \frac{c}{\lambda^2} \delta\lambda \approx 1.13 GHz \approx 0.038 cm^{-1}. \quad (564nm) \quad (6.30)$$

To reach the resonance wavelength in the OH AX (1,0) band, the fundamental beam at $574 nm$ is frequency doubled (wavelength “halved”) to $282 nm$. In this process where a portion of the fundamental beam is converted to the second harmonic at $\omega \rightarrow 2\omega$, the corresponding linewidth of the second harmonic radiation should be twice the linewidth of the fundamental radiation. At $\approx 282 nm$ the linewidth is expected to be $\Delta\nu_L \approx 0.075 cm^{-1} \approx 2.26 GHz$.

The phase matching bandwidth obtained with the second-harmonic generation unit is $\Delta\nu_{SHG} \approx 10.5 cm^{-1}$ (see Fig. 6.22a). This means that for a fixed crystal orientation the wavelength of the resonator can be tuned by $\approx 10.5 cm^{-1}$ (specified at the second harmonic) before the intensity of the doubled light drops by a factor of 2. This is convenient when scanning over a molecular lineshape with measured linewidths of only $\approx 0.22 cm^{-1}$, since it obviates the need for servo control of the crystal angle as the wavelength is tuned. Instead, one may simply optimize the crystal position near the center wavelength and worry only about tuning the resonator.

A small fraction (two $\sim 4\%$ reflections off of uncoated Pyrex) of fundamental light ($\approx 564 \text{ nm}$) is coupled into a multimode fiber (105 μm core diameter) and sent to a wavemeter (EXFO: WA-4550) for continuous measurement of the frequency at the second harmonic. The resolution of the wavemeter is nominally, $0.01 \text{ cm}^{-1} \approx 300 \text{ MHz}$. This value is significantly greater than the doppler linewidth at $T \approx 1 \text{ K}$ ($\Delta\nu_D \approx 0.006 \text{ cm}^{-1} \approx 184 \text{ MHz}$ for OH) but is less than the linewidth of the laser at 282 nm which is estimated to be $\approx 0.08 \text{ cm}^{-1}$ and which is sufficient for finding the line center. Although the wavemeter is equipped with an internal reference HeNe for absolute frequency calibration, based on comparisons of measured line centers to literature values, we find a systematic shift of $\sim 0.105 \text{ cm}^{-1}$ (wavemeter reads too low of frequency). These estimates are confirmed by comparisons to sub-doppler ^{87}Rb lines at 780 nm [284].

6.5.2.2 Photon Counting with Photomultiplier Tubes

The OH fluorescence is detected with a photomultiplier tube (PMT). The electron multiplication process is similar to MCP's except that PMT's have discrete dynodes. Like the MCP, the principle advantage of PMT's, and as a consequence, the LIF detection method, is their extremely low intrinsic (dark) noise. The PMT used for all experiments presented in this thesis is 9125SB from E&T inc. This low noise, coupled with the high gain of the electron multiplier stage, can allow for detection of extremely low levels of light. For very low light levels, the output from a PMT consists of a large number of "spikes" which correspond to the detection of individual photons. The PMT output is fed into counting electronics that register a "count" if the output voltage exceeds a certain discriminator threshold. By carefully setting the discriminator threshold above the level of technical noise (which in a lab with Q-Switched lasers, excimer thyratrons, and Stark decelerators can be as large as 10 mV) but significantly below the average pulse height, traditional (analog) noise sources such as Johnson noise and variations in the peak height/gain can be completely suppressed.

For an average number of detected photons of N_s , the standard deviation will be $\sqrt{N_s}$ as determined by Poisson statistics. Therefore, the best possible (shot noise limited) SNR is

$$\frac{S}{N} = \frac{N_s}{\sqrt{N_s}} = \sqrt{N_s} \quad (6.31)$$

The situation is complicated due to the finite bandwidth of the PMT and the counting electronics. For

an average photon flux Φ [$\#/s$], the average photoelectron count rate is $K = \eta\Phi$, where η is the quantum efficiency of the PMT. The probability of detecting N counts in a gate width T is

$$N = KT \times e^{-K\Delta t} \quad (\text{Observed \# Number Counts}) \quad (6.32)$$

where Δt is the pulse pair resolution of the counting electronics and T is the temporal gate width. The first term, $KT = \eta\Phi T$, can be attributed to the average incident count rate, and the second term $e^{-K\Delta t}$ is due to the finite capability of the counter to resolve photons occurring close together in time. If the photoelectrons are broken up into contributions from the signal K_s , and the background K_b , the number of detected true signal counts, N_s , is

$$N_s = K_s T \times e^{-(K_s + K_b)\Delta t} \quad (\text{Signal Count}) \quad (6.33)$$

Similarly, the total # of counts, N_t , is

$$N_t = (K_s + K_b) T \times e^{-(K_s + K_b)\Delta t} \quad (\text{Total Count}) \quad (6.34)$$

Stochastic fluctuations (shot noise) arise from both the signal and the background. Then the standard deviation of the total count rate is [285]

$$\sigma_{N_t} = [(K_s + K_b) T]^{1/2} \left[1 + (K_s + K_b)^2 T \times \Delta t \right]^{1/2} e^{-(K_s + K_b)\Delta t} \quad (6.35)$$

The SNR is simply N_s/σ_{N_t} ,

$$\begin{aligned} SNR &= \frac{K_s T e^{-(K_s + K_b)\Delta t}}{[(K_s + K_b) T]^{1/2} \left[1 + (K_s + K_b)^2 T \times \Delta t \right]^{1/2} e^{-(K_s + K_b)\Delta t}} \\ &= \frac{K_s \sqrt{T}}{(K_s + K_b)^{1/2} \left[1 + (K_s + K_b)^2 T \times \Delta t \right]^{1/2}} \end{aligned} \quad (6.36)$$

The most important consequences of Eq. 6.36 are that 1) background photons and signal photons contribute equally to shot noise as the signal, and 2) the SNR grows as the square root of the measurement

time. If M experimental runs, are averaged together, the total measurement time becomes $M \times T$. As a consequence, improving the signal to noise of the measurement by a factor of 2, takes $4 \times$ as long.

6.5.2.3 Photon Collection

In any optoelectronic measurement, it is critical to collect as many “signal” photons as possible, while simultaneously discriminating against those you don’t want. This is especially important for LIF detection of OH at the end of a decelerator where signal sizes are relatively low and background scattered light can be high. The typical pulse energies at 282 nm used for LIF excitation are $\approx 5\text{-}10$ mJ. Considering that at 282 nm, every mJ contains $\approx 1.4 \times 10^{15}$ photons, a fluorescence signal consisting of $\approx 1\text{-}100$ photons/shot can easily be completely swamped in scattered light. Furthermore, since the background counts also contribute shot noise, they can significantly degrade the SNR.

To discriminate against scattered light we use a combination of spatial, spectral and temporal filtering. For spectral filtering, it is key to not only suppress directly scattered light, but also red-shifted fluorescence at longer wavelengths. A summary of the fractional transmissions of various filters tested for OH LIF detection is shown in Table 6.3 and a plot of the % transmission of these filters is shown in Fig. 6.23a. The filter cascade used for OH LIF detection at the end of the decelerator is shown in Fig. 6.23b (linear vertical axis) and Fig. 6.23c (logarithmic vertical axis). This particular filter combination was chosen for having high transmission at 313 nm as well as high extinction at 282 nm (achieved by the 10CGA-305 filters) and for red-shifted light (achieved by UG11 filter).

A sketch of the telescope used for fluorescence detection is shown in Fig. 6.24. Carefully adjusting the PMT’s position and using an iris to select only the central portion of the incident laser beam with an iris, is absolutely critical for minimization of scattered light. With careful alignment of these two parameters, the iris on the PMT assembly could be closed down to a diameter of ≈ 1.5 mm strongly suppressing scattered light, without an significantly affecting the OH fluorescence signal.

In our experiment, the closest that we could place a lens mounted outside the vacuum chamber is $d = 40$ mm away from the trap center. The collection solid angle is further obstructed by the rods used to mount the trap electrodes and TOFMS. The solid angle is estimated to be $\alpha = \frac{d\Omega}{4\pi} \approx 0.0035$.

Table 6.3: Summary of measured filter fractional transmissions of various filters at different wavelengths (T_λ) for OH LIF detection. Columns 6 and 7 gives the ratio of transmission at the fluorescence wavelength of 313 nm to the excitation light at 282 nm and the red-shifted light. (The exact wavelength of 420 nm is not important.) A plot of the transmission of these filters is shown in Fig. 6.23a. The abbreviations for the filter type are: CG= colored glass (absorptive), DC = dielectric coating (interference). The filter from Laser Optik is designed to be a high reflectivity mirror at 282 nm, having high transmission at 313 nm. The filter from Omega is a narrow bandpass filter.

Model (Manufacturer)	Type	T_{282}	T_{313}	T_{420}	T_{313}/T_{282}	T_{313}/T_{420}
UG5 (Schott)	CG	0.82	0.88	0.01	1.07	88
UG11 (Schott)	CG	0.695	0.829	1×10^{-5}	1.2	8.3×10^4
10CGA-305 (Newport)	DC	2×10^{-5}	0.77	0.92	3.8×10^4	0.83
1310562 (Laser Optik)	DC/Mirror	1.08×10^{-2}	0.96	0.81	89	1.2
313BP10 (Omega)	DC/Narrow	9×10^{-4}	0.14	1×10^{-5}	155	1.4×10^4

6.5.2.4 LIF Sensitivity

LIF will have the highest sensitivity if the transition is saturated, so that all ground-state molecules are excited to the upper state. The fraction of OH that fluoresces at 313 nm is given by the branching ratio: $\gamma \approx 0.645$ (Eq. 6.22). The sensitivity of OH LIF can be estimated by considering the photon collection efficiency and volume from which the fluorescence is detected. Estimating the photon collection efficiency is not trivial and, for the current data set, represents the largest source of uncertainty in an absolute calibration of OH density. We note that techniques such as Rayleigh scattering [286] and Raman scattering allow for an *in situ* calibration of the absolute photon collection efficiency [287] [288] [289] [290]. However, these techniques were not used here.

Our estimate of the number of detectable photons per shot is given by

$$N_{pe} = (\alpha * \beta * \chi * f_{gate}) * \gamma * N_{abs} \quad [\#\text{photoelectrons/shot}] \quad (6.37)$$

$\gamma \approx 0.645$ is the branching ratio given earlier and the quantities in parentheses represent the “loss factors” due to various experimental constraints. Explicitly, these are,

- (1) $\alpha = \frac{d\Omega}{4\pi} \approx 0.0035$: Geometric solid angle of photon collection
- (2) $\beta \approx 0.355$: Spectral transmission of optics in fluorescence collection system
- (3) $\chi \approx 0.26$: PMT quantum efficiency at fluorescence wavelength

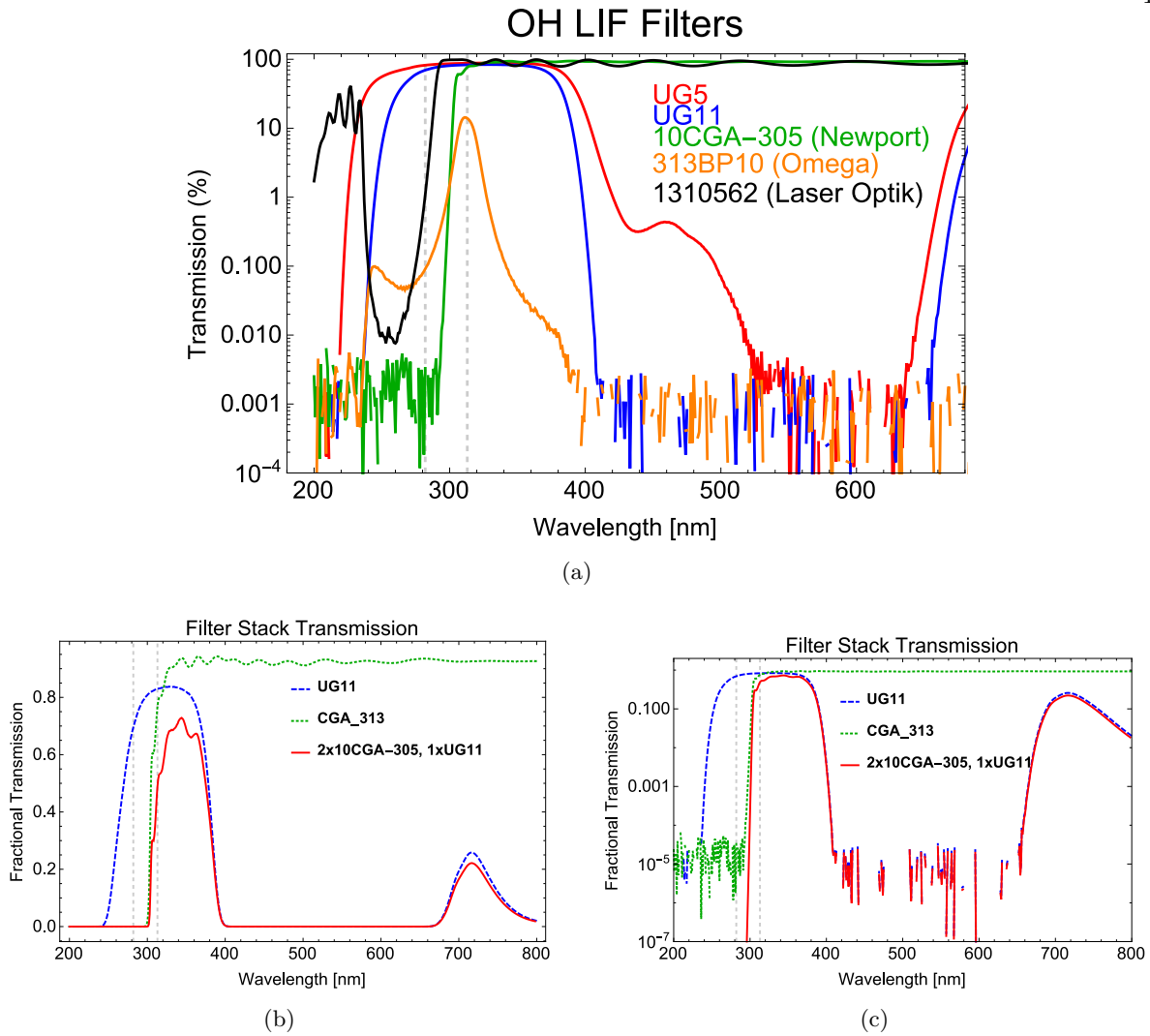


Figure 6.23: Optical filters used for LIF detection of OH in the AX (1,0) band. (a) shows an overview of the various filters tested. (b) and (c) show a selection of the two filters found to be most useful for LIF detection as well as the calculated transmission of the filter stack/cascade (2x CGA and 1x UG11) used for all OH LIF detection described in this thesis.

(4) $f_{gate} \approx 0.75$: Temporal fraction of collected fluorescence

The temporal fraction of fluorescence is estimated using

$$f_{gate} = \frac{\int_{\Delta t_d}^{\Delta t_d + T} e^{-t/\tau} dt}{\int_0^{\infty} e^{-t/\tau} dt} \approx 0.75 \quad (6.38)$$

where $\Delta t_d \approx 165$ ns is the delay between the excitation laser pulse and when the PMT turns on, $T = 2$ μ s is the measurement gate duration, and $\tau = 750$ ns is the radiative lifetime of the $A^2\Sigma^+$ state. Then, in total,

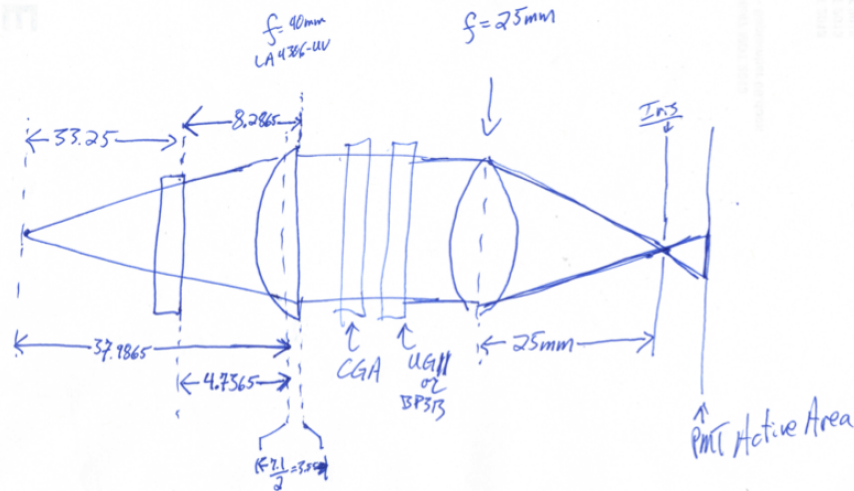


Figure 6.24: Sketch of the fluorescence detection assembly used for LIF detection at the end of the decelerator. The light is collimated before passing through the dielectric coating filter (10CGA-305-see Table 6.3) to prevent an angle dependent shift of the pass band.

we can express the LIF detection efficiency (in our experiment) in terms of the # photoelectron cts per OH molecule using Eq. 6.37

$$\eta_{LIF} = (\alpha * \beta * \chi * f_{gate}) * \gamma \approx 1.5 \times 10^{-4} \quad [\#cts/molecule] \quad (6.39)$$

Knife-edge measurements of the dye laser beam indicate the beam waists in the horizontal and vertical directions to be $w_0 = 1.7$ and $w_0 = 2$ mm. Taking an average value of these two to give a cross-sectional area of $A = \pi w_0^2 \sim 0.11$ cm². Assuming that the interaction length of the molecules and the laser beam is determined by the clear aperture of the Stark decelerator; $L_{int} = 0.2$ cm], this gives a total volume of $V_{int} = A * L_{int} = 0.11$ cm² * 0.2 cm = 0.022 cm³. Then, if we assume that the observed counts come from the interaction volume, V_{int} , then every observed count implies a density of

$$n_{OH} \approx \frac{1}{\eta_{LIF}} \frac{N_{sig}}{\Delta V_{int}} \quad [\#/cm^3] \quad (6.40)$$

Using photon counting methods, count rates less than 1 can be routinely measured. This method is best suited for a detection system that is optimized when the apparatus is operated at high count rates and then reduced in some way (such as going from optimization of the peak bunching signal to trapping).

However, following the maxim “you can’t tweak zero,” we define the detection limit as the # photons required to reliably generate a single count (1 photoelectron) every shot. Taking $N_{sig} = 1$ in Eq. 6.40 gives the minimum detectable concentration as

$$n_{OH}^{(min)} \approx 2.9 \times 10^5 \quad [\#/cm^3] \quad (6.41)$$

6.5.3 OH Ionization Schemes

The relatively small photon collection efficiency given by Eq. 6.39 is a significant limitation of the SNR of the LIF technique. Thus, one is led to wonder about other possible detection methods. As mentioned previously, the majority of laser-based molecular detection strategies involve excitation of electronic transitions. It is then important to consider electronic energy levels of the molecule of interest to establish which levels can be exploited for a given detection method. The first ten electronic states of OH are shown in Fig. 6.25. Two features are immediately apparent. The first is that there are only four bound electronic states ($X^2\Pi$, $A^2\Sigma^+$, $3^2\Pi$, and $C^2\Sigma^+$) and, secondly, with the exception of the well-known $A \leftarrow X$ band [283], all transitions from the $X^2\Pi(\nu = 0)$ ground state lie in the VUV where tunable laser sources are scarce. After the $A^2\Sigma^+$, the lowest bound states are the $D^2\Sigma^-$ and the $3^2\Sigma^-$ Rydberg states at vertical energies of 10.1 and 10.9 eV respectively. This presents a serious problem for the experimentalist since it places significant constraints on the flexibility of possible detection methods.

Ionization schemes are, in principle, quite sensitive since the ion collection efficiency, η_{ion} , can be much larger than the photon collection efficiency given in Eq. 6.39. Photoionization of OH is complicated by its high ionization potential (IP) of 13.017 eV and the lack of suitable intermediate states (for a multiphoton process) easily accessible by conventional lasers. The REMPI schemes that have been developed require light in the deep UV ($\approx 250nm$) and have subsequently not replaced the standard AX-band LIF method. The 2+1 scheme using the $D^2\Sigma^-(\nu' = 0) - X^2\Pi(\nu'' = 0)$ transition has a reasonably large two-photon cross-section and radiative lifetime (1.5-3.5 ns) [291]. However, due to coupling to the repulsive $1^2\Pi$ and $1^4\Pi$ states, the total lifetime of the $D^2\Sigma^-(\nu')$ and $3^2\Sigma^-(\nu')$ states due to predissociation is limited to $\tau = 40-400 ps$. As a result, this technique (at least when used with ns-pulsed lasers) has not been found to be especially sensitive

[292].

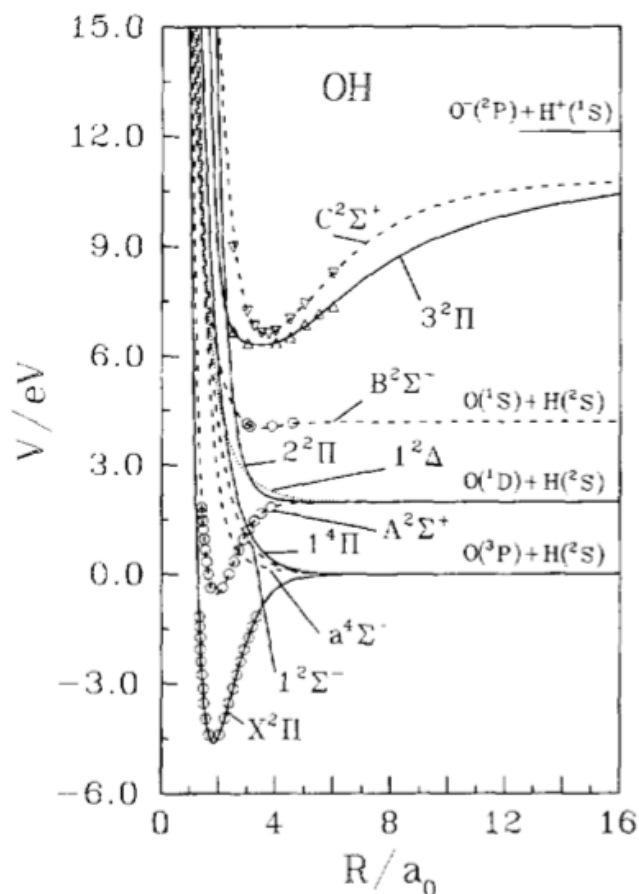


Figure 6.25: First ten electronic states of the OH radical (of which, only four are bound). With the exception of the AX band, all transition from the ground state lie in the VUV. Figure from [6]

Another alternative is to use the $A^2\Sigma^+$ state as a resonant intermediate followed by ionization with a VUV photon. The ground state of the OH^+ cation has an electron configuration of

$$\text{OH}^+ X^3\Sigma^- : (1\sigma)^2(2\sigma)^2(3\sigma)^2(1\pi)^2 \quad (6.42)$$

and is best described with case (b) coupling [293]. The OH (neutral) $A^2\Sigma^+$ excited state has an electron configuration of

$$A^2\Sigma^+ : (1\sigma)^2(2\sigma)^2(3\sigma)^1(1\pi)^4. \quad (6.43)$$

which suggests that ionization from the $A^2\Sigma^+$ state would require two electrons to change orbitals, indicating that this operation should be forbidden by parity. Fortunately, several Rydberg series of neutral OH at energies above the IP of 13.01 eV have been found. These include those that converge on the $a^1\Delta$ [294], as well as on the $b^1\Sigma^+$ and $A^3\Pi$ [295]. The latter of these undergoes auger autoionization to produce $A^3\Pi(\nu = 0, 1)$. It just so happens that the 118nm photons are nearly exactly resonant with the $\nu = 0$ level of this Rydberg state and fortunately the transition from the $A^2\Sigma^+$ state to the $A^3\Pi(\nu = 0)$ state is dipole allowed.

For the detection of OH at the end of the decelerator, where only $|f\rangle$ (low field seeking) molecules will be present, one must use either the [case (a) notation] $Q_{21}(1.5)/P_{21}(1.5)$ main branch line at ≈ 282 nm or the $R_{21}(1.5)$ satellite line at ≈ 280.7 nm. Since the $R_{21}(1.5)$ line has been measured to have a larger intensity [27], that line was chosen. Initial measurements of the OH ion signal at the end of the decelerator, using the light source presented in Ch. 5 are shown in Fig. 6.28. Fig. 6.28a shows measured time-of-flight signals of OH^+ alongside ND_3^+ , which was used to calibrate the ion-flight distance for this particular alignment of the 118 nm beam. Panel Fig. 6.28b shows the dependence of the OH^+ signal as a function of the delay between the resonant excitation laser at 282 nm and the ionizing laser at 118 nm. The observed dependence is consistent with the radiative lifetime of the $A^2\Sigma^+$ state of $\tau \approx 750$ ns.

6.5.3.1 Efficiency of Ionization

If we consider multistep ionization in terms of the relevant rate equations then the basic requirement for efficient ionization is that the ionizing step should be fast compared with all other relaxation processes. Then the relevant quantities to compare are

$$k_{2i} \stackrel{?}{\leftrightarrow} 1/\tau \quad (6.44)$$

where $k_{2i} = \sigma_{2i}\Phi_{2i}/A$ is the excitation rate in s^{-1} and $1/\tau = A$ is the total radiative relaxation rate. If predissociation or other processes are significant then they must be included in the total lifetime.

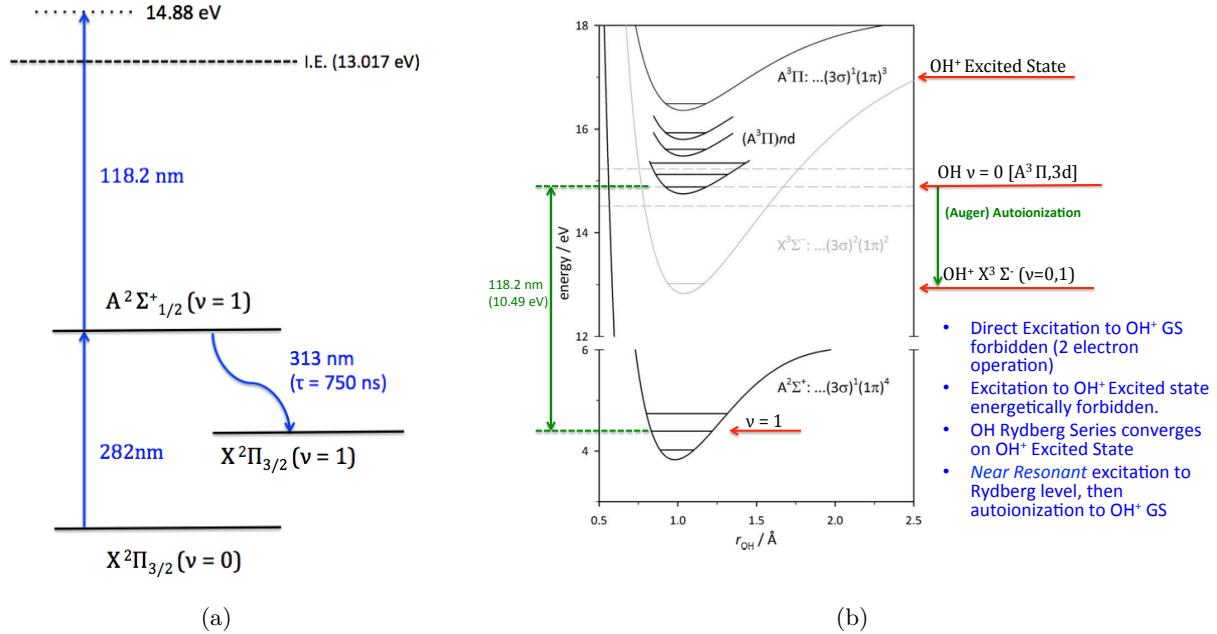


Figure 6.26: Energy level diagrams relevant to 1+1' REMPI of OH. (a) shows a simplified level scheme and (b) shows more detailed description of the proposed ionization mechanism [27]. The dark intermolecular potentials are the neutral OH levels, and the gray lines correspond to the OH. This figure is an annotated version of Fig. 2 of Ref. [28].

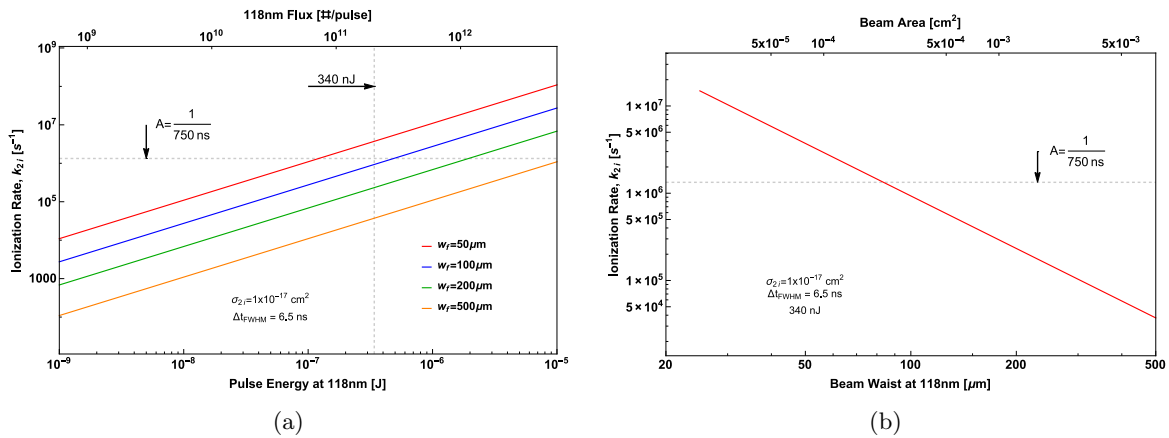


Figure 6.27: (a) Ionization rates as a function of 118nm for various beam waists (radii). Ionization rates are calculated as $k_{2i} = \sigma_{2i} \frac{\Phi}{A}$, with $\sigma_{2i} = 1.0 \times 10^{-17}$ and assuming Gaussian pulses with FWHM of $\Delta t_{FWHM} = 6.5 ns$ energies.

6.5.3.2 Deceleration Data

Time-of-flight data for decelerated OH are presented in Fig. 6.29 for both LIF and 1+1' MPI. Unfortunately, due to experimental constraints, simultaneous data for optimized LIF and MPI are not possible at

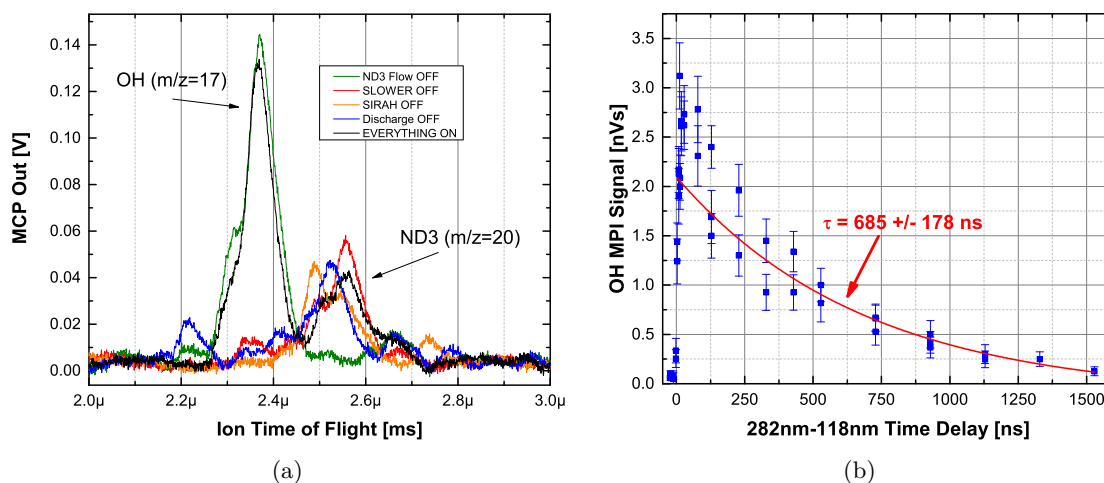


Figure 6.28: Initial Measurements of OH MPI at the end of a decelerator. (a) shows the ion TOF of OH^+ detected simultaneously with ND^+ and (b) shows the time dependence of the OH^+ ion signal as a function of the delay between the excitation and ionization lasers. The signal to noise ratio has been improved since these measurements were taken. For details, see text.

the moment. As a result, the measurements shown in Fig. 6.29 were not taken simultaneously. As a consequence of the dependence of the OH beam to small changes in the discharge operating conditions (differing gas load, valve opening, etc.), the velocities of the two data sets are slightly different: (436 m/s for the LIF data vs. 440 m/s for the MPI data). Furthermore, the line at 282 nm is used for LIF and the line at 280.7 nm is used for MPI. However, the LIF measurements are a good representation of the best SNR observed thus far for OH. As can be seen, both detection methods generate a comparable number of “counts” per pulse. Investigations of possible improvements are currently underway by John Gray, but given the 118 nm flux measurements presented earlier in this chapter, one can only reasonably expect improvements of a factor of ~ 2 -3.

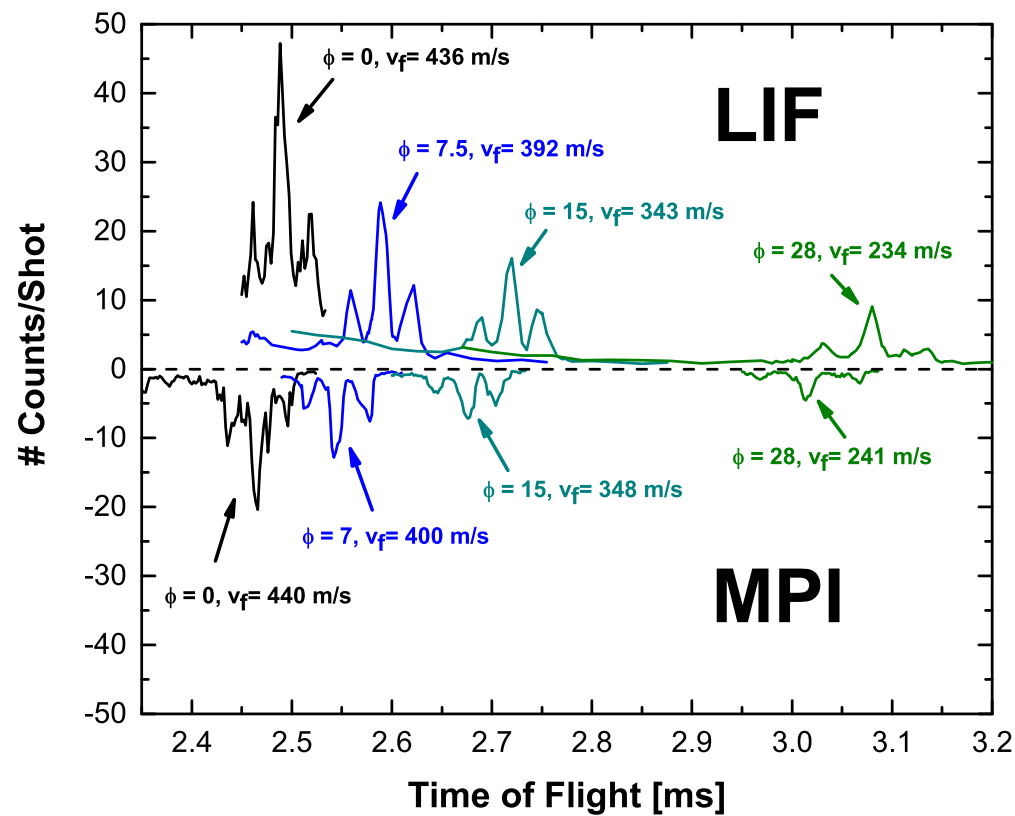


Figure 6.29: Comparison of the OH deceleration time of flight for LIF and 1+1' MPI. MPI data are plotted as negative counts. Note that the vertical scale for each is 0 \rightarrow 50 "counts." For details, including discussion of the different OH beam velocities, see text.

Bibliography

- [1] VA Alekseev and DW Setser. Generation and kinetic studies of Xe ($5d [3/2] 1$) resonance state atoms. The Journal of Physical Chemistry A, 103(42):8396–8403, 1999.
- [2] E Matthias, RA Rosenberg, ED Poliakoff, MG White, S-T Lee, and DA Shirley. Time resolved VUV spectroscopy using synchrotron radiation: Fluorescent lifetimes of atomic Kr and Xe. Chemical Physics Letters, 52(2):239–244, 1977.
- [3] Jorge Luque and David R Crosley. Transition probabilities in the $A\Sigma^+-X^2\Pi$ electronic system of OH. Journal of Chemical Physics, 109(2):439–448, 1998.
- [4] L. D. Carr, D. DeMille, R. V. Krems, and J. Ye. Cold and Ultracold Molecules: Science, Technology and Applications. New J. Phys., 11(5):055049, 2009.
- [5] Richard N Zare. Angular momentum: understanding spatial aspects in chemistry and physics. Wiley-Interscience, 1988.
- [6] AJC Varandas and AI Voronin. Calculation of the asymptotic interaction and modelling of the potential energy curves of OH and OH^+ . Chemical physics, 194(1):91–100, 1995.
- [7] Mark Brouard and Claire Vallance. Tutorials in molecular reaction dynamics. Royal Society of Chemistry, 2010.
- [8] W Ronald Gentry and Clayton F Giese. Ten-microsecond pulsed molecular beam source and a fast ionization detector. Review of Scientific instruments, 49(5):595–600, 1978.
- [9] W Ronald Gentry. Low-energy pulsed beam sources. Atomic and molecular beam methods, 1:54, 1988.
- [10] Michael Borysow. A high-intensity cold atom source. University of Texas-Austin, 2012.
- [11] H Okabe. Photodissociation of HNCO in the vacuum ultraviolet; production of NCO $A \Sigma$ and NH ($A \ 3\pi, \pi\sigma$). The Journal of Chemical Physics, 53(9):3507–3515, 1970.
- [12] RA Brownsword, T Laurent, RK Vatsa, H-R Volpp, and J Wolfrum. Photodissociation dynamics of HNCO at 248 nm. Chemical physics letters, 258(1):164–170, 1996.
- [13] H Laine Berghout, Shizuka Hsieh, and F Fleming Crim. Relative product yields in the one-photon and vibrationally mediated photolysis of isocyanic acid (HNCO). Journal of Chemical Physics, 114(24):10835–10844, 2001.
- [14] John M Meek and John D. Craggs. Electrical breakdown of gases. Oxford University Press, 1953.
- [15] Yuri P Raizer, Vitaly I Kisin, and John E Allen. Gas discharge physics, volume 1. Springer-Verlag Berlin, 1991.
- [16] T Harb, W Kedzierski, and JW McConkey. Production of ground state oh following electron impact on h2o. Journal of Chemical Physics, 115:5507–5512, 2001.

- [17] Yukikazu Itikawa and Nigel Mason. Cross sections for electron collisions with water molecules. Journal of Physical and Chemical reference data, 34(1):1–22, 2005.
- [18] Scott Davis, David T Anderson, Geoffrey Duxbury, and David J Nesbitt. Jet-cooled molecular radicals in slit supersonic discharges: sub-doppler infrared studies of methyl radical. The Journal of chemical physics, 107(15):5661–5675, 1997.
- [19] LP Parazzoli, NJ Fitch, PS Żuchowski, JM Hutson, and HJ Lewandowski. Large effects of electric fields on atom-molecule collisions at millikelvin temperatures. Physical review letters, 106(19):193201, 2011.
- [20] AH Kung. Third-harmonic generation in a pulsed supersonic jet of xenon. Optics letters, 8(1):24–26, 1983.
- [21] Rita Mahon, T McIlrath, V Myerscough, and David W Koopman. Third-harmonic generation in argon, krypton, and xenon: bandwidth limitations in the vicinity of Lyman- α . Quantum Electronics, IEEE Journal of, 15(6):444–451, 1979.
- [22] James AR Samson. Techniques of vacuum ultraviolet spectroscopy. John Wiley and Sons, 1967.
- [23] E Chevallay, J Durand, S Hutchins, G Suberlucq, and M Wurgel. Photocathodes tested in the dc gun of the cern photoemission laboratory. Nuclear Instruments and Methods in Physics Research Section A: Accelerators, Spectrometers, Detectors and Associated Equipment, 340(1):146–156, 1994.
- [24] Herbert B Michaelson. The work function of the elements and its periodicity. Journal of Applied Physics, 48(11):4729–4733, 1977.
- [25] Joseph Ladislav Wiza. Microchannel plate detectors. Nuclear Instruments and Methods, 162(1):587–601, 1979.
- [26] J Luque and DR Crosley. Lifbase: Database and spectral simulation program (version 1.5). SRI international report MP, 99(009), 1999.
- [27] Joseph M Beames, Fang Liu, and Marsha I Lester. $1+1'$ resonant multiphoton ionisation of oh radicals via the $A^2\Sigma^+$ state: insights from direct comparison with AX laser-induced fluorescence detection. Molecular Physics, 112(7):897–903, 2014.
- [28] Joseph M Beames, Fang Liu, Marsha I Lester, and Craig Murray. Communication: A new spectroscopic window on hydroxyl radicals using UV+ VUV resonant ionization. The Journal of chemical physics, 134(24):241102, 2011.
- [29] David R Miller. Free jet sources. Atomic and molecular beam methods, 1:26, 1988.
- [30] M. H. Anderson, J. R. Ensher, M. R. Matthews, C. E. Wieman, and E. A. Cornell. Observation of Bose-Einstein condensation in a dilute atomic vapor. Science, 269:198–201, 1995.
- [31] K. B. Davis et. al. Bose-Einstein condensation in a gas of sodium atoms. Physical Review Letters, 75:3969–3973, 1995.
- [32] Lev Pitaevskii, Sandro Stringari, and Anthony Leggett. Bose-einstein condensation. Physics Today, 57(10):74–76, 2004.
- [33] James F Annett. Superconductivity, superfluids and condensates. Oxford Univ. Press, 2004.
- [34] Christopher J Pethick and Henrik Smith. Bose-Einstein condensation in dilute gases. Cambridge university press, 2002.
- [35] JJ Hudson, DM Kara, IJ Smallman, BE Sauer, MR Tarbutt, and EA Hinds. Improved measurement of the shape of the electron. Nature, 473(7348):493–496, 2011.

- [36] Jacob Baron, Wesley C Campbell, David DeMille, John M Doyle, Gerald Gabrielse, Yulia V Gurevich, Paul W Hess, Nicholas R Hutzler, Emil Kirilov, Ivan Kozyryev, et al. Order of magnitude smaller limit on the electric dipole moment of the electron. *Science*, 343(6168):269–272, 2014.
- [37] Huanqian Loh, Kevin C Cossel, MC Grau, K-K Ni, Edmund R Meyer, John L Bohn, Jun Ye, and Eric A Cornell. Precision spectroscopy of polarized molecules in an ion trap. *science*, 342(6163):1220–1222, 2013.
- [38] T. Softley and M. Bell. Ultracold molecules and ultracold chemistry. *Molecular Physics*, 107:99–132, 2009.
- [39] S Ospelkaus, K-K Ni, D Wang, MHG De Miranda, B Neyenhuis, G Quéméner, PS Julienne, JL Bohn, DS Jin, and J Ye. Quantum-state controlled chemical reactions of ultracold potassium-rubidium molecules. *Science*, 327(5967):853–857, 2010.
- [40] ES Shuman, JF Barry, and D DeMille. Laser cooling of a diatomic molecule. *Nature*, 467(7317):820–823, 2010.
- [41] M. T. Hummon, M. Yeo, B. K. Stuhl, A. L. Collopy, Y. Xia, and J. Ye. 2D magneto-optical trapping of diatomic molecules. *Physical Review Letters*, 110:143001, 2013.
- [42] JF Barry, DJ McCarron, EB Norrgard, MH Steinecker, and D DeMille. Magneto-optical trapping of a diatomic molecule. *Nature*, 512(7514):286–289, 2014.
- [43] Alejandra L Collopy, Matthew T Hummon, Mark Yeo, Bo Yan, and Jun Ye. Prospects for a narrow line mot in YO. *New Journal of Physics*, 7 May 2015.
- [44] Mark Yeo, Matthew T Hummon, Alejandra L Collopy, Bo Yan, Boerge Hemmerling, Eunmi Chae, John M Doyle, and Jun Ye. Rotational state microwave mixing for laser cooling of complex diatomic molecules. *arXiv preprint arXiv:1501.04683*, 2015.
- [45] K-K Ni, S Ospelkaus, MHG De Miranda, A Pe’er, B Neyenhuis, JJ Zirbel, S Kotochigova, PS Julienne, DS Jin, and J Ye. A high phase-space-density gas of polar molecules. *science*, 322(5899):231–235, 2008.
- [46] Deborah S Jin and Jun Ye. Polar molecules in the quantum regime. *Phys. Today*, 64(5):27, 2011.
- [47] Bo Yan, Steven A Moses, Bryce Gadway, Jacob P Covey, Kaden RA Hazzard, Ana Maria Rey, Deborah S Jin, and Jun Ye. Observation of dipolar spin-exchange interactions with lattice-confined polar molecules. *Nature*, 501(7468):521–525, 2013.
- [48] Jonathan D Weinstein, Thierry Guillet, Bretislav Friedrich, John M Doyle, et al. Magnetic trapping of calcium monohydride molecules at millikelvin temperatures. *Nature*, 395(6698):148–150, 1998.
- [49] David Patterson and John M Doyle. Bright, guided molecular beam with hydrodynamic enhancement. *The Journal of chemical physics*, 126(15):154307, 2007.
- [50] JF Barry, ES Shuman, and D DeMille. A bright, slow cryogenic molecular beam source for free radicals. *Physical Chemistry Chemical Physics*, 13(42):18936–18947, 2011.
- [51] Nicholas R Hutzler, Maxwell F Parsons, Yulia V Gurevich, Paul W Hess, Elizabeth Petrik, Ben Spaun, Amar C Vutha, David DeMille, Gerald Gabrielse, and John M Doyle. A cryogenic beam of refractory, chemically reactive molecules with expansion cooling. *Physical Chemistry Chemical Physics*, 13(42):18976–18985, 2011.
- [52] B. K. Stuhl, M. T. Hummon, M. Yeo, G. Quéméner, J. L. Bohn, and J. Ye. Evaporative cooling of the dipolar hydroxyl radical. *Nature*, 492:396–400, 2012.
- [53] Martin Zeppenfeld, Barbara GU Englert, Rosa Glöckner, Alexander Prehn, Manuel Mielenz, Christian Sommer, Laurens D van Buuren, Michael Motsch, and Gerhard Rempe. Sisyphus cooling of electrically trapped polyatomic molecules. *Nature*, 491(7425):570–573, 2012.

- [54] Martin Zeppenfeld, Michael Motsch, Pepijn WH Pinkse, and Gerhard Rempe. Optoelectrical cooling of polar molecules. Physical Review A, 80(4):041401, 2009.
- [55] Sotir Chervenkov, Xing Wu, Josef Bayerl, A Rohlfes, Thomas Gantner, Martin Zeppenfeld, and Gerhard Rempe. Continuous centrifuge decelerator for polar molecules. Physical review letters, 112(1):013001, 2014.
- [56] Manish Gupta and Dudley Herschbach. Slowing and speeding molecular beams by means of a rapidly rotating source. The Journal of Physical Chemistry A, 105(9):1626–1637, 2001.
- [57] M Streb, F Stienkemeier, and M Mudrich. Improved setup for producing slow beams of cold molecules using a rotating nozzle. Physical Review A, 81(3):033409, 2010.
- [58] Sadiqali A Rangwala, Tobias Junglen, Thomas Rieger, Pepijn WH Pinkse, and Gerhard Rempe. Continuous source of translationally cold dipolar molecules. Physical Review A, 67(4):043406, 2003.
- [59] Thomas Rieger, Tobias Junglen, Sadiqali A Rangwala, Pepijn WH Pinkse, and Gerhard Rempe. Continuous loading of an electrostatic trap for polar molecules. Physical review letters, 95(17):173002, 2005.
- [60] H. L. Bethlem, G. Berden, and G. Meijer. Decelerating neutral dipolar molecules. Phys. Rev. Lett., 83(8):1558–1561, 1999.
- [61] H. L. Bethlem, G. Berden, F. M. H. Crompvoets, R. T. Jongma, A. J. A. Van Rooij, and G. Meijer. Electrostatic trapping of ammonia molecules. Nature, 406:491–494, 2000.
- [62] H. L. Bethlem, F. M. H. Crompvoets, R. T. Jongma, S. Y. T. van de Meerakker, and G. Meijer. Deceleration and trapping of ammonia using time-varying electric fields. Physical Review A, 65:053416, 2002.
- [63] Nicolas Vanhaecke, Urban Meier, Markus Andrist, Beat H Meier, and Frédéric Merkt. Multistage zeeman deceleration of hydrogen atoms. Physical Review A, 75(3):031402, 2007.
- [64] Stephen D Hogan, Daniel Sprecher, Markus Andrist, Nicolas Vanhaecke, and Frédéric Merkt. Zeeman deceleration of H and D. Physical Review A, 76(2):023412, 2007.
- [65] E. Narevicius, A. Libson, C. G. Parthey, I. Chavez, J. Narevicius, U. Even, and M. G. Raizen. Stopping supersonic beams with a series of pulsed electromagnetic coils: An atomic coilgun. Phys. Rev. Lett., 100(9):093003, 2008.
- [66] E. Narevicius, A. Libson, C. G. Parthey, I. Chavez, J. Narevicius, U. Even, and M. G. Raizen. Stopping supersonic oxygen with a series of pulsed electromagnetic coils: A molecular coilgun. Phys. Rev. A, 77:051401, 2008.
- [67] John M Brown and Alan Carrington. Rotational spectroscopy of diatomic molecules. Cambridge University Press, 2003.
- [68] Wolfgang Demtroder. Molecular Physics. Wiley VCH, 2003.
- [69] Lev Davidovič Landau, Lev Davidovic Landau, Lev Davidovich Landau, Evgenii Mikhailovich Lifshitz, and Evgenij Michajlovič Lifšic. Quantum Mechanics (Non-Relativistic Theory). Butterworth-Heinemann, 1950.
- [70] Helene Lefebvre-Brion and Robert W. Field. The Spectra and Dynamics of Diatomic Molecules. Elsevier, 2004.
- [71] Charles H Townes and Arthur L Schawlow. Microwave spectroscopy. Dover Publications, 2013.
- [72] Robert J. Gordon Valeria D. Kleiman, Hongkun Park and Richard N. Zare. Companion to Angular Momentum. Wiley-Interscience, 1998.

- [73] Donald Allan McQuarrie. Quantum chemistry. University Science Books, 2008.
- [74] Brian Harold Bransden and Charles Jean Joachain. Physics of atoms and molecules. Pearson Education India, 2003.
- [75] Seung E Choi and Richard B Bernstein. Theory of oriented symmetric-top molecule beams: Precession, degree of orientation, and photofragmentation of rotationally state-selected molecules. The Journal of chemical physics, 85(1):150–161, 1986.
- [76] Philip CD Hobbs. Building electro-optical systems: making it all work, volume 71. John Wiley & Sons, 2011.
- [77] Walther Gerlach and Otto Stern. Das magnetische moment des silberatoms. Zeitschrift für Physik A Hadrons and Nuclei, 9(1):353–355, 1922.
- [78] S. Y. T. van de Meerakker, H. L. Bethlem, N. Vanhaecke, and G. Meijer. Manipulation and control of molecular beams. Chemical Reviews, 112:4828–4878, 2012.
- [79] Jim P Gordon, Herb J Zeiger, and Charles H Townes. Molecular microwave oscillator and new hyperfine structure in the microwave spectrum of n h 3. Physical Review, 95(1):282, 1954.
- [80] Graeme Austin Bird. Molecular gas dynamics and the direct simulation of gas flows. Clarendon, 1994.
- [81] Norman Foster Ramsey. Molecular beams. Oxford University Press, New York, NY, 1985.
- [82] Giovanni Sanna and Giuseppe Tomassetti. Introduction to molecular beams gas dynamics. World Scientific, 2005.
- [83] Hans Wolfgang Liepmann and Anatol Roshko. Elements of gasdynamics. Courier Corporation, 1957.
- [84] J Peter Toennies and Klaus Winkelmann. Theoretical studies of highly expanded free jets: Influence of quantum effects and a realistic intermolecular potential. The Journal of Chemical Physics, 66(9):3965–3979, 1977.
- [85] HCW Beijerinck and NF Verster. Absolute intensities and perpendicular temperatures of supersonic beams of polyatomic gases. Physica B+ C, 111(2):327–352, 1981.
- [86] Jue Wang, Vasgen A Shamamian, Bruce R Thomas, James M Wilkinson, Joelle Riley, Clayton F Giese, and W Ronald Gentry. Speed ratios greater than 1000 and temperatures less than 1 mK in a pulsed he beam. Physical review letters, 60(8):696, 1988.
- [87] Kfir Luria, Wolfgang Christen, and Uzi Even. Generation and propagation of intense supersonic beams. The Journal of Physical Chemistry A, 115(25):7362–7367, 2011.
- [88] U Even. Pulsed supersonic beams from high pressure source: Simulation results and experimental measurements. Advances in Chemistry, 2014, 2014.
- [89] Christopher M Lovejoy and David J Nesbitt. Slit pulsed valve for generation of long-path-length supersonic expansions. Review of scientific instruments, 58(5):807–811, 1987.
- [90] Christopher M Lovejoy, Michael D Schuder, and David J Nesbitt. High resolution ir laser spectroscopy of van der waals complexes in slit supersonic jets: Observation and analysis of $\nu 1$, $\nu 1 + \nu 2$, and $\nu 1 + 2\nu 3$ in ArHF. The Journal of chemical physics, 85(9):4890–4902, 1986.
- [91] Fei Luo, George C McBane, Geunsik Kim, Clayton F Giese, and W Ronald Gentry. The weakest bond: Experimental observation of helium dimer. The Journal of Chemical Physics, 98(4):3564–3567, 1993.
- [92] M. Hillenkamp, S. Keinan, and U. Even. Condensation limited cooling in supersonic expansions. Journal of Chemical Physics, 118(19), 2003.

- [93] Richard E. Smalley, Lennard Wharton, and Donald H. Levy. Molecular optical spectroscopy with supersonic beams and jets. Accounts of Chemical Research, 10(4):139–145, 1977.
- [94] Charles T Rettner, Ernesto E Marinero, Richard N Zare, and Andrew H Kung. Pulsed free jets: novel nonlinear media for generation of vacuum ultraviolet and extreme ultraviolet radiation. The Journal of Physical Chemistry, 88(20):4459–4465, 1984.
- [95] RL Byer and MD Duncan. A 100 μ sec, reliable, 10 Hz pulsed supersonic molecular beam source. The Journal of Chemical Physics, 74(4):2174–2179, 1981.
- [96] Katherine L Saenger and John B Fenn. On the time required to reach fully developed flow in pulsed supersonic free jets. The Journal of chemical physics, 79(12):6043–6045, 1983.
- [97] K. L. Saenger. Pulsed molecular beams: a lower limit on pulse duration for fully developed supersonic expansions. Journal of Chemical Physics, 75, 1981.
- [98] Wolfgang Christen. Stationary flow conditions in pulsed supersonic beams. The Journal of chemical physics, 139(15):154202, 2013.
- [99] Inc. Jordan TOF Products. <http://rmjordan.com>.
- [100] B. Yan, F. H. Claus, B. G. M. van Oorschot, L. Gerritsen, a. T. J. B. Eppink, S. Y. T. van de Meerakker, and D. H. Parker. A new high intensity and short-pulse molecular beam valve. Review of Scientific Instruments, 84:023102, 2013.
- [101] Charles E Otis and Philip M Johnson. A simple pulsed valve for use in supersonic nozzle experiments. Review of Scientific Instruments, 51(8):1128–1129, 1980.
- [102] D Bassi, S Iannotta, and S Niccolini. Pulsed molecular beam source. Review of Scientific Instruments, 52(1):8–11, 1981.
- [103] Luis Abad, Dionisio Bermejo, Víctor J Herrero, J Santos, and Isabel Tanarro. Performance of a solenoid-driven pulsed molecular-beam source. Review of scientific instruments, 66(7):3826–3832, 1995.
- [104] Parker Automation. <http://ph.parker.com/us/12051/en/miniature-micro-dispensing-valves>.
- [105] U. Even, J. Jortner, D. Noy, and N. Lavie. Cooling of large molecules below 1 K and He clusters formation. Journal of Chemical Physics, 112(18), 2000.
- [106] Jon B. Cross and James J. Valentini. High repetition rate pulsed nozzle beam source. Review of Scientific Instruments, 53(1):38–42, 1982.
- [107] D. Proch and T. Trickl. A high-intensity multi-purpose piezoelectric pulsed molecular beam source. Review of Scientific Instruments, 60, 1989.
- [108] D. Irimia, D. Dobrikov, R. Kotekaas, H. Voet, D. A. van den Ende, W. A. Groen, and M. H. Janssen. A short pulse (7 μ s FWHM) and high repetition rate (dc-5kHz) cantilever piezovalve for pulsed atomic and molecular beams. Review of Scientific Instruments, 80:113303, 2009.
- [109] P. Andresen, M. Faubel, D. Haeusler, G. Kraft, H. Å. R. W. Luelf, and J. G. Skofronick. Characteristics of a piezoelectric pulsed nozzle beam. Review of Scientific Instruments, 56(11):2038–2042, 1985.
- [110] Chamara Abeysekera, Baptiste Joalland, Yuanyuan Shi, Alexander Kamasah, James M Oldham, and Arthur G Suits. Note: A short-pulse high-intensity molecular beam valve based on a piezoelectric stack actuator. Review of Scientific Instruments, 85(11):116107, 2014.
- [111] Prof. Dieter Gerlich. Fast pulsed piezo valve. https://www.tu-chemnitz.de/physik/ION/Technology/Piezo_Valve/index.html.

- [112] Physik Instrumente. Displacement modes of piezoelectric actuators. <http://piceramic.com/piezotechnology/properties-piezo-actuators/displacement-modes.html>.
- [113] Parker Hannifin Corporation. Parker o-ring handbook.
- [114] William Brewster Chapman. Quantum state resolved inelastic and reactive scattering dynamics in molecular systems via high resolution IR laser spectroscopy. University of Colorado-Boulder, 1997.
- [115] Hans Pauly. Atom, Molecule, and Cluster Beams I: Cluster Beams, Fast and Slow Beams, Accessory Equipment and Applications, volume 1. Springer Science & Business Media, 2000.
- [116] R Campargue. Progress in overexpanded supersonic jets and skimmed molecular beams in free-jet zones of silence. The Journal of Physical Chemistry, 88(20):4466–4474, 1984.
- [117] U. Bossel, F. C. Hurlbut, and F. S. Sherman, Edited by L. Trilling and H. Y. Wachman. Rarefied Gas Dynamics, II:945–964, 1969.
- [118] U Bossel. Entropie, 42(12), 1971.
- [119] Beam Dynamics Inc., 2013. http://www.beamdynamicsinc.com/skimmer_description.htm.
- [120] GA Bird. Transition regime behavior of supersonic beam skimmers. Physics of Fluids (1958-1988), 19(10):1486–1491, 1976.
- [121] J Braun, PK Day, JP Toennies, G Witte, and E Neher. Micrometer-sized nozzles and skimmers for the production of supersonic he atom beams. Review of scientific instruments, 68(8):3001–3009, 1997.
- [122] DC Jordan, R Barling, and RB Doak. Refractory graphite skimmers for supersonic free-jet, supersonic arc-jet, and plasma discharge applications. Review of scientific instruments, 70(3):1640–1648, 1999.
- [123] MJ Verheijen, HCW Beijerinck, WA Renes, and NF Verster. A quantitative description of skimmer interaction in supersonic secondary beams: Calibration of absolute intensities. Chemical physics, 85(1):63–71, 1984.
- [124] T. G. Dietz, M. A. Duncan, D. E. Powers, and R. E. Smalley. Laser production of supersonic metal cluster beams. The Journal of Chemical Physics, 74(11):6511–6512, 1981.
- [125] JB Hopkins, PRR Langridge-Smith, MD Morse, and RE Smalley. Supersonic metal cluster beams of refractory metals: Spectral investigations of ultracold Mo₂. The Journal of Chemical Physics, 78(4):1627–1637, 1983.
- [126] RE Smalley. Laser studies of beams. Laser Chem, 2:167–184, 1983.
- [127] Xibin Gu, Ying Guo, Ed Kawamura, and Ralf I Kaiser. Characteristics and diagnostics of an ultrahigh vacuum compatible laser ablation source for crossed molecular beam experiments. Journal of Vacuum Science & Technology A: Vacuum, Surfaces, and Films, 24(3):505–511, 2006.
- [128] Aaron E Leanhardt, JL Bohn, H Loh, P Maletinsky, ER Meyer, LC Sinclair, RP Stutz, and EA Cornell. High-resolution spectroscopy on trapped molecular ions in rotating electric fields: A new approach for measuring the electron electric dipole moment. Journal of Molecular Spectroscopy, 270(1):1–25, 2011.
- [129] KM Evenson and JM Brown. 5. free radical sources. Atomic, Molecular, and Optical Physics: Atoms and Molecules. Series: Experimental Methods in the Physical Sciences, ISBN: 9780124759763. Elsevier, vol. 29, pp. 85-94, 29:85–94, 1996.
- [130] Paul C Engelking. Spectroscopy of jet-cooled ions and radicals. Chemical Reviews, 91(3):399–414, 1991.
- [131] Joaquim Henrique Teles, Günther Maier, B Andes Hess, Lawrence J Schaad, Manfred Winnewisser, and Brenda P Winnewisser. The chno isomers. Chemische Berichte, 122(4):753–766, 1989.

- [132] RN Dixon and GH Kirby. Ultra-violet absorption spectrum of isocyanic acid. Transactions of the Faraday Society, 64:2002–2012, 1968.
- [133] Thomas A Spiglanin, Robert A Perry, and David W Chandler. Photodissociation studies of isocyanic acid: heat of formation and product branching ratios. The Journal of Physical Chemistry, 90(23):6184–6189, 1986.
- [134] Thomas A Spiglanin and David W Chandler. Rotational state distributions of NH ($a^1\Delta$) from HNCO photodissociation. The Journal of chemical physics, 87(3):1577–1581, 1987.
- [135] Thomas A Spiglanin, Robert A Perry, and David W Chandler. Internal state distributions of CO from HNCO photodissociation. The Journal of chemical physics, 87(3):1568–1576, 1987.
- [136] Whikun Yi and Richard Bersohn. The hydrogen atom channel in the photodissociation of HNCO. Chemical physics letters, 206(1):365–368, 1993.
- [137] RA Brownsword, T Laurent, RK Vatsa, H-R Volpp, and J Wolfrum. Branching ratio for the H+ NCO channel in the 193 nm photodissociation of HNCO. Chemical physics letters, 249(3):162–166, 1996.
- [138] RA Brownsword, M Hillenkamp, T Laurent, RK Vatsa, and H-R Volpp. Photodissociation dynamics in the UV laser photolysis of DNCO: Comparison with HNCO. The Journal of chemical physics, 106(11):4436–4447, 1997.
- [139] Richard N Zare and Richard B Bernstein. State-to-state reaction dynamics. Physics Today, 33(11):43–50, 1980.
- [140] Y. T. Lee. Molecular-beam studies of elementary chemical processes. Science, 236(4803):793–798, 1987.
- [141] Stanley Paul Sander, RR Friedl, DM Golden, MJ Kurylo, GK Moortgat, PH Wine, AR Ravishankara, CE Kolb, MJ Molina, BJ Finlayson-Pitts, et al. Chemical kinetics and photochemical data for use in atmospheric studies evaluation number 15. JPL Publication 06-2, 2006.
- [142] Hideo Okabe et al. Photochemistry of small molecules, volume 431. Wiley New York, 1978.
- [143] Hiroyasu Sato. Photodissociation of simple molecules in the gas phase. Chemical reviews, 101(9):2687–2726, 2001.
- [144] RD Kenner, F Rohrer, and F Stuhl. Generation of NH ($a^1\delta$) in the 193 nm photolysis of ammonia. The Journal of chemical physics, 86(4):2036–2043, 1987.
- [145] Walter S Drozdowski, A-P. Baronavski, and J-R. McDonald. Photodissociation of hnco at 193 nm. nh ($a^1\delta$) internal energy distribution and reaction rate with o₂. Chemical Physics Letters, 64(3):421–425, 1979.
- [146] GT Fujimoto, ME Umstead, and MC Lin. Dynamics of CO formation in the photodissociation of HNCO and CH₂CO at 193nm. Chemical Physics, 65(2):197–203, 1982.
- [147] M Zyrianov, Th Droz-Georget, A Sanov, and H Reisler. Competitive photodissociation channels in jet-cooled HNCO: Thermochemistry and near-threshold predissociation. The Journal of chemical physics, 105(18):8111–8116, 1996.
- [148] F Rohrer and F Stuhl. The 193 (and 248) nm photolysis of HN₃: Formation and internal energy distributions of the NH ($a^1\Delta$, b^1+ , $a^3\Pi$, and $c^1\Pi$) states. The Journal of chemical physics, 88(8):4788–4799, 1988.
- [149] AP. Baronavski, RG Miller, and JR McDonald. Laser induced photodissociation of HN₃ at 266 nm. i. primary products, photofragment energy distributions and reactions of intermediates. Chemical Physics, 30(2):119–131, 1978.

- [150] Sebastiaan YT van de Meerakker, Paul HM Smeets, Nicolas Vanhaecke, Rienk T Jongma, and Gerard Meijer. Deceleration and electrostatic trapping of OH radicals. Physical review letters, 94(2):023004, 2005.
- [151] Ludwig Scharfenberg, Jacek Kłos, Paul J Dagdigian, Millard H Alexander, Gerard Meijer, and Sebastiaan YT van de Meerakker. State-to-state inelastic scattering of stark-decelerated OH radicals with Ar atoms. Physical Chemistry Chemical Physics, 12(36):10660–10670, 2010.
- [152] Moritz Kirste, Xingan Wang, H Christian Schewe, Gerard Meijer, Kopin Liu, Ad van der Avoird, Liesbeth MC Janssen, Koos B Gubbels, Gerrit C Groenenboom, and Sebastiaan YT van de Meerakker. Quantum-state resolved bimolecular collisions of velocity-controlled OH with NO radicals. Science, 338(6110):1060–1063, 2012.
- [153] A Schiffman, DD Nelson Jr, and DJ Nesbitt. Quantum yields for OH production from 193 and 248 nm photolysis of HNO₃ and H₂O₂. The Journal of chemical physics, 98(9):6935–6946, 1993.
- [154] O Rattigan, E Lutman, RL Jones, RA Cox, K Clemitshaw, and J Williams. Temperature-dependent absorption cross-sections of gaseous nitric acid and methyl nitrate. Journal of Photochemistry and Photobiology A: Chemistry, 66(3):313–326, 1992.
- [155] Louis J Stief, Walter A Payne, and R Bruce Klemm. A flash photolysis–resonance fluorescence study of the formation of O (1D) in the photolysis of water and the reaction of O (1D) with H₂, Ar, and He-. The Journal of Chemical Physics, 62(10):4000–4008, 1975.
- [156] Eizi Hirota. Microwave and infrared spectra of free radicals and molecular ions. Chemical reviews, 92(1):141–173, 1992.
- [157] AT Droege and PC Engelking. Supersonic expansion cooling of electronically excited OH radicals. Chemical Physics Letters, 96(3):316–318, 1983.
- [158] P. C. Engelking. Corona excited supersonic expansion. Review of Scientific Instruments, 57(9):2274–2277, 1986.
- [159] Toomas H Allik, Brian B Brady, George W Flynn, and Garry B Spector. Translational energy characteristics of radicals and ions in a capillaritron supersonic nozzle discharge. The Journal of Physical Chemistry, 88(15):3204–3208, 1984.
- [160] K Luria, N Lavie, and U Even. Dielectric barrier discharge source for supersonic beams. Review of Scientific Instruments, 80(10):104102, 2009.
- [161] Alexander Ershov and Jacek Borysow. Dynamics of OH ($X^2\Pi$, $v=0$) in high-energy atmospheric pressure electrical pulsed discharge. Journal of Physics D: Applied Physics, 28(1):68, 1995.
- [162] HJ Lewandowski, Eric R Hudson, JR Bochinski, and Jun Ye. A pulsed, low-temperature beam of supersonically cooled free radical OH molecules. Chemical physics letters, 395(1):53–57, 2004.
- [163] Jérôme Remy, Ludovic Biennier, and Farid Salama. Plasma structure in a pulsed discharge environment. Plasma Sources Science and Technology, 12(3):295, 2003.
- [164] BHP Broks, WJM Brok, J Remy, JJAM Van der Mullen, A Benidar, L Biennier, and F Salama. Numerical investigation of the discharge characteristics of the pulsed discharge nozzle. Physical Review E, 71(3):036409, 2005.
- [165] M J Verheijen, H C W Beijerinck, L H A M van Moll, J Driessen, and N F Verster. A discharge excited supersonic source of metastable rare gas atoms. Journal of Physics E: Scientific Instruments, 17(10):904, 1984.
- [166] MC Van Beek and JJ Ter Meulen. An intense pulsed electrical discharge source for OH molecular beams. Chemical physics letters, 337(4):237–242, 2001.

- [167] Daniel Irimia, Rob Kortekaas, and Maurice HM Janssen. In situ characterization of a cold and short pulsed molecular beam by femtosecond ion imaging. Physical Chemistry Chemical Physics, 11(20):3958–3966, 2009.
- [168] CIM Beenakker, FJ De Heer, HB Krop, and GR Möhlmann. Dissociative excitation of water by electron impact. Chemical Physics, 6(3):445–454, 1974.
- [169] Stephen D Hogan, Michael Motsch, and Frédéric Merkt. Deceleration of supersonic beams using inhomogeneous electric and magnetic fields. Physical Chemistry Chemical Physics, 13(42):18705–18723, 2011.
- [170] H. L. Bethlem, G. Berden, A. J. A. van Roij, F. M. H. Crompvoets, and G. Meijer. Trapping neutral molecules in a traveling potential well. Phys. Rev. Lett., 84(25):5744–5747, 2000.
- [171] Wolfgang Paul. Electromagnetic traps for charged and neutral particles. Reviews of modern physics, 62(3):531–, 1990.
- [172] William H Wing. Electrostatic trapping of neutral atomic particles. Physical Review Letters, 45(8):631, 1980.
- [173] William H Wing. On neutral particle trapping in quasistatic electromagnetic fields. Progress in Quantum Electronics, 8(3):181–199, 1984.
- [174] W Ketterle and DE Pritchard. Trapping and focusing ground state atoms with static fields. Applied Physics B, 54(5):403–406, 1992.
- [175] Harold J Metcalf and WD Phillips. Electromagnetic trapping of neutral atoms. Metrologia, 22(4):271, 1986.
- [176] Thomas F Gallagher. Rydberg Atoms. Cambridge University Press, 1994.
- [177] E Vliegen, SD Hogan, H Schmutz, and F Merkt. Stark deceleration and trapping of hydrogen rydberg atoms. Physical Review A, 76(2):023405, 2007.
- [178] SD Hogan, Ch Seiler, and F Merkt. Rydberg-state-enabled deceleration and trapping of cold molecules. Physical review letters, 103(12):123001, 2009.
- [179] LD Landau. Mechanics: Volume 1 (Course Of Theoretical Physics) Author: LD Landau, EM Lifshitz, Publisher: Butterwor. Butterworth-Heinemann, 1976.
- [180] John L. Safko Herbert Goldstein, Charles P. Poole. Classical Mechanics. Pearson Education, 2000.
- [181] Walter Greiner. Classical Mechanics: systems of particles and Hamiltonian dynamics. Springer Science & Business Media, 2009.
- [182] Allan J Lichtenberg. Phase-space dynamics of particles. Wiley, 1969.
- [183] Harold J Metcalf and Peter Van der Straten. Laser cooling and trapping. Springer Science & Business Media, 1999.
- [184] Wolfgang Ketterle and David E Pritchard. Atom cooling by time-dependent potentials. Physical Review A, 46(7):4051, 1992.
- [185] S. Y. T. van de Meerakker, N. Vanhaecke, H. L. Bethlem, and G. Meijer. Higher-order resonances in a Stark decelerator. Phys. Rev. A, 71:053409, 2005.
- [186] Hendrick L Bethlem and Gerard Meijer. Production and application of translationally cold molecules. International reviews in physical chemistry, 22(1):73–128, 2003.
- [187] S. Y. T. van de Meerakker, N. Vanhaecke, H. L. Bethlem, and G. Meijer. Transverse stability in a Stark decelerator. Physical Review A, 73:023401, 2006.

- [188] J. Veldhoven, H. L. Bethlem, M. Schnell, and G. Meijer. Versatile electrostatic trap. Physical Review A, 73:063408, 2006.
- [189] J. J. Gilijamse, S. Hoekstra, N. Vanhaecke, S. Y. T. van de Meerakker, and G. Meijer. Loading Stark-decelerated molecules into electrostatic quadrupole traps. Eur. Phys. J. D, 57:33–41, 2010.
- [190] Brian C Sawyer, Benjamin K Stuhl, Dajun Wang, Mark Yeo, and Jun Ye. Molecular beam collisions with a magnetically trapped target. Physical review letters, 101(20):203203, 2008.
- [191] H. L. Bethlem, J. Veldhoven, M. Schnell, and G. Meijer. Trapping polar molecules in an ac trap. Physical Review A, 74:063403, 2006.
- [192] J. Kupper, B. Friedrich, M. Schleier-Smith, H. Haak, and G. Meijer. A Linear AC Trap for Polar Molecules in Their Ground State. Journal of Physical Chemistry A, 111 (31):7411–7419, 2007.
- [193] T Bergeman, Gidon Erez, and Harold J Metcalf. Magnetostatic trapping fields for neutral atoms. Physical Review A, 35(4):1535, 1987.
- [194] James A Samson, David L Ederer, Thomas Lucatorto, and Marc De Graef. Vacuum ultraviolet spectroscopy I, volume 1. Academic press, 1998.
- [195] James A Samson, David L Ederer, Thomas Lucatorto, and Marc De Graef. Vacuum ultraviolet spectroscopy II, volume 2. Academic press, 1998.
- [196] Cheuk-Yiu Ng. Vacuum ultraviolet spectroscopy and chemistry by photoionization and photoelectron methods. Annual review of physical chemistry, 53(1):101–140, 2002.
- [197] Daniel R Albert and H Floyd Davis. Studies of bimolecular reaction dynamics using pulsed high-intensity vacuum-ultraviolet lasers for photoionization detection. Physical Chemistry Chemical Physics, 15(35):14566–14580, 2013.
- [198] Arman Cingöz, Dylan C Yost, Thomas K Allison, Axel Ruehl, Martin E Fermann, Ingmar Hartl, and Jun Ye. Direct frequency comb spectroscopy in the extreme ultraviolet. Nature, 482(7383):68–71, 2012.
- [199] Nelson De Oliveira, Mourad Roudjane, Denis Joyeux, Daniel Phalippou, Jean-Claude Rodier, and Laurent Nahon. High-resolution broad-bandwidth fourier-transform absorption spectroscopy in the vuv range down to 40 nm. Nature Photonics, 5(3):149–153, 2011.
- [200] S Hannemann, EJ Salumbides, S Witte, R Th Zinkstok, E-J Van Duijn, KSE Eikema, and W Ubachs. Frequency metrology on the $E F \Sigma g+ 1? X \Sigma g+ 1 (0, 0)$ transition in H_2 , HD, and D_2 . Physical Review A, 74(6):062514, 2006.
- [201] Wade G Rellergert, D DeMille, RR Greco, MP Hehlen, JR Torgerson, and Eric R Hudson. Constraining the Evolution of the Fundamental Constants with a Solid-State Optical Frequency Reference Based on the Th 229 Nucleus. Physical review letters, 104(20):200802, 2010.
- [202] EE Eyler, DE Chieda, Matthew C Stowe, Michael J Thorpe, TR Schibli, and Jun Ye. Prospects for precision measurements of atomic helium using direct frequency comb spectroscopy. The European Physical Journal D-Atomic, Molecular, Optical and Plasma Physics, 48(1):43–55, 2008.
- [203] Robert W Boyd. Nonlinear optics. Academic press, 2003.
- [204] Yuen-Ron Shen. Principles of nonlinear optics. Wiley-Interscience, New York, NY, USA, 1984.
- [205] Geoffrey New. Introduction to Nonlinear Optics. Cambridge University Press, 2011.
- [206] GD Miller, RG Batchko, WM Tulloch, DR Weise, MM Fejer, and RL Byer. 42%-efficient single-pass cw second-harmonic generation in periodically poled lithium niobate. Optics letters, 22(24):1834–1836, 1997.

- [207] Thomas A Driscoll, Hanna J Hoffman, Richard E Stone, and Patrick E Perkins. Efficient second-harmonic generation in KTP crystals. JOSA B, 3(5):683–686, 1986.
- [208] DA Kleinman. Nonlinear dielectric polarization in optical media. Physical Review, 126(6):1977, 1962.
- [209] E Cromwell, T Trickl, YT Lee, and AH Kung. Ultranarrow bandwidth VUV-XUV laser system. Review of scientific instruments, 60(9):2888–2892, 1989.
- [210] OJ Luiten, HGC Werij, MW Reynolds, ID Setija, TW Hijmans, and JTM Walraven. VUV spectroscopy of magnetically trapped atomic hydrogen. Applied Physics B, 59(3):311–319, 1994.
- [211] F Mühlberger, R Zimmermann, and A Kettrup. A mobile mass spectrometer for comprehensive on-line analysis of trace and bulk components of complex gas mixtures: Parallel application of the laser-based ionization methods vuv single-photon ionization, resonant multiphoton ionization, and laser-induced electron impact ionization. Analytical chemistry, 73(15):3590–3604, 2001.
- [212] SJ Hanna, P Campuzano-Jost, EA Simpson, DB Robb, I Burak, MW Blades, JW Hepburn, and AK Bertram. A new broadly tunable (7.4-10.2 eV) laser based VUV light source and its first application to aerosol mass spectrometry. International Journal of Mass Spectrometry, 279(2):134–146, 2009.
- [213] Jonathan R Woodward, Hirokazu Watanabe, Shun-Ichi Ishiuchi, and Masaaki Fujii. A two-color tunable infrared/vacuum ultraviolet spectrometer for high-resolution spectroscopy of molecules in molecular beams. Review of Scientific Instruments, 83(1):014102, 2012.
- [214] Daniel R Albert, David L Proctor, and H Floyd Davis. High-intensity coherent vacuum ultraviolet source using unfocussed commercial dye lasers. Review of Scientific Instruments, 84(6):063104, 2013.
- [215] Anthony E Siegman. Lasers university science books. Mill Valley, CA, 37, 1986.
- [216] AH Kung, John Frederick Young, and SE Harris. Generation of 1182-Å radiation in phase-matched mixtures of inert gases. Applied Physics Letters, 22(6):301–302, 1973.
- [217] Donald F Heath and Paul A Sacher. Effects of a simulated high-energy space environment on the ultraviolet transmittance of optical materials between 1050 Å and 3000 Å. Applied optics, 5(6):937–943, 1966.
- [218] G Hass and WR Hunter. Laboratory experiments to study surface contamination and degradation of optical coatings and materials in simulated space environments. Applied Optics, 9(9):2101–2110, 1970.
- [219] Marilyn J Dodge. Refractive properties of magnesium fluoride. Applied optics, 23(12):1980–1985, 1984.
- [220] P Laporte, JL Subtil, M Courbon, M Bon, and L Vincent. Vacuum-ultraviolet refractive index of LiF and MgF₂ in the temperature range 80-300 K. JOSA, 73(8):1062–1069, 1983.
- [221] Nouredine Melikechi, Shubhagat Gangopadhyay, and Edward E Eyler. Generation of vacuum ultraviolet radiation for precision laser spectroscopy. Applied optics, 36(30):7776–7778, 1997.
- [222] Center for X-Ray Optics, 2013. http://henke.lbl.gov/optical_constants/gastrn2.html.
- [223] Terrill A Cool, Juan Wang, Koichi Nakajima, Craig A Taatjes, and Andrew Mellroy. Photoionization cross sections for reaction intermediates in hydrocarbon combustion. International Journal of Mass Spectrometry, 247(1):18–27, 2005.
- [224] Gary C Bjorklund. Effects of focusing on third-order nonlinear processes in isotropic media. Quantum Electronics, IEEE Journal of, 11(6):287–296, 1975.
- [225] R Miles and S Harris. Optical third-harmonic generation in alkali metal vapors. Quantum Electronics, IEEE Journal of, 9(4):470–484, 1973.

- [226] Von R. FISCHER und L.-W. WIECZOR. Theorie der optimalen fokussierung für die direkte erzeugung höherer optischer harmonischer. Annalen der Physik, 7(3):147–149, 1978.
- [227] L Zych and J Young. Limitation of 3547 to 1182 Å conversion efficiency in Xe. Quantum Electronics, IEEE Journal of, 14(3):147–149, 1978.
- [228] Herbert Scheingraber, H Puell, and CR Vidal. Quantitative analysis of resonant third-harmonic generation in strontium. Physical Review A, 18(6):2585, 1978.
- [229] H Junginger, H Puell, H Scheingraber, and C Vidal. Resonant third-harmonic generation in a low-loss medium. Quantum Electronics, IEEE Journal of, 16(10):1132–1137, 1980.
- [230] H Scheingraber and CR Vidal. Near resonant third harmonic generation. Optics Communications, 38(1):75–80, 1981.
- [231] HERBERT Scheingraber and C Vidal. Saturation of resonant third-harmonic generation due to self-defocusing and a redistribution of the population densities. Quantum Electronics, IEEE Journal of, 19(12):1747–1758, 1983.
- [232] WF Chan, G Cooper, X Guo, GR Burton, and CE Brion. Absolute optical oscillator strengths for the electronic excitation of atoms at high resolution. iii. the photoabsorption of argon, krypton, and xenon. Physical Review A, 46(1):149, 1992.
- [233] Alan Corney. Atomic and laser spectroscopy. Clarendon Press Oxford, 1978.
- [234] Wanda R Ferrell, MG Payne, and WR Garrett. Resonance broadening and shifting of spectral lines in xenon and krypton. Physical Review A, 36(1):81, 1987.
- [235] W. C. Martin and W. L. Wiese. Atomic spectroscopy: A compendium of basic ideas, notation, data and formulas. <http://physics.nist.gov/Pubs/AtSpec/index.html>.
- [236] Gordon WF. Drake. Springer handbook of atomic, molecular, and optical physics. Springer Science & Business Media, 2006.
- [237] DI Rosen and G Weyl. Laser-induced breakdown in nitrogen and the rare gases at 0.53 and 0.357 μm. Journal of Physics D: Applied Physics, 20(10):1264, 1987.
- [238] R Hilbig and R Wallenstein. Enhanced production of tunable VUV radiation by phase-matched frequency tripling in krypton and xenon. Quantum Electronics, IEEE Journal of, 17(8):1566–1573, 1981.
- [239] Heinz Puell, K Spanner, W Falkenstein, W Kaiser, and CR Vidal. Third-harmonic generation of mode-locked Nd: glass laser pulses in phase-matched Rb-Xe mixtures. Physical Review A, 14(6):2240, 1976.
- [240] Jun Ye, Long-Sheng Ma, and John L Hall. Ultrasensitive detections in atomic and molecular physics: demonstration in molecular overtone spectroscopy. JOSA B, 15(1):6–15, 1998.
- [241] Wolfgang Demtröder. Laser spectroscopy: basic concepts and instrumentation. Springer Science & Business Media, 2003.
- [242] Paul Horowitz, Winfield Hill, and Thomas C Hayes. The art of electronics, volume 3. Cambridge university press Cambridge, 2015.
- [243] Gary C Bjorklund. Frequency-modulation spectroscopy: a new method for measuring weak absorptions and dispersions. Optics Letters, 5(1):15–17, 1980.
- [244] JL Hall, L Hollberg, T Baer, and HG Robinson. Optical heterodyne saturation spectroscopy. Applied Physics Letters, 39(9):680–682, 1981.

- [245] GC Bjorklund, MD Levenson, W Lenth, and C Ortiz. Frequency modulation (fm) spectroscopy. Applied Physics B, 32(3):145–152, 1983.
- [246] Manfred Gehrtz, Gary C Bjorklund, and Edward A Whittaker. Quantum-limited laser frequency-modulation spectroscopy. JOSA B, 2(9):1510–1526, 1985.
- [247] Joel A Silver. Frequency-modulation spectroscopy for trace species detection: theory and comparison among experimental methods. Applied optics, 31(6):707–717, 1992.
- [248] Philip CD Hobbs. Ultrasensitive laser measurements without tears. Applied optics, 36(4):903–920, 1997.
- [249] Livio Gianfrani, Richard W Fox, and Leo Hollberg. Cavity-enhanced absorption spectroscopy of molecular oxygen. JOSA B, 16(12):2247–2254, 1999.
- [250] Giel Berden, Rudy Peeters, and Gerard Meijer. Cavity ring-down spectroscopy: Experimental schemes and applications. International Reviews in Physical Chemistry, 19(4):565–607, 2000.
- [251] Florian Adler, Michael J Thorpe, Kevin C Cossel, and Jun Ye. Cavity-enhanced direct frequency comb spectroscopy: technology and applications. Annual Review of Analytical Chemistry, 3:175–205, 2010.
- [252] Anthony O’Keefe and David AG Deacon. Cavity ring-down optical spectrometer for absorption measurements using pulsed laser sources. Review of Scientific Instruments, 59(12):2544–2551, 1988.
- [253] JJ Scherer, JB Paul, A O’keefe, and RJ Saykally. Cavity ringdown laser absorption spectroscopy: history, development, and application to pulsed molecular beams. Chemical reviews, 97(1):25–52, 1997.
- [254] Eric M Gullikson, Raj Korde, LR Canfield, and RE Vest. Stable silicon photodiodes for absolute intensity measurements in the VUV and soft x-ray regions. Journal of Electron Spectroscopy and Related Phenomena, 80:313–316, 1996.
- [255] <http://optodiode.com/products.html#IRD-UV-Photodiodes>.
- [256] James AR Samson. Photocathodes: Their efficiency and stability. Nuclear Instruments and Methods in Physics Research, 222(1):215–220, 1984.
- [257] LR Canfield, RG Johnston, and RP Madden. NBS detector standards for the far ultraviolet. Applied optics, 12(7):1611–1617, 1973.
- [258] NIST: Far and Extreme Ultraviolet Detector Calibrations, 2013. http://www.nist.gov/pml/div685/grp07/detector_cal.cfm.
- [259] RB Cairns and JAR Samson. Metal photocathodes as secondary standards for absolute intensity measurements in the vacuum ultraviolet. JOSA, 56(11):1568–1573, 1966.
- [260] Rob Vest, NIST Far and Extreme Ultraviolet Detector Calibrations. Private Communications.
- [261] William C Walker, N Wainfan, and GL Weissler. Photoelectric yields in the vacuum ultraviolet. Journal of Applied Physics, 26(11):1366–1371, 1955.
- [262] NORIMAN N AXELROD. Photoelectric effect in metals in the vacuum ultraviolet. JOSA, 57(11):1393–1394, 1967.
- [263] Silvano Donati. Photodetectors. Prentice Hall PTR, 1999.
- [264] Yukikazu Itikawa, M Hayashi, A Ichimura, K Onda, K Sakimoto, K Takayanagi, M Nakamura, H Nishimura, and T Takayanagi. Cross sections for collisions of electrons and photons with nitrogen molecules. Journal of physical and chemical reference data, 15(3):985–1010, 1986.

- [265] George Rieke. Detection of Light: from the Ultraviolet to the Submillimeter. Cambridge University Press, 2003.
- [266] RL Smith and T Honda. Impulse rise and fall times of biplanar vacuum photodiodes. Applied optics, 12(7):1606–1610, 1973.
- [267] G Beck. Photodiode and holder with 60 psec response time. Review of Scientific Instruments, 47(7):849–853, 1976.
- [268] PE Dyer, HV Snelling, and CD Walton. A simple fast-time-response photoemissive detector for vacuum ultraviolet (VUV) F2 lasers. Measurement Science and Technology, 13(1):92, 2002.
- [269] Helmuth Spieler. Introduction to radiation detectors and electronics. Lecture Notes Physics, 198, 1998.
- [270] Helmuth Spieler. Semiconductor detector systems, volume 12. Oxford university press, 2005.
- [271] David Kliger, editor. Ultrasensitive laser spectroscopy. Academic Press, 2983.
- [272] Sheng Hsien Lin. Multiphoton spectroscopy of molecules. Elsevier, 2012.
- [273] KK Hamamatsu Photonics. Mcp assembly (mcphamamatsu), 2006.
- [274] J Oberheide, P Wilhelms, and M Zimmer. New results on the absolute ion detection efficiencies of a microchannel plate. Measurement Science and Technology, 8(4):351, 1997.
- [275] RS Gao, PS Gibner, JH Newman, KA Smith, and RF Stebbings. Absolute and angular efficiencies of a microchannel-plate position-sensitive detector. Review of scientific instruments, 55(11):1756–1759, 1984.
- [276] Stanford Research Systems. Bayard-alpert ionization gauges. <http://thinkSRS.com>.
- [277] KN Joshipura, Minaxi Vinodkumar, and Umesh M Patel. Electron impact total cross sections of chx, nhx and oh radicals vis-à-vis their parent molecules. Journal of Physics B: Atomic, Molecular and Optical Physics, 34(4):509, 2001.
- [278] TD Märk, F Egger, and M Cheret. Ionization of ammonia and deuterated ammonia by electron impact from threshold up to 180 eV. The Journal of Chemical Physics, 67(8):3795–3802, 1977.
- [279] Brian C. Sawyer. Cold polar molecules for novel collision experiments at low energies. PhD Thesis, University of Colorado-Boulder, 2010.
- [280] RJ Stanley, O Echt, and AW Castleman Jr. Resonance-enhanced multiphoton ionization ($2+1$) of the b and c states of ammonia. Applied Physics B, 32(1):35–38, 1983.
- [281] Noah J. Fitch. Traveling-Wave Stark-Decelerated Molecular Beams for Cold Collision Experiments. PhD Thesis, University of Colorado-Boulder, 2013.
- [282] Gerhard Herzberg. The spectra and structures of simple free radicals: an introduction to molecular spectroscopy. Dover Publications, 1971.
- [283] GH Dieke and HM Crosswhite. The ultraviolet bands of oh fundamental data. Journal of Quantitative Spectroscopy and Radiative Transfer, 2(2):97–199, 1962.
- [284] Daniel Steck. Rb 87 D Line Data. <http://steck.us/alkalidata/>.
- [285] Stanford Research Systems. Application note #4: Signal recovery with pmts. <http://thinkSRS.com>.
- [286] Richard B Miles, Walter R Lempert, and Joseph N Forkey. Laser rayleigh scattering. Measurement Science and Technology, 12(5):R33, 2001.

- [287] William K Bischel, Douglas J Bamford, and Leonard E Jusinski. Absolute calibration of a fluorescence collection system by raman scattering in h 2. Applied optics, 25(7):1215–1221, 1986.
- [288] J Thaddeus Salmon and Normand M Laurendeau. Calibration of laser-saturated fluorescence measurements using rayleigh scattering. Applied optics, 24(1):65–73, 1985.
- [289] J Luque and DR Crosley. Absolute ch concentrations in low-pressure flames measured with laser-induced fluorescence. Applied Physics B, 63(1):91–98, 1996.
- [290] Arin Mizouri, LZ Deng, Jack S Eardley, N Hendrik Nahler, Eckart Wrede, and David Carty. Absolute density measurement of sd radicals in a supersonic jet at the quantum-noise-limit. Physical Chemistry Chemical Physics, 15(45):19575–19579, 2013.
- [291] Mark PJ van der Loo and Gerrit C Groenenboom. Ab initio calculation of $(2+ 1)$ resonance enhanced multiphoton ionization spectra and lifetimes of the $(D, 3) 2S$ -states of OH and OD. Journal of Chemical Physics, 123(7):74310–74310, 2005.
- [292] Margaret E Greenslade, Marsha I Lester, Dragana Č Radenović, André JA van Roij, and David H Parker. $(2+ 1)$ resonance-enhanced ionization spectroscopy of a state-selected beam of oh radicals. The Journal of chemical physics, 123(7):074309, 2005.
- [293] RT Wiedmann, RG Tonkyn, MG White, Kwanghsi Wang, and V McKoy. Rotationally resolved threshold photoelectron spectra of oh and od. The Journal of chemical physics, 97(2):768–772, 1992.
- [294] PM Dehmer. Photoionization of oh in the region 750–950 Å. Chemical physics letters, 110(1):79–84, 1984.
- [295] JN Cutler, ZX He, and JAR Samson. Relative photoionization cross section study of oh and od from 68 nm to 95 nm. Journal of Physics B: Atomic, Molecular and Optical Physics, 28(21):4577, 1995.
- [296] M. D. Morse. Supersonic beam sources. Experimental Methods in the Physical Sciences, 29B:21–47, 1996.
- [297] Alain Miffre, Marion Jacquy, Matthias Büchner, Gérard Tréneç, and Jacques Vigué. Parallel temperatures in supersonic beams: Ultracooling of light atoms seeded in a heavier carrier gas. The Journal of chemical physics, 122(9):094308, 2005.

Appendix A

OH Cheat Sheets

The following two pages compile the most important properties of OH relevant to Stark decelerator.

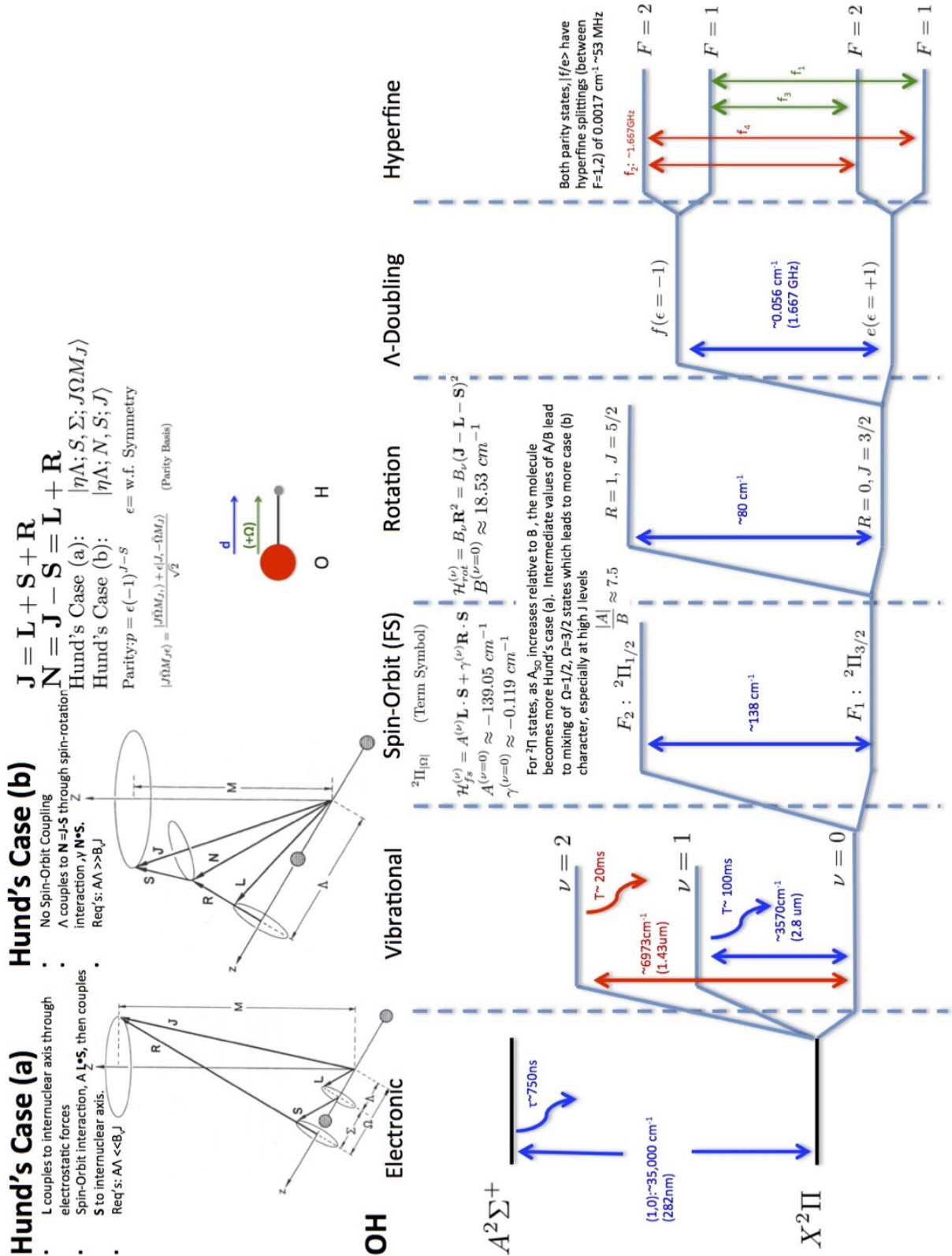
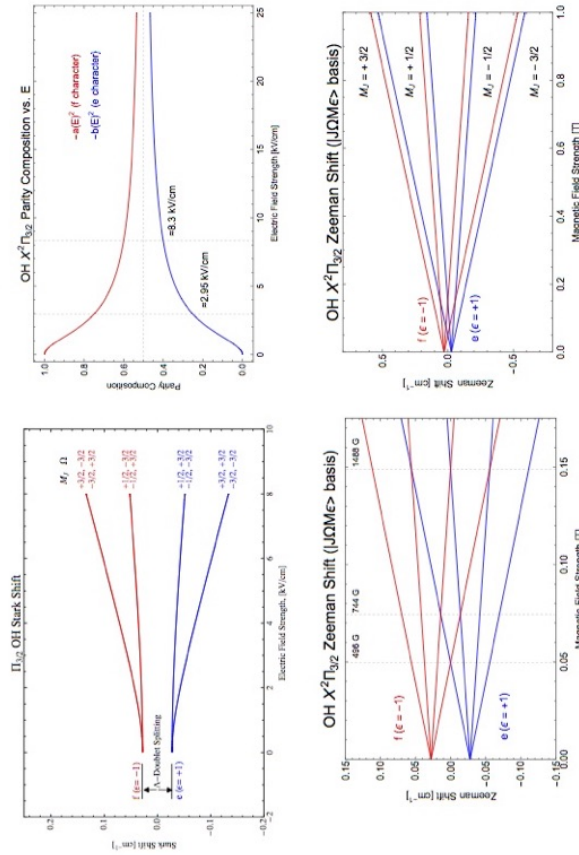


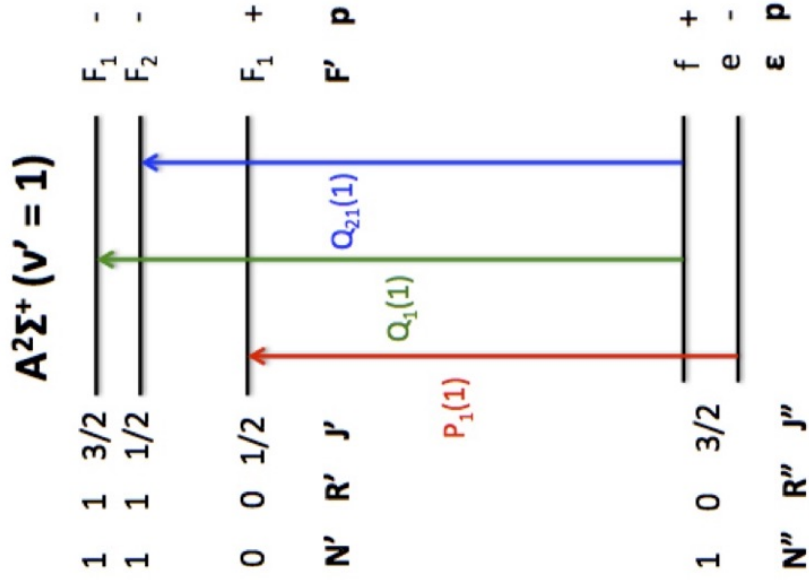
Figure A.1: OHcheatSHEETpage1

External Fields (w/o Hyperfine and assuming pure Hund's Case-a) and AX band e-dipole allowed transitions

Initially pure f state



$$\mu_B^{(e,f)} = \mu_B \frac{M\Omega}{J(J+1)} \quad (\text{Lab Frame})$$



$$F_1: X^2\Pi_{3/2} (v'' = 0)$$

Figure A.2: OHcheatSHEETpage2

Appendix B

Analytic Results for Modeling Supersonic Beam Properties

The purpose of this appendix is to compile some important results from compressible flow (macroscopic) and collisional (microscopic) theory to estimate properties of continuous supersonic beams. As such, it is an extension of Ch. 3. The basic equations can be used to estimate the properties of pulsed supersonic beams provided that one uses the appropriate effective nozzle diameter for the pulsed source (see Sec. 3.4.1 for more information.) The primary sources for this material are Refs [83] [29] [82] [115] [296].

B.1 Centerline Flow Properties

It turns out to be convenient to express the flow velocity, u , (see Eqs 3.7 and 3.8) in terms of the (classical) local speed of sound $a_s(T)$, by using the *Mach number*, $M = \frac{u}{a_s(T)}$. For an ideal gas, $a_s(T)$ is given by

$$a_s(T) = \sqrt{\frac{\gamma RT}{W}} = \sqrt{\frac{\gamma k_B T}{m}} \quad (\text{local speed of sound}) \quad (\text{B.1})$$

Then setting, $u = M * a_s(T) = M * \sqrt{\frac{\gamma k_B T}{m}}$ gives the centerline beam velocity as

$$u(M) = M \sqrt{\frac{\gamma k_B T_0}{m}} \left(1 + \frac{\gamma - 1}{2} M^2 \right)^{-\frac{1}{2}}. \quad (\text{B.2})$$

where m is the molar mass in [kg]. Dividing Eq. B.2 by the speed of sound in the reservoir, $a_s(T_0) = \sqrt{\frac{\gamma RT_0}{W}}$ yields

$$\frac{u(M)}{a_s(T_0)} = M \left(1 + \frac{\gamma - 1}{2} M^2 \right)^{-\frac{1}{2}} \quad (\text{B.3})$$

Eq. B.3 is plotted in Fig.B.1 for monatomic gases ($\gamma = 5/3$). At first thought it may be surprising that the beam forward velocity asymptotes to a maximum value that is only a factor $\sqrt{3}$ larger than the speed of sound in the reservoir, while the mach number continues to increase. This may be understood by recalling that the Mach number is defined as the ratio of beam velocity to the *local* speed of sound (Eq. B.1). As we have seen, the isentropic expansion converts random thermal motion into directed mass flow. Since there is only a finite amount of random energy available in the reservoir, the increase in mass flow velocity must be finite even in the case of infinite Mach number which corresponds to complete energy conversion from *thermal* \rightarrow *flow*. In fact, at infinite Mach number the mass flow velocity is only $(\frac{5}{3})^{1/2} = 1.29$ times as large as the most probable speed of molecules in an effusive beam. This limiting value is approached early on in the expansion, and from then on the mass flow velocity hardly increases at all. Thus, we come to the conclusion that the mach number can only increase because of a commensurate decrease in the local speed of sound due to the dropping temperature. Another possibly confusing point is that the velocity starts from zero inside the reservoir (the origin of the expansion) where clearly thermal sample of molecules will have a nonzero average velocity. The difference is that we are talking about a "bulk" flow-velocity out of the nozzle and not the average molecular speed.

In addition to the flow velocity $u(M)$, isentropic analysis ($\gamma = \text{constant}$) of the expanding gas also yields expressions for the temperature and density of the flow field as a function of Mach number. For 1-dimensional isentropic gas flow the relation is [83]

$$\left(\frac{n(M)}{n_0} \right) = \left(\frac{T(M)}{T_0} \right)^{\frac{1}{\gamma-1}} = \left(1 + \frac{\gamma - 1}{2} M^2 \right)^{-\frac{1}{\gamma-1}} \quad (\text{B.4})$$

where T_0 ($T(M)$) and n_0 ($n(M)$) are the temperature, and number density in the reservoir (beam) respectively. If the Mach number, M , is known then all thermodynamic variables can be computed for a supersonic expansion. It is important to note that the basic result of Eq. B.4 does not depend on the particular species of monatomic gas.

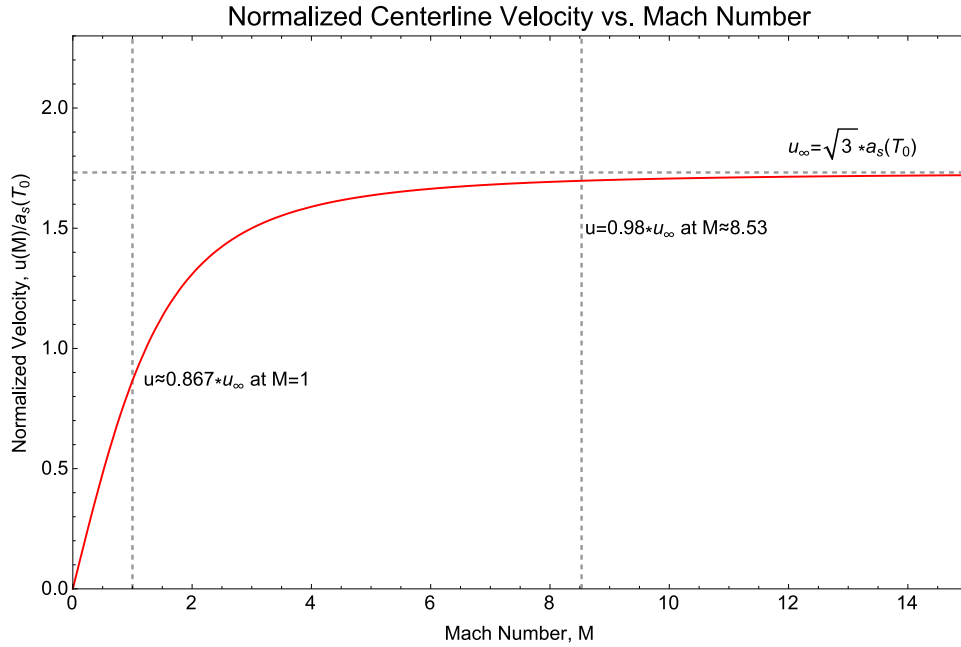


Figure B.1: Plot of centerline beam flow velocity vs. Mach number (Eq. B.3) for $\gamma = 5/3$. Note that the flow velocity has been normalized to the speed of sound in the *reservoir*. The dashed line indicates the asymptotic value of $u_\infty/a_s(T_0) = \sqrt{3}$ where a_s is the speed of sound in the reservoir. An important result of this plot is very early on in the expansion, the flow velocity has already reached 98% of the terminal velocity at a Mach number of ~ 8.5 .

For a monatomic gas ($\gamma = 5/3$), the expression for the temperature as a function of Mach number simplifies to

$$\frac{T}{T_0} = \left(1 + \frac{1}{3}M^2\right)^{-1}. \quad (\text{B.5})$$

Similarly, the expression for the number density is

$$\frac{n}{n_0} = \left(1 + \frac{1}{3}M^2\right)^{-3/2} \quad (\text{B.6})$$

Eq. B.5 and B.6 are plotted in Figs B.2 and B.3 respectively, for a reservoir temperature of $T_0 = 300K$.

B.1.1 The Method of Characteristics-Spatial Dependence of the Mach Number

In the previous Sec. the beam temperature, density and velocity were expressed in terms of the Mach number, M . This section gives basic expressions (without derivation) for the dependence of the Mach number on the position in space. The most important result of this analysis is that it allows the temperature

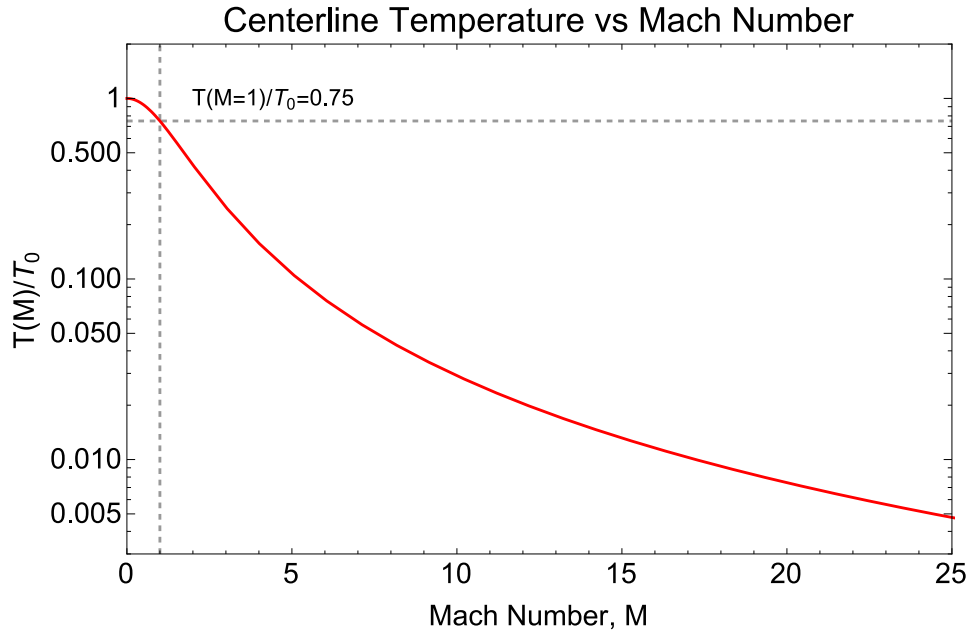


Figure B.2: Plot of centerline beam temperature vs. Mach number (Eq. ??). Note that at the sonic surface ($M=1$) the beam temperature has already cooled to $T = 0.75 * T_0$

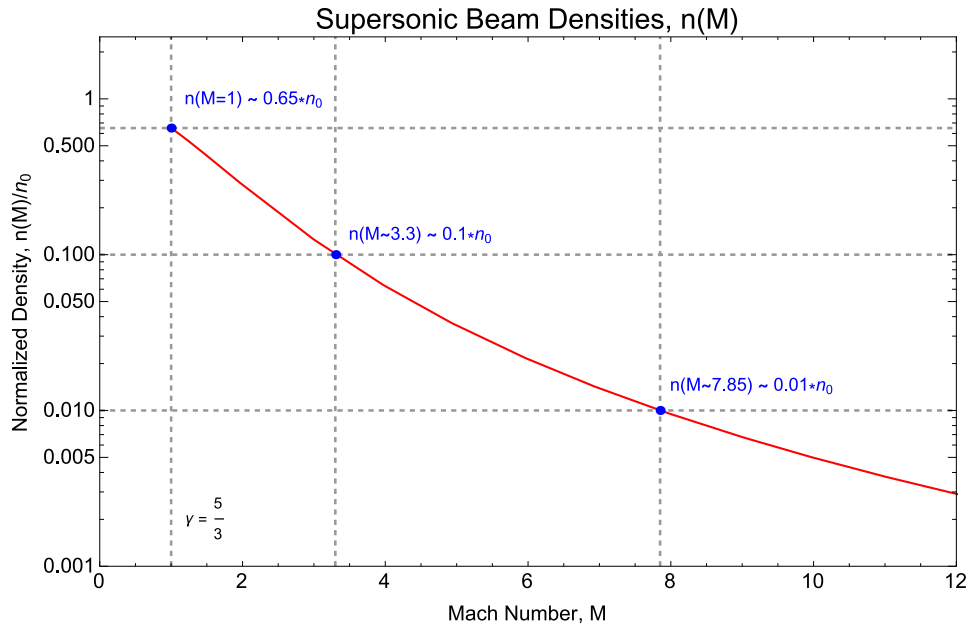


Figure B.3: Analytic dependence of the centerline density of a supersonic beam density (normalized against the value in the reservoir, n_0) a function of Mach number, M (Eq. ??) for $\gamma = 5/3$. The dashed lines indicate particular points of interest. At the *sonic surface* where $M=1$ the density has already fallen to $\sim 0.65 * n_0$. At, $M \sim 3.3$ and $M \sim 7.85$ the density has fallen by a factor of 10 and 100 respectively.

γ	x_0/d	A	ϕ	$(x/d)_{\min}$	Source	j	γ	C_1	C_2	C_3	C_4	A	B
1.67	0.075	3.26	1.365	2.5	3D	1	5/3	3.232	-0.7563	0.3937	-0.0729	3.337	-1.541
1.40	0.40	3.65	1.662	6	3D	1	7/5	3.606	-1.742	0.9226	-0.2069	3.190	-1.610
1.2857	0.85	3.96	1.888	4	3D	1	9/7	3.971	-2.327	1.326	-0.311	3.609	-1.950
1.20	1.00	4.29	—	—	2D	2	5/3	3.038	-1.629	0.9587	-0.2229	2.339	-1.194
1.10	1.60	5.25	—	—	2D	2	7/5	3.185	-2.195	1.391	-0.3436	2.261	-1.224
1.05	1.80	6.44	—	—	2D	2	9/7	3.252	-2.473	1.616	-0.4068	2.219	-1.231

$$M = A \left(\frac{x-x_0}{d} \right)^{\gamma-1} - \frac{1}{2} \frac{\left(\frac{\gamma+1}{\gamma-1} \right)}{A \left(\frac{x-x_0}{d} \right)^{\gamma-1}} \quad \left(\frac{x}{d} \right) > \left(\frac{x}{d} \right)_{\min}$$

$$\frac{\rho(y, x)}{\rho(0, x)} = \cos^2 \theta \cos^2 \left(\frac{\pi\theta}{2\phi} \right) \quad \frac{\rho(R, \theta)}{\rho(R, 0)} = \cos^2 \left(\frac{\pi\theta}{2\phi} \right)$$

$$\tan \theta = \frac{y}{x} \quad R^2 = x^2 + y^2$$

$$\frac{x}{d} > 0.5: \quad M = \left(\frac{x}{d} \right)^{(\gamma-1)j} \left[C_1 + \frac{C_2}{\left(\frac{x}{d} \right)} + \frac{C_3}{\left(\frac{x}{d} \right)^2} + \frac{C_4}{\left(\frac{x}{d} \right)^3} \right]$$

$$0 < \frac{x}{d} < 1.0: \quad M = 1.0 + A \left(\frac{x}{d} \right)^2 + B \left(\frac{x}{d} \right)^3$$

(a)
(b)

Figure B.4: Method of characteristics (MOC) fits for supersonic expansions. Panel (a) shows the results for the results of Ashkenas and Sherman (Eq. B.7) and panel (b) shows two the parameters for the other two expressions (Eqs B.12 and B.13). Both (a) and (b) are taken from [29].

and density of the beam to estimated as a function distance along the expansion.

Ashkenas and Sherman [29] developed a very accurate fit of the variation of the Mach number as a function of the distance x from the nozzle can be obtained by the function

$$M^{(1)} = A \left(\frac{x-x_0}{d} \right)^{\gamma-1} - \frac{1}{2} \frac{\left(\frac{\gamma+1}{\gamma-1} \right)}{A \left(\frac{x-x_0}{d} \right)^{\gamma-1}}; \quad \left(\frac{x}{d} \right) > \left(\frac{x}{d} \right)_{\min} \quad (\text{B.7})$$

where x is the distance from the nozzle, d is the nozzle diameter and A is a constant dependent on γ . The values of the contents A and x_0 obtained by Ashkenas and Sherman for several values of $\gamma = \frac{C_p}{C_v}$ are given in Fig. B.4a.

For monoatomic gases (the primary case of interest) we can take $\gamma = 5/3$ and Eq. B.7 reduces to

$$M^{(1)} = A \left(\frac{x-x_0}{d} \right)^{2/3} - \frac{1}{2} \frac{4}{A \left(\frac{x-x_0}{d} \right)^{2/3}}; \quad \left(\frac{x}{d} \right) > \left(\frac{x}{d} \right)_{\min} \quad (\text{B.8})$$

After a few nozzle diameters we can take $x-x_0 \approx x$ and drop the second term in Eq. B.8 entirely to yield

$$M \approx A(x/d)^{2/3} \quad (\text{B.9})$$

For monatomic gases, the prefactor is $A_{mono} \approx 3.26$.

The angular distribution of the supersonic expansion from a sonic nozzle can be estimated with

$$\frac{n(R, \theta)}{n(R, 0)} = \cos^2 \left(\frac{\pi \theta}{2\phi} \right) \quad (\text{B.10})$$

where for a monatomic gas, $\phi = 1.365$ (See Fig. B.4a). The FWHM of this distribution is determined by

$$\cos^2 \left(\frac{\pi \theta}{2\phi} \right) = 1/2 \quad (\text{B.11})$$

which gives a full divergence angle of $\theta_{FWHM} = 2 \times 0.6825 \text{Rad} \approx 2 \times 39^\circ = 78^\circ$

Despite its prevalence in the literature, Eq. B.7 is not the best possible fit. A second expression, $M^{(2)}$, has been used to obtain better fits at small distances. This fit is given below

$$M^{(2)} = \left(\frac{x}{d} \right)^{\frac{\gamma-1}{\gamma}} \left[C_1 + \frac{C_2}{\left(\frac{x}{d} \right)} + \frac{C_3}{\left(\frac{x}{d} \right)^2} + \frac{C_4}{\left(\frac{x}{d} \right)^3} \right] \quad \frac{x}{d} > 0.5 \quad (\text{B.12})$$

Eq. B.12 has the added benefit that it also applies to slit jet (2D) expansions. The differences are of the order $\sim 1\%$ for $\frac{x}{d} > 10$, but the second (Eq. B.12) is preferable for $(x/d) < 3$.

A third fit, $M^{(3)}$, for distances very close to the nozzle is

$$M^{(3)} = 1.0 + A \left(\frac{x}{d} \right)^2 + B \left(\frac{x}{d} \right)^3; \quad 0 < \frac{x}{d} < 1 \quad (\text{B.13})$$

B.2 Departures from the Idealized Continuum Model/Transition to Nonequilibrium conditions

The continuum model presented in Sec B.1 is based on the assumption that the gas is a continuous fluid, where in reality it is composed of discrete atoms and molecules. It remains a good approximation for high density gases where the collision frequency is high enough that thermal equilibrium is maintained throughout the expansion. At large distances from the nozzle however the gas becomes so rarefied (fundamentally due to $1/r^2$ falloff), and the two-body collision rate so low, that the assumption of local thermal equilibrium fails. This marks the beginning of the transition from continuum flow to collisionless effusive/free molecular flow. The boundary between the continuum and the effusive regime is referred to as the *quitting*

surface, because past this point the beam temperatures ceases to continue dropping. The location of the quitting surface can be estimated by determining the location at which the number of collisions *remaining* in the expansion crosses unity. This is the focus of the next section.

B.2.1 2–body collision Rates in the Expansion

In this section, expressions for the two body collision rate in a supersonic expansion is developed. Our basic approach is to use the results of the continuum model to express the collision frequency in terms of the Mach number (using the expression for $n(M)$). The collision rate can then be expressed in terms of the distance from the nozzle by using the results of the MOC.

The number of two-body collisions a single molecule makes in a time interval dt is given by

$$dZ_2 = \sigma_{eff} \langle v_{rel}(z) \rangle n(z) dt \quad (\text{B.14})$$

where n is the number density [$\#/cm^3$], $\langle v_{rel} \rangle$ is the average relative velocity in [cm/s], and σ_{eff} is the “effective” (to be defined in more detail later) collision cross-section in [cm^2]. The time interval dt our reference molecule spends between the position interval z and $z + dz$ is determined by the flow velocity, $u(z)$,

$$dt = \frac{dz}{u(z)} \quad (\text{B.15})$$

Plugging Eq. B.15 into Eq. B.14 gives the number of collisions in a experienced over a distance dz , as

$$dZ_2 = n(z) \sigma_{eff} \frac{\langle v_{rel}(z) \rangle}{u(z)} dz \quad (\text{B.16})$$

Clearly, the dependence of the collisions rate on distance, (Eq. B.16) can equivalently be expressed in terms of Mach number, M . To keep notation tidy in the next few lines we drop the explicit dependence of various flow properties (i.e.: $u[M(z)]$ etc) and keep only the Mach number. Then Eq. B.16 becomes

$$dZ_2 = \sigma_{eff} n(M) \frac{\langle v_{rel}(M) \rangle}{u(M)} dz \quad (\text{B.17})$$

The explicit expression the dependence of the flow velocity on the Mach number is given by Eq. B.2. Plugging Eq. ?? into Eq. B.2 gives allows the flow velocity to be expressed in terms of temperature, T , i.e.:

$$u(M) = \sqrt{\frac{\gamma k_B T_0}{m}} M \left(\frac{T(M)}{T_0} \right)^{1/2} \quad (\text{B.18})$$

In addition we can also use express the number density as $n(M) = n_0 \left(\frac{T(M)}{T_0} \right)^{-\frac{1}{\gamma-1}}$ (Eq. B.4), $\langle v_{rel} \rangle = \sqrt{\frac{8k_B T(M)}{\pi \mu}}$ where $\mu = \frac{m}{2}$ is the reduced mass of the collision pair (here assumed to be two identical atoms of mass m). Putting it all together yields for Eq. B.17:

$$\begin{aligned} dZ_2 &= n(M) \sigma_{eff} \frac{\langle v_{rel}(M) \rangle}{u(M)} dz \\ &= n_0 \sigma_{eff} \left(\frac{T(M)}{T_0} \right)^{-\frac{1}{\gamma-1}} \frac{\sqrt{\frac{8k_B T(M)}{\pi \mu}}}{M \sqrt{\frac{\gamma k_B T_0}{m}} \left(\frac{T(M)}{T_0} \right)^{1/2}} dz \\ &= n_0 \sigma_{eff} \frac{\sqrt{\frac{8k_B}{\pi \mu}}}{\sqrt{\frac{\gamma k_B}{m}}} \left(\frac{T(M)}{T_0} \right)^{-\frac{1}{\gamma-1}} \frac{\left(\frac{T(M)}{T_0} \right)^{1/2}}{M \left(\frac{T(M)}{T_0} \right)^{1/2}} dz \\ &= n_0 \sigma_{eff} \sqrt{\frac{16}{\gamma \pi}} \frac{1}{M} \left(\frac{T(M)}{T_0} \right)^{-\frac{1}{\gamma-1}} dz \end{aligned} \quad (\text{B.19})$$

At this point use the MOC where the distance from the nozzle is expressed in terms of the reduced distance from the nozzle, $\xi = z/d^*$ (i.e.: the ‘‘natural’’ longitudinal dimension for supersonic expansions) (using $dz = d^* d\xi$) gives

$$\boxed{dZ_2 = n_0 * d^* \sigma_{eff} \sqrt{\frac{16}{\pi \gamma}} \frac{1}{M(\xi)} \left(1 + \frac{\gamma-1}{2} M(\xi)^2 \right)^{\frac{1}{\gamma-1}} d\xi} \quad (\text{B.20})$$

The ‘‘number of collisions remaining in the expansion’’ follows by integrating Eq. B.20 from ξ to infinity. For the hard sphere model with an effective cross section independent of temperature, gives the following result,

$$\begin{aligned}
Z_2^{(tot)} &= \int_{\xi'}^{\infty} dZ_2 \\
&= n_0 * d^* \sigma_{eff} \sqrt{\frac{16}{\pi}} \frac{1}{\gamma} \int_{\xi'}^{\infty} \frac{1}{M(\xi)} \left(1 + \frac{\gamma-1}{2} M(\xi)^2\right)^{\frac{1}{\gamma-1}} d\xi \\
&= n_0 * d^* \sigma_{eff} \sqrt{\frac{16}{\pi}} F_{hs}^{(2)}(\xi, \gamma)
\end{aligned} \tag{B.21}$$

where we have identified,

$$F_{hs}^{(2)}(\xi, \gamma) = \frac{1}{\gamma} \int_{\xi}^{\infty} \frac{1}{M(\xi')} \left(1 + \frac{\gamma-1}{2} M(\xi')^2\right)^{\frac{1}{\gamma-1}} d\xi' \tag{B.22}$$

Using Eq. B.7 for the dependence of the Mach number on distance, $M(\frac{x}{d} = \xi)$ allows Eq. B.20 to be evaluated numerically. One of the most important things to note about Eq. B.21 is that the total number of 2 body collisions which are responsible for the cooling, are proportional to the product $P_0 * d$. Fig. B.5 shows a plot of Eq. B.21 for the rare gases, Kr, Ar, and Ne. Fig. B.6 plots Eq. B.21 for various nozzle diameters and a stagnation pressure of $p_0 = 2200 \text{ Torr}$ (the pressure used for the creation of OH beams).

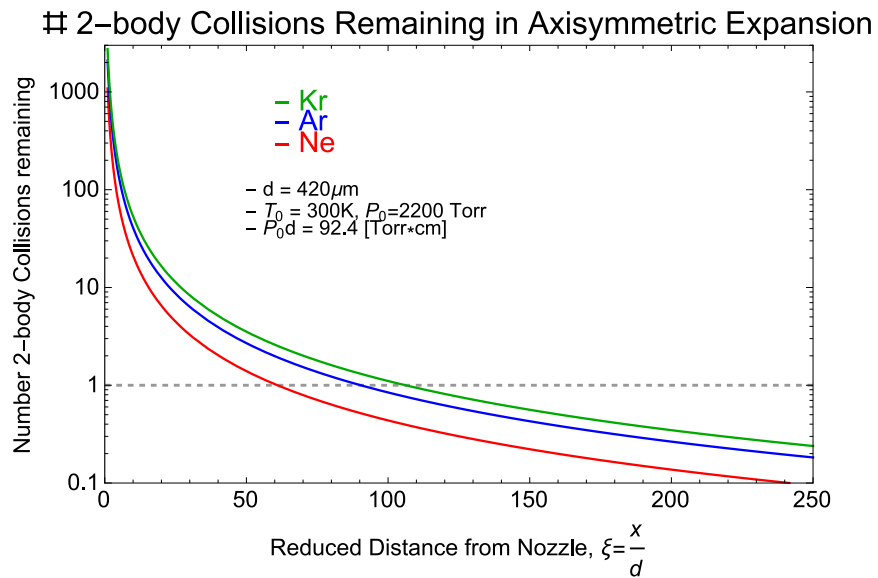


Figure B.5: Number of 2-body collisions remaining in an axisymmetric expansion. The distance where the curves crosses unity, serves to identify the location of the quitting surface.

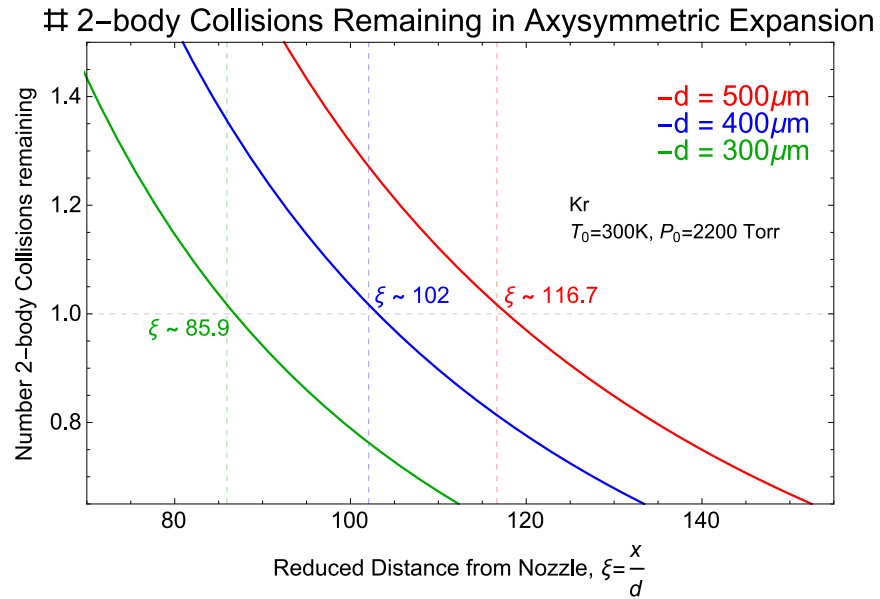


Figure B.6: Calculation for the location of the quitting surface for a pure krypton beam at various effective nozzle diameters, d . For $d = 300\mu\text{m}$, we have $x_q = 300\mu\text{m} * 85.9 \approx 2.6[\text{cm}]$. For $d = 400\mu\text{m}$, we have $x_q = 400\mu\text{m} * 102 \approx 4.1[\text{cm}]$. For $d = 500\mu\text{m}$, we have $x_q = 500\mu\text{m} * 116.7 \approx 5.8[\text{cm}]$.

B.2.1.1 Terminal Temperature and Speed Ratio

The results of the previous section allow the approximate location of the quitting surface to be identified. Also of great interest is the terminal temperature of the beam. This could be determined by correlating the location of the quitting surface with the terminal Mach number (the value of M at ξ_q) but in this regime of collisionless flow, the physical interpretation of the Mach number is unclear. Instead the thermal velocity spread is often characterized in terms of the *speed ratio* which is defined as the ratio of kinetic energy of the bulk flow to the characteristic thermal energy in the moving frame:

$$S = \left(\frac{\frac{1}{2}mu^2}{k_B T} \right)^{1/2} \quad (\text{B.23})$$

Equivalently, the speed ratio can be expressed in terms of the most probable thermal velocity, $v_{mp} = \sqrt{\frac{2k_b T}{m}}$:

$$S = \frac{u}{v_{mp}} = \frac{u}{\sqrt{\frac{2k_b T}{m}}} \quad (\text{B.24})$$

The speed ratio can be trivially related to the Mach number, $M = \frac{u}{a_s} = \frac{u}{\sqrt{\frac{\gamma RT_0}{W}}}$,

$$\boxed{S = \frac{u}{v_{mp}} = \sqrt{\frac{\gamma}{2}} M} \quad (\text{Speed Ratio}) \quad (\text{B.25})$$

The most accurate models for supersonic beams must account for dependence of the collision rate on the nature of the intermolecular potential between the atoms in the supersonic expansion [115] [29]. This is in contrast to simply taking a hard-sphere collision-cross section as was done Sec B.2.1 for simplicity. The two most careful analyses of the terminal speed ratio of supersonic beams are the treatments by Toennies and Winkelmann (denoted here by TW) [84] and Beijerinck and Verster (denoted here by BV) [85]. The notation used in the two works is different, but the terminal speed ratios predicted by both TW and BV can be written in the same form [297] by

$$S_{//\infty} = A \left[n_0 d \left(\frac{C_6}{k_B T} \right)^{1/3} \right]^\delta \quad (\text{B.26})$$

The TW values are $A = 1.413$ and $\delta \approx 0.53$ and the BV values are $A = 1.313$ and $\delta \approx 0.545$. The terminal speed ratio as a function of stagnation pressure, P_0 , for a nominal effective nozzle diameter, $d_{eff} = 500 \mu m$ is shown in Fig. B.7 for the noble gases. The relevant C_6 coefficients for each gas have been taken from Ref [29].

Close inspection of Fig. B.7 reveals some surprising things. The general trend is to predict that larger, heavier, more polarizable gases (i.e.: Xe, Kr) will have larger terminal speed ratios (reach colder final temperatures). This is basically because the heavier gases, with larger C_6 coefficients, will have larger collision cross sections. However, this simple estimate doesn't tell the whole story.

Anyone familiar with the state of the art of molecular beams is aware that the coldest molecular beams are not those with Kr or Xe carrier gases, but are in fact those with the *lightest* carrier gases (especially helium). While the large C_6 coefficient does give a larger collision cross section, it also implies a larger "well depth" for a bound state to be formed. Long story short, the basic reason that the terminal speed ratios shown in Fig. B.7 are not realized in practice is due to clustering, which is the topic of the next section.

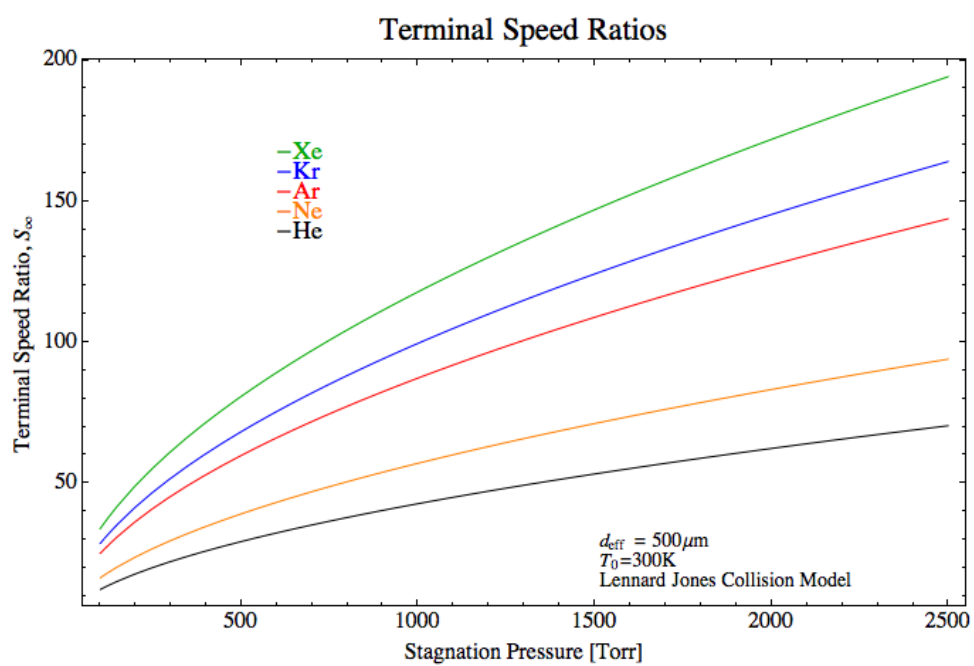


Figure B.7: Terminal Speed Ratio as a function of stagnation pressure, P_0 .